

INTERFEROMETRIC AND HARDNESS STUDIES  
OF SURFACES OF CRYSTALS

THESIS PRESENTED FOR THE DEGREE OF

DOCTOR OF PHILOSOPHY

IN THE

UNIVERSITY OF LONDON

BY

TARANIKANTI SHRIRAMMURTY

MAY, 1962

C7 - 9 MAY 1962

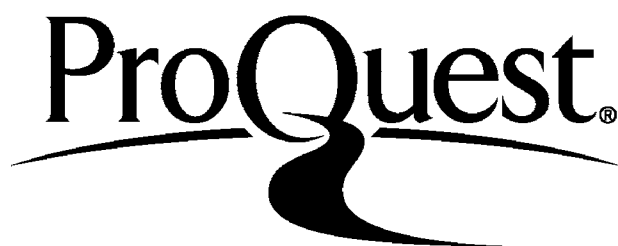
ProQuest Number: 10096680

All rights reserved

INFORMATION TO ALL USERS

The quality of this reproduction is dependent upon the quality of the copy submitted.

In the unlikely event that the author did not send a complete manuscript and there are missing pages, these will be noted. Also, if material had to be removed, a note will indicate the deletion.



ProQuest 10096680

Published by ProQuest LLC(2016). Copyright of the Dissertation is held by the Author.

All rights reserved.

This work is protected against unauthorized copying under Title 17, United States Code.  
Microform Edition © ProQuest LLC.

ProQuest LLC  
789 East Eisenhower Parkway  
P.O. Box 1346  
Ann Arbor, MI 48106-1346



## ABSTRACT

Part I of the thesis commences with a general picture of the various concepts of hardness and the relationship of indentation hardness to other physical properties. Types of measurement of hardness are reviewed with special reference to static indentation tests. The optical techniques and the apparatus made and used are described, including the interferometric techniques employed.

The following aspects of hardness of silicon carbide are studied:

- (1) The variation of hardness with load, the relation between 'recovered' and 'unrecovered' hardness and the surface distortions around the indentations.
- (2) The variation of hardness with direction: it is found that the  $[11\bar{2}0]$  and  $[01\bar{1}0]$  are respectively the directions of maximum and minimum hardness. An attempt is made to explain the results in terms of the shear stress on the slip plane.
- (3) Ring cracks formed by steady pressure made by a diamond ball: the distortions round the cracks and the profiles of sections are studied by multiple-beam interferometry and phase-contrast microscopy. Hertz's classical equation is applied to compare the results.

The micro-slip lines observed on a rare trigonal

pyramid face of a silicon carbide crystal due to diamond ball impacts are described.

A description is given of the analysis of silicon carbide crystals by X-rays.

Part II of the thesis gives a description of various types of micro-features observed on transparent crystals of silicon carbide. The features are studied by applying the techniques of multiple-beam interferometry and phase-contrast microscopy. The special point about these features is that they are depressions. An attempt is made to explain their existence on the basis of a theory postulated by Tolansky and the dislocation theory of evaporation of crystals by Cabrera and Levine.

A description is given of spiral-like features observed at the edge of some silicon carbide crystals.

An appendix to the thesis gives a brief account of interferometric studies made on sawn surfaces of diamond.

# C O N T E N T S

## PART. I

### HARDNESS STUDIES ON SILICON CARBIDE CRYSTALS

	Page
Chapter I    CONCEPT OF HARDNESS	
Introduction	1
Methods of Hardness Testing	3
Theories of Hardness	6
Relation between Hardness and other Physical Properties	10
Chapter II    HARDNESS MEASUREMENT BY INDENTATION	
Brinell Test	16
Meyer Hardness	17
Recovery of Indentation	18
Deformation around Indentation	19
Absolute Hardness	19
Diamond Pyramid Indenter	20
Ludwik Cone Test	22
Rockwell Hardness Test	25
Knoop Indenter	26
Double-Cone Indenter	27
Chapter III    PLASTIC DEFORMATION BY SLIP	
Slip	31
Direction and Planes of Slip	32
Critical Shear Stress	32
Crystallographic Nature of Slip	34
Consecutive Slip and Dislocations	35
Theoretical Shear Stress	36

	Page
Ideal Plastic Material	38
Plastic Deformation under Combined Stresses	39
Application to Hardness Tests	42
Chapter IV THEORIES OF CRYSTAL GROWTH	
Growth of Perfect Crystals	46
Surface Nucleation	50
Dislocations	53
Growth of Imperfect Crystals	54
Dislocation Theory of Evaporation of Crystals	56
Chapter V FORMATION AND CRYSTAL STRUCTURE OF SILICON CARBIDE	
Formation	62
Mode of Growth	63
Description of Types	65
Mixed Types	69
Chapter VI EXPERIMENTAL TECHNIQUES	
Multiple-Beam Interferometry	71
Fizeau Fringes	71
Fringes of Equal Chromatic Order	78
Thin-film Technique	80
Multi-layer Technique	81
Light-Profile Technique	82
Phase-Contrast Microscopy	83
Evaporation Technique	87
Indentation Apparatus	89
Robust Hardness Tester	90



	Page
Chapter VII X-RAY CRYSTALLOGRAPHY	
Diffraction of X-rays by Crystalline Matter	92
Reciprocal Lattice	93
Laue Photograph	97
Oscillation Photograph	98
Bernal Chart	100
Chapter XII Unit Cell Dimensions	102
Indexing Reflections	103
Stereographic Projection	104
Chapter VIII HARDNESS VARIATION WITH LOAD	
Review of previous Work	106
Elastic and Plastic Hardness	110
Chapter XII Vickers and Double-Cone Indentations with low loads in the present work	114
Vickers Indentations with higher loads in the present work	116
Double-Cone Indentations with higher loads in the present work	120
Discussion of Results	126
Chapter IX DIRECTIONAL VARIATION OF HARDNESS	
Introduction	131
Choice of Indenter	133
Vickers Indents-Observations and Measurements	136
Double-Cone Indents-Observations and Measurements	138
Discussion of the Results	142

	Page
Chapter X INTERFEROMETRIC STUDY OF RING- CRACKS ON SILICON CARBIDE	
Introduction	148
Observations	152
Measurements	157
Discussions of the Results	158
Impacts on Trigonal Pyramid Face	159
Chapter XI X-RAY ANALYSIS OF SILICON CARBIDE CRYSTALS	
Experimental Details	162
Observations and determination of Unit-Cell dimensions	164
Space Group Determination	172
<u>PART II</u>	
Chapter XII OPTICAL AND INTERFEROMETRIC STUDIES ON SILICON CARBIDE CRYSTALS	
Introduction	176
Description of Crystals	177
Description of Features	178
Category (a)	179
Category (b)	181
Category (c)	182
Category (d)	185
Discussion of the Observations	186
Chapter XIII STUDY OF SOME ADDITIONAL FEATURES ON SILICON CARBIDE CRYSTALS	
Growth Layers on (1011) Face	195
Floral Patterns	197

APPENDIXChapter XIV INTERFEROMETRIC STUDIES OF THE  
SAWN SURFACES OF DIAMOND

202

Hardness is expressed by the words: hard or hardness - used as the contrary of soft. Several attempts have been made to treat hardness as an original mechanical property of materials in addition to properties designated by the terms: elasticity, ductility, or strength. A closer examination of these numerous attempts will show that unfortunately the term hardness is often used in different senses by engineers, metallurgists, and mineralogists. While the term has no refer to very different properties, it is in fact was already brought out by Thomson (1925) when he stated that "hardness in common parlance represents a hazy conception of a complex aggregate of properties of a material some of which are related to each other." These properties include such varied things as resistance to abrasion, resistance to plastic deformation, high modulus of elasticity, high yield point and high strength. Although the immediate usefulness of hardness tests is to determine the uniformity of materials, it should not be allowed to obscure the real need for a fundamental investigation of hardness.

The recent and increasing serious difficulties in finding a general definition and a quantitative testing

## CHAPTER 1.

### CONCEPT OF HARDNESS

#### INTRODUCTION

Difficulties have been encountered in attempting to find an exact definition of the property of materials which is expressed by the words: hard or hardness - used as the contrary of soft. Several attempts have been made to treat hardness as an original mechanical property of materials in addition to properties designated by the terms: elasticity, ductility, or strength. A closer examination of these numerous attempts will show that unfortunately the term hardness is often used in different senses by engineers, metallurgists, and mineralogists while the same term may refer to very different properties. This fact was clearly brought out by Tuckerman (1925) when he stated that "hardness in common parlance represents a hazily conceived conglomeration or aggregate of properties of a material more or less related to each other." These properties include such varied things as resistance to abrasion, resistance to plastic deformation, high modulus of elasticity, high yield point and high strength. Although the immediate usefulness of hardness tests is to determine the uniformity of materials, it should not be allowed to obscure the real need for a fundamental investigation of hardness.

The second and perhaps more serious difficulty in finding a general definition and a quantitative testing



method of measuring hardness was encountered in the fact that practically in most, or perhaps all, of the methods proposed for the measurement of hardness the distributions of stress, actually applied, are not of a simple nature. It was, therefore, not possible to predict these stress distributions more accurately. The distributions of stress in the vicinity of an indentation is, furthermore, affected by many factors, among which elasticity, plasticity, afterflow, and strength must be mentioned first.

The precise definition of hardness also depends entirely on the method of measurement which will determine the scale of hardness obtained. Probably the best definition of hardness was given by Ashby (1951) according to which hardness is a measure of the resistance to permanent deformation or damage. Two scales of hardness are not necessarily related unless certain conditions of similarity in the mode of testing are fulfilled. This is so because the methods of making hardness tests embrace such diverse properties as resistance to penetration under pressure, resistance to scratching by a sharp point and resistance to abrasion when one surface is rubbed against another. Various tests have been devised to determine hardness as represented by one or other of the above properties.

## METHODS OF HARDNESS TESTING

The various types of tests and the methods that have been used for assessing the hardness of materials can be classified under four groups.

### Scratch Hardness.

It is the oldest form of hardness measurement and was first developed by mineralogists. It can be further divided into two types (a) a comparison test in which one material is said to be harder than another if the second material is scratched by the first, (b) a scratch is made with a diamond or steel indenter traversing the surface at a steady rate and under a definite load. The hardness is expressed in terms of the width or depth of the groove formed. The method was first put on a semi-quantitative basis by Mohs (1822) who selected ten minerals as standards, beginning with talc (scratch hardness) and ending with diamond (scratch hardness 10). The scratch hardness tests although useful in studying the relative hardness of materials, is difficult to operate. The scratching process itself is a complicated function of the elastic, plastic and frictional properties of the surfaces so that the method does not easily lend itself to a theoretical analysis.

### Static Indentation Hardness.

The static indentation methods are most widely used for hardness measurements and cover a large number of testing conditions, the main variants being the nature

of the indenter and the load applied. The methods involve the formation of a permanent indentation by the penetration of an indenter of known shape, applied under a known force for a definite amount of time. The hardness of the material is then given by the ratio of the applied load to the surface area of the indentation. It is necessary to make the indenter from a very hard material and for this reason either a hardened steel sphere or a diamond pyramid or cone is employed. As the distribution of stress will be different with indenters of different shape, the values of hardness will also be different. A detail description of various indenters will be given later.

#### Dynamical or Rebound Hardness.

Dynamical or rebound hardness may be defined as the resistance of the material to local indentation when the indentation is produced by a rapidly moving indenter. In most practical methods a steel sphere or diamond cone is allowed to fall under gravity on to the surface of the testing material. The hardness is either expressed in terms of the energy of impact and the size of the remaining indentation or it is expressed in terms of the height of rebound of the indenter.

The impact made by a hard spherical indenter, when it is dropped on the horizontal flat surface of a softer material, can be divided into four main stages according to Tabor (1948). At first the region of

contact will be deformed elastically and if the impact is sufficiently gentle the surface will then recover elastically and separate without residual deformation. The collision in this case is purely elastic and the time of impact, mean pressures, and deformations are given by Hertz's equations for elastic collisions. The second stage occurs if the impact is such that the mean pressure exceeds about  $1.1 Y$ , where  $Y$  is the yield stress or elastic limit of the material. A slight amount of plastic deformation will occur and the collision will no longer be truly elastic; this onset of plastic deformation occurs for extremely small impact energies. At higher energies of impact the deformation rapidly passes over to a condition of 'full' plasticity (stage 3) and full-scale plastic deformation proceeds until the whole of the kinetic energy of the indenter is consumed. Finally a release of elastic stresses in the indenter and the indentation takes place as a result of which rebound occurs (stage 4). The above analysis holds good for an 'ideal' plastic material. Any attempt to make a full analysis of the four phases involved in the collision process is extremely complicated and difficult.

#### Abrasive and Cutting Hardness.

Abrasive hardness may be defined as resistance to wearing away. Resistance to wear or abrasion is generally thought of as the amount of material removed



under certain conditions. Abrasion between two materials will vary with the coefficient of friction between surfaces, surface conditions, speed of test, cold working and other factors. Many investigators have developed a wear tester which gives them important and valuable results in so far as their one particular problem is concerned; but little has been accomplished in adapting the test to different substances on a universal basis.

Cutting hardness is an indication of the workability of materials. The workability or machinability of materials by a machine tool depends on many factors, such as toughness, abrasive qualities and hardness as determined by resistance to permanent indentation. These tests are comparable for different materials only within very narrow limits. The tests are generally made on a specially modified machine tool and the variables involved include sharpness of cutting tool, speed of test and amount of pressure applied to the cutting tool.

### 3. THEORIES OF HARDNESS

A study of the various theories of hardness leaves one with a feeling that they overlap widely and are more or less confusing. This is natural, no doubt, because of our ignorance concerning the property of hardness. The theory which seems most consistent with itself and has more experimental evidence to support

it than others, is the one advanced by Jefferies and Archer. It is called 'The slip interference theory of the hardness of metals'. As hardness is a general property of solids, whether metals or non-metals, it can be extended to all solids. The theory is built up by defining hardness as 'resistance to permanent deformation'. But if hardness is to be treated as 'resistance to penetration' allowance will have to be made for the forces of friction between the atoms of the body tested and those of the penetrator.

Permanent deformation may be characterised by the point of yield in the stress-strain curve. Solids owe their resistance to deformation to the forces between the atoms. These forces are both attractive and repulsive. Repulsive forces are manifested by the resistance of materials to hydrostatic pressure by which the atoms are forced closer together in all directions. Under direct tension the distances between atoms are increased in the direction of the load and decreased at right angles that is, in the direction of the secondary compressive stresses. There is no condition of loading corresponding to a negative hydrostatic pressure, under which interatomic distances would be increased in all directions. Any permanent deformation of a material involves changes in the relative positions of some of the atoms, and therefore, the breaking, temporarily at

least, of some interatomic 'bonds'. The rupture of any material, whether with or without permanent deformation, also involves the breaking of interatomic and inter molecular bonds. The greatest possible resistance that a material can offer to deformation or rupture, is the summation of all the interatomic bonds on a plane through the specimen normal to the stress, a summation which may, for convenience be termed as the 'absolute cohesion' of the material. Actually, such a summation of forces is never realised, because rupture always takes place by degrees, and the breaking of atomic or molecular bonds is not simultaneous. The tensile strength of a material merely represents the maximum number of atomic bonds that came into play simultaneously during the test.

Crystalline materials are built up of atoms arranged in a definite and repeated patterns. The regularity of atomic arrangement gives rise to certain planes of weakness or low resistance to shearing stress. When an external load produces a shearing stress on such a plane, which exceeds the resistance of the crystal to shear on that particular plane, fracture of the crystal takes place. The fragments formed may or may not adhere to each other. If they do not, the failure of the crystal is complete, and it is said to be brittle. The plane of weakness is known as a "cleavage plane". In many crystals the fragments adhere and merely glide or slip

over each other. The result of such slip, repeated on many planes, is a measurable permanent deformation. The crystal is ductile, and the planes of weakness are called 'slip planes'.

The first appreciable formation of slip planes marks the beginning of plastic deformation and, therefore, the passing of the elastic limit. The resistance to permanent deformation, which is a general measure of hardness and strength, represents resistance to the beginning and propagation of slip. Anything that serves to hinder slip is a source of strength and hardness. The hardening and strengthening of materials by any known methods may be considered as due principally to interference with slip.

One other theory is suggested this is known as Hertz's theory of hardness. The theory may be exemplified by considering two rounded bodies which just touch each other. When these are pressed together, the original point of contact increases to a definite area, and when both bodies are spherical or one is plane and the other spherical, the contact area is a circle. From purely elastic considerations Hertz derived expressions for the stresses and strains at all points in the two bodies, and hence for a known pressure and from measurements of the contact circle, the maximum shear



stress in the material can be obtained. His analysis is in approximate agreement with experimental measurements, when the elastic limits of the material are not greatly exceeded. Accordingly, the mean normal pressure over the contact area at the first deviation from elasticity can be taken as a rational measure of the hardness when two materials are in contact, and is definitely related to the elastic constants and elastic limits of the material. Unfortunately, the elastic limit of most materials is not very definite and the measurement of the small contact area is difficult, so the method cannot be used as a general test, despite its rational basis.

Relation between Hardness and other Physical Properties.

Although the fundamentals of indentation hardness are most difficult to define, many attempts have been made to relate hardness to other physical properties of a material. An attempt to give a physical interpretation of indentation hardness on the basis of the stress/strain relationship obtained in a tensile test was given by Richer (1945). He considered that when an indenter is loaded and penetrates a material, the depth of penetration increases until the condition of the lattice immediately below the indenter has the same characteristics as that of a specimen in which the saturation value of compressive strain has been

attained. Holm and others (1949) have discussed the relationship between hardness and the yield point. They showed that under certain conditions of work hardening and geometry of the indentation, the hardness was approximately equal to three times the yield stress. Tabor (1951) has shown that for an ideal plastic material, the mean pressure  $P$  between a Vickers indenter and the material is given approximately by  $P=3.2\sigma_y$ , where  $\sigma_y$ , is the yield stress in tension and frictionless compression. Hill, Lee and Tupper (1947) obtained a theoretical solution for the deformation produced by a rigid frictionless wedge penetrating a plastic material; they calculated the variation in the penetrating force with wedge angle in terms of the yield stress. Meyer (1951) related the hardness numbers obtained in indentation tests with balls, pyramids and cones with the plastic and workhardening properties of the material. Cardullo (1924) expressed the hardness number as  $H=c E^m L^n$ , where  $c$  is a constant,  $E$  the modulus of elasticity,  $L$  the elastic limit in compression and  $m$  and  $n$  are small positive numbers which Cardullo considered to be near unity. Arbtin and Murphy (1953) showed that maximum tensile stress= $A+BH$ , where  $H$  is the hardness and  $A$  and  $B$  varied considerably with elastic modulus. Braun (1953) attempted to express the hardness in terms of the stress/strain curve, taking into account the elastic and plastic properties.

He deduced the expression for pyramid hardness

$$H = L \left( 1 + \frac{L}{H_0 d_c} \right)^2$$

where  $d$  is the diagonal for load  $L$  and both  $H_0$  and  $d_c$  are constants. He distinguished between a fully annealed material and one which has been cold-worked to give a permanent strain and introduced the conception that there was a relationship between the hardness and the extension to fracture, the latter being determined by the degree of coldwork.

Effect of crystallographic orientation of surface  
indented on hardness.

The first indication of a variation of hardness with crystal orientation was obtained by Huygens as early as 1690 while making scratch hardness tests on Iceland Spar. O'Neill (1923) reported that ball indentations on single crystals of aluminium produced elliptical impressions due to hardness variations in different directions. He also (1934) showed that the scratch hardness of a crystal is least in the direction parallel to the cleavage plane. Schultz and Hanemann (1941) observed slight asymmetries in the indents of aluminium crystals by using Vickers pyramid indenter. They found directional variations up to 7% by rotating the crystal relative to the indenting tool. Meincke (1950, 1951) also reported directional variations in the case of single crystals of Al, Zn and Cu.

Although the irregular impressions produced by

indentation tests with ball and pyramid indenters are an indication of a directional variation of the hardness of a material, a quantitative investigation of the directional hardness was not made until Daniel and Dunn (1949) studied the same on single crystals of silicon ferrite and zinc by using a Knoop indenter. Later Tolansky and Williams (1953) studied the directional hardness variation on single crystals of tin and bismuth by using a double-cone indenter. But there is no evidence in the literature of a similar study for non-metals, particularly for hard crystals.

Flow pattern of the material surrounding the indent.

Except for the work of Tolansky and Williams (1953) there is no evidence in the works quoted above of making a study of the flow pattern of the material surrounding the indent. Tolansky and Nickols (1949,1950) for the first time, revealed the existence of curious flow anomalies closely related to crystallographic directions by applying multiple-beam interferometric methods to the examination of surface flow around Vicker's pyramid indents on single crystals of tin. A similar study was made by Tolansky and Williams (1953) on single crystals of tin and bismuth by using a double-cone indenter.

Micro-hardness Tests.

According to Bergsman (1945) and others



micro-hardness testing of hardness required examination of small specimens at small loads, below 100 gm. Williams (1949) suggested extending micro-hardness testing to soft metals with a load of 350 gm. and Grodzinski (1951) recommended the use of loads up to 1000 or 2000 gm. for the micro-hardness testing of hard materials. The term 'micro-hardness testing' has no real significance although it is generally accepted as implying the measurement of hardness at low loads. The suggestion has been made that a more correct term is 'micro-indentation' hardness testing, which relates the type of test to that involving small dimensions of the impression obtained. This suggests that testing conditions which would fall into this class for a very hard material would not apply for a softer material, as the impression would be too large. The term 'micro-hardness' could be taken to imply that the hardness at low loads is necessarily different to that measured at high loads and this cannot be assumed. To obviate this difficulty, O'Neill has suggested that the methods should be referred to as 'hardness micro-testing'. In this thesis most of the results have been obtained in the range of 1 to 5kg. as they appear very relevant to the general discussion of low load testing of hard materials. Experiments have, however, shown that the indentation hardness at low loads, varied with the load. Theories put forward to explain this variation are conflicting

and often misleading. This aspect will be taken up in detail, while discussing the hardness variation of silicon carbide with load.

In this chapter an account will be given of the various types of tools used for indentation hardness measurements. The processes involved in the different hardness tests and the disturbances which occur around the indentations will also be discussed while describing the various methods. As the entire hardness measurements in this thesis have been made by static indentation methods, the word hardness whenever referred to in future, will always imply static indentation hardness.

#### Brinell Test.

The beginning of the twentieth century marked a milestone in the history of hardness testing. In 1900 Brinell described his ball test. In it a hardened steel ball is forced under a definite load into a flat surface of the material to be tested. When equilibrium has been reached, say after 15 or 30 seconds, the load and the indenter are removed. The diameter of the depression produced is measured and the hardness number is taken as the load divided by the area of the curved spherical surface of the cavity. If  $D$  is the diameter of the depression and  $d$  is diameter of the ball (which is assumed to remain spherical), then the area of the

## CHAPTER II

### HARDNESS MEASUREMENT BY INDENTATION

As has been stated earlier, the commonest form of making hardness measurements, is by indentation tests. In this chapter an account will be given of the various shapes of tools used for indentation hardness measurements. The processes involved in the different hardness tests and the disturbances which occur around the indentations will also be discussed while describing the various methods. As the entire hardness measurements in this thesis have been made by static indentation methods, the word hardness whenever referred to in future, will always imply static indentation hardness.

#### Brinell Test.

The beginning of the twentieth century marked a milestone in the history of hardness testing. In 1900 Brinell described his ball test. In it a hardened steel ball is forced under a definite load into a flat surface of the material to be tested. When equilibrium has been reached, say after 15 or 30 seconds, the load and the indenter are removed. The diameter of the depression produced is measured and the hardness number is taken as the load divided by the area of the curved spherical surface of the cavity. If  $d$ , is the diameter of the depression and  $D$  is diameter of the ball (which is assumed to remain spherical), then the area of the

curved spherical surface of the cavity is

$$A = \frac{1}{2} \pi D (D - \sqrt{D^2 - d^2})$$

If W is the total load in kg. then by definition

$$\text{Brinell Hardness} = \frac{W}{A}$$

where A is in square mm., that is when D and d are measured in mm. Evidently if W and D are fixed  $\frac{W}{A}$

depends on d, which is the measurement made in this test. Actually different loads (W) and different diameters of the ball, give somewhat different results but the Brinell test is now standardised by the adoption of a ball of 10 mm. in diameter and a load of 3000 kg. To eliminate various errors and to preserve geometrical similarity of the impressions as much as possible the diameter of the impression should be kept within the range of 0.25 to 0.50 times the diameter of the ball.

#### Meyer Hardness.

Brinell hardness number (B.H.N.) is not a satisfactory physical concept, for the ratio of the load to the curved area of the indentation does not give the mean pressure over the surface of the indentation. The mean pressure between the surface of the indenter and the indentation is equal to the ratio of the load to the projected area of the indentation. This quantity, as a measure of the hardness, was first proposed by Meyer



in 1908 and is referred to as the Meyer Hardness. Thus

$$\text{Meyer Hardness} = \frac{4W}{\pi d^2}$$

Relation between load and size of indentation.

The relation between the load and the size of the indentation for spherical indenters is given by Meyer's Law according to which

$$W = kd^n,$$

where W is the load and d is the chordal diameter of the remaining indentation; k and n are constants for the material under examination. The value of n is generally greater than 2 and usually lies between 2 and 2.5.

Recovery of indentation.

It is found that when the load and the indenter are removed, the indentation left in the material has a larger radius of curvature than that of the indenter. Foss and Brumfield (1922) have shown that the indentation is symmetrical and of spherical form, but that its radius of curvature may, for hard materials, be as much as three times as large as that of the indenter. This effect is referred to as 'shallowing' in the hardness literature and is ascribed to the release of elastic stresses in the material. There is also a diminution in the chordal diameter of the indentation when the indenter is removed but in general the effect is very small. Hence depth measurements of the 'recovered' indentation are much more unreliable than measurements of the chordal diameter of the 'recovered' indentation.

In effect the mean pressure calculated from the diameter of the 'recovered' indentation will be nearly the same as the mean pressure existing between the indenter and the surface before the load is removed.

#### Deformation around the indentation

As a result of the displacement of the material from the indentation itself, there is appreciable deformation of material around the indentation. In some cases there is an upward extrusion of displaced material so as to form a raised crater. This effect is known as 'piling-up' and is observed with highly worked materials (1951) (figures 1a & 2a). On the other hand with annealed materials, there is a tendency for the material to be depressed around the indentation (figures 1b & 2b) and this effect is known as 'sinking-in'. This depression is only observed close to the rim of the indentation, and at distances well removed from the indentation, a slight elevation of the material above the original surface level is usually found. The 'piling-up' and 'sinking-in' contribute some uncertainty to the diameter of the indentation.

#### Absolute Hardness

It is well known that during the formation of the indentation, the effective hardness of the material itself increases due to the work-hardening of the material during the indentation process. Attempts have been made

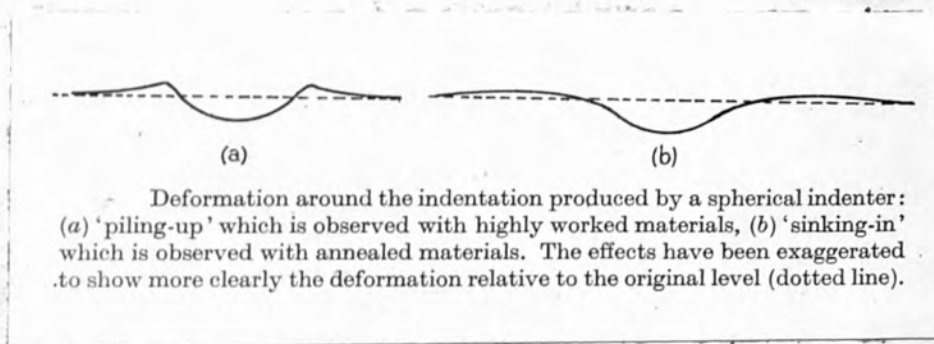


FIG. 1

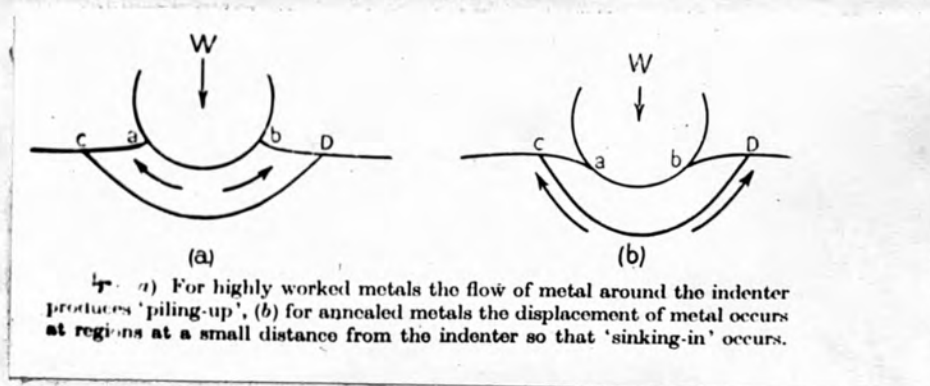


FIG. 2

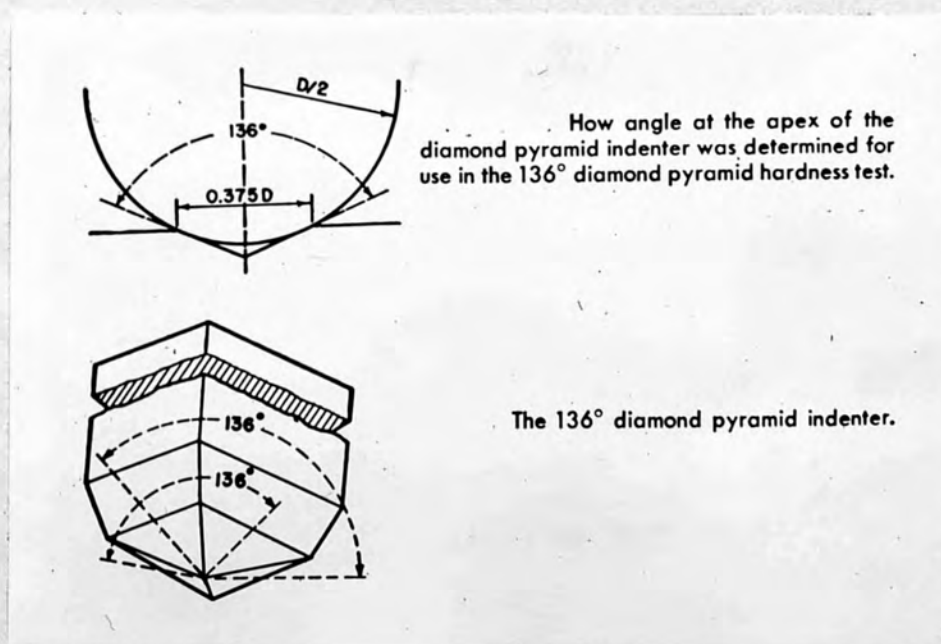


FIG. 3

to devise methods to determine the hardness of materials, in which no work-hardening takes place during indentation. This is possible only when no appreciable plastic deformation of the material takes place while testing the material; in other words the method should be plastically strainless.

Harris (1922) and Mahin and Foss (1939) carried out experiments to determine this 'absolute' hardness and showed that it was about  $1/3$  that of the 'normal' hardness in the case of metals.

#### DIAMOND PYRAMID INDENTERS

The diamond pyramid indenter, commonly known as Vickers indenter, was introduced by Smith and Sandland (1922) for hardness measurements. The indenter is made of diamond and is in the form of a square-based pyramid, having an angle of  $136^{\circ}$  between the opposite faces. The choice of this angle is based on an analogy with the Brinell test. In the Brinell test the range of the chordal diameter allowed  $0.25D$  to  $0.50D$ , where  $D$  is the diameter of the ball: the average of these is  $0.375D$ . When tangents are drawn from the point of contact of an impression of this diameter and the circumference of the ball indenter, the included angle comes out to be  $136^{\circ}$ . This is shown in figure (3a). Figure (3b) shows the form of the pyramid indenter. This indenter is used on the well known Vickers hardness machine with which loads in the range of 1 to 120 kg.



may be applied automatically for a standard period of 30 seconds. On removal of the load, the two diagonals of the impression are measured and the mean taken. A micro-hardness tester has been designed for use with a Vickers projection microscope, manufactured by Messrs. Cooke, Troughton and Simms. In this instrument loads in the range of 1 to 200 gm. can be used. This instrument (fig.45) will be described later.

The hardness values given by the Brinell and Vickers tests for a given material are practically identical in the lower ranges; but above a Brinell value of about 500, the numbers obtained with the ball become lower than those with the diamond pyramid because of the deformation of the ball indenter. The geometry of the indenter is such that the base of the pyramid has an area equal to 0.927 times the surface area of the faces. As in the case of the Brinell number, the Diamond Pyramid Hardness (D.P.H.) or the Vickers hardness number ( $H_V$ ) is given by the ratio of the load in kg to the contact area of the impression in  $\text{mm}^2$ .

$$\text{D.P.H.} = \frac{2W \sin \frac{\theta}{2}}{d^2} = \frac{1.8544W}{d^2} ; \text{ where}$$

$W$  = load in kg.,  $d$  = diagonal of impression in mm.

$\theta = 136^\circ$  = angle between opposite faces of the pyramid.

A dimensional analysis indicates that the Vickers hardness number should be independent of the load for

homogeneous plastic distortion; but variations are observed at low loads due to the mechanism of indentation at low loads being different to that at high loads. Although the indenter, being made of diamond, suffers very little deformation during the formation of the indentation, it is generally found that when the indenter is removed, the impression is not a perfect square. For annealed materials it is found that the impression has concave boundaries ( pin-cushion appearance) corresponding to 'sinking-in' of the material around the flat faces of the pyramid. In such a case the diagonal measurement gives a high value of both the projected and contact areas of the indentation and produces erroneously low hardness numbers. For highly worked materials the indentation has convex boundaries (barrel-shaped appearance) corresponding to 'pile-up' of the material around the faces of the indenter. This leads to the diagonal measurement giving a low value of the area and erroneously high hardness numbers. Empirical corrections for these effects have been suggested.

#### LUDWIK CONE TEST

In an effort to simplify the Brinell test and to make the hardness number independent of the load and the dimensions of the impression, Ludwik (1908) proposed the use of the cone test. He used a cone of  $90^{\circ}$  angle and defined the hardness as the mean pressure

over the surface of the indentation. Thus

$$\text{Ludwik Hardness Number } (H_L) = \frac{\text{load}}{\text{conical contact area}} = \frac{W}{\pi d^2 / 4 \sin \frac{\alpha}{2}},$$

where  $W$  = load in kg.,  $d$  = diameter of the indentation in mm. and  $\alpha$  = cone angle. Putting  $\alpha = 90^\circ$

$$H_L = \frac{4W}{\sqrt{2} \pi d^2}$$

The true pressure  $P$  between the indenter and the indentation, if there is no friction between the surfaces, is again given by the ratio of the load to the projected area of the indentation, that is  $P = \frac{4W}{\pi d^2}$ . It follows, therefore, that the Ludwik hardness number is simply  $\frac{1}{\sqrt{2}}$  of the mean yield pressure  $P$ .

Experiments show that the Ludwik hardness is practically independent of the load though it depends on the angle of the cone. It is seen that the more pointed the cone, the larger is the yield pressure. Hankins (1925) suggested that this increase in yield pressure may be explained in terms of the friction between the cone and the material. He assumed that there is an intrinsic yield pressure  $P$  which is independent of the shape of the indenter. Then over any element of surface, of the cone, of area  $ds$ , the force normal to the element is  $P ds$  (figure 4). If the coefficient of friction between the surface of the cone and the indentation is  $\mu$ , the frictional force tangential to the element is  $\mu P ds$ . The components of these forces in

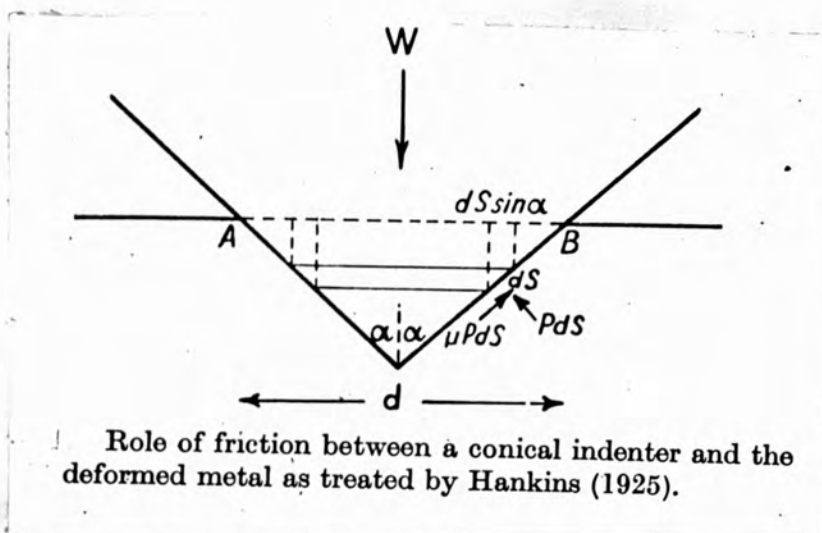


FIG.4

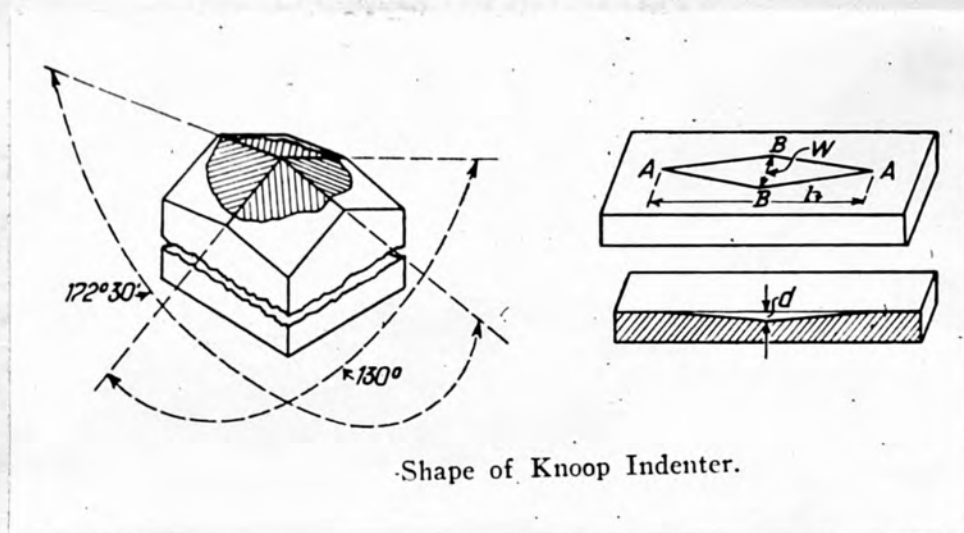


FIG.5

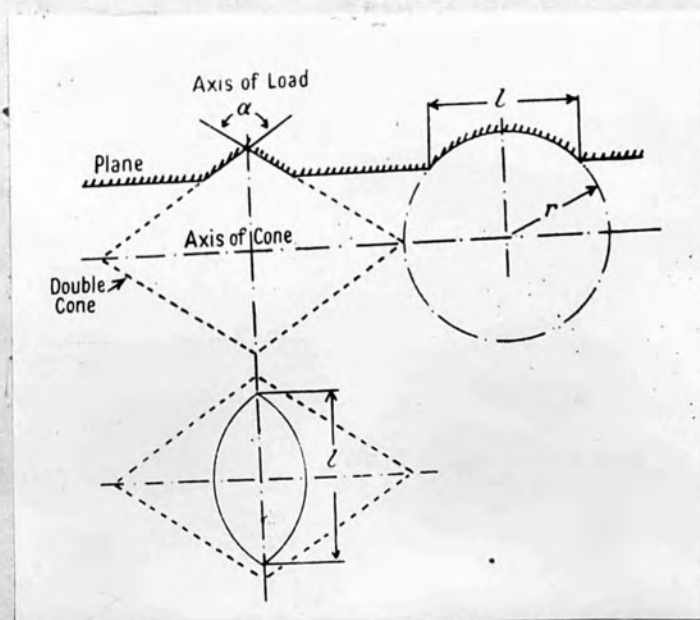


FIG.6



the horizontal direction, when summed over the whole area of the cone, cancel out because of symmetry. The components in the vertical are  $Pds \sin \alpha$  and  $\mu Pds \cos \alpha$  and these, when summed over the area of the cone, must be equal to the normal force  $W$ .

$$\text{Hence } W = \int dW = \int (Pds \sin \alpha + \mu Pds \cos \alpha) \\ = P(1 + \mu \cot \alpha) \int \sin \alpha ds.$$

$$\text{But } \int \sin \alpha ds = \text{the area of the section AB} \\ = \frac{\pi d^2}{4}$$

$$\text{Therefore } W = P(1 + \mu \cot \alpha) \frac{\pi d^2}{4} \\ \text{or } P = \frac{4W}{\pi d^2} \left( \frac{1}{1 + \mu \cot \alpha} \right) = P_0 \left( \frac{1}{1 + \mu \cot \alpha} \right),$$

where  $P_0$  is the yield pressure when there is no friction.

From this analysis it is seen that  $P$  is larger the smaller the value of  $\alpha$ . This treatment however is not satisfactory on general physical grounds; for instance when a cone becomes a flat cylindrical punch i.e.  $\alpha = 90^\circ$ ,  $P$  has the value  $\frac{4W}{\pi d^2}$ ; this would mean that the yield pressure is independent of the friction between the face of the indenter and the indentation. The full plastic treatment shows that this is not true. This point will again be referred to while discussing the plasticity of the material.

Devries (1949) carried out tests using cones of  $60^\circ$  and  $90^\circ$  on copper, iron and steel and noted that the apparent hardness number decreased with increasing load. O'Neill (1934) however, states that the hardness

should be practically independent of the load, if the measurements of the diameter or depth of the indentation also include any piled-up ridges present.

#### ROCKWELL HARDNESS TEST

This hardness measuring device has attained an enviable reputation because of its speed, accuracy and wide range of adaptability. The Rockwell hardness number (1922) is based on the additional depth to which a test point or ball, is driven by a heavy load beyond the depth to which the same penetrator has been driven by a definite light (initial) load. This load is generally 10 kg. For exceptionally hard bodies the indenter is made of a diamond cone of  $120^{\circ}$  angle with a mechanically lapped spherical point. The standard major load for this indenter ( Rockwell 'C' ) is 150 kg. For soft materials a specially hardened steel ball, 1/16th inch in diameter is used as the indenter (Rockwell 'B' ). The standard major load for this is 100 kg. The tester is so designed that the hardness number is automatically indicated on a dial. This test has two great advantages. (1) The application and retention of the minor load, prepares the surface upon which the increment in penetration due to the major load is based. (2) The hardness value is read directly on the dial gauge and optical measurements of the indentation diameter are unnecessary. As there may be appreciable

elastic 'recovery' in depth, when the major load is removed, this method will tend to give higher hardness values.

#### THE KNOOP INDENTER.

A modified pyramidal indenter was brought out by Knoop (1939) in which he altered the angles between the opposite faces of the pyramid to give lozenge shaped (rhomb) indentations. The diagonals of these indentations have an approximate ratio of 7 to 1 instead of 1 to 1 as in the case of Vickers pyramid indenter. Figure (5) gives a line drawing of the shape of the indenter. The length,  $l$ , of the indenter is 7 times that of the width  $w$ . The pyramid shape has included longitudinal angles of  $172^{\circ} 30'$  and included transverse angles of  $130^{\circ} 0'$ . The depth of the indentation is about  $1/20$  of its length. It was found that the greatest strain came at B-B and relatively little strain at all exists beyond A-A. As a result, elastic recovery of the indentation takes place largely along the direction B-B rather than along A-A. This means that from the dimensions of the indenter and the dimensions of the recovered indentation it is possible to ascertain both the recovered and the unrecovered dimensions of the indentation (1942). This instrument makes possible a study of the fundamentals of indentation (hardness) testing that are not afforded by ball, cone and square-based pyramidal indenters, which, because

of their symmetrical form, yield recovered dimensions only. Since the long diagonal  $l$ , changes little in length, it is used as a basis for the hardness measurement and is also useful in the study of directional hardness. The hardness is given by the ratio of the applied load to the unrecovered projected area.

$$\text{Knoop Hardness Number } (H_k) = \frac{W}{Cl^2} ;$$

where  $W$  = load in kg.,  $l$  = measured length of the long diagonal in mm., and  $C$  = a constant relating  $l$  to the projected area.

#### THE DOUBLE-CONE INDENTER.

The pyramid indenters described above have pointed ends, so that when they are pressed against a hard material, they are subjected to high stresses with a high stress concentration near the point. The stressed material is also subjected to similar stresses, therefore, there is a possibility of either the point breaking or the walls of the indentation breaking off. To eliminate this drawback, Grodzinski (1952) designed the double-cone indenter, which, instead of a pointed end, has a strong edge. The double-cone, although cut from a single diamond, may be regarded as the equivalent of two right circular cones placed with bases in contact and vertices opposing, such that the curved surfaces meet to include an angle exceeding  $120^\circ$ . Such an



indenting tool has a strong edge and when a load is applied as shown schematically in figure (6) the result is the production of an elongated, shallow, boat-shaped impression. The theory of the instrument has been given by Grodzinski (1951) who has calculated the area of the indent, assuming no recovery, and thus derived an expression for double-cone indentation hardness analogous to that of the widely used Vickers pyramid hardness.

The area of the impression is, closely enough,

$$A = \frac{l^3 \tan \frac{\alpha}{2}}{6R}$$

in which R is the radius of the cone,  $\frac{1}{2}\alpha$  the angle between the normal to the plane being indented and the cone, as shown in figure (7), and l the length of the indent. The depth is approximately  $= \frac{l^2}{8R}$  and the width

$$\frac{1}{4} \frac{l^2 \tan \frac{\alpha}{2}}{R} .$$

For any particular indenter, R and  $\alpha$  can be regarded as constants and if a load of W kg. has been employed to produce the indent then since indentation hardness is defined as W/A, the hardness is given by

$$\text{Double-cone Hardness (Hdc)} = \frac{W}{C l^3}$$

in which C is instrument constant  $= \frac{\tan \frac{\alpha}{2}}{6R}$

For the indenter used in this work  $R = 2\text{mm.}$ ,  $\alpha = 154^\circ$  so that C works out to be 0.361. Therefore

$$H_{dc} = \frac{W}{0.361 l^3} .$$

Since the length l appears as a cubic function, small variations in it will lead to large variations in

hardness values. This can be an advantage because it produces a hardness scale of great spread, but on the other hand, considerable care in measurement is imposed. To avoid doubt, it may be stated that since  $C$  has the dimensions of length  $^{-1}$ , the dimensions of  $l$  reduce to a square as in the case of Vickers hardness formula. While calculating hardness with this indenter, it is assumed that very little recovery takes place in the length of the indent, and all recovery due to deformation occurs along the width, which however does not enter in the formula.

The indenter gives a shallow depth compared with length, much more so than in the case of Vickers and Knoop indenters. The following table, given by Grodzinski, for a hard specimen, shows the numerical comparisons; the indentations were made on three hard materials (carbides) of comparable hardness, but not quite identical.

	H.N.	length mm.	width mm.	depth mm.	$\frac{\text{width}}{\text{length}}$	$\frac{\text{depth}}{\text{length}}$
D.C.	2013	0.155	0.005	0.0015	1/31	1/103
V.P.	1678	0.33	0.33	0.00475	1	1/7
Kn	1663	0.925	0.13	0.0042	1/7	1/22

CHAPTER III

PLASTIC DEFORMATION BY SLIP

Many crystalline materials can be deformed both elastically and plastically (1958). Theories have been developed to explain the existence and nature of these two kinds of deformation in terms of crystal structures and of the forces between atoms. Elastic deformation is now well understood. The mechanical stability of solids is due to the existence of balanced forces between their constituent atoms. Attractive forces cause the atoms to cohere to one another while short-range repulsive forces prevent the atoms from approaching too closely. Normally the atoms occupy positions where these forces are balanced, but when an external force is applied, this balance is upset. To restore equilibrium the atoms move slightly to near-by positions where there is a balance between the attractive, repulsive and external forces. The elastic response of a crystal to a given applied force can thus be calculated if the law of force between its atoms is known.

It is reasonable to suppose that a similar theory of the plastic deformation of crystalline substances could be developed as a straight forward extension of the molecular theory of elasticity to the case where the strains are large. As will be seen later, such an approach fails, because the plastic properties of

crystals can only be understood by taking account of fine details which can be ignored when considering elastic properties.

### Slip

Experiments on single crystals (1936,1950) have provided clear evidence on the nature of the process of plastic deformation. Many crystals deform plastically by means of a translation slip, in which one part of a crystal slides as a unit across a neighbouring part; the movement is concentrated in a succession of planes leaving the intervening layers undeformed, like the movement of cards in a pile when the pile is distorted (figure 7). Ideally this movement is a pure translation so that the crystal orientations of the different parts remain coincident. In general, the surface on which slip takes place is cylindrical with the slip direction as its axis; but in many cases the slip surface is planar. The crystallographic plane along which the displacement takes place is called the slip plane. The line of intersection of a slip plane with the outer surface of a crystal is a slip band. The fact that slip bands can be seen on deformed crystals, shows that deformation by slip is inhomogeneous. Intense plastic strain occurs on certain slip surfaces, while the layers of the crystal lying between these surfaces remain practically undeformed. The thickness of the undeformed layers or



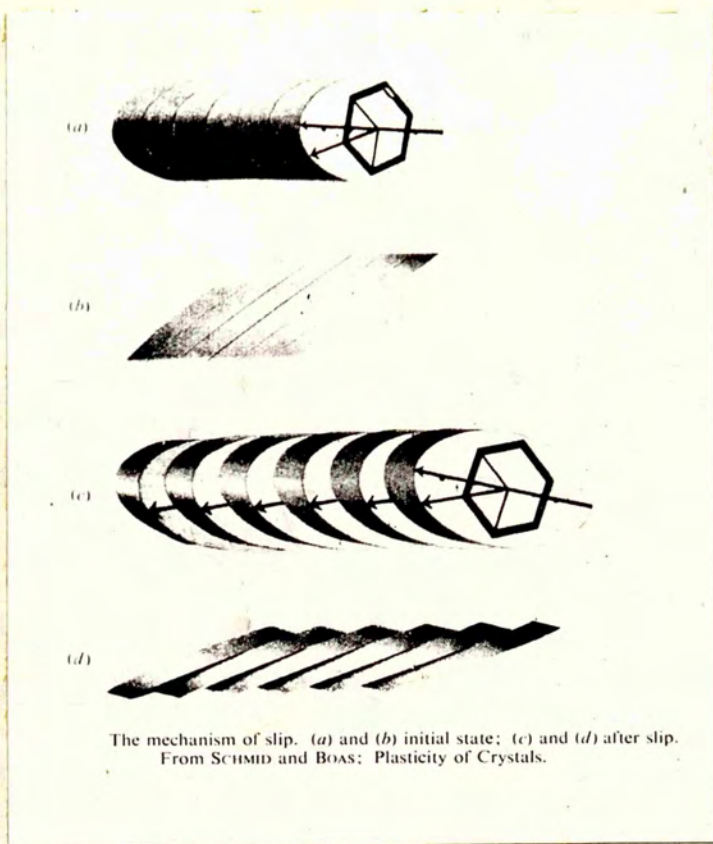


FIG.7

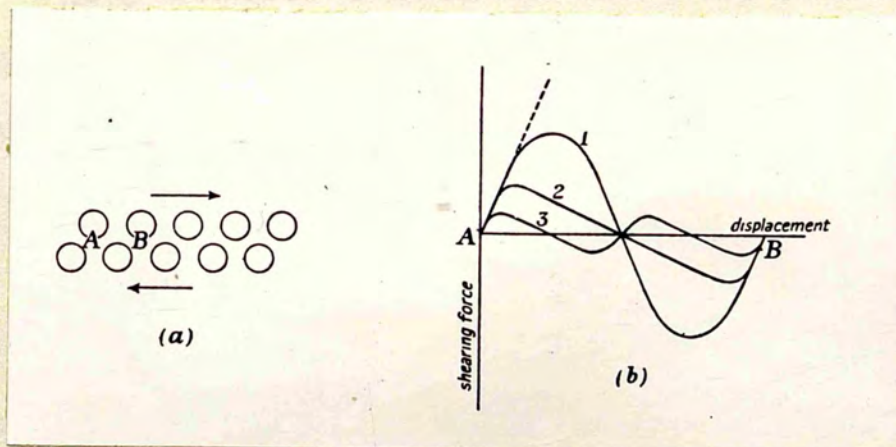


FIG.8

glide packets, varies with the conditions of deformation but is of the order of  $10^{-3}$  -  $10^{-4}$  cm.

### Directions and Planes of Slip

Slips occur more readily along certain crystal planes and directions than along others. The preferred slip planes are those which are most densely occupied by atoms and in these planes the lines of densest packing are the preferred slip directions. For the three most frequently occurring types we have, therefore:

<u>Crystal type</u>	<u>Slip plane</u>	<u>Slip direction</u>
Face-centred cubic	(111)	[110]
Body-centred cubic	(110)	[111]
Close-packed hexagonal	(0001)	[11 $\bar{2}$ 0]

The possibility of slip allows a certain degree of plasticity to exist in the crystal. The lower the number of symmetry elements, the fewer will be the slip planes of a material, and the more brittle it will tend to be. Body-centred cubics are more brittle than face-centred cubic materials, since they have only four slip directions as against six.

### The Critical Shear Stress

According to Schmid's law (1924) slip takes place along a given slip plane and direction when the shear stress acting along them reaches a critical value. Since most crystals have several crystallographically equivalent planes and directions of slip, slip occurs



first on the plane and direction along which the maximum stress acts; the others remain inactive unless the stress on them is increased.

Consider a cylindrical crystal under a uniaxial tensile load  $P$ . The component of the force in the slip direction is  $P \cos \lambda$ , where  $\lambda$  is the angle between this direction and the axis of tension. This force is spread over a slip plane of area  $A/\cos \phi$ , where  $A$  is the area of cross-section and  $\phi$  is the angle between the normal to the plane and the axis of tension. Thus the resolved shear stress is  $\tau = \frac{P}{A} \cos \phi \cos \lambda$ .

According to Schmid's law the yield  $P/A$  varies inversely with the orientation factor  $\cos \phi \cos \lambda$ ;

$\tau$  is a constant for a given crystal at a given temperature. This law has been verified in the case of several materials (1924, 1937), especially the close-packed hexagonal metals.

For most pure crystals, the critical shear stress is in the range  $10-100 \text{ gm.mm}^{-2}$ . Precise values for individual crystals have little significance apart from their order of magnitude; because the critical stress not only depends on the temperature and speed of straining but is also very structure-sensitive. Variation in the purity of the material, the conditions of growth and the state of the surface of the crystal, all greatly affect its shear strength (1936).

### Crystallographic Nature of Slip

It is clear from observed slip bands that when a crystal undergoes plastic deformation, most of the atoms do not move relative to their neighbours; only on occasional slip planes is there any such movement and this takes the form of sliding, through a distance of many atomic diameters, of one part of the crystal over another, along a simple crystallographic direction. Since slip always takes place along a crystallographic direction, even when this is not the direction of maximum shear stress in the slip plane, the material in the slip planes remains crystalline during slip; slip ought to take place along the direction of maximum stress if the crystal were to melt, but there is not enough energy available to produce a profound change such as melting in a slip plane.

The density of elastic strain energy in a crystal under the stress at which slip begins is  $\frac{\sigma^2}{2\mu}$  where  $\sigma$ , the applied shear stress, is  $\sim 10^7$  dynes.  $\text{cm}^{-2}$ . and  $\mu$ , the shear modulus, is  $\sim 10^{11}$  dynes.  $\text{cm}^{-2}$ . This density which is of the order  $10^3$  ergs per cc. could increase the temperature of the crystal very little; as in crystals the specific heat at room temperature is about  $10^7$  ergs per cc. The additional energy available due to the work done by applied forces during plastic deformation can also be estimated. Suppose that a displacement of



10 atomic spacings occurs along a slip plane; then the increase in energy density due to this is approximately  $10^5 \sim 10^8$  ergs per c.c. If none of this energy were to leak away from the slipped region, a rise in temperature of about  $10^\circ\text{C}$  could occur locally; but still no local melting is possible because the latent heat of melting involves an increase of energy density of  $10^9$ - $10^{10}$  ergs per cc. So the problem of slip is taken to be the explanation of how large shear deformations are produced in a structure which always remains crystalline.

#### Consecutive Slip and Dislocations

If it is assumed that the planes of atoms on a slip plane slide as rigid entities across each other, then the atoms must also be assumed to move simultaneously. Simultaneous slip is possible only when the shearing force causing it has the same value at every point on the slip plane. The existence of thermal vibrations makes such a uniformity unattainable and also it is difficult to apply a uniformly distributed force. So we conclude that atoms slip consecutively instead of simultaneously; slip starts at one place or at a few places in the slip plane and then spreads outwards over the rest of the plane at some finite speed. This is possible since the atoms in the slip plane are only flexibly coupled to each other. During consecutive slipping, a line could be drawn in the slip plane round the boundary of each slipped region. The boundary

is called a slip dislocation and the line which marks it is called the line of dislocation. The concept of dislocation, thus appears a reasonable inference from the experimental facts of slip. An estimation of the magnitude of the forces for slip shows also that dislocations are indispensable.

### Theoretical Shear Stress

The stress required to deform, many crystals, plastically is very small compared to their estimated theoretical shear stress. In an annealed crystal of pure zinc or aluminium, slip begins under a stress, on the slip planes, of less than  $10^{-4}\mu$ .

Consider (1926,1958) the shearing of two rows of atoms past each other in a strained crystal. Let the spacing between the rows be  $a$ , that between atoms along the slip direction  $b$ , and suppose that the shear displacement of the upper row over the lower one is  $x$ , when the shear acting on them is  $\sigma$ . The shearing force is zero at positions such as A and B (figure 8a) (1940), since they are normal lattice sites, and also at positions half way between them, by symmetry. Each atom is attracted towards its nearest lattice site, as defined by the atoms of the other row, so that shearing force must be a periodic function of  $x$ , with period  $b$ . If it is assumed sinusoidal

$$\sigma = K \sin \frac{2\pi x}{b} \quad (1)$$

as in curve 1 of figure (8b). The constant  $k$  is determined by the condition that the initial slope must agree with the shear modulus of the material. Near the origin

$$\sigma = \frac{k^2 \pi x}{b} \quad \text{from (1) and also } \sigma = \frac{\mu x}{a} \quad \text{from Hook's law.}$$

Therefore

$$\sigma = \frac{b \mu}{a^2 \pi} \sin \frac{2 \pi x}{b} \quad (2)$$

The critical shear stress at which the lattice becomes mechanically unstable and slip should take place is thus

$$\sigma_m = \frac{b \mu}{a^2 \pi} \quad (3)$$

Since  $a \sim b$ , this theoretical shear strength is about  $\frac{\mu}{2\pi}$  which is several orders of magnitude greater than the observed value on soft crystals. It is thus impossible to produce slip in a perfect crystal under the small stresses at which real crystals begin to slip.

### Refinement of Theoretical Shear Strength

A refinement (1958) of calculations, considering the repulsive forces between atoms, can further reduce the theoretical shear strength. Suppose the force between two atoms in a crystal is represented by;

$$F = K \left[ \left( \frac{r_0}{r} \right)^n - \left( \frac{r_0}{r} \right)^m \right] \quad (4)$$

where  $K$  is a constant,  $r$  is the spacing of the atoms,

$r_0$  is the equilibrium spacing and the index  $m$  of the repulsive component of the force is greater than  $n$ , that of the attractive component. Equating  $\frac{dF}{dr}$  to zero shows that  $F$  has a maximum at a spacing

$$r_1 = r_0 \left( \frac{m}{n} \right)^{\frac{1}{m-n}} \quad (5)$$

For soft compressible atoms, we can put  $m = 4$  and

assuming  $n=2$ ,  $\frac{\kappa_1}{\kappa_0} \approx 1.4$ . In full metals like copper and ionic salts, the repulsion is due mainly to overlapping of closed shells and the atoms are less compressible and large values of  $m$  have to be used. Taking  $m=12$  and  $n=2$ ,  $\frac{\kappa_1}{\kappa_2} \approx 1.2$ . For  $m=12$  and  $n=7$  (Van der Waal's attraction),  $\frac{\kappa_1}{\kappa_2} \approx 1.11$ . The critical strain which must be exceeded to break the bonds is smaller for hard atoms than for soft ones as was pointed out by Orowan (1940,1958). This correction alters the shearing force/shear displacement curve to that shown by 2 in figure (8b).

The theoretical shear strength can further be reduced by taking account of possible configurations of mechanical stability through which the lattice may pass as it is sheared. The face-centred cubic metals, for example, pass through twinning and body-centred cubic configurations when sheared on their slip planes. In such cases the force/displacement relation will oscillate over smaller periods than the lattice spacing as in curve 3 of fig.(8b).

Mackenzie (1949), taking account of both the above effects, showed that the theoretical shear strength can be reduced to about  $\mu/30$ . This is still greater than the observed strength of soft crystals.

#### Shear Strength of a Crystal of Bubbles

Bragg and Lomer (1949) prepared single two-dimensional crystals of bubbles in the form of rafts floating on soap solution and observed that the critical



strain was  $3.25^\circ$ , which gives a shear strength of about

$\mu/30$ . This means that the observed and calculated strengths agree in the one case where we are certainly dealing with a perfect crystal. It can, therefore, be concluded that slip cannot be started in a perfect crystal at low stresses at which real crystals can slip. This is the reason why the theory of crystal plasticity cannot be developed by simply extending the theory of elasticity to the case where the strains are large.

#### Sources of Slip in Real Crystals

Sources of mechanical weakness must, therefore, exist in real crystals, so that slip can start from them at very low applied stresses (1921, 1922). Two alternatives have to be considered for the imperfections which cause slip. The first is that dislocations may already exist in the crystal, in which case the yield strength is the stress required to move them; the second is that cracks or intercrystalline boundaries may be present from which slip can be started easily in which case the yield strength is either the stress needed to start slip at these defects or to propagate the slip away from them across the rest of the slip plane. In either case slip takes place by the movement of dislocations and thus is established a basis for a theory of slip in terms of dislocations.

#### Ideal Plastic Material

An 'ideal' plastic material ( in the form of a cylinder), when deformed, has a stress/strain curve

shown in figure (9). Over the region A the material deforms elastically and the slope of the line OA gives its Young's modulus. Beyond the elastic limit  $Y_0$ , the cylinder will increase in length in a non-reversible way and follow the straight line BC if there is no work-hardening. If at point D, the stress is removed and then reapplied, the stress/strain curve will be DO'D. In practice, however, a slight hysteresis is shown by most materials and the curve is of the type D'O''D''. Since all materials work-harden as a result of deformation, the stress/strain curve is of the type shown in figure (10).

#### Plastic Deformation Under Combined Stresses

When an indenter is pressed on to a surface, stresses in various directions are set up under it and the resultant plastic flow takes place under these combined stresses. Experimental evidence has shown that a hydrostatic pressure does not produce plastic deformation.

If  $p_1, p_2$  and  $p_3$  represent the principal (orthogonal) stresses, then the combined stress is the sum of a hydrostatic component  $\frac{1}{3}(p_1+p_2+p_3)$  and reduced stresses  $p_1 - \frac{1}{3}(p_1+p_2+p_3)$ ,  $p_2 - \frac{1}{3}(p_1+p_2+p_3)$  and  $p_3 - \frac{1}{3}(p_1+p_2+p_3)$ .

Experimentally plastic deformation occurs when the reduced stresses satisfy the condition

$$\left[p_1 - \frac{1}{3}(p_1+p_2+p_3)\right]^2 + \left[p_2 - \frac{1}{3}(p_1+p_2+p_3)\right]^2 + \left[p_3 - \frac{1}{3}(p_1+p_2+p_3)\right]^2 = \text{const.} \quad (1)$$

$p_2=p_3=0$  for uniaxial tension and plastic deformation occurs when the axial stress  $p_1$  is equal to the yield

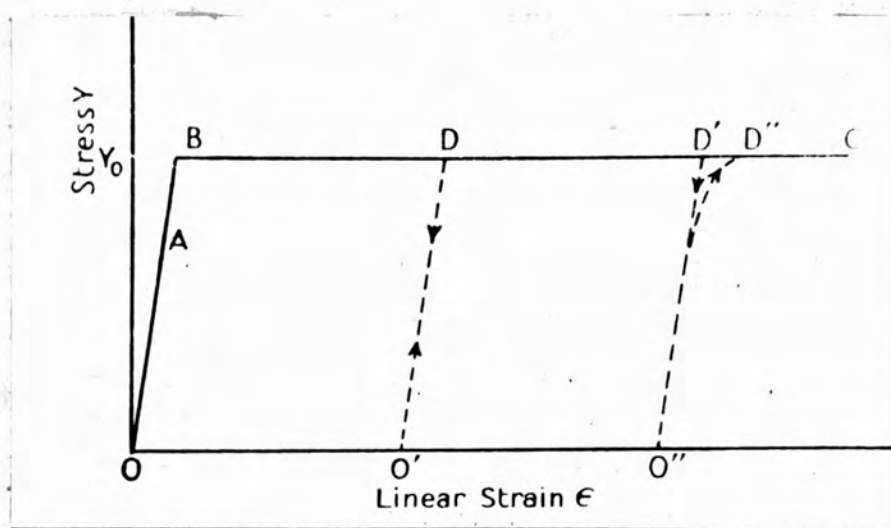


FIG.9

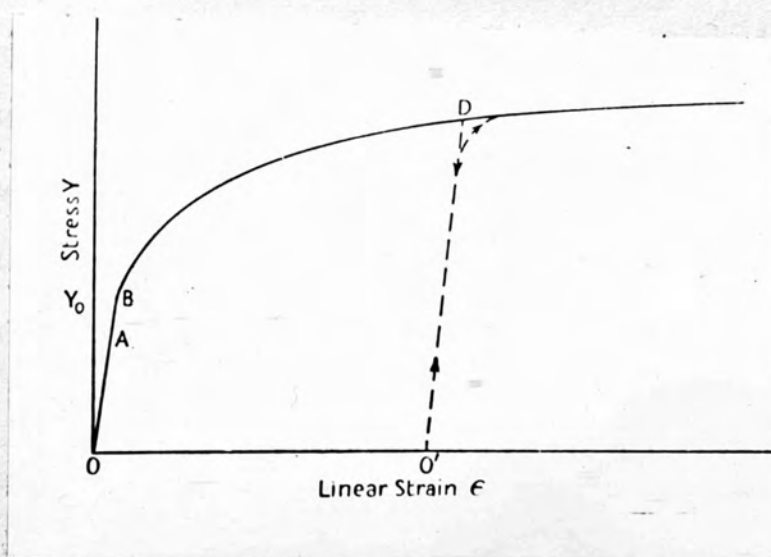


FIG.10

stress  $Y$ . Equation (1), therefore, becomes

$$(p_1 - p_2)^2 + (p_2 - p_3)^2 + (p_3 - p_1)^2 = 2Y^2 \quad \text{--- (2)}$$

This relation is known as the Huber-Mises (1904, 1913) criterion of plasticity.

Treaca (1864) and Mohr (1903) held the view that plastic deformation occurs when the maximum shear stress reaches a certain critical value. If  $p_1 > p_2 > p_3$  in the shear stresses  $\frac{1}{2}(p_1 - p_2)$ ,  $\frac{1}{2}(p_2 - p_3)$  and  $\frac{1}{2}(p_3 - p_1)$ , then the maximum shear stress is  $\frac{1}{2}(p_1 - p_3)$ . For the special case of uni-axial tension ( $p_2 = p_3 = 0$ ), the maximum shear stress is  $\frac{1}{2}p$  and plastic deformation occurs when this is equal to  $\frac{1}{2}Y$ . In general the Tresca or Mohr criterion for plastic flow is given by

$$p_1 - p_3 = Y \quad \text{when } p_1 > p_2 > p_3 \quad \text{--- (3)}$$

If  $p_2 = p_3$  in equation (2), then it becomes identical to eg.(3). The two criteria also become identical in the case of two-dimensional deformation or plain strain.

Introducing the condition for zero plastic deformation

[by putting  $p_2 = \frac{1}{2}(p_1 + p_3)$ ] in the direction of  $p_2$  eg. (2) becomes

$$p_1 - p_3 = \frac{2}{\sqrt{3}} Y \simeq 1.15 Y.$$

Thus the condition for plasticity is a maximum shear stress condition as in eg. (3), but the value of the constant is 1.15 times larger in Huber-Mises criterion.



### Two-Dimensional Plastic Flow.

Problems of plastic deformation are tackled by assuming that two dimensional flow occurs when the maximum shear stress reaches a critical value  $k$  given by

$$2k=1.15Y \quad (\text{Huber-mises criterion})$$

$$\text{or } 2k=Y \quad (\text{Tresca-Mohr criterion})$$

A two-dimensional element subjected to principal (orthogonal) compressive stresses  $P$  and  $Q$  (figure 11) will have a maximum shear stress at  $45^\circ$  to  $P$  and  $Q$ , of magnitude  $\frac{1}{2}(P-Q)$ . It can be shown (diagrammatically as in figure 11) that when plastic deformation occurs, the stresses at any point can be represented by the sum of a hydrostatic pressure  $p$  and the shear stress  $k$ .  $k$  is a constant while  $p$  may vary from point to point. The lines of maximum shear stress  $k$  are called slip lines (they are entirely different from the slip lines or slip bands observed under the microscope). The whole domain of plastic flow may be covered by two families of slip lines, the  $\alpha$  and  $\beta$  curves, each of which cuts the other orthogonally. Knowing the hydrostatic pressure, the principal stresses at any point can be deduced by the relations

$$\begin{aligned} P &= p+k \\ Q &= p-k \end{aligned} \quad (4)$$

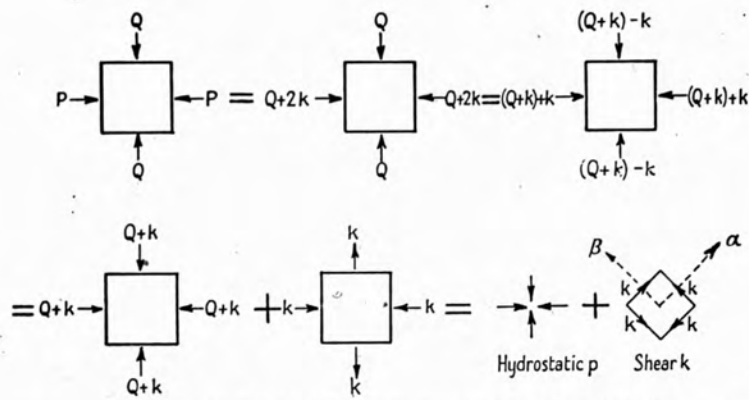
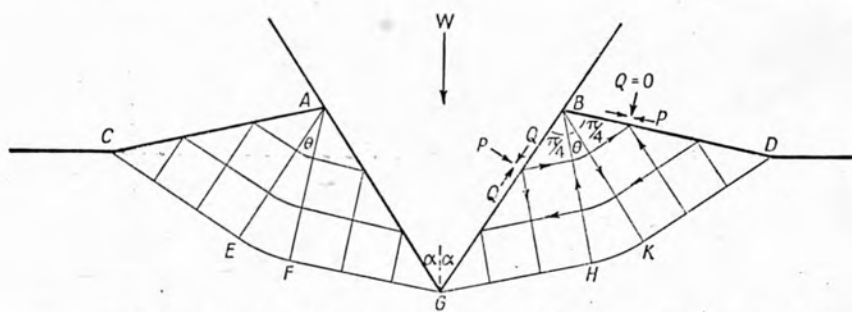


Diagram showing that for two-dimensional stress, the principal stresses  $P$  and  $Q$  may be replaced by a hydrostatic pressure  $p$  and a maximum shear stress  $s$ , where  $p = Q+k = P-k = \frac{1}{2}(P+Q)$  and  $s = k$ .

FIG. 11



Slip-line pattern for a two-dimensional wedge penetrating an ideally plastic material of yield stress  $Y$  (Hill, Lee, and Tupper, 1947). The pressure across the face of the indenter is uniform and has the value  $P = 2k(1+\theta)$ , where  $\theta$  is the angle  $HBK$  in radians. This analysis allows for the displacement of the deformed material.

FIG. 12

### Application to Hardness Tests

Although the above analysis, due to theoretical limitations, so far, could not be applied to the ball, the conical or the pyramidal indenters, Hill, Lee and Tupper (1947) succeeded in obtaining a theoretical solution for the two-dimensional wedge. Figure (12) shows the computed slip-line pattern when the wedge penetrates an ideally plastic material; this is in agreement with experiments on a plastic model. The pressure normal to the surface of the indenter is given by

$$P=p+k \text{ and also}$$

$$P=1.15Y(1+\theta) \quad (5)$$

for Huber-Mises criterion, where  $\theta$  is the angle shown in the figure.  $\theta$  is related to the semi-angle ( $\alpha$ ) of the wedge by the relation

$$\cos(2\alpha-\theta) = \frac{\cos \theta}{1+\sin \theta} \quad (6)$$

For  $\alpha$  lying between  $70^\circ$  and  $90^\circ$ , the yield pressure is given by

$$P_m \simeq 3Y.$$

This value will be less for Tresca criterion. This result is in fair agreement with experiments on work-hardened materials (1951).

The above treatment shows that indentation hardness is essentially a measure of the elastic limit or the yield stress of the material in a macroscopic sense. Zwikker (1954) also shows the close connection between

hardness and yield strength ( $\sigma_{\text{yield}}$ ) by giving the relation

$$\sigma_{\text{yield}} \simeq \frac{1}{3} H_{\text{Brinell}} \simeq \frac{1}{3} H_{\text{Vickers}},$$

where  $\sigma$  is measured at a strain speed of one per cent per minute, in the same units as H.

In the case of metals, for most indenters, the yield pressure between the metal and the indenter, when appreciable plastic flow has occurred, is about three times its effective yield stress. This is still to be verified for non-metals.

The above theoretical analysis holds good for 'ideal' plastic materials; its extension to all types of materials is still a matter for further investigation.

is crystals; but still there is a large divergence between theoretical and practical work on the growth of crystals. It is therefore necessary to compare various aspects of real crystals with the theoretical concepts of crystal growth.

#### Historical Review

Gibbs (1876) was the first to give a quantitative theory for crystal growth based on thermodynamic considerations; but the importance of his work was overlooked for a long time. Curie (1893) put forward a theory in which he proposed that there was an intimate connection between the crystalline form and the surface energy of the solid. He, however, did not take into



## CHAPTER IV

### THEORIES OF CRYSTAL GROWTH

#### Introduction

Crystal formation problems are of great interest in science and technology, Modern solid-state physics is closely bound-up with the study and use of large uniform crystals, to grow which demands a many-sided and profound study of crystallisation processes. The increasing industrial use of synthetic crystals, has stimulated much theoretical and experimental work on crystal growth. The theories put forward for the growth of perfect and imperfect crystals, have tried to answer many problems of growth and dissolution mechanism in crystals; but still there is a large divergence between theoretical and practical work on the growth of crystals. It is therefore necessary to compare various aspects of real crystals with the theoretical concepts of crystal growth.

#### Historical Review

Gibbs (1878) was the first to give a quantitative theory for crystal growth based on thermodynamic considerations; but the importance of his work was overlooked for a long time. Curie (1885) put forward a theory in which he proposed that there was an intimate connection between the crystalline form and the surface energy of the solid. He, however, did not take into

account the actual atomic arrangements of the crystal surfaces while proposing the theory and hence it had to be abandoned. Bravais (1866) proposed that the velocities of growth of the different faces of a crystal depended on the densities of the lattice points (reticular densities) in the various planes. His idea was extended by Donnay and Harker (1937,38,39) with some success to explain crystal morphology.

The first theory, which was a step forward relative to the previous ones, was proposed by Kossel (1927,28) and Stranski(1928,1948) independently. This was further developed by Becker and Doring (1935,1949), Volmer (1939) and Frenkel (1945,1946). Although this theory ignores crystal imperfections and introduces a number of simplifying assumptions in analysing growth processes, it uses for the first time, X-ray structural data and lattice potential calculations and considers crystal growth from the point of view of minimum free energy. Burton and Cabrera (1949) re-examined the basis of this theory and suggested refinements concerning the shape of the critical nucleus. Even with their amendment the theory implies that the supersaturation at which growth starts in a perfect crystal should be 50% instead of the 0.8 - 1% which observations show. This contradiction is resolved by the dislocation theory developed by Burton, Cabrera and Frank (1949).

A brief account of the 'theory of growth of a perfect crystal' will be given as many of its concepts and results have been incorporated in the dislocation theory.

### Growth of a Perfect Crystal

A perfect crystal can be considered as bound by faces which are one of two types: low-index faces which are close-packed surfaces and perfectly plane or high-index faces which are non-close packed surfaces and stepped; the latter can also be regarded as formed from terraces which are sections of a close-packed face. The problem of crystal growth is essentially a consideration of the growth of its close-packed surfaces because experiments have shown that in a supersaturated state the high index faces of a crystal are rapidly eliminated. Hence the growth rate of a crystal will depend on the rate at which fresh steps are created and advance on the close-packed faces. It is, therefore, necessary to postulate a mechanism by which steps could be created continuously upon its close-packed surfaces.

Figure 13 shows the structure of a close-packed surface of a perfect crystal (kossel model) at absolute zero of temperature. In general the step will have a 'kink' (A in figure 13). These kinks play an important part as 'exchange sites' in the positioning of new molecules, in the building up of the crystal in order

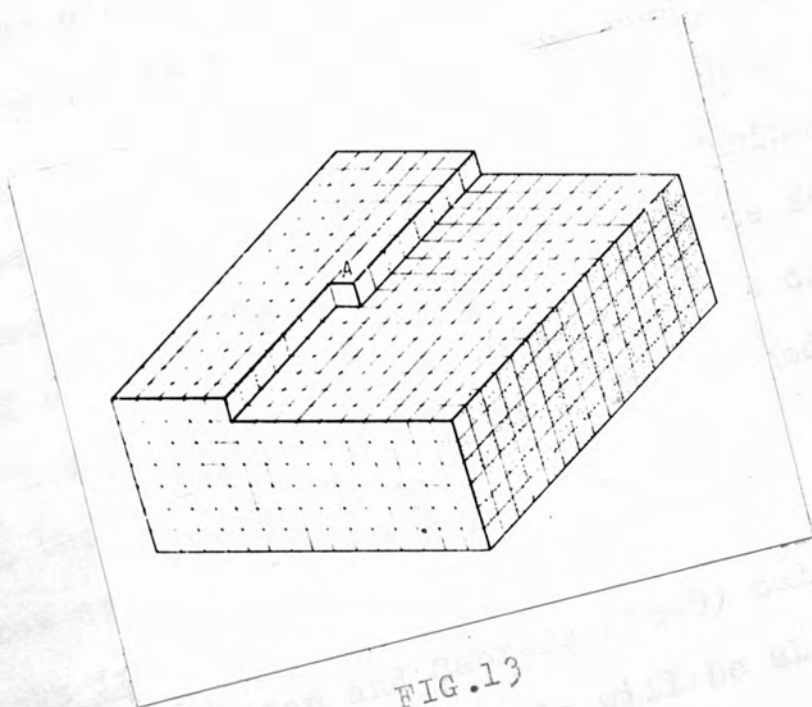


FIG.13

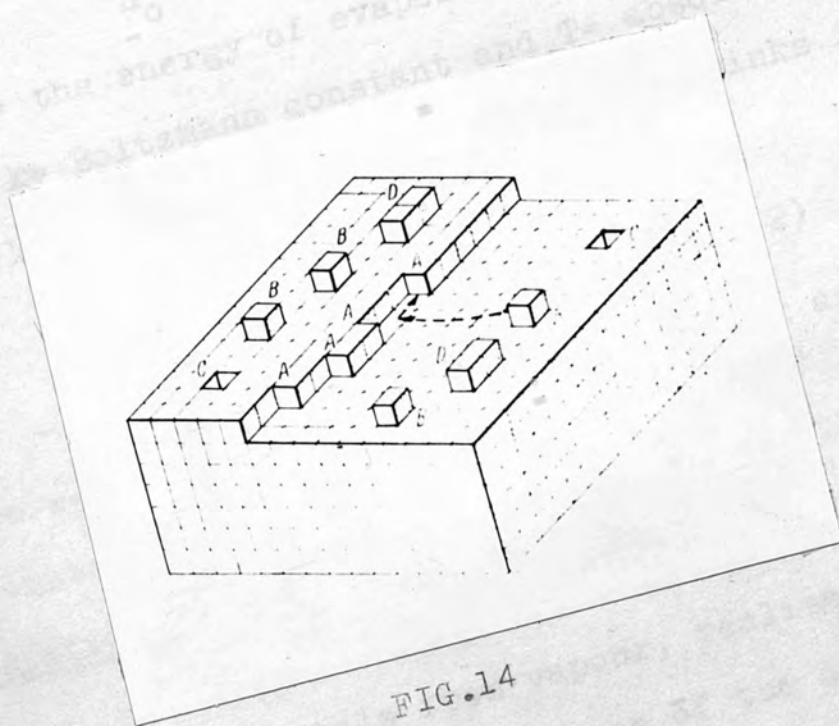


FIG.14



to complete a new layer. Figure 14 shows the surface of the crystal at a higher temperature. It is different from figure 13 in two ways: (a) the number of kinks has increased (b) a number of molecules (such as B and D) have been absorbed on the surface and surface vacancies like C have been created. In this state some molecules will leave and others will arrive at the crystal surface from the vapour, equilibrium being reached when the two rates are equal.

### Kinks in a Step

Burton and Cabrera (1949) calculated the probability that a molecule will be absorbed at a kink directly from vapour; it is given by

$$\frac{n}{n_0} = \exp \left( -\frac{W_s}{kT} \right) \quad (1)$$

where  $W_s$  = the energy of evaporation of a molecule from a kink,  $k$  = Boltzmann constant and  $T$  = absolute temperature. Similarly the mean distance ( $X_0$ ) between kinks is given by

$$X_0 \sim \frac{1}{2} a \exp \left( w/kT \right) \quad (2)$$

where  $w$  = the energy needed to form a kink and  $a$  = the interatomic distance.

### Migration of Molecules

Volmer (1921), from his studies on the growth of mercury crystals from vapour, realised that the rate of extension of the main faces of the crystals, was

largely due to the surface flow of the molecules during their life time on the surface. The rate of growth of a step will, therefore, depend on the relative importance of the following three processes: (a) direct deposition from the vapour (b) the diffusion of adsorbed molecules towards the steps (c) the diffusion of adsorbed molecules along the edges of the steps towards a kink. The mean displacement ( $X_s$ ) of adsorbed molecules (the distance covered by the molecule between the time it hits the surface and the time it evaporated again) is shown to be

$$X_s = a \exp \left\{ \frac{(W'_s - U_s)}{kT} \right\} \quad (3)$$

where  $W'_s$  = evaporation energy from the surface to vapour per molecule and  $U_s$  = activation energy for surface diffusion (migration from one site to another).

For growth under typical conditions in which temperatures lies between 0.5 and 0.8 times the boiling point in degrees K, it is estimated that

$\frac{W_s}{kT} \sim 12$ ;  $\frac{w}{kT} \sim 2$ ;  $\frac{W'_s}{kT} \sim 12$ ; and  $\frac{U_s}{kT} \sim 1.2$ . (1950).  
Substituting these values in formulae (1), (2) and (3) it is seen that

$$\frac{n}{n_0} \sim 10^6, \quad X_0 \sim 4a \text{ and } X_s \sim 4 \times 10^2 a.$$

From this it follows that in growth from the vapour, the rate of arrival of molecules directly from the vapour, is negligible compared with that due to surface migration.

When the crystal is in equilibrium with the vapour, molecules join and leave the kinks with equal frequency; the rate of departure depends only on temperature while the rate of arrival is proportional to the vapour concentration. So when the vapour pressure is increased above the equilibrium value, more molecules join the kinks than leave them and the step advances.

#### Rate of advance of a straight step

Any ideal crystal face with a step will continue to grow due to the presence of kinks till the step travels to the edge of the crystal and disappears leaving a complete crystal surface. The rate of advance ( $v_{\infty}$ ) of a straight step is given by

$$v_{\infty} = 2(\alpha - 1) X_s \nu \exp\left(-\frac{W}{RT}\right) \quad (4)$$

where  $\alpha = \frac{p}{p_0}$  (p is the actual pressure of the vapour and  $p_0$  is its saturation value),

$\nu$  = a frequency factor of the order of atomic frequency of vibration  $\sim 10^{13} \text{ sec}^{-1}$  for monatomic substances; and  $X_s$  = mean distance of diffusion. Equation (4) implies that all the molecules which hit the surface in the 'diffusion zone' of width  $2X_s$  will reach the advancing step and will be absorbed by it due to the existence of a large number of kinks. A curved step with a radius of curvature  $\rho$  advances with a velocity

$$v_{\rho} = v_{\infty} \left(1 - \frac{\rho_c}{\rho}\right) \quad (5)$$

where  $\rho_c$ , the critical radius of curvature to be defined later is given by

$$\rho_c = \frac{a\phi}{2kT \log \alpha} \quad (6)$$

since  $v_\infty$  is proportional to  $(\alpha-1) (= \frac{\Delta p}{p})$  which is the supersaturation,  $\sigma$ , it means that a partly covering layer on a low-index crystal surface will grow at a speed proportional to  $\Delta p$  until it covers the whole surface. Any further growth will be possible only if new steps can be formed.

### Surface Nucleation

Frenkel (1945, 1946) suggested that surface steps could result from thermodynamic fluctuations, like the way kinks are formed on a step. Burton, Cabrera and Frank (1949, 1951) have shown that this effect was only appreciable above a certain critical temperature, which for close-packed surfaces was near or above the melting point, when the surface rapidly becomes rough. So the rate of growth of a perfect crystal is limited not by  $v_\infty$  but by the difficulty of starting new layers which is a nucleation process.

Under given conditions of supersaturation a two-dimensional nucleus will grow if it exceeds a certain critical value. Assuming it to be circular Mott (1950) calculated the critical radius

$$\rho_c = \frac{a\phi}{2kT \log \alpha} \quad (7)$$



where  $\frac{1}{2}\phi = 5a$ ,  $\phi$  being the nearest neighbour binding energy. Becker and Doring (1935, 1949) calculated the activation energy  $A_0$  for the formation of a square nucleus of critical size. The values of  $A_0$  and the length of the sides of the square are given by

$$A_0 = \frac{\phi^2}{RT \log \alpha} \quad (8)$$

$$l = \frac{a\phi}{RT \log \alpha} \quad (9)$$

Since  $\phi = \frac{1}{6}W$  which gives  $\frac{\phi}{RT} \sim 4$  for  $\alpha \sim 1.01$ ,

$$\frac{A_0}{RT} = \left(\frac{\phi}{RT}\right)^2 \frac{1}{\log \alpha} \sim 16 \times 10^2$$

therefore  $\frac{A_0}{RT} \gg \frac{45}{RT}$ ;

that is, the activation energy for surface nucleation greatly exceeds that necessary for surface diffusion.

The number of nuclei formed per sec. on a  $\text{cm}^2$  of surface is, from (8), given by

$$N \sim A \exp\left\{-\frac{A_0}{RT}\right\} \quad (10)$$

where  $A$  is of the order of  $10^{20}$ . Burton and Cabrera found the critical nucleus to be a figure with rounded corners which can be inscribed in the square nucleus of Becker and Doring's theory. In general they showed that the rate of formation of the nuclei is given by

$$N \sim A \exp\left\{\frac{F}{2RT}\right\} \quad (11)$$

where  $F$  is the edge free energy of the critical nucleus of any shape. The effect of the correction is to reduce  $F$  in the same ratio as the area of the critical nucleus.

For any observable growth rate equation (10) or (11) shows that a critical supersaturation of 25-50% is required. Thus the formation of a two-dimensional nucleus of critical size is a very sensitive function of the supersaturation. Above the critical supersaturation the growth process is not limited by nucleation.

In contrast to the above theoretical considerations Volmer and Schultze (1931) found that crystals of Napthalene, White Phosphorous and iodine, when grown from their vapours at  $0^{\circ}\text{C}$ , for different supersaturations have shown finite growth rates at supersaturations as low as 3-4%. Burton, Cabrera and Frank (1949, 1951) have proposed that these discrepancies can be explained by recognizing that real crystals are not perfect. They suggested a mechanism by which a surface remains stepped no matter how far the steps advance and thus enable the crystal face to grow.

#### Imperfect Crystal

There is a great discrepancy between the theoretically calculated value of the strength of a perfect crystal and the actual value possessed by real crystal. Griffith (1921) attributed the reduction in the mechanical strength to surface cracks; Darwin (1914, 1921), with the help of X-rays, showed that real crystals are internally disordered and have a mosaic structure. Polanyi (1934), Taylor (1934) and Orowan (1934) were the

first to associate the mechanical weakness of crystalline solids to geometrical distortions of the perfect lattice, which were termed 'dislocations'.

### Dislocations

On any lattice plane of a perfect crystal, a line may be drawn from one lattice point to the next, such that it forms a closed loop; such a line is called a Burgers circuit. If by tracing a line in a real crystal, the line does not form a closed loop, then a geometrical fault of the dislocation type is present. The vector required to close the path is defined as the Burgers vector of the dislocation. The lattice disorder which constitutes a dislocation is believed to have a lateral extension of a few atomic diameters. On a macroscopic scale a dislocation may be regarded as a line fault in the crystal. Since the Burgers vector of a dislocation line is invariant, every line must either form a closed loop or terminate on the crystal surface.

### Edge Dislocation

The type of dislocation, which was first introduced by Taylor, Polanyi, and Orowan (1934), is called 'edge dislocation'. In this the dislocation line is perpendicular to the Burgers vector. Figure 15 shows an edge dislocation in which the dislocation line EF terminates on crystal faces which are parallel to its Burgers vector; the Burgers vector is given by the displacement of P and P' (two originally coincident points) relative to each other in

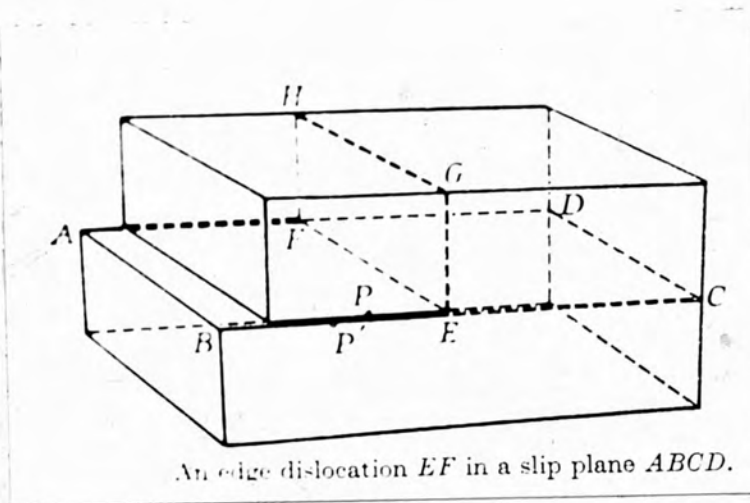
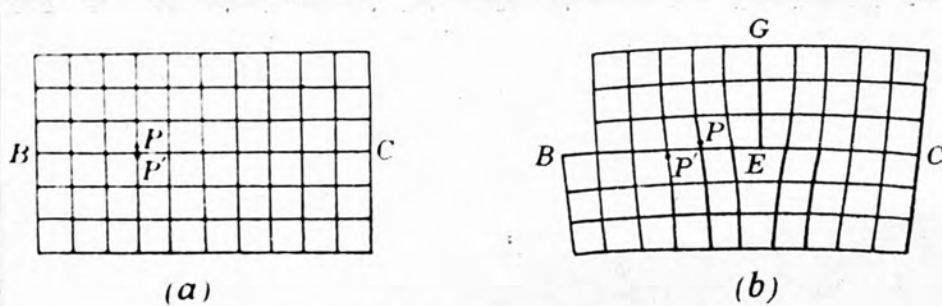


FIG.15



The strain pattern of an edge dislocation.

FIG.16

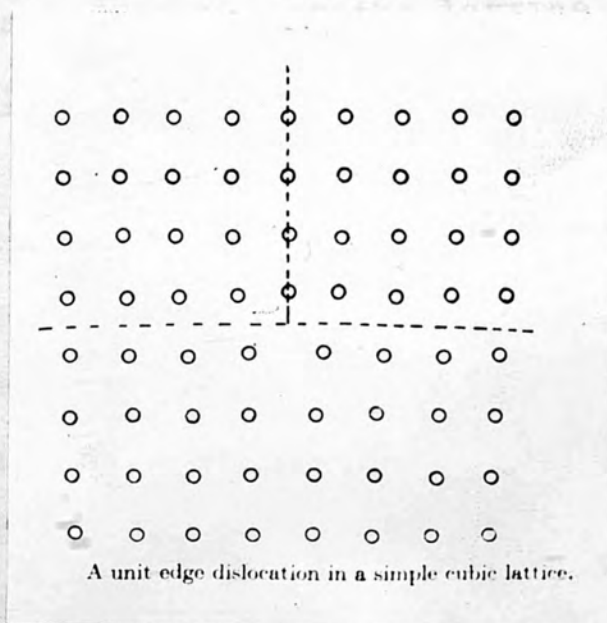


FIG.17



the slip direction BC. Figure 16 shows the strain pattern and figure 17 the corresponding atomic disorder in a plane perpendicular to the dislocation line.

### Screw Dislocation

Burgers (1939) was the first to introduce the screw dislocation in which the dislocation line is parallel to its Burgers vector. Figure 18 shows the screw dislocation in which EF is the dislocation line, the Burgers vector of which is determined by the displacement of P relative to P'. Figure 19 shows the strain pattern and figure 20 the atomic arrangement in the two successive planes containing the dislocation line.

Whenever a dislocation emerges upon a crystal face, there arises in it a terminated step whose height is equal to the component of the Burgers vector perpendicular to the surface. The height of the step is equal to an inter-planer spacing of the lattice.

### Growth of an Imperfect Crystal

Frank (1949) realised that the presence of a terminated step due to the emergence of a dislocation upon the crystal face, provides a continuous site for the deposition of molecules and obviates the need for two-dimensional nucleation. The terminated step is fixed at the point of emergence of the dislocation and can only advance by rotation about the dislocation point.

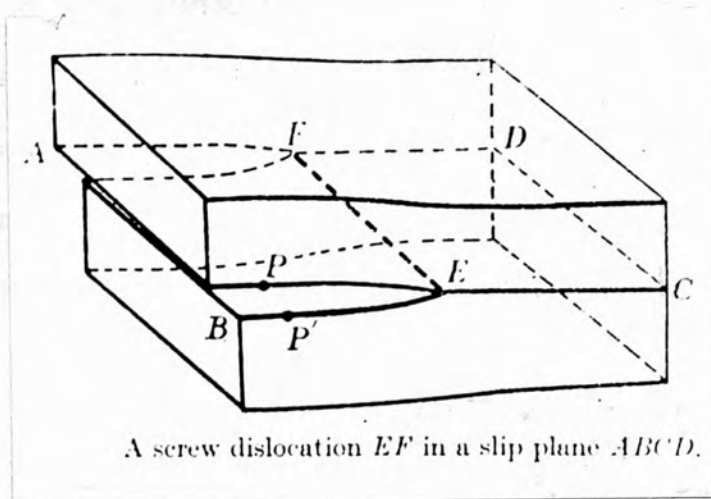


FIG.18

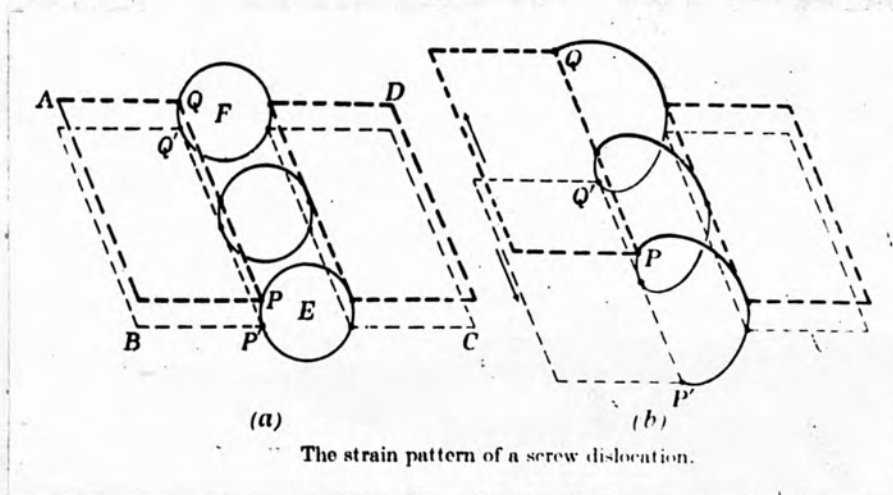


FIG.19

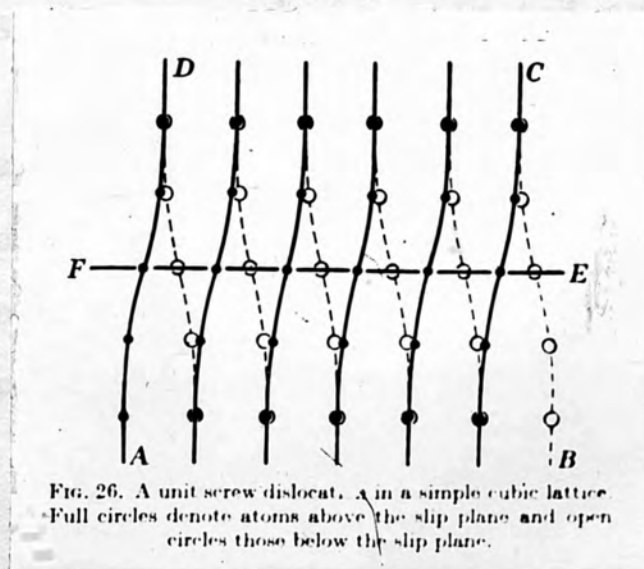


FIG.20

Frank has shown that in growth from vapour under steady conditions of supersaturation, the terminated step will assume a spiral form. When the velocity of advance is independent of crystallographic orientation, each point of the step will initially advance with the same velocity. The section of the step nearest the dislocation point, will have the highest angular velocity and the step will develop a curvature which is greatest towards the centre. The radial velocity ( $v_r$ ) of a curved step is given by equation (5), from which it is seen that as the curvature of the step increases, its radial velocity of advance will decrease.

The different stages of a growth spiral are shown in figure 21. In the steady state all sections of the step will have the same angular velocity and the step has the spiral form shown in figure 22. The distance ( $Y_0$ ) between successive turns of the spiral at large distances from the growth centre was estimated as

$$Y_0 = 4\pi p_c$$

Burton, Cabrera and Frank (1949,1951) have shown that when two or more dislocations emerge upon a crystal face, the growth will depend upon the supersaturation and the separation of the dislocation centres. Two equal dislocations of opposite sign emerging near the centre of a crystal face, cause continuous growth if the supersaturation is such that the critical nucleus (correctly

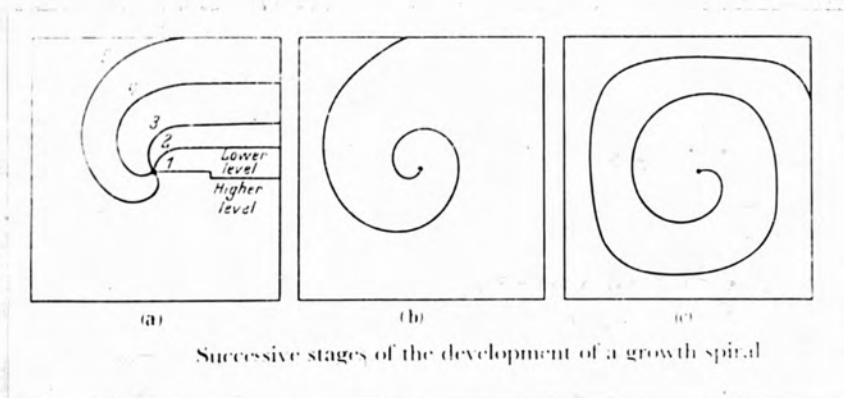


FIG. 21

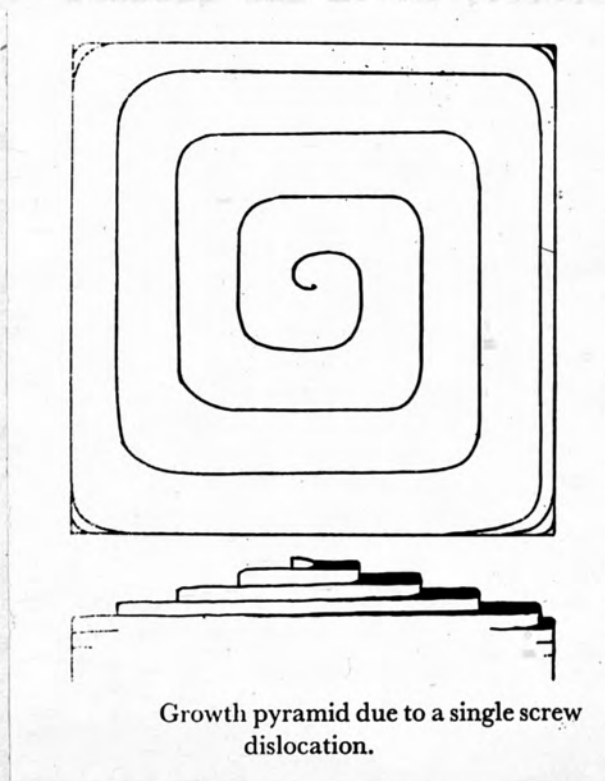


FIG. 22



oriented) will pass between them. Growth fronts in the form of closed loops (figure 23) then occur with a separation of  $\sim 4\pi\rho_c$  between successive loops. A pair of dislocations of like sign give a more complex situation.

The theory outlined above applies only to growth from the vapour but without much difference it could be extended to growth from the solution. It is difficult to say whether similar considerations apply to growth from the melt.

#### Dislocation Theory of Evaporation of Crystals

Cabrera and Levin (1956) extended the theory of the spiral growth of crystals to evaporating crystals. The word evaporation was meant to include dissolution, chemical etching and oxidation. To distinguish between growth and evaporation, they took account of the supplementary energy localized around the dislocation itself. They showed that the normal velocity of advance ( $v$ ) of a step on the crystal face located at a distance  $r$  from the point of emergence of the dislocation and having a localized radius of curvature  $\rho$ , is given by

$$v = v_\infty \left[ 1 - \frac{\rho_c}{\rho} - \frac{\kappa_0 \rho_c}{\kappa^2} \right] \quad (12)$$

The quantities  $v_\infty$ ,  $\rho_c$  and  $\kappa_0$  have the following meaning;

- (i)  $v_\infty$  is the velocity of a straight step far from the origin.

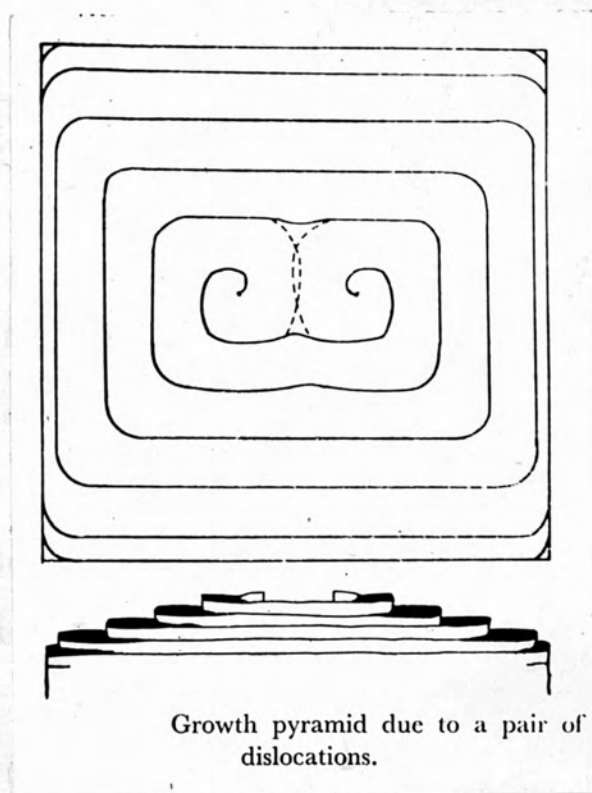


FIG. 23

(ii)  $\rho_c$  ( the radius of the critical nucleus) =  $\frac{\gamma \Omega}{\Delta \mu_0}$

where  $\gamma$  is the surface energy per unit surface of the edge of the step;  $\Omega$  is the volume per molecule in the crystal and  $\Delta \mu_0$  is the difference in the chemical potential of a molecule in the surrounding medium and in the crystal (supposed perfect). According whether  $\Delta \mu_0 \geq 0$  the crystal is growing or evaporating.

(iii)  $\kappa_0 = \frac{\mu b^2}{8\pi^2 \gamma}$  where  $\mu$  is shear modulus and  $b$  is the Burgers vector of the dislocation;  $\kappa_0$  represents a measure of the strain energy around the dislocation.

Equation (1) is valid for both growth and evaporation; in the latter case  $\rho_c$  and  $\rho$  become negative, this does not change the second term in (1) but changes the sign of the third term because the strain energy due to the presence of the dislocation opposed growth and favours evaporation. Eg. (1) is valid only under the following conditions:

(i) the step is far away from any other step so that the diffusion fields are independent of each other (ii) the curvature of the step is everywhere small, so that it cannot advance by surface nucleation (iii) the influence of the crystallographic orientation of the step is completely neglected. The last condition seems to be satisfied for a multi-atomic step centred on a dislocation of large Burgers vector ( for instance the spirals in SiC crystals).

Cabrera and Lavin calculated the radius of a hollow core of the dislocation, which is given by

$$\begin{aligned} r'_0 &= \frac{1}{2} r_c \left\{ \left[ 1 + \frac{4r_0}{r_c} \right]^{1/2} - 1 \right\} \quad \text{for growth} \\ r'_0 &= \frac{1}{2} |r_c| \left\{ 1 - \left[ 1 - \frac{4r_0}{|r_c|} \right]^{1/2} \right\} \quad \text{for evaporation} \end{aligned} \quad (13)$$

The critical value of the chemical potential  $|\Delta\mu_{oc}|$  is given by

$$|\Delta\mu_{oc}| = \frac{2\pi\gamma^2\Omega}{\mu b^2} \quad (14)$$

Beyond this value a dislocation in an evaporating crystal cannot remain closed; otherwise it must 'open up'.

Then the crystal evaporates from the free surface as well as sidewise from the core of the dislocation outwards, forming a macroscopic pit. At the critical value itself  $\{ |r_c| = 4r_0 \}$  the radius of the core  $r'_0 = 2r_0$  remains sub-microscopic.

In the simplest cases of evaporation in a vapour or dissolution into a dilute solution  $|\Delta\mu_o| = RT \log \frac{p_o}{p}$  where  $p_o$  is the saturated pressure (concentration) and  $p$  the actual one occurring above the crystal; then  $p_c$ , the critical pressure below which the dislocation should open up is given by

$$\frac{p_c}{p_o} = \exp \left[ - \frac{2\pi\gamma^2\Omega}{RT\mu b^2} \right] \quad (15)$$

Assuming  $\gamma \sim 5 \times 10^2 \text{ erg/cm}^2$ ;  $\mu \sim 5 \times 10^{11} \text{ erg/cm}^3$ ,  $\Omega \sim 10^{-22} \text{ cm}^3$

and  $kT \sim 10^{-13} \text{ erg}$ , we get  $\frac{p_o - p_c}{p_o} \sim 10^{-2}$  if  $b \sim 10^{-6} \text{ cm}$  and

$\frac{p_c}{p_o} \sim 10^{-4}$  if  $b \sim 10^{-8} \text{ cm}$  (1956). This indicates that a very low undersaturation will be sufficient to



open-up a dislocation of large Burgers vector; on the contrary very large undersaturations might be necessary to open-up dislocations with an elementary Burgers vector. The actual values of  $\frac{p_c}{p_0}$  will of course, be very sensitive to the assumed value of  $\gamma$ . Further, it is well known that the crystal surface remains practically flat as long as  $|\Delta\mu_0|$  is small; so that the semi-vertical angle  $\beta$  of the conical surface of the crystal is practically equal to  $\frac{\pi}{2}$ . This is also true for the obtainable value of  $\Delta\mu_0$  above a growing crystal. In the case of an evaporating crystal, for the critical value of  $|\Delta\mu_c|$ ,  $\tan \beta = d/b = 0.19 \times \frac{\mu b}{\gamma}$ . Assuming the same characteristic values for  $\mu$  and  $\gamma$ ,  $\tan \beta \sim 2 \times 10^8 b$ , which means  $\beta$  remains very nearly  $\frac{1}{2}\pi$  for a large Burgers vector but diminishes to values of the order of  $\frac{\pi}{3}$  when  $b \sim 10^{-8}$  cm.

Doubts about the spiral growth theory have been expressed by some workers (1953), notably by Buckley. He suggests that spiral formation is not always essential to growth but is a late incident in growth due to vortices or eddies which would impress on the uppermost surface a spiral character. Tolansky and Pandya (1954) have given some evidence by etching diamond that growth has proceeded by layer formation. Tolansky (1961) has recently observed a spiral on synthetic diamond, although so far no spirals have been observed in natural diamonds.

These uncertainties about the growth mechanism indicate that still, there is a wide field for enlarging our knowledge about crystal growth processes.

modifications which are simple in principle and closely related to one another and to the tetrahedral structures typified by the cubic diamond,  $\text{SiC}$ , and the hexagonal graphite. These  $\text{SiC}$  crystals are built up of tetrahedral units of four carbon atoms, which surround each silicon atom in such a way that each carbon atom is also surrounded tetrahedrally by four silicon atoms. Among the modifications one cubic form has been observed (called 'amorphous carbon' by Ovi) which has essentially the same type of structure as  $\text{SiC}$  or diamond, but with silicon atoms occupying the centers of the tetrahedra, which are normally occupied by carbon atoms in diamond. The cubic structure may be looked upon as made up of parallel sheets of tetrahedra which lie perpendicular to the trigonal axis of the cube. The various hexagonal modifications can be derived from the cubic variety by rotating the tetrahedra in alternate sheets so that they lie in parallel or antiparallel directions.

The unit cell dimensions and the space groups of the various forms which have been so far isolated, are given in table (1). Four of the modifications are illustrated in figure 24. In addition to the forms

## CHAPTER V

### The Formation and Crystal Structure of Silicon Carbide

Silicon carbide (1925,1948) occurs in several modifications which, in spite of a formal complexity, are simple in basic principle and closely related to one another and to the tetrahedral structures typified by the cubic zinc blende,  $\text{ZnS}$ , and the hexagonal zincite,  $\text{ZnO}$ . Thus  $\text{SiC}$  crystals are built up of tetrahedral units of four carbon atoms, which surround each silicon atom in such a way that each carbon atom is also surrounded tetrahedrally by four silicon atoms. Among the modifications one cubic form has been observed (called 'amorphous carborumdum' by Ott) which has essentially the same type of structure as  $\text{ZnS}$  or diamond, but with silicon atoms occupying the centres of the tetrahedra, which are normally occupied by carbon atoms in diamond. The cubic structure may be looked upon as made up of parallel sheets of tetrahedra which lie perpendicular to the trigonal axis of the cube. The various hexagonal modifications can be derived from the cubic variety by rotating the tetrahedra in alternate sheets so that they lie in parallel or anti-parallel directions.

The unit cell dimensions and the space groups of the various forms which have been so far isolated, are given in table (1). Four of the modifications are illustrated in figure 24 . In addition to the forms

TABLE (1)

## The relationship between the forms of SiC

SiC designation Ori, Thibault-Ramsdell	Space group	Lattice parameters Absolute Angstrom units	Axial ratio $c/a$	Molecules per hexagonal cell	Authority for parameter data
Undiscovered Type	$C_{6h}^4-C6mc$	$a = 3.0817$ (Predicted) $c = 5.0394$ (values)	$1.0 \times 1.63529$	2	Taylor and Laidler
Mod. IV	$T_d^2-F43m$	$a_w = 4.3590$	$1.5 \times 1.633$	4	Taylor and Laidler
Mod. III	$C_{6h}^4-C6mc$	$a = 3.079$ $c = 10.254$	$2.0 \times 1.633$	4	Thibault
Mod. II	$C_{6h}^4-C6mc$	$a = 3.0817$ $c = 15.1183$	$3.0 \times 1.63529$	6	Taylor and Laidler
Mod. I	$C_{3v}^2-R3m$	$a = 3.079$ $c = 37.78$ $a_{rh} = 12.72$ $\alpha = 13$ $54.5'$	$7.5 \times 1.633$	15	Thibault
—	$C_{3v}^2-R3m$	$a = 3.079$ $c = 52.88$ $a_{rh} = 17.72$ $\alpha = 9$ $58'$	$10.5 \times 1.633$	21	Thibault
33R $\alpha$ -SiC VI.	$C_{3v}^2-R3m$	$a = 3.079$ $c = 83.10$ $a_{rh} = 27.75$ $\alpha = 6$ $21.5'$	$16.5 \times 1.633$	33	Thibault
Mod. V	—	$a = 3.079$ $c = 128.434$ $a_{rh} = 42.85$ $\alpha = 4$ $07'$	$25.5 \times 1.633$	51	Ramsdell
—	$C_{3v}^2-R3m$	$a = 3.079$ $c = 219.094$ $a_{rh} = 73.011$ $\alpha = 2$ $25'$	$43.5 \times 1.633$	87	Ramsdell



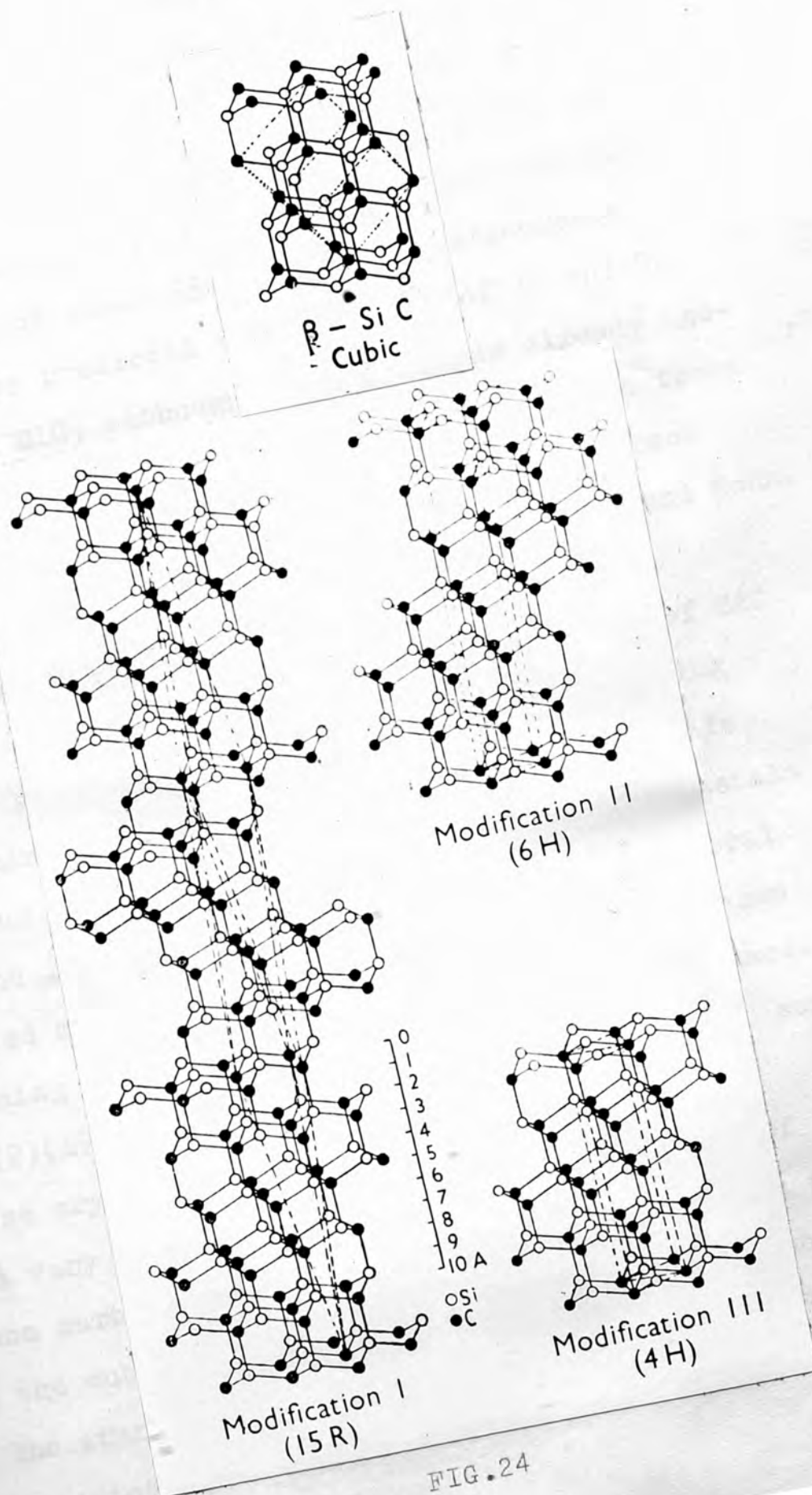


FIG. 24

given in the table, more modifications have been reported. Ramsdell and Kohn (1951), by observing the disagreement between crystal symmetry and X-ray diffraction data have shown the existence of a form SiC 10H. Gasilova, Beletskii and Sokhor (1952) found a 27 layer structure for SiC with space group  $R\bar{3}m$  and packing arrangement (222.3)3. They predicted the existence of 39 and 51 layer types of SiC, although the latter was already isolated by Ramsdell. Gasilova and Sokhor (1952) also found an 8 layer SiC with packing arrangement 4.4 and space group  $C6mc$ . This is also mentioned by Ramsdell and Kohn.

#### Formation of SiC crystals

In 1890 Acheson obtained blue crystals of SiC while attempting to crystallize carbon by dissolving it in aluminium silicate. He called these crystals carborundum. Small hexagonal plates of these crystals were found in a meteorite in Arizona and this mineral was called moissanite. Now these crystals are grown by reducing silica with carbon in an electric furnace. Table (2)(1950) gives the method of preparation of some of these crystals.

A very interesting feature in the formation of silicon carbide under laboratory conditions, seems to be that the cubic form,  $\beta$ -SiC, is always obtained, no matter how the starting materials were varied. Only when the cubic variety was heated almost to the decomposition

temperature, were the hexagonal modifications produced. Although formation temperatures for silicon carbide varying from  $1220^{\circ}\text{C}$  to above  $2000^{\circ}\text{C}$  (1950) are quoted, most authors agree on a decomposition temperature of approximately  $2200^{\circ}\text{C}$ , although  $2700^{\circ}\text{C}$  has also been reported. Density values ranging from 3.10 to 3.30 have been reported for silicon carbide.

Variation in colour ranging from the palest green to jet black with intermediate yellows, browns, greys and purples are to be found in commercial samples of silicon carbide. These colours are probably caused by traces of impurity, mainly iron, in the lattice, and although the lattice parameters and the intensities of the diffraction spectra seem to be in no way affected by the coloration, great variations can be obtained in the electrical characteristics. In the course of preparation, the addition of a little common salt ensures removal of the iron in the form of volatile chloride. Good commercial samples are almost colourless or pale green; chemical analysis shows them to be at least 99.8%  $\text{SiC}$ .

#### Mode of Growth

Experiments by Taylor and Laidler (1950) indicate that silicon and graphite react together in the solid state at as low a temperature as  $1150^{\circ}\text{C}$ . It would appear, however, that the carbide, when prepared from a

mixture of silica and graphite, is formed via a vapour phase reaction at about  $1450^{\circ}\text{C}$ . The X-ray powder diagrams show conclusively that below  $2000^{\circ}\text{C}$  only the cubic variety is formed. Above this temperature and in the region of  $2200^{\circ}\text{C}$  the cubic form partially transforms into the hexagonal variety (6H) after heating for four hours. Evidently there is also some decomposition at this higher temperature, for graphite lines also make their appearance in the powder photographs. These graphite lines are quite sharp, indicating a growth of the carbon decomposition product into crystals larger than  $10^{-5}\text{cm}$  in size. In the process, the more volatile silicon evaporates off leaving the carbon behind. However, the carbonundum residue still has the stoichiometric composition  $\text{SiC}$  even though the crystal symmetry is changed. The complete conversion of the cubic form into a hexagonal polymorph necessitates a much longer heating than four hours. In large-scale commercial processes the period of heating is of the order of 36 hours and temperatures of  $2200^{\circ}\text{C}$  are reached. It is probably for this reason and on account of the higher vapour pressures which are attained that the commercial forms of carborundum are almost invariably hexagonal.

Since silicon carbide decomposes at  $2200^{\circ}\text{C}$  (its melting point was estimated to be  $2230^{\circ}\text{C}$  by Weigel in 1915), it cannot grow from its vapour. The most likely



presumption (1951) is that carbon and silica present in the furnace react at that temperature, generating more volatile gases SiO and CO which supply C and Si needed for the growth of silicon carbide crystals. It is thought that these gases will be adsorbed on the surface of the growing crystal and will undergo surface diffusion reacting with one another to form SiC, the excess oxygen being removed as CO<sub>2</sub> (or perhaps O<sub>2</sub>) which generates CO on the hot carbon, while CO also reduces SiO<sub>2</sub> to the relatively more volatile SiO. The surface of the growing crystal may have a layer of combined oxygen; the state of the surface would vary with temperature and with CO-CO<sub>2</sub> balance in the atmosphere and would be quite complex.

#### Description of Types

To distinguish the various forms of SiC a special term 'polytypism' is used and the various modifications are called the 'polytypes' of silicon carbide. The different types were called type I, II, III etc., in the order of their discovery without referring to their crystal structure. X-ray studies revealed that all types are composed of identical layers and differ only in their arrangement of these. Each type is uniquely distinguished by the number of layers necessary for the arrangement to repeat itself. Thus the total number of layers within the length of the c-axis for the types with

hexagonal unit cell or the rhombohedral types referred to the hexagonal unit, may be taken to represent the type. Ramsdell (1947) added the letter 'H' or 'R' depending upon whether the unit cell is hexagonal or rhombohedral respectively. But this notation does not reveal the geometry of the regular arrangement of the different layers of the unit cell.

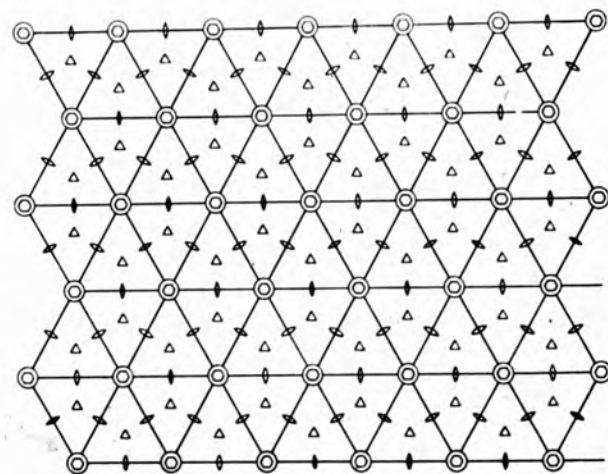
Ott (1925) described the structure in terms of the sequence of silicon (or carbon) atoms along the symmetry axis. For type I 15-layered rhombohedral crystal, in a given axis there are five atoms, which are separated by layer intervals 2,4,3,4 and 2. Thus the (24342) was used to describe the structure. For the 33 and 51 layered rhombohedral types the interval sequences are (24243334242) and (24242433333424242) respectively. This method of representation becomes unwieldy when the number of layers in the unit cell becomes very large and also it cannot be applied to hexagonal structures.

#### ABC Notation

The structure of silicon carbide can be described in terms of the close-packed layers of spheres. The centres of equal spheres will occupy the corners of equilateral triangles when the spheres are close-packed in a plane. Each sphere will touch six others in its own plane. Three-dimensional close-packed structures can be regarded as being made up of layers of this sort.

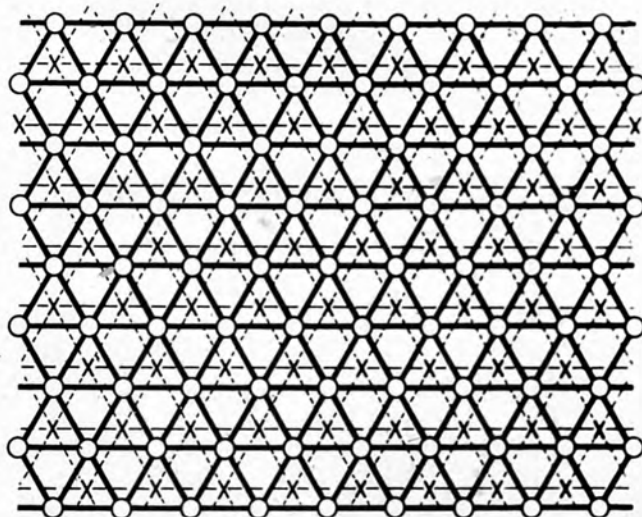
The normal projections of the spheres from different layers, on a plane parallel to one of the layers will lie in any three positions, A,B, or C. Any sequence of these letters with no successive letters alike, will give a possible close-packing arrangement. Hexagonal close-packing can thus be represented as AB,AB, AB - - - etc. and cubic closed packing as ABC,ABC,ABC, - - - etc.

Silicon carbide crystals have a silicon lattice and displaced from it in the direction of the c-axis , an identical interpenetrating carbon lattice. All silicon and carbon atoms lie on the symmetry axes which are in the (11 $\bar{2}$ 0) plane. So its structure can be conveniently represented in a projection on a plane which is parallel to (0001) plane (figures 25 & 26). It is easy to see that Si and C lattices will coincide in this projection; so that each corner of equilateral triangles represents both Si and C atoms. If Si atoms are represented by A,B and C and the carbon atoms by  $\alpha$ ,  $\beta$  and  $\gamma$  , then the closed packed layers of silicon carbide can be designated as A $\alpha$  , B $\beta$  and C $\gamma$  . The different types of SiC crystals will be built of such layers with no two successive layers identical. For brevity  $\alpha$ ,  $\beta$  and  $\gamma$  are omitted and the layers are called A, B and C layers. Some of the types are represented as follows in this notation.



Symmetry elements of SiC lattice in projection on the (0001) plane

FIG.25



Projection on the (0001) plane ; A layer marked O, B layer marked X

FIG.26



<u>Type</u>	<u>ABC notation</u>
4H	ABCB
6H	ABCACB
15R	ABCACBCABACBCB

This notation also becomes more and more unwieldy with the increasing number of layers.

### Nabarro-Frank Notation

The arrangement of the successive layers in silicon carbide is best represented in terms of relationship between two layers or in terms of the stacking 'operators'. Though all the layers are equivalent to each other, they are displaced or rotated through  $60^\circ$  with respect to each other. The pair AB and BA are to be treated as different from each other. If the layer B (figure 26) is on top of A, each atom of B (marked x) lies at the centre of an equilateral triangle formed by the three atoms of A (represented by O). These triangles are oriented as  $\triangle$ . If the layer A lies on top of B, the atoms of A lie at the centre of the equilateral triangles formed by the atoms of layer B and oriented as  $\nabla$ . Thus the relationship between the layers can be expressed as  $\triangle$  and  $\nabla$  respectively. It is easy to see that if A, B and C layers follow each other in this cyclic order, the relationship between the layers is always  $\triangle$ . If, however, A follows B, B follows C and C follows A, the arrangement will be represented by  $\nabla$ .

In this representation a  $60^\circ$  rotation converts the operator  $\triangle$  to  $\nabla$ . This notation is referred to as Nabarro-Frank notation (1951). This notation is further contracted in the Zhdanov symbol (1945). Table (3) shows both ways of representation for some types of silicon carbide.

Table (3)

Crystal Modification	Nabarro-Frank Notation	Zhdanov Symbol
15R	$(\triangle \triangle \triangle \nabla \nabla) \triangle \triangle \triangle \nabla \nabla$	(32)
6H	$(\triangle \triangle \triangle \nabla \nabla \nabla)$	(33)
4H	$(\triangle \triangle \nabla \nabla)$	(22)
33R	$(\triangle \triangle \triangle \nabla \nabla \nabla \triangle \triangle \triangle \nabla \nabla)$ $\triangle \triangle \triangle \nabla \nabla \nabla \triangle \triangle \triangle \nabla \nabla$ $\triangle \triangle \triangle \nabla \nabla \nabla \triangle \triangle \triangle \nabla \nabla$	(3332)

'Mixed' Types

Ramsdell and Kohn (1952) postulated that in the growth of silicon carbide by sublimation, there are formed certain cluster of atoms (polymers), each characterised by a particular temperature stability range. At a given characteristic temperature a single type of polymer would produce a 'pure type', with the sequence consisting of identical pairs. If stability

ranges overlap two polymers might exist simultaneously resulting in a 'mixed' type. It would not be possible to have three polymers stable simultaneously hence no type should be composed of more than two polymers.

0.5g Cey. graphite 0.4 Silicon (crystalline)	Preparation made in a evacuated carbon tube furn. Samples in the form of powders, were placed in a pure graphite test tube which was lowered into the carbon heater element, Time 2h at 1800C	Film formed over charge at about 1500C Same light green crystals were observed in main charge by microscope.	Face-centred SiC + un- changed graphite.
0.5g charcoal 2g silicon	Method of prep. same as (2). Time 5h at 1800C.	Charge gray in colour.	Face-centred SiC with smaller than 1000C. Un- changed silicon also present
Commercial charge 4g coke 0.10g saw dust 5.35g sand & 0.15g NaCl.	Carbonized at 900C for 2h, then 4h at 1300C.	Carbonization first in air at 900C to get uniform charge for furnace.	Face-centred cubic SiC + little carbon
0.5g Cey. graph. 0.25g Si.	1 h at 1800C, 1 h at 2000C, 2 h at 2300C	Film of amorph. material formed near top of tube. 'Collar' of f.c.c. SiC formed above main charge in cooler part of tube.	Main charge hex. SiC + f.c. SiC-graphite
Pre-1. SiC from 'best' charge at 1800C for 4h	4h at 2200C	Product contain- ed much free graphite.	Hexag. and small amount of f.c.c. SiC
Pre-1. SiC from 'best' charge at 1800C for 4h	2h at 2000C	Charge went black, some	Hex. SiC and strong graphitic particulate

TABLE (2)

No	Material used	Furnace used and conditions	Experimental observations	X-ray data
(1)	2g Ceylon graphite 2g crushed quartz	Prepared in air in a graphite crucible in an induction furnace. Kept for 2h at 1600°C in the furnace.	Feathery mass of vitreous SiO <sub>2</sub> on top of main charge (small light green crystals).	Face-centred cubic SiC+a little unchanged graphite. Feathery mass of SiO <sub>2</sub> gave the broad band of Vitreous Silica
(2)	0.8g Cey. graphite 0.4 silicon (crystalline)	Preparation made in a evacuated carbon tube furnace. Samples in the form of powders, were placed in a pure graphite test tube which was lowered into the carbon heater element, Time 2h at 1800C	Film formed over charge at about 1500C. Same light green crystals were observed in main charge by microscope.	Face-centred SiC + unchanged graphite.
(3)	0.6g charcoal 2g silicon	Method of prep. same as (2). Time 3h at 1200C.	Charge grey in colour.	Face-centred SiC quite sharply defined (cry size greater than 1000AU. Unchanged silicon also present.
(4)	Commercial charge 4g coke; 0.50g saw dust 5.35g sand & 0.15g NaCl.	Carbonized at 900C for 1h, then 4½h at 1900C.	Carbonization first in air at 900C to get uniform charge for furnace.	Face-centred cubic SiC+a little carbon.
(5)	0.5g Cey. graph. 2.25g Si.	1 h at 1800C, 1 h at 2000C, 2 h at 2300C	Film of amorph. material formed near top of tube. 'Collar' of f.c.c. SiC formed above main charge in cooler part of tube.	Main charge hex. SiC+f.c.c. SiC+graphite
(6)	F.c.c. SiC from 'Comm' charge at 1900C for 4½h	4h at 2200C	Product contained much free graphite.	Hexag. lines & much stronger graph. lines.
(7)	Light green comm. hex. SiC 6H.	2h at 2050C	Charge went black.	Hex. SiC and strong graphite pattern.



CHAPTER VI

EXPERIMENTAL TECHNIQUES

Multiple-Beam Interferometry

The technique of multiple-beam interferometry was developed by Tolansky (1944,1945,1946) some seventeen years ago. Since then it has made considerable progress and now has wide application (1960). This technique has been extensively used in the study of microtopography and this includes measurement of surface distortions caused by indentation, using the ball, the Vickers and the double-cone indenters (1949,1952,1955,1954). In this chapter only the salient features of the interferometric technique will be described.

Fizeau Fringes

Fizeau (1862) was the first to introduce interference methods for the study of surface features. He showed that when optical interference takes place in a thin transparent wedge of refractive index  $\mu$ , straight-line fringes occur at wedge thickness  $t$ , given by

$$n\lambda = 2\mu t \cos \phi \quad (1)$$

where  $\phi$  is the angle of incidence of light,  $\lambda$  the wave length and  $n$ , the order of interference. It is necessary to view such a wedge in reflection as then the amplitudes of the two interfering beams are

similar and the fringe visibility is good. The intensity distribution along the wedge follows a  $\cos^2$  curve. In transmission, on the contrary, fringes of similar intensity and distribution are super-imposed upon an intense background and are consequently hardly visible.

It is seen from (1) that any irregularity in the wedge surfaces will cause a corresponding change in the fringe pattern. Although this method has been widely used in the study of surfaces, its sensitivity in measurement is limited by the  $\cos^2$  distribution of intensity. A sensitive optical refinement of two beam interferometry is the multiple-beam interference technique.

Airy (1831) considered the effect of multiple reflection in a parallel plate system (figure 27) and showed that the intensity distribution is given by

$$I_T = \frac{T^2}{(1-R)^2} \cdot \frac{1}{1 + \frac{4R}{(1-R)^2} \sin^2 \frac{\delta}{2}} \quad (2)$$

for transmission or

$$I_R = \frac{4R \sin^2 \frac{\delta}{2}}{(1-R)^2 + 4R \sin^2 \frac{\delta}{2}} \quad (3)$$

for reflection; T and R are the transmission and

reflection coefficients respectively and  $\delta = \frac{2\pi}{\lambda} \cdot 2\mu t \cos \phi$

$\phi$  is the constant phase lag between successive beams.

R and T should be replaced by  $\sqrt{R_1 R_2}$  and  $\sqrt{T_1 T_2}$  if the two surfaces of the parallel plate have different reflection and transmission co-efficients.

From (2) it is seen that when  $\sin^2 \frac{\delta}{2} = 0$ ,  $I_T = \frac{T^2}{(1-R)^2}$

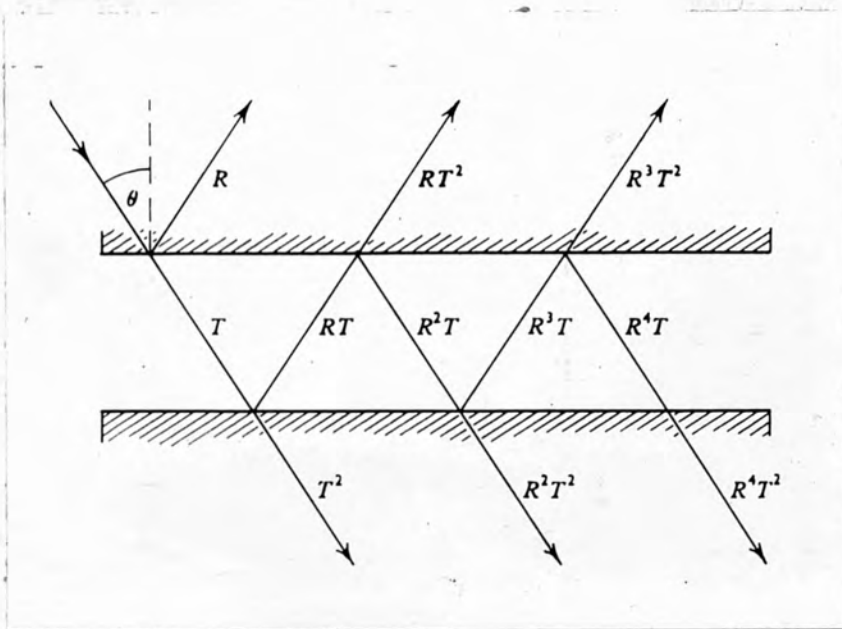


FIG. 27

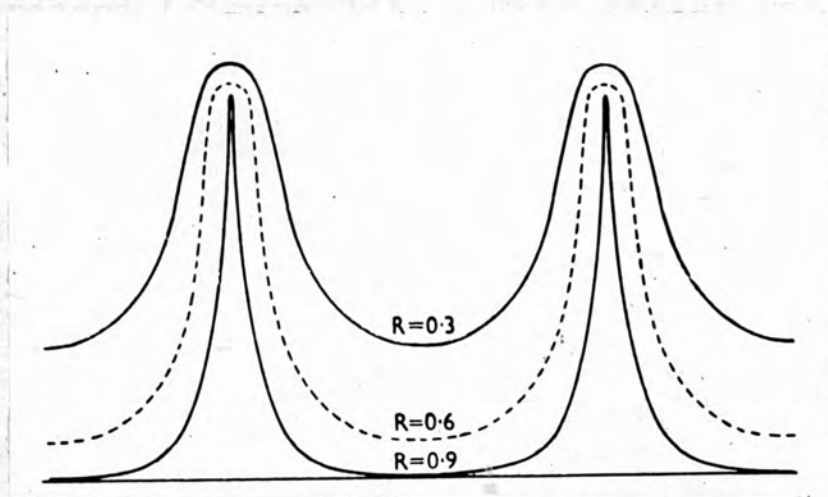


FIG. 28

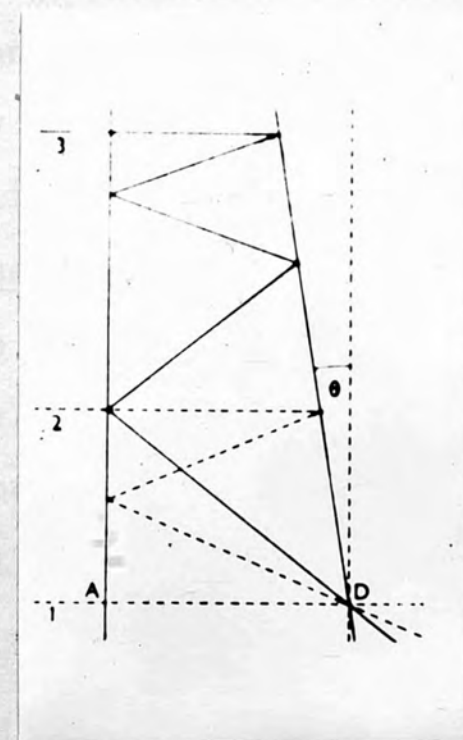


FIG. 29

which is unity when there is no absorption, since  $R+T = 1$ . So the fringe peak maximum has the same intensity as that of incident light.

When  $\sin^2 \frac{\delta}{2} = 1$ ,

$$I_{T_{min}} = \frac{(1-R)^2}{(1+R)^2}.$$

The fringe shape is independent of  $T$  and is determined only by the reflectivity  $R$ .

Boulouch (1893) showed that the intensity maxima in transmission become much sharper when the value of  $R$  is increased (figure 28). This effect was used in the Fabry-Perot interferometer (1897). Although Fabry and Buisson (1919) used a thin wedge silvered on both sides to produce reasonably sharp Fizeau fringes, they did not analyse the conditions required to produce really sharp wedge fringes. Tolansky (1946) for the first time pointed out that the Airy summation only holds strictly for a parallel plate. He, however, carried out an analysis to show that a close approximation to the Airy formula can be achieved for a doubly silvered wedge, if certain critical conditions are fulfilled.

### The phase Lag

The distinguishing feature between the wedge and the parallel plate is that in the latter the phase difference between successive pairs of beams at one angle is equal, the emergent beams being parallel and the fringes at infinity, While in the wedge, the phase lag



depends on the thickness of the wedge, the wedge angle and the angle of incidence (figure 29) the successive beams entering the collecting lens at different angles and the fringes being localized in the wedge.

Tolansky (1946) first calculated the phase lag for successive reflections in a wedge in the case of normal incidence and then later an improved calculation was made by Brossel (1947). In figure 30 AC, CB represent the wedge and also the wavefronts reflected at each surface, angle ACB being the wedge angle.  $CD_1$ ,  $CD_2$  - - -  $CD_n$  represent the successive wave-fronts after multiple reflections. The calculated path difference between the first, and the nth beam at the point P(x,y) given first by Tolansky is

$$\Delta = 2nt - \frac{4}{3} n^3 \theta^2 t \quad (4)$$

If the path difference between the first and the  $n^{\text{th}}$  beam is  $\frac{\lambda}{2}$ , then the beams of this order will oppose the Airy summation, and fringe definition will be reduced.

In this case

$$\frac{4}{3} n^3 \theta^2 t = \frac{\lambda}{2} \quad \text{and} \quad t_c = \frac{3}{8} \frac{\lambda}{n^3 \theta^2}$$

If there are X fringes per cm., then

$$\theta = \frac{X\lambda}{2} \quad \text{and} \quad t_c = \frac{3}{2n^3 \lambda X^2} \quad (5).$$

Taking  $n=60$  and  $\lambda = 5.46 \times 10^{-5}$  cm., gives  $t_c = \frac{1}{7.9X^2}$  cm.

This is the upper limit for  $t_c$  and in fact it should be below the value calculated.

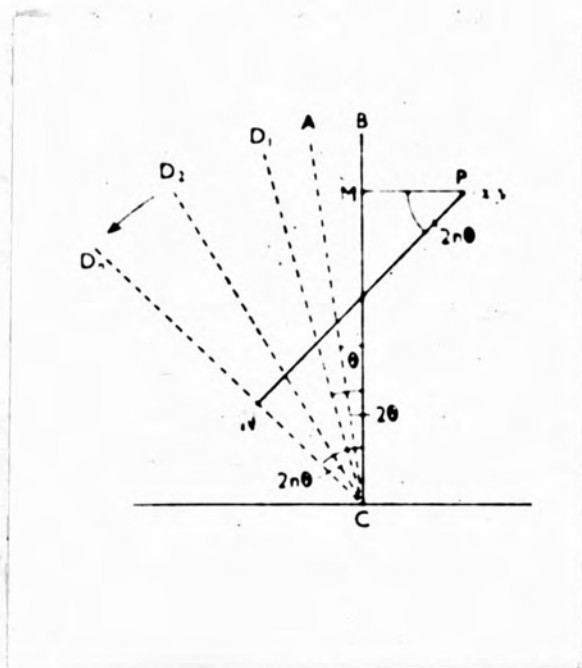


FIG. 30

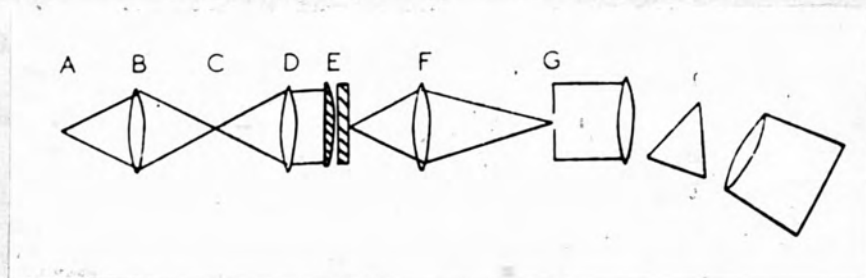


FIG. 31

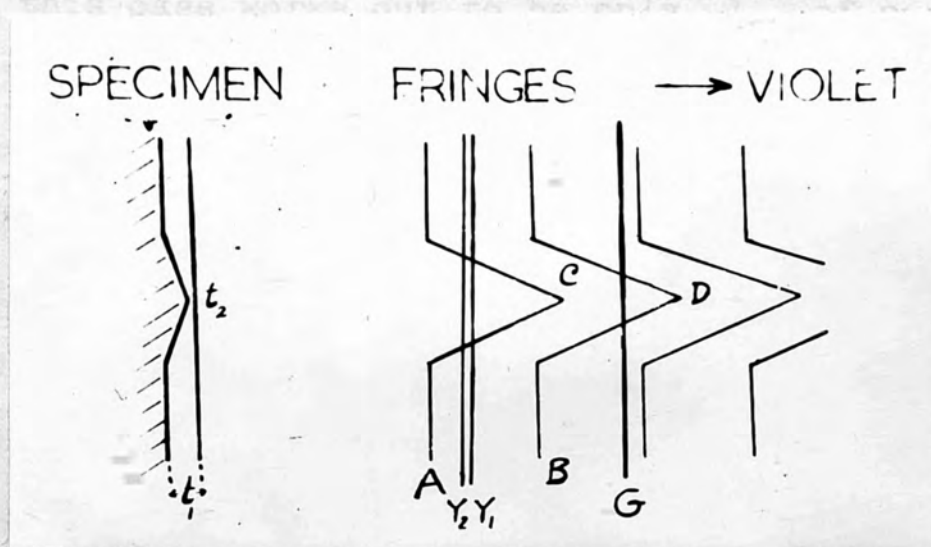


FIG. 32

Linear Displacement; Numerical Aperture of the Objective;  
and Parallelism of Beams

From figure 29 it is easy to see that the higher order beams come from regions progressively further away from the first beam. The linear separation on the surface of the wedge between the first and the  $n^{\text{th}}$  beam is

$$\begin{aligned} d_n &= 2n(n+1) t\theta \\ &= 2n^2 t\theta \quad (\text{for larger values of } n). \end{aligned}$$

Using the relation  $\theta = \frac{X}{2}\lambda$ ,

$$d_n = n^2 t \lambda X \quad (6)$$

For  $n=60$  and  $\lambda = 5.46 \times 10^{-5} \text{ cm}$ ,  $d_n \simeq \frac{tX}{5}$ . Since it is necessary for  $t$  to be small to satisfy the phase condition, the value of  $d$  will also become small as can be seen from equation (6).

When viewing objects at higher powers one can take  $X=100$ , which gives a dispersion of  $\frac{1}{10}$  th mm; (taking  $t_c = \frac{1}{10X^2}$ )  $t_c$  for this case works out to be only  $\frac{1}{10^4}$  of a mm., which is one-fifth of a light wave and  $d_n = 0.002 \text{ mm}$ . The whole of the 60 beams can thus come from a region comparable to the resolving power of the microscope.

The beams which emerge from the wedge diverge increasingly from the normal even though the incident light is parallel. It can be shown from figure 29 that the  $n^{\text{th}}$  beam emerges making an angle  $2n\theta$  to the original direction.

The beams are thus, displaced in one direction and the illumination is not symmetrical. Hence, the microscope objective aperture should be large enough to collect all the beams in its semi-angle of collection. If the numerical aperture of the objective is smaller it may not be able to collect all the beams which will result in the broadening of the fringes.

### Effect of Imperfect Parallelism

Due to the finite size of the source and the imperfections of the lens, the incident beam is not strictly parallel. This leads to a range of angles of incidence which results in fringe broadening. The fringe broadening can be expressed as a fraction of an order by the relation

$$\delta n = \frac{\mu t}{\lambda} \phi^2$$

where  $\phi$  is the angle of incidence assumed to be small. Fringes usually have a half-width of about  $\frac{1}{40}$ th of an order. If the fringes are not to be increased in width by more than a fifth of this then  $\delta n = \frac{1}{200}$ . The tolerance in  $\phi$ , when  $t = \frac{1}{1000}$ th mm., is  $3^\circ$  taking

$\lambda = 5 \times 10^{-5}$  cm. If a 10 cm lens is used for producing the parallel beam, the size of the aperture that can be permitted at the lens focus is 6mm.

### Absorption Effects

The transmitted intensity can be written as

$$I_T = \frac{T^2}{(1-R)^2} \cdot \frac{1}{1 + F \sin^2 \frac{\delta}{2}} \quad \text{where } F = \frac{4R}{(1-R)^2}$$



and is called the coefficient of finesse (or fineness), since it determines the fringe shape. If there is absorption in the silver film, the transmission will no longer be equal to  $1+R$  but  $T+R+A=1$ , where  $A$  is the fraction absorbed at each silver film.  $\left(\frac{T}{1-R}\right)^2$  then becomes

$$K = \left( \frac{1}{1 + \frac{A}{T}} \right)^2$$

The width of a fringe is usually described by a quantity  $W$ , which is defined as the width at half intensity. It can be shown that  $W$  occupies a fraction of the space between two orders equal to  $\frac{0.63}{F^{1/2}}$ , which is near enough  $\frac{1-R}{3R^{1/2}}$ . Since the coefficient of fineness  $F$  still remains independent of  $A$ , the absorption merely reduces the transmitted pattern in intensity by the factor  $K$  and not its shape.

In the case of reflected fringes it can be shown that the fringe contrast is high for low absorption and the fringe minima dip very low and appear dark against an intense bright back ground. If the absorption is high, the fringes will still be narrow but they will hardly be visible. So we see that fringe width is determined by reflectivity and fringe visibility is decided by absorption only.

#### Line-Width of the Source

The smallness of  $t$  has an important bearing on

the monochromaticity of the source used for the multiple-beam Fizeau fringes. Tolansky (1960) has shown that a natural line-width of as much as 5Å can still be tolerated and yet only produce broadening amounting to the acceptable one-fifth of the width of a fringe for a  $t$  value of  $\frac{1}{1000}$ th of a mm. The widths of the lines from a vacuum mercury arc are usually below this. It means quite a hot bright source can be tolerated with no fringe broadening, provided  $t$  is small.

### Conclusion

The following conditions should, therefore, be fulfilled for the production of sharp Fizeau fringes.

- (1) The surface must be coated with a highly reflecting film of minimal absorption.
- (2) This film should contour the surface exactly and be highly uniform in thickness.
- (3) Monochromatic light or at most a few widely-spaced monochromatic wave-lengths should be used.
- (4) The interfering surfaces must be separated by at most a few wave-lengths of light.
- (5) A parallel beam should be used (within a  $1^\circ$ - $3^\circ$  tolerance).
- (6) The incidence should preferably be normal.

### Fringes of Equal Chromatic Order

These fringes were first described by Tolansky in 1945. If the image of a section of an interferometer wedge is projected on to the slit of a spectrograph (fig.31)

and the mercury source is replaced by a white light source, fringes of equal chromatic order are observed in the focal plane of the spectrograph. Over any section of the wedge,  $t$  and  $\lambda$  are variables and fringes are formed at constant  $t/\lambda$  and since the fringes cover a wave-length range they are chromatic. Assuming normal incidence, for an air film we can write

$$n=2vt \text{ where } v \text{ is the wave number.}$$

Differentiating

$$dn=2 \, dv \, t.$$

For successive orders  $dn=1$ , therefore

$$t = \frac{1}{2 \, v}$$

For any given value of  $t$ , the fringes are equally spaced and as distinct from Fizeau fringes dispersion is independent of the wedge angle. These fringes are readily related to the surface topography over the region selected by the spectrograph slit. If the surface is curved the fringes are also curved, and if the surface is concave the fringes are convex towards the red, where as if the surface is convex, the fringes are convex towards the blue.

#### Method of Measurement

The spectrograph used was a constant deviation glass prism spectrograph. Measurement of wave-lengths were made by exposing photographic plates to both the fringes of equal chromatic order and the mercury spectrum.

Suppose the height  $(t_1 - t_2)$  of the hill shown in figure 32 is to be measured. If  $n$  and  $(n+1)$  are the orders of the fringes A and B respectively, then

$$2t_1 = n\lambda_A = (n+1)\lambda_B \quad (1)$$

$$\text{and } 2t_2 = n\lambda_C = (n+1)\lambda_D \quad (2)$$

$$\text{from which } n = \frac{\lambda_B}{\lambda_A - \lambda_B} = \frac{\lambda_D}{\lambda_C - \lambda_D} \quad (3)$$

Then the height  $(\Delta t)$  of the hill is given by

$$\Delta t = t_1 - t_2 = \frac{1}{2} \frac{\lambda_B}{\lambda_A - \lambda_B} (\lambda_A - \lambda_C) \quad (4)$$

In practice two successive fringes A and B are selected near the mercury green and yellow doublet lines. The horizontal distances of A, B, C, D, G and  $Y_2$  are measured from  $Y_1$  and the wave-lengths of A, B, C and D are calculated from the dispersion curve of the spectrograph.

It is easily possible to measure step heights to an accuracy of  $\pm 15 \text{ \AA}$  using a constant deviation spectrograph.

#### Thin-Film Technique (1960)

The surface to be studied is first coated with a silver film of thickness 700  $\text{\AA}$ . Tolansky has established that such a film has high reflectivity and fits closely enough any surface micro-structure down to within crystal dimensions. A 2% solution of collodion in amyl acetate is then poured over the silvered surface. From electron microscopy, it is known that such a solution produces a replicating film of very high fidelity. This film, if allowed to dry, will not be useful for interferometric work because both top and bottom of the film would



tend to follow the surface contour. For interferometry the film should fit closely the microtopography on its lower face and its upper surface should be as smooth and flat as possible. To achieve this a more concentrated solution of collodion is poured immediately after pouring the dilute solution on the surface. It is, then, at once drained off to get an interferometric thin film wedge. After drying, the top surface is again silvered. Thus a thin collodion film, silvered on both sides, is got; the lower side of this film replicates the microtopography of the crystal and the upper side, which is slightly curved, acts as the reference surface. With this system Joshi and Tolansky (1960) have reached a resolution and definition which has not been possible to achieve, so far, by any other method.

#### Multi-layer Technique

With opaque surface, to get better reflection fringes, it is often a great advantage to coat the matching flat with a dielectric multi-layer. The multi-layer has very low absorption and hence it is possible to secure high contrast in reflection fringes.

If a thin film of thickness  $\lambda/4$ , of a dielectric material of refractive index greater than glass is deposited on to glass, then the reflectivity of that glass is enhanced. Zinc sulphide with its refractive index 2.37 (for sodium light) is a suitable material for

this purpose. Because the retardation at normal incidence of the light from the two faces is  $\lambda/2$  and as there is a  $\lambda/2$  path difference due to phase change, (as the lowest face is in contact with a lower refractive index), the beams reflected from top and bottom of the film interferometrically unite and reinforce. This combined effect from the double interface coupled with high reflectivity at each inter-face due to the high refractive index, makes the reflectivity of the coated glass jump from 0.04 to 0.31.

The reflectivity can be increased to 0.67 by putting on top of this ZnS film, first a low-index film of thickness  $\lambda/4$  (cryolite has a refractive index of 1.36 and is generally used) and then again on top of this another high index ZnS  $\lambda/4$  film. It is found that 5 such layers give a reflectivity of 0.87, seven layers give reflectivity 0.94 and nine layers give reflectivity 0.97. Zinc sulphide and cryolite (sodium aluminium fluoride) are colourless transparent crystals and in thin films of  $\lambda/4$  thickness have very low absorption, which is also a great advantage.

#### Light-profile Technique

For features with depth greater than one micron, multiple-beam interferometry is not suitable. To cover this range (1952) Tolansky developed the light-profile technique based on the work of Schmaltz (1936).

The salient points about the technique will only be given. The image of a thin wire is projected on to the surface under study by an off-centre illumination and viewed as indicated in the figure 33. This is very well achieved by using a Vickers Projection Microscope (figure 34). The field viewed will consist of the image of the specimen which is crossed by a dark profile whose lateral shifts give the corresponding depth changes of the specimen surface. If  $M'$  is the magnification in profile,  $M$  the linear magnification of the microscope, then it can be shown that

$$M' = Mx \frac{2 \tan i}{\mu}$$

where  $i$  is the effective angle of incidence of the pencil and  $\mu$  is the refractive index of the medium between the specimen and the objective.  $M'$  is obtained by evaluating  $i$  or by direct calibration from a known depth determined by interferometry; this leads to the determination of  $\frac{2 \tan i}{\mu}$ , which is known as the profile constant. For 8 mm, 4 mm and 2 mm objectives, the profile constant was found to be 0.56, 1.23 and 1.5; the latter reduced to 1.0 when an oil-immersion 2 mm objective was used.

### Phase-Contrast Microscopy

Many specimens are incapable of producing sufficiently large variations in the intensity of the image formed by bright-field technique to render their



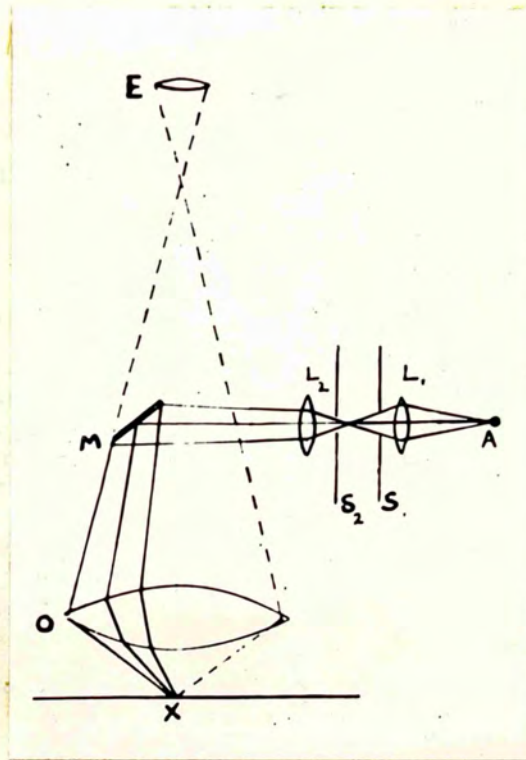


FIG. 33

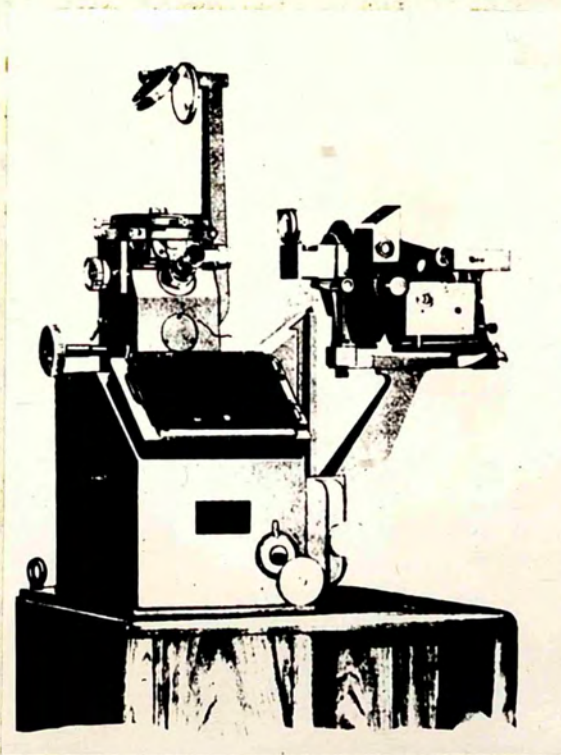


FIG. 34



structure visible. Slight phase changes are, however, present within the emergent beams and in phase-contrast microscopy they are used to provide amplitude contrast in the final image by interference. The principles of phase-contrast microscopy were first given by Zernike (1934,1935) and later a number of workers have contributed to the development of its mathematical theory and also to its practical applications (1951).

#### Elements of the Theory

Let a small transparent specimen, embedded in a medium of almost the same refractive index as the specimen, be located on the optic axis of a microscope optical system. The slight difference in the refractive index between the specimen and the surrounding medium will give rise to a slight difference in optical path between the specimen and its surroundings. If the refractive index of the specimen is higher than the surrounding medium, then an incident light wave will be retarded after transmission through the specimen; in other words a small phase difference is introduced between the waves S and P as shown in figure 35. The difference between the two sine waves S and P is given by the sine wave D, which is about  $1/4$  wavelength out of phase with S, provided the retardation of P is small. D, then represents the light deviated by diffraction at the specimen. The light represented by S acts as if no specimen were present,

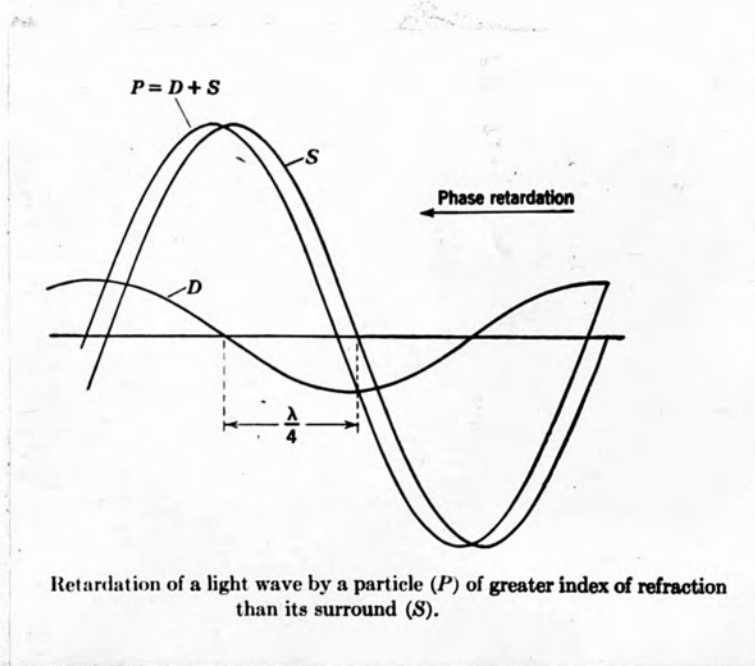


FIG. 35

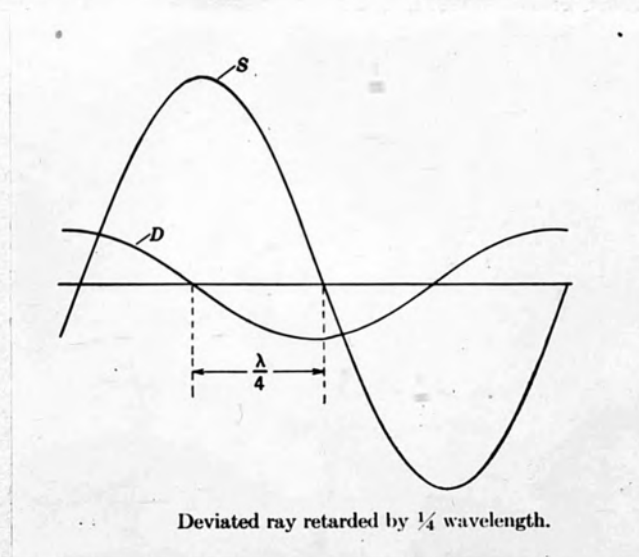


FIG. 36

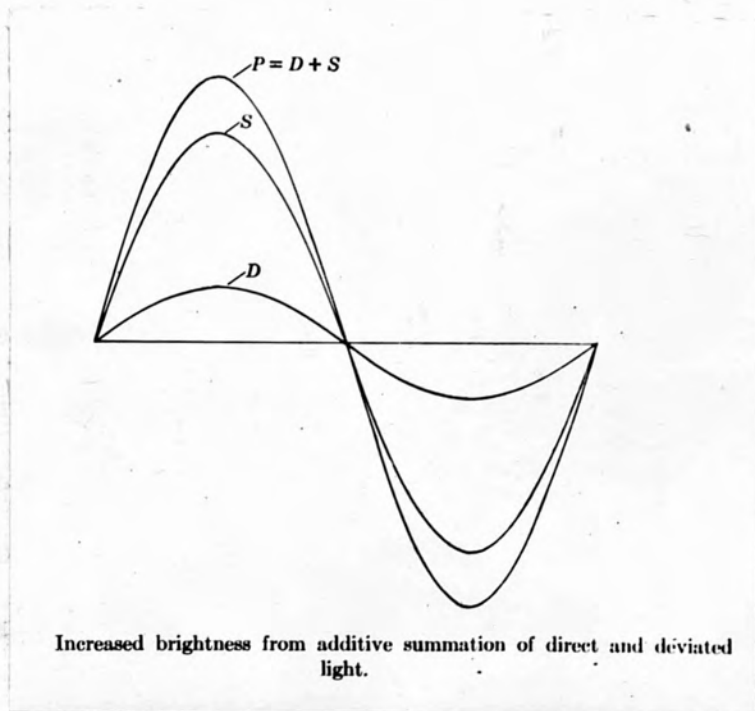


FIG. 37

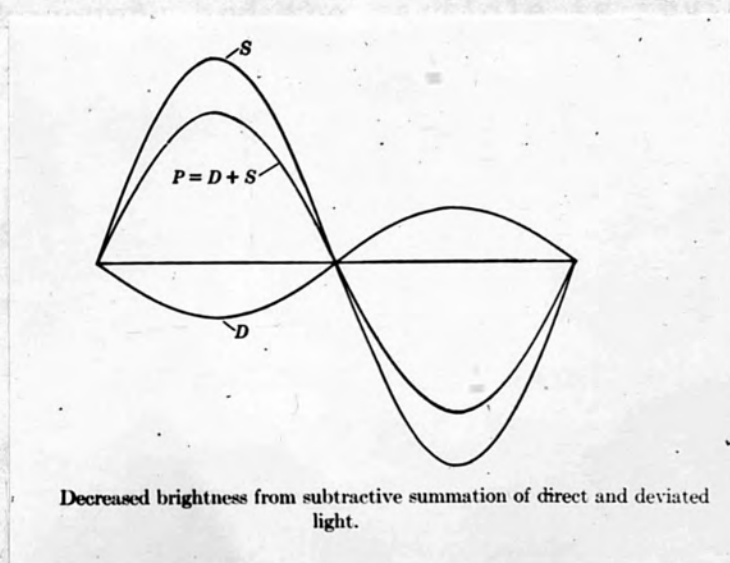


FIG. 38

that is, it is undeviated. S and D thus represent the two waves entering the microscope objective. If S is obstructed by blocking it off in the objective lens system, there will be simply darkfield illumination; if D is obstructed and S is let through, no detailed imagery of the specimen will be seen. Microscopic images are, in general, obtained by allowing both the undeviated wave, S, and the deviated (by diffraction) wave, D (fig.36), to pass through the microscope objective and interfere in the neighbourhood of the geometrical image of the particle formed by the objective. Here the waves D and S recombine and form the wave P. The image of the surround is formed by the wave S. Since the amplitudes of S and P are equal, because the specimen is transparent, there is no contrast between the image of the particle and its background, and the particle is invisible. This situation is characteristic of the ordinary microscope.

If the phase of D can be changed with respect to S, so that S and D are either in exactly the same phase or  $\frac{1}{2}$  wavelength out of phase, a striking contrast can be obtained between the specimen and its background. This shift in phase can be accomplished by artificial means. Figure 37 represents the combination of the waves D and S when the phase of D has been advanced (or that of S retarded) by  $\frac{1}{4}$  wavelength. It can be seen that the amplitude of D+S representing the light in the image of



the particle, is considerably greater than that of S, the background light and the particle will appear lighter than its background (negative phase-contrast).

If the deviated wave, D is retarded by  $1/4$  wavelength ( or S advanced by the same amount), the condition shown in figure 38 will be the result. The light in the image of the particle is now S-D, and, as in the previous example, the background remains of amplitude S. The particle will appear darker than the remainder of the field of view (positive phase-contrast).

Thus, if the phase of the deviated light can be changed with respect to the direct (undeviated) light from a single point in the original source of illumination, we have a means for changing the invisible phase difference arising in the specimen into amplitude differences in its image, which is thereby rendered visible.

Figure 39 illustrates how this change is accomplished in a simple case.

#### Reflection Phase-Contrast Microscope

The reflection phase-contrast microscope is essentially the same as the transmission one, only the optical system is altered to give vertical incident illumination. The phase differences in the wave fronts reflected from an opaque object arise from differences in the general surface level, diffracting structure on the surface and any slight variations in the penetration

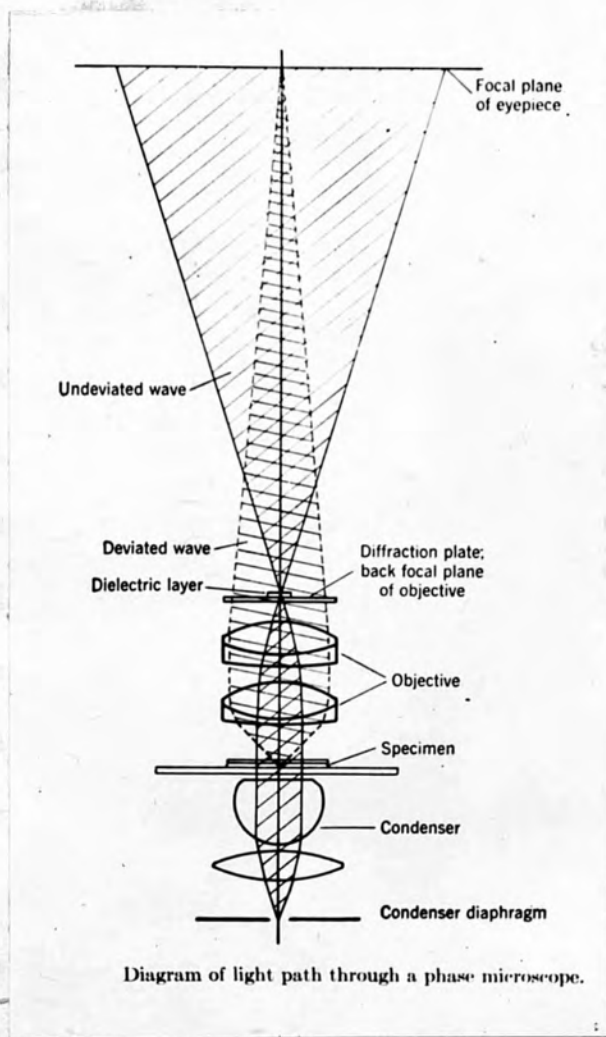


FIG. 39

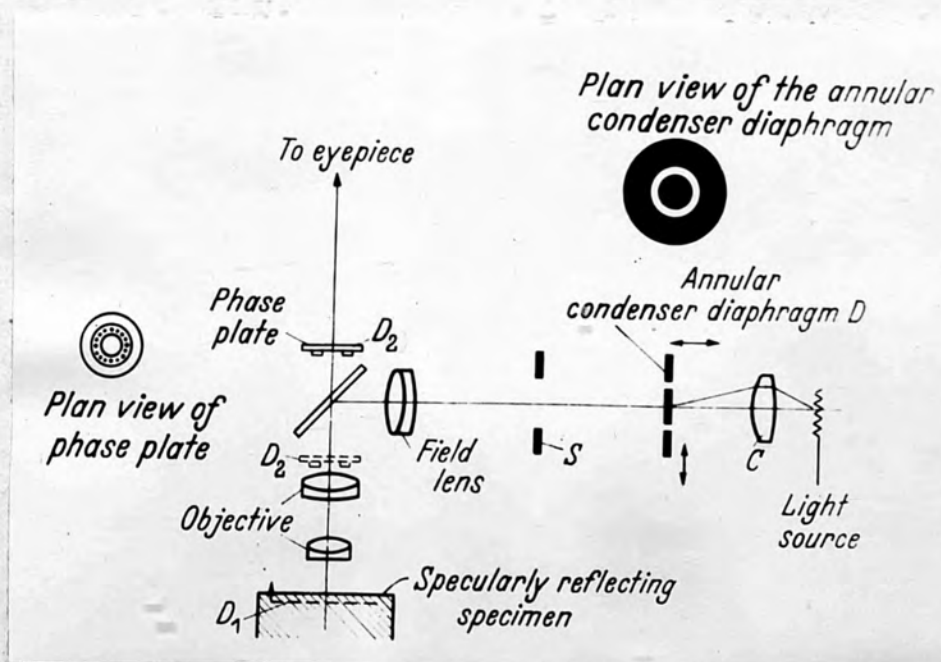


FIG. 40

of the incident light into the surface. Figure 40 gives a diagrammatic sketch of such a microscope. The annular diaphragm D serves as the entrance pupil of the optical system consisting of a field lens, the microscope objective and the reflecting surface of the specimen. The condenser lens C focusses the light source on D. The field lens and the objective form an image  $D_1$  of the diaphragm D, below the specularly reflecting surface of the object specimen. The light is reflected by the surface of the specimen and passed through the objective to form a real image  $D_2$  of D. Image  $D_2$  becomes the exit pupil and therefore the location of the diffraction plate. Figure 41 is the Olympus microscope which was used in this work.

#### Phase plates

The diffracting plate (the phase changing annulus) may be a groove in the glass, which reduces the optical path length in this area and thereby advances the direct beam relative to the diffracted beams to provide so called positive phase-contrast. Alternately it may be a transparent layer of dielectric material (such as magnesium fluoride) which retards the phase of the direct beam to produce negative phase contrast. Figure 42 shows both the types of phase plates.

#### EVAPORATION TECHNIQUE

An Edward's coating unit type E3 (fig.43) was



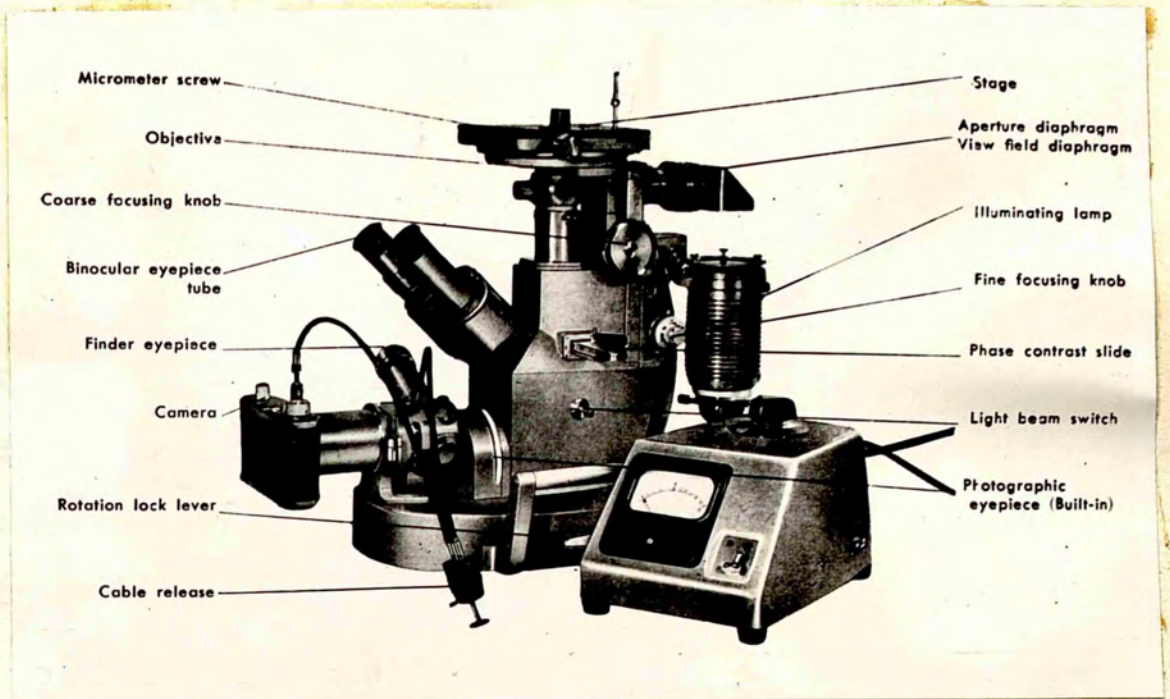


FIG.41

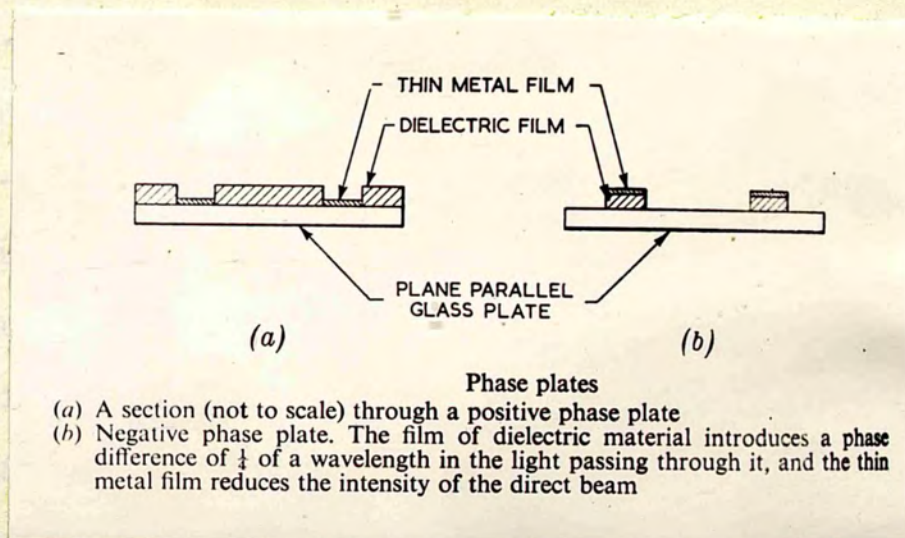


FIG.42



used to evaporate silver in vacuum. Figure 44 gives a diagrammatic sketch of the plant. The bell jar, which is 60 cm high and 40 cm in diameter, is evacuated by silicon oil diffusion pump backed by a rotary pump. A Pirani gauge indicates the pressure in the backing line and the pressure in the jar is measured by a Phillips cold-cathod ionisation gauge. The silver is heated on a molybdenum filament placed at a distance of 30 cm from the specimen; this ensures a uniform deposition of silver film on the specimen, to within one per cent, over an area of 2 cm square.

#### Silvering Operation

The specimen is thoroughly cleaned by the now standard method, using first a detergent and later hydrogen-peroxide. It is, then, placed in the bell jar facing the filament, which is covered by an adjustable shutter. The pressure in the chamber is reduced to 0.1 mm. Hg by the rotary pump, which is connected through a by-pass to the chamber. At this pressure the rotary pump is made to back the oil diffusion pump and the vacuum chamber is slowly opened to the diffusion pump. The final cleaning of the specimen is done by ionic bombardment, by passing a H.T. discharge for 2 or 3 minutes, between two circular rings within the chamber. The H.T. voltage used is 3300 volts and the primary current of the transformer is not allowed to exceed 4 amperes.

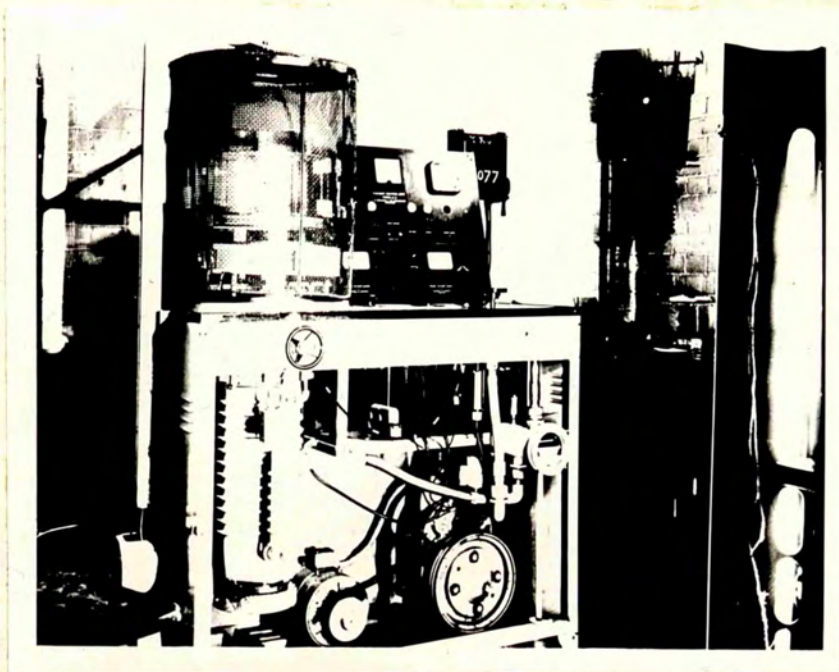


FIG. 43

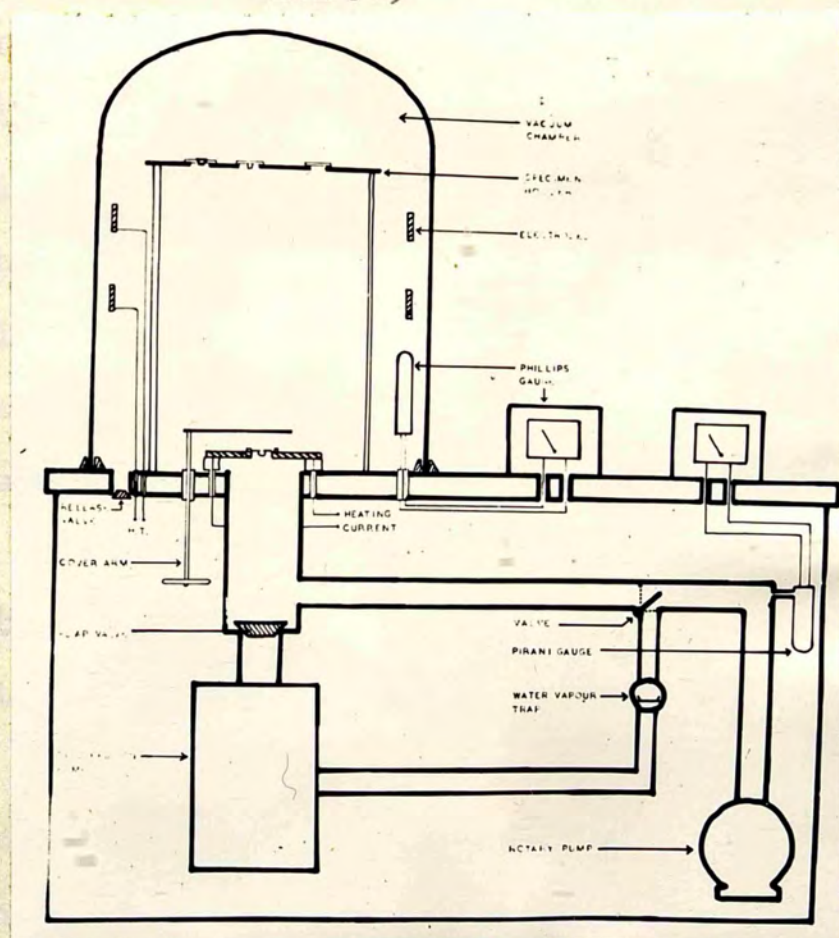


FIG. 44



When the pressure indicated by the Phillips gauge is 0.1  $\mu$  Hg, silver is evaporated on to the specimen at a filament current of 120 amperes for 15-40 seconds depending on the film thickness required.

#### The Indentation Appartus

For low load hardness tests the standard indentation apparatus made by Cooke, Troughton and Simms was used. Figure 45 shows the indentation apparatus set up on the Vickers Projection Microscope. The different letters in the figure stand for the following parts of the apparatus:

- A - Coarse motion operation head
- B - Fine       "       "       "
- C - Diamond indenter objective
- D - Socket and support block for load centre indicator
- E - Rotation stop to load centre indicator
- F - Base plate
- G - Securing screws
- H - Counter weight
- I - Vertical pillar
- J - Pivot axle bearing with adjusting screws
- K - Pocket for auxiliary counter-weights
- L - Auxiliary counter-weights
- M - Beam
- N - Lamp housing with red glass window
- O - Horizontal bar support to indicator pin

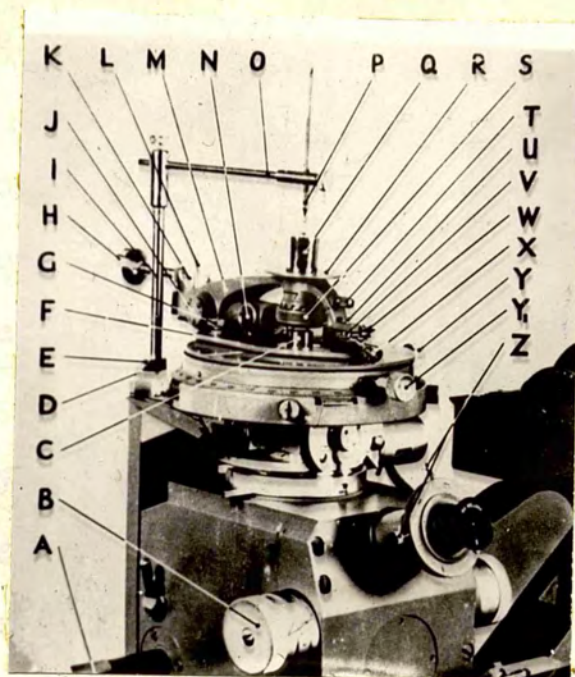


FIG.45

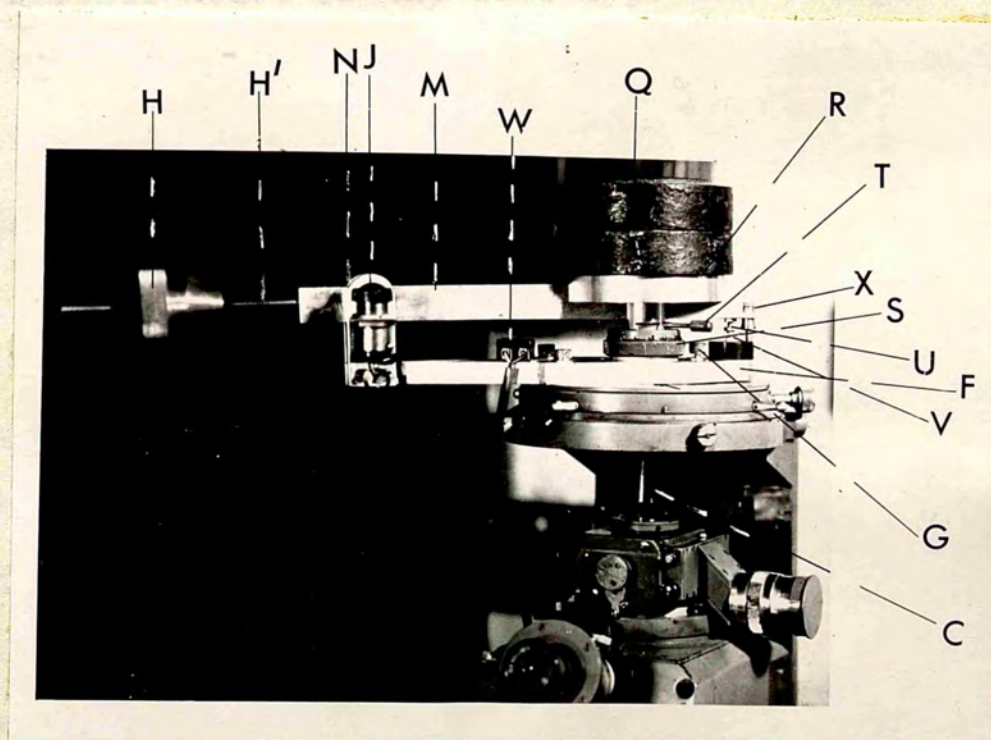


FIG.46



- P - Load position indicator pin
- Q - Chemical balance weight used to apply load
- R - Load plate
- S - Collet chuck securing specimen
- T - Clamp to collet chuck
- U - Beam contact tip
- V - Base plate contact anvil
- W - Electricity supply terminals
- X - Hinged screw lock
- Y - Stage cross traversing screw
- Y<sub>1</sub> - Stage longitudinal traversing screw
- Z - Eye-piece centring screw .

Since this apparatus is meant to take loads upto 200 gm, another model of the same type was designed and made to take loads upto 7000 gm and at the same time remain as sensitive as the commercial model.

#### Robust Hardness Tester

This instrument was designed and made by Mr. F.J. Lawton, departmental technician, to replace the Cooke, Troughton and Simms model of the indenter described above. The requirements were that it should be capable of loading upto 7 kg. and remain as sensitive as the Cooke model. For obvious reasons it had to be as light as possible so as not to overload the Vickers projection microscope in conjunction with which it is used. Figure 46 is the photograph of the tester, shown mounted on the Vickers

projection microscope. The letters stand for the same parts of the instrument as in figure 45 of the micro-indenter.

#### Details of construction

The base plate (F) was machined from  $\frac{1}{2}$ " thick dural sheet and was secured to the Vickers microscope stage by three fixing screws (G).

The beam (M) was machined out of  $\frac{3}{4}$ " x  $\frac{1}{2}$ " dural. The load plate (R) was also dural and was machined to locate the laboratory balance weights (Q).

The counter-balance weight (H) was machined out of mild steel and was attached to the beam on a mild screw (H'), which is 5" long x  $\frac{5}{16}$ " dia x 22TPI. The pivot axle (J) was machined out of silver steel, the bearings were standard light-weight ball bearings aligned to a total error of less than  $\frac{1}{10,000}$ ".

The difficulty was to disperse the friction, normal in this type of bearing, so as to maintain the sensitivity necessary. This was achieved by running the bearings in at a very high speed (10,000 R.P.M) before fitting; after running in the bearings were plated with  $\text{MoS}_2$ .

When assembled and tested in the workshop, it was found that the instrument would stand 10 kg. load without ill effect and was sensitive to less than 2 mg.

The entire experimental work on ring cracks and hardness (with heavier loads) was done with this apparatus.

## CHAPTER VII

### X-RAY CRYSTALLOGRAPHY

#### Diffraction of X-rays by Crystalline Matter

Ideally a crystal is an arrangement of atoms that repeats itself indefinitely in three dimensions. The repeating group of atoms occupies a small parallelepiped, the unit-cell. The edges of the unit cell are the crystal axes. The complete crystal is made by the regular packing together of these units. In all, it is possible to have fourteen kinds of lattice (Bravais space lattice) in crystalline matter.

The simpler observations in X-ray crystallography can be treated on the idea that X-rays are reflected from layers of atoms in the crystal, and that the beams reflected by successive parallel layers interfere with one another. But for the study of more complex crystals, some means of exhibiting neatly the information given by the large number of spots on moving-crystal photographs is necessary, and the device known as the reciprocal lattice is convenient for this purpose. X-ray photographs resemble the reciprocal lattice much more than they resemble the crystal lattice. One could perhaps say that the photograph is merely a more or less distorted reciprocal lattice. For special purposes cameras have been designed that reproduce a section of the reciprocal lattice with little or no distortion

(Buerger, 1944).

### Reciprocal Lattice

Many of the characteristics of a crystal are most simply represented by means of the Bravais lattice. But other characteristics are more easily dealt with in terms of the reciprocal lattice, which like the Bravais lattice, consists of a set of points through which may be drawn a framework of equidistant and parallel lines. Each reciprocal point represents a family of planes in the Bravais lattice. The reciprocal point lies on the normal through the origin to a set of parallel and equidistant planes in the Bravais lattice, and its distance from the origin is inversely proportional to the spacing of the planes. The definition may be expressed formally as

$$d_{hkl}^* = \frac{K}{d_{hkl}}$$

where  $d_{hkl}^*$  is the distance from the origin to the reciprocal point corresponding to the family of planes having the spacing  $d_{hkl}$ . The co-efficient of proportionality  $K$ , is arbitrary; in this thesis unless otherwise stated,  $K$  will be taken equal to the wavelength.

### Co-ordinates used in reciprocal lattice

The reciprocal lattice (1953) is normally employed in the interpretation of various types of X-ray photographs. There are several ways of specifying



the position of a point in three-dimensional space.

The axes of reference are normally chosen as follows:

(1) OX (Fig.47) parallel to the incident beam of X-rays, the positive direction being that from the origin towards the source of X-rays.

(2) OV, the axis of oscillation or rotation, or if the crystal is stationary, any selected direction passing through the origin and perpendicular to the direction of the incident beam. The positive direction is usually taken to be upwards from the origin.

(3) OS, a direction perpendicular to OX and OV. The positive direction of OS will be taken as forming with the directions OX and OV a right-handed set of axes when read in the order OX,OS,OV. The position of the reciprocal point N may be defined in terms of cylindrical co-ordinates  $\xi$ ,  $\zeta$  and  $\phi$  such that  $\xi$  is the radius of a cylinder having OV as axis and passing through N,

$\zeta$  is the distance from the origin of a plane perpendicular to OV and passing through N, and  $\phi$  is the angle between two planes intersecting in OV and passing through N and OS respectively.

The position of N may also be defined by the indices  $h,k,l$  of the corresponding lattice planes. The co-ordinates of N are  $ha^*$ ,  $kb^*$  and  $lc^*$  and these lengths are measured parallel to the edges of the reciprocal unitcell (figure 48). When it is necessary to define only the

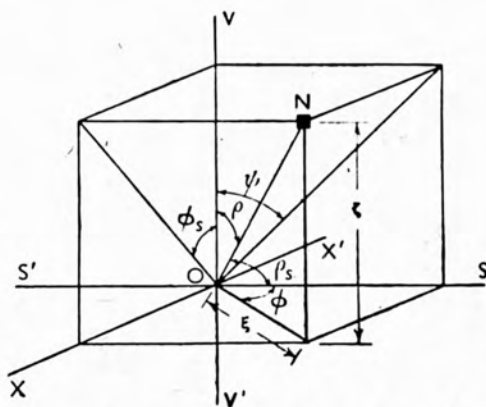
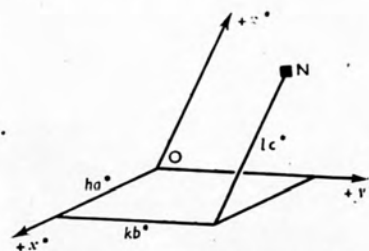


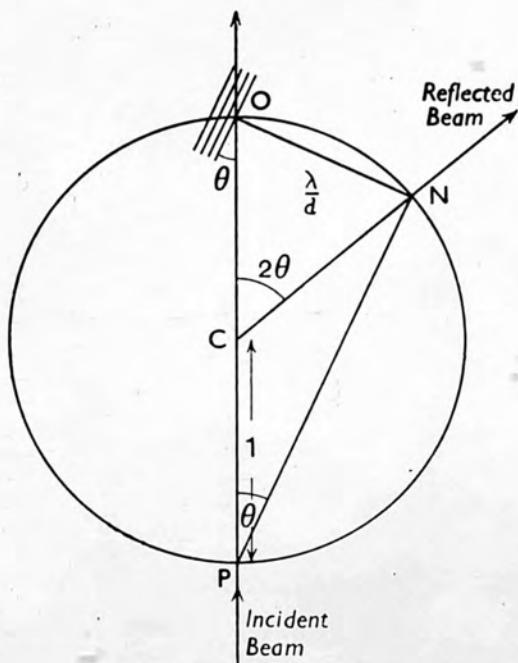
Diagram showing the relation of the cylindrical co-ordinates and the pairs of polar co-ordinates.  
Angle  $NOX = (\pi/2 - \theta)$

FIG.47



Co-ordinates of reciprocal point N

FIG.48



Great circle through O and N on reflecting sphere

FIG.49

direction of the normal to the reflecting planes, ON, as distinct from the position of the point N, this may be done by polar co-ordinates  $\rho$  and  $\phi$ . The polar co-ordinate  $\rho$  is the angle NOV and  $\phi$  is the angle already defined. A further pair of polar co-ordinates which may be used is  $(\frac{\pi}{2} - \theta)$  and  $\psi$ . Since the reflecting planes make an angle  $\theta$  with the incident beam, the angle NOX is  $(\frac{\pi}{2} - \theta)$ .

#### Interpretation of the Bragg Law in terms of the Reciprocal Lattice

There is a important relation between the reciprocal lattice and a sphere known as the reflecting sphere which is constructed in the following way: on the line OP, (figure 49) which passes through the origin parallel to the incident X-ray beam, the point P is chosen at a distance of two units of length from the origin. On OP as diameter the reflecting sphere is constructed. If a reciprocal point lies on the surface of this sphere, then it can be shown that the corresponding lattice planes are in the correct setting relative to the incident beam and have the correct spacing to reflect X-rays. In figure 49 the circle on OP as diameter is a central section of the sphere, that is, a great circle, which passes through the reciprocal point N. The angle ONP is, therefore, a right angle and

$$\frac{ON}{OP} = \frac{\lambda}{d/2}.$$

Further PN is parallel to the planes corresponding to N and hence angle NPO =  $\theta$  . Since  $\sin = \frac{ON}{OP} = \frac{\lambda}{2d}$ , the Bragg law is thus obeyed and these planes corresponding to N can reflect the X-rays. It will be noted that the direction of the reflected beam is given by the line CN. The simple relations of the construction described above are of great use in the interpretation of X-ray photographs of all kinds.

### X-ray Photographs

From the Bragg equation it can be seen that, for a given set of lattice planes, reflection can occur in general only if there is a variation either in the wavelength of X-rays ( $\lambda$ ) or in the orientation of the planes ( $\theta$ ). If white radiation is used with a single crystal, a Laue photograph is obtained and if a characteristic radiation is used, there must be variation of the angle  $\theta$ , and this can be brought about in different ways depending on the form in which the material occurs. If the specimen is a single crystal, variation of the angle  $\theta$  can be obtained either by turning the crystal or by means of a convergent X-ray beam. In the first case the crystal is either rotated or oscillated about the axis of the X-ray goniometer; when the film (flat or cylindrical) is stationary, the rotation or oscillation photograph results. There are two main features of a single-crystal photograph, namely the position of the



spots and the intensity of the spots. From the position of the spots we can derive the shape and size of the unit cell of the lattice; after indexing the various reflections we can obtain information required in the determination of the space group.

### The Laue Photograph

In this X-ray diffraction photograph, a narrow beam of 'white' X-rays impinges on a stationary single crystal and the diffracted beams are registered on a flat film. Since the crystal is stationary, the angle  $\theta$  is fixed for any given set of lattice planes and when characteristic radiation alone is used no diffraction beams would, in general, occur. The film may be cylindrical, with its plane normal to the incident beam, or flat, usually with its plane normal to the incident beam. When the flat plate intercepts only diffracted beams with low angles of deviation, it is called a front plate and the photograph a transmission Laue photograph. When the incident beam passes through a hole in the film before impinging on the crystal, the film is called a back-plate and the photograph a back-reflection Laue photograph. The interpretation of Laue photographs is generally more difficult than the interpretation of other types of X-ray photographs. Laue photographs are at present used in the study of the symmetry of crystals and in the determination of the orientation of crystals.

### Rotation and Oscillation Photographs

In the rotation method a narrow beam of characteristic radiation falls on a single-crystal specimen, which is turned during the exposure. In the rotation goniometer, the specimen is set with a zone axis parallel to the axis of the instrument and is rotated continuously about this axis during the exposure. The film may be cylindrical with its axis coincident with the rotation axis of the crystal, or else a flat plate for transmission or back reflection photographs. From such rotation photographs, the lengths of the sides of the unit cell can be quickly determined with an accuracy of about one per cent. But in most rotation photographs there is considerable overlapping of spots, and this limits the possibility of indexing the reflections unambiguously. To overcome this difficulty oscillation photographs are taken instead of rotation photographs.

### Interpretation of Oscillation Photographs

In this method since the crystal is oscillated about an axis perpendicular to the incident X-ray beam, many lattice planes are allowed to come into the appropriate positions for reflecting the characteristic radiation. If white radiation is present in the beam, a streak is produced on the film by the reflections by each of the sets of lattice planes, and spots are produced by the characteristic radiation. The task of assigning indices

to each reflection is most conveniently done if a crystallographic axis is chosen as the oscillation axis.

### The Oscillation Goniometer

The crystal is set on two mutually perpendicular adjusting arcs fitted with centring slides and mounted on a spindle as on an ordinary spectrometer; the positions of the arcs may be read to tenths or to sixths of a degree. The X-ray beam enters through a collimating slit system at right angles to the oscillation axis and passes out through a hole in the camera or else is absorbed by a lead stop. A low power microscope is fitted for adjusting the crystal visually and for centring it; the removal of a lens turns this microscope into a telescope for viewing signals reflected by crystal faces from an optical collimator which can be attached to the instrument. The camera used is a cylindrical one with a radius of 3cm, the axis of the camera being coincident with the oscillation axis of the crystal. The method of oscillating the crystal is by means of an arm attached to the axis of the instrument at one end while the other end is kept pressed against a cam which is rotated by a motor.

### Use of Reciprocal lattice

The reciprocal lattice is helpful to understand the formation of the spots on an oscillation photograph. The crystal is represented by its reciprocal lattice in

the correct orientation and the condition of reflection given by the Bragg equation is expressed by the geometrical construction shown in figure 49. The Bragg law is obeyed for a set of lattice planes when the reciprocal point corresponding to them lies on the surface of the reflecting sphere. When the crystal is oscillated, a number of reciprocal points pass through the surface of the reflecting sphere and so can be imagined as giving rise to the reflections which are recorded on the film.

#### Bernal Chart

When an oscillation photograph is taken on a cylindrical film, with a zone axis of the crystal as the oscillation axis, the photograph shows a set of parallel straight lines of spots. A zone axis is a direction in the Bravais lattice to which a group of lattice planes is parallel; the normals to all these planes lie in the plane perpendicular to the zone axis. Passing through the origin, there is correspondingly, a plane of reciprocal points perpendicular to the zone axis direction. From the nature of the reciprocal lattice there are exactly similar planes of points parallel to the first one. These planes of reciprocal points intersect the sphere of reflection in small circles. If the centre of the reflecting sphere is joined to these intersections, a series of cones co-axial with the north-south axis of the sphere is obtained; the semi-angle



of the cone is  $(90-\mathcal{V})$ , where  $\mathcal{V} = \sin^{-1}\zeta$  (figure 50). Each of these cones is the locus of reflections which correspond to the points lying in the appropriate plane of the reciprocal lattice. The cones of reflected rays intersect the circumscribing cylindrical film in a series of circles which form straight lines when the film is laid flat. The zero layer line, for which  $\mathcal{V}=0$ , always passes through the point of exit of the incident beam, but the positions of the non-zero layer lines vary with the angle  $\mathcal{V}$ . Thus all spots on the  $n^{\text{th}}$  layer line correspond to reciprocal points on the  $n^{\text{th}}$  plane of reciprocal points perpendicular to the oscillation axis. Such a plane is specified by the axial co-ordinate  $\zeta$  of the set of cylindrical co-ordinates. All reciprocal points on this plane and the corresponding spots on the  $n^{\text{th}}$  layer line have the same value of  $\zeta$ .

Considering the surface in reciprocal space defined by a single value of the radial cylindrical co-ordinate  $\zeta$  it can be seen from figure 51 that this is a cylinder with its axis through the origin of the reciprocal lattice. A set of such cylinders, with  $\zeta$  varying in steps of 0.05 from zero upto two units, intersects the sphere in a set of curves. If  $\zeta$  were greater than 2.00 the cylinder would not intersect the sphere. If we join the centre of the sphere to these intersections, the surfaces of reflected rays are produced which intersect the film in

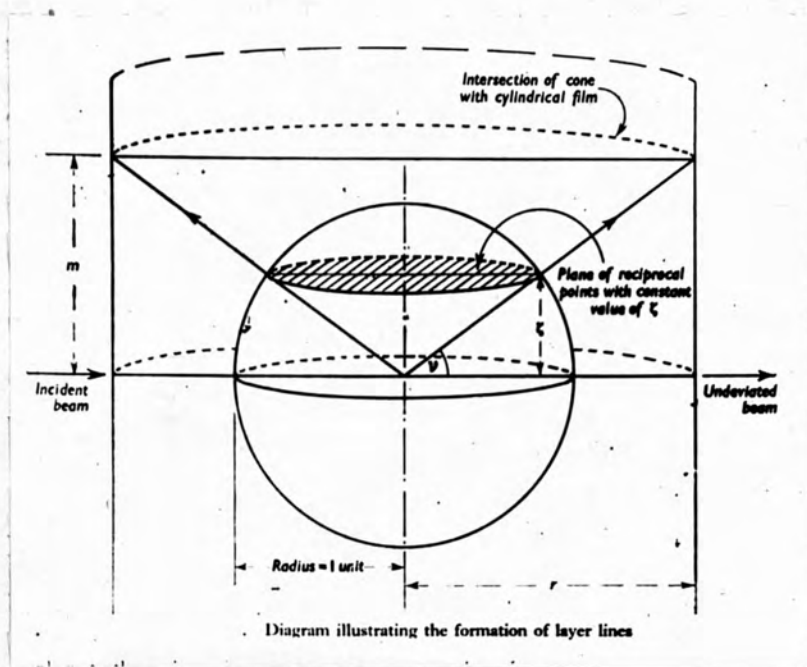


FIG.50

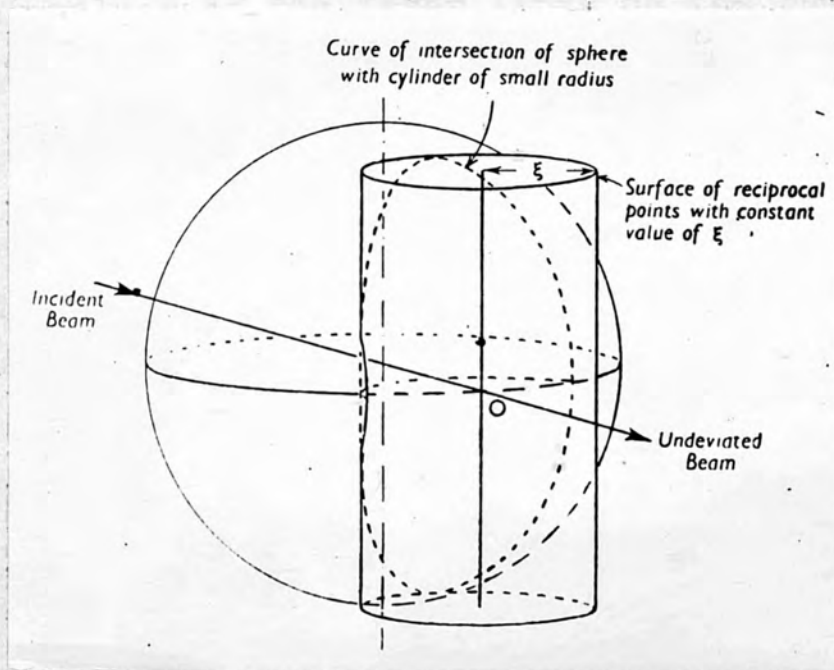


FIG.51

a set of curves for which  $\zeta$  is constant. These are called row lines. It is clear that a chart of curves of constant  $\zeta$  and  $\xi$  is useful in the study of oscillation photographs. Such charts have been prepared by Bernal for any given crystal-to-film distance. If a Bernal chart is not available, the value of  $\zeta$  can be easily obtained from a measurement of the distance of any layer line from the zero layer line. From figure 50 it is clear that  $\zeta_1 = \sin \nu$ , and for a cylindrical camera of radius  $r$ ,  $\frac{m}{r} = \tan \nu$ , where  $m$  is the height of the layer line above the zero layer line.

#### Determination of unit-cell dimensions

Layer lines are produced only when a zone axis of the crystal is taken as the oscillation axis. From the  $\zeta$  values of the layer lines on the photographs, one can obtain directly the repeat distance of the Bravais lattice along the direction of the zone axis, which is taken as the oscillation axis. Since a set of parallel planes through reciprocal points exists perpendicular to each zone axis in the Bravais lattice, it can be shown that

$$d_{[uvw]} = \frac{n\lambda}{\zeta_n}$$

where  $d_{[uvw]}$  is the repeat distance along a zone axis in the Bravais lattice and  $\zeta_n$  is the value of  $\zeta$  for the  $n^{\text{th}}$  layer line in a photograph taken with the zone axis as the oscillation axis. Thus, by taking oscillation

photographs with each of the three crystallographic axes as oscillation axis in turn, one can determine the unit-cell dimensions of any crystal.

### Indexing the reflections

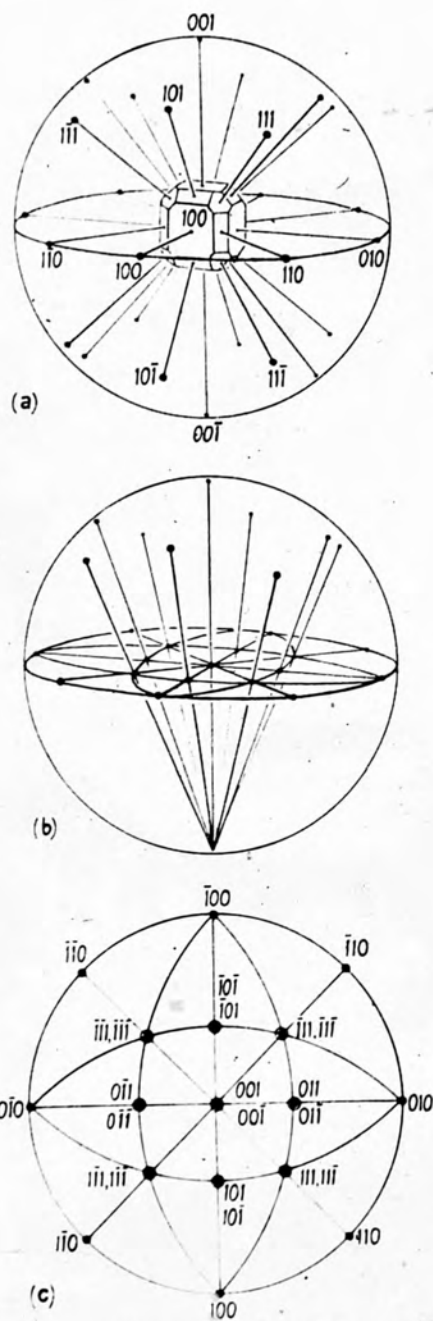
From a knowledge of unit-cell dimensions it is possible to construct the reciprocal lattice, for which a convenient scale of  $\phi$  10 cm to one unit, is chosen. Projections of the reciprocal lattice are drawn, one perpendicular to each crystallographic axis as oscillation axis. When layers of the reciprocal lattice have been drawn, the appropriate reflecting circles are inserted. Each layer of the reciprocal lattice cuts the reflecting sphere in a circle, the radius of which is given by  $r' = \sqrt{1 - \zeta^2}$ . Each reflecting circle inserted on the reciprocal lattice has its centre on a vertical line which intersects the horizontal incident X-ray beam at a distance of one unit from the origin. However, it is only the equatorial reflecting circle on the zero layer of the reciprocal lattice that passes through the origin of the layer. The appropriate oscillation of the reciprocal lattice relative to the stationary reflecting circle and incident X-ray beam would correspond to the actual movement of the crystal. It is however, easier to move the reflecting circle, carrying with it the incident X-ray beam. A clock-wise movement of the crystal from its initial



position ( looking down  $\phi$  ) corresponds to anti-clockwise movement of the reflecting circle. When the two reflecting circles corresponding to the two limits of the oscillation have been drawn, they define two lune-shaped areas. Only those reciprocal points, which lie within these lunes, represent lattice planes which could reflect, because only these points have passed through the surface of the reflecting sphere during the oscillation. Since the movement of the reflecting circle is made to correspond to that of the crystal, the points on the right side of the reciprocal lattice give rise to spots on the right side of the film and similarly for the left side.

### Stereographic Projection

In a crystal, the variation of the sizes and shapes of its faces often, hinders the study of its true symmetry relationships. To be able to do that it is useful to represent on paper the three-dimensional relations between its interfacial angles. This is achieved by some type of crystal projection (1949). From a point within the crystal let normals be drawn to all its faces (figure 52a). Round the crystal a sphere is described with the point as its centre. The points at which these normals meet the surface of the sphere are called the poles of the faces. The essential angular relationships of the crystal are then represented in a spherical projection. The sphere is then projected on



The stereographic projection.

FIG. 52

to a selected plane, the equatorial plane in figure 52b, by joining all points on its upper half to the 'south pole' and all points on its lower half to the 'north pole'. Poles in the northern hemisphere are denoted by dots, those in the southern hemisphere by little rings (figure 52c). This is the stereographic projection. The Wulff net, which retains the angular relationships of the spherical projection, is used to measure the various angles from the stereographic projection by rotating it about its centre.

$$L = a^n d^n$$
$$\log L = \log a^n + n \log d$$

where  $L$  is the load,  $d$  is the diameter of the impression and  $a$  and  $n$  are constants for a given material. Meyer also demonstrated that the value of  $n$  was related to the degree of cold work received by the material and was therefore a measure of the workhardening capacity. For materials in the annealed condition the value of  $n$  is in the region 2.5 to 3 and thus approaches 2.0 in the fully worked state as shown by O'Neill and Guthrie (1931) for various metals and alloys. Thus the lower the workhardening capacity, the nearer the value of  $n$  to 2.0.

Tabor (1944) has pointed out that both the amount of work-hardening and the elastic limit increase with the size of the indentation. Thus for a given size of ball, the yield pressure will generally increase with

CHAPTER VIII

HARDNESS VARIATION WITH LOAD

Review of previous work

The most controversial aspects of indentation hardness testing at low loads are the question whether the recovered hardness number is independent of the load, and the significance of the logarithmic index when the Double-cone, Vickers or Knoop indenters are used. In 1908 Meyer showed that for Brinell tests at different loads, using a fixed ball diameter on a given specimen,

$$L = ad^n \text{ from which}$$

$$\log L = \log a + n \cdot \log d;$$

where  $L$  is the load,  $d$  is the diameter of the impression and  $a$  and  $n$  are constants for a given material. Meyer also demonstrated that the value of  $n$  was related to the degree of cold work received by the material and was therefore a measure of the workhardening capacity. For materials in the annealed condition the value of  $n$  is in the region 2.5 to 3 and thus approaches 2.0 in the fully worked state as shown by O'Neill and Cuthbertson (1931) for various metals and alloys. Thus the lower the workhardening capacity, the nearer the value of  $n$  to 2.0.

Tabor (1954) has pointed out that both the amount of work-hardening and the elastic limit increase with the size of the indentation. Thus for a given size of the ball, the yield pressure will generally increase with



load. Similar considerations apply to double-cone indentations but not to Vickers and Knoop impressions which are geometrically similar irrespective of their depth; so that the mean pressure producing plastic flow under the indenter should be independent of the indentation size. This implies that the unrecovered Vickers hardness ( $H_v$ ) ought to be constant over a wide range of loading, but the hardness definition is based on the recovered diagonal length  $d_k$ , according to the formula

$$H_v = \frac{1.854L}{d_k^2}$$

If  $d_E$  is the reduction in the diagonal length due to elastic recovery the unrecovered diagonal  $d_U$  is given by  $d_U = (d_R + d_E)$ . Thus

$$H_v = \frac{1.854 L}{(d_U - d_E)^2}$$

so that  $H_v$  will vary with load unless  $(d_U - d_E)$  is proportional to  $\sqrt{L}$ .

#### Concept of Onitsch

$H_v$  is generally found to be independent of the load at loads greater than 2.5 kg and it is only for tests made with loads of less than 1 kg that doubts have arisen as to its constancy. Onitsch and co-workers (1947, 1956) have suggested that the constant hardness number obtained at high loads shall be referred to as the 'macrohardness' and that the term 'microhardness' be

applied to the lower range of loading for which variable results have been obtained. Onitsch suggested that there is a correlation between the value of the logarithmic index  $n$  and the hardness. For very hard materials  $n$  is low (little greater than 1) and for soft materials  $n$  approaches 2.0. The different values of  $n$  for a given substance as obtained from macro- and microhardness numbers are attributed by Onitsch to the fact that the microhardness impression can be entirely within a single grain, in contrast to the multiplicity of grains covered by an impression at higher loads. The size of a small indentation therefore will often depend on a crystallographic slip system for the particular grain in which it was placed, whereas if several grains are indented simultaneously the size of the impression will be governed by the mutual interaction of the slip systems of all grains involved. The value of  $n$  at low loads was regarded by Onitsch as a measure of the ease of slip of the material, and for two specimens of equal microhardness but differing values of  $n$  it could be presumed that their tendencies to slip were different.

Grodzinski (1952), on the basis of work by Waizenegger (1921) and Meincke (1942) and his own tests with Vickers and Double-cone indenters, considered that as the load was decreased an increase in hardness to a maximum value occurred, according to a hyperbolic law and then dropped

to almost zero with a nearly proportional descent as in figure 53. He attempted to find a new definition for hardness which would allow for the variation with load on the basis of two assumptions. These were (a) there is no fundamental difference between the micro- and the macro- ranges as suggested by Onitsch and (b) Meyer's law holds over the whole range. Meyer's law is  $L=ad^n$  and Grodzinski's new definition of hardness  $h$  is

$$h = \frac{L}{d^n} ;$$

so that  $h$  is the load producing a recovered indentation of unit length in the material. The experience of many workers in this field (1956) has shown that a log-log plot of  $d$  and  $L$  gives a straight line over a wide range of loading. The value of  $h$  is based on the dimensions of the recovered impression, but if measurements could be made of the indentation size while the load was on, the unrecovered hardness number  $h_u$  would be obtained.

The treatments of Onitsch and Grodzinski are based on the assumption that the logarithmic index is not equal to 2.0; that is there is a real variation of hardness with load. It is interesting to note that Onitsch's experimental values of  $n$  lie between 1.0 and 2.0 while Grodzinski's show variations of  $n$  from 1.3 to 4.9. Many other workers have investigated the apparent change of hardness with load and their results can be classified

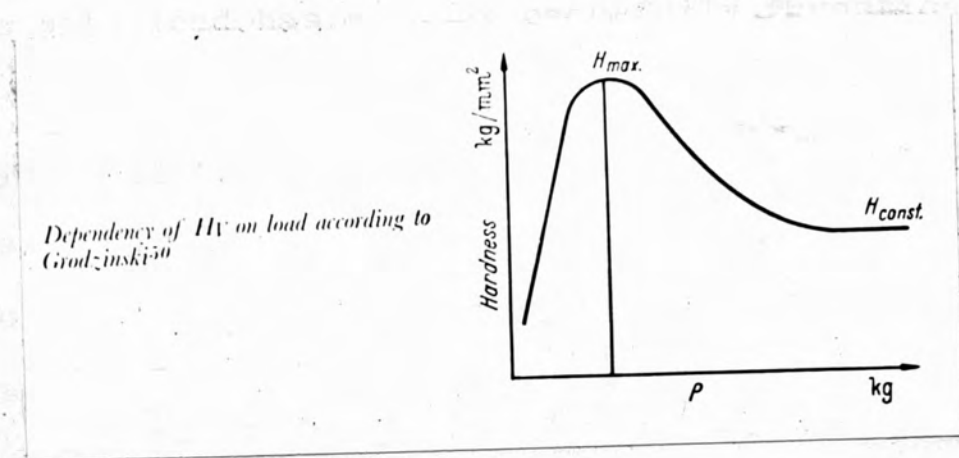


FIG.53



FIG.54

x50



in the three groups for which  $n > 2.0$ ,  $n < 2.0$  and  $N=2.0$  respectively. But the nature of the variation of apparent hardness with load has not yet been fully investigated; factors such as greater hardness at the surface, elastic recovery of the size of the indentation and the change of shape of the indenter near the point or edge may contribute to the observed apparent variation, as well as a change in the sensitivity of the hardness tester itself.

#### Elastic and Plastic hardness

In most of the micro-hardness tests, the indenter has to be removed to measure the indentation; the hardness is then calculated from the area of the recovered indentation. This may be called plastic hardness (1952). With elongated indenters, and partly with square-base pyramid indenters, it can be assumed that the recovery in the direction of the diagonal or longest diagonal can be disregarded; while this seems to be correct for large deformations, it has not yet been proved correct for very small deformations in hard materials (1949,1952).

It was suggested that in the case of a hard material pressed by a hard diamond indenter, where no plastic deformation could be observed at lower loads, a thin evaporated silver film should be used to make the contact area visible. Grodzinski (1952) showed that this can

be a very sensitive method for determining 'elastic' hardness. A thin evaporated silver layer of about 0.1 micron thickness, while fully adhering to the surface, forms a brittle coat. Once disturbed by a contact pressure, it cannot recover and remains torn. A microscopic inspection can thus reveal the full area of contact which existed when the maximum pressure had been exerted. Brodie and Smoluchowski (1945) as well as Bergsman (1951) used a thin coat on the diamond indenter to make the elastic deformation of the specimen visible; but with such a method it is only possible to perform one test before further coating. The method suggested and followed by us permits a large number of indentations to be made one after the other.

#### Deformations due to indentations

The distortions around hardness test indentations are often referred to in literature as flow patterns. Workers have always experienced some difficulty in measuring them. Foss and Brumfield (1922) and Yakutovich, Vandyashev and Surikova (1948) used a probe method to measure indentations and flow patterns. A probe, attached to an accurate dial gauge, is lowered until it makes electrical contact with the surface under study. By means of a traversing mechanism and a dial reading, a profile section of the surface may be found. This method is satisfactory for measuring large

indentations (chordal diameter greater than 1mm), but it is not sufficiently accurate for indentations smaller than this.

O'Neill and Cuthbertson (1931) derived the piling-up by means of the convexity of barrel-shaped diamond pyramid indentations. This method is not quite satisfactory because of the inherent difficulties in making accurate measurements. Krupkowski (1931) calculated flow patterns for ball and cone indentations made in work-hardened copper, from measurements of the diameter and depth of the indentation and the depth of penetration of the indenter. He assumed that the volume of the flow pattern was equal to that of the indentation which is not true in general. Tolansky and Nickols (1949,1952) applied multiple-beam interferometric methods to evaluate the surface contours around hardness test indentations made on various metals and alloys. These methods reveal the shape of the whole surface and can easily measure flow patterns whose heights are as small as 0.05 microns. Tolansky and Nichols also measured flow patterns around indentations in tungsten carbide, various steels, duraluminium and single crystals of tin. They reported that the flow patterns caused by various sized diamond pyramid indentations in steel were geometrically similar.

#### Present investigation

The purpose of the present investigation is to

study the hardness variation of silicon carbide crystals with load using both the Vickers and the Double-cone indenters. This study was limited to the basal plane (0001) of the crystals as that was the only plane well developed in almost all the crystals available. The crystals were either green or black in colour and about 10 to 12 mm in length. A commercial micro-indentation apparatus was employed for most of the indentations made with lower loads. But this apparatus is designed to take loads upto 200 gm, so a model was designed and constructed for observations with higher loads. This apparatus which is described in Chapter VI, is as sensitive as the commercial micro-indentation apparatus and a number of observations were taken with it covering both low loads and heavy loads; this was especially convenient for taking continuous observations ranging from 5 gm to 7000 gm.

The crystal was mounted as described later in the chapter on 'ring cracks' and indentations were made with the Vickers pyramid indenter and the double-cone indenter. The time of indentation for Vickers pyramid indenter was 15 seconds and that for Double-cone 30 seconds. These are the suggested timings in literature to be followed while using the indenters. It was found in silicon carbide that at loads upto 200 gm the Vickers pyramid indenter gave very small and poor impressions and the double-cone



indenter did not give any visible impression at all. So the crystals were thinly silvered by vacuum evaporation and indented. While making indentations care was taken to see that the range of deformation due to any one indent was not affected by neighbouring indents, by sufficiently spacing the indents. With the double-cone indenter all the indentations were made parallel to one another to eliminate any suspected effects due to directional variation in hardness as shown (for higher loads) in figure 54. In each case the area to be indented was reviewed before and after indentation by using a 16 mm microscope objective. The graticule in the eye-piece was calibrated with the eye-piece clamped to the instrument eye-piece tube and pushed in to maintain the standard tube length of 250 mm for which the objectives were corrected. With the help of the calibrated graticule the indentations were measured. In a large number of cases photographs of the indentations were taken and the length verified by using a Hilgers comparator.

Table (1) shows the apparent hardness values computed for three different varieties of silicon carbide crystals and figure 55 shows the graphs drawn from these, in which apparent hardness is plotted against load. Without silvering on the surface, the double cone indentations other than those with largest load were not visible at all; only the 500 gm indentations were indeed just

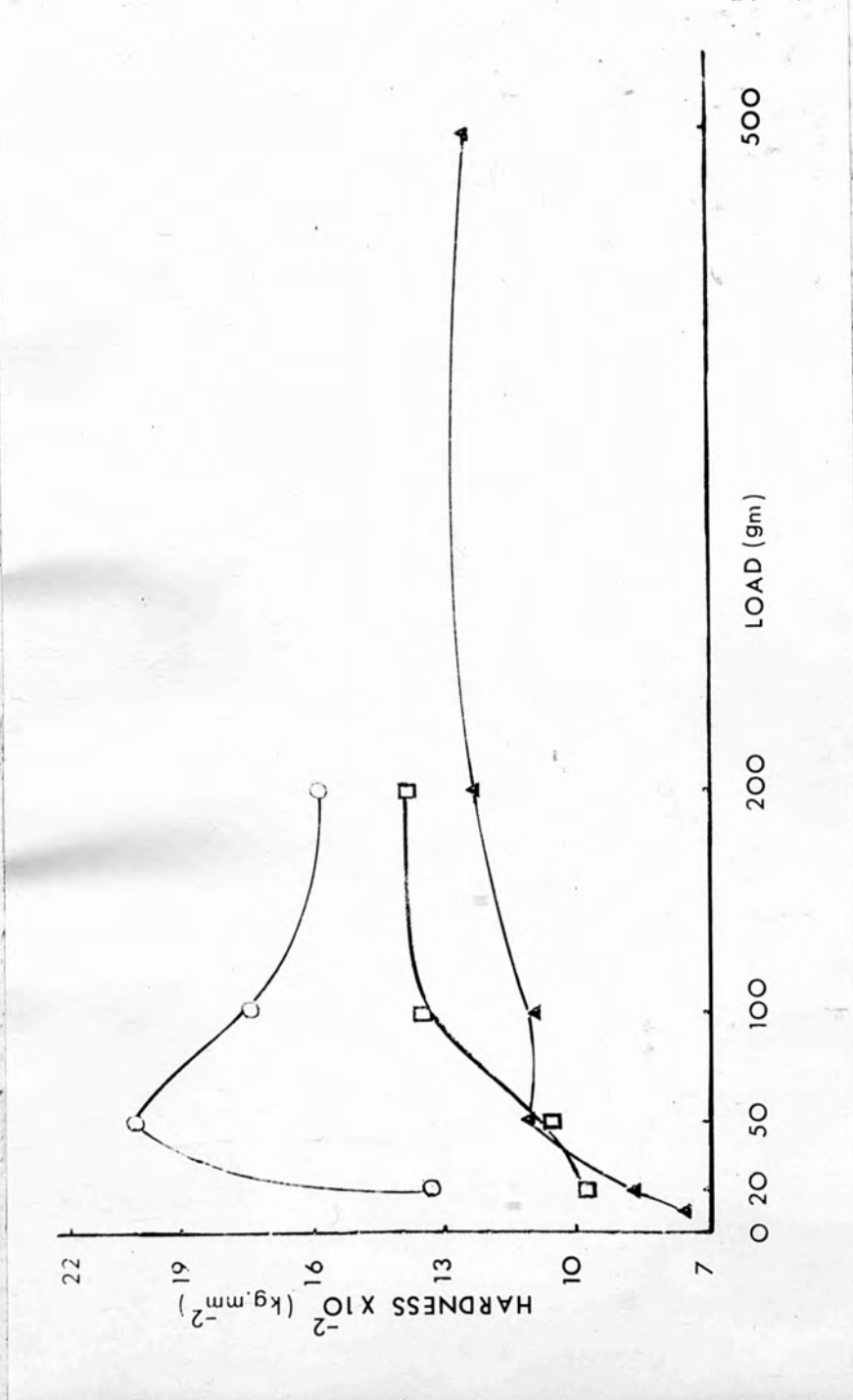


FIG. 55

visible in some cases. The reason for this may be the complete elastic recovery of the surface after the removal of the indenter. Hence the hardness figure given in table (1) may be described as the 'elastic' hardness of silicon carbide. It is in fact deduced from the silver area subject to damage. Swiss Sample 1 was also plastically indented with a Vickers pyramid indenter using a load of 100 gm. The average length of the diagonals of the real indentation was 0.45 mm for a magnification of 40.7. This gives a value of 1517 kg/mm<sup>2</sup> as its Vickers hardness.

TABLE 1

Sample	'Load (W) in gm	'd in mm x61*	'H <sub>DC</sub> in km/mm <sup>2</sup>
Swiss 1	20	2.35	968.5
(Pale green, traslu., well formed hex., brilliant lustre)	50	3.1	1054.0
	100	3.6	1348.0
	200	4.5	1380.0
Westinghouse	20	2.15	1329.0
3	50	2.50	2012.0
(Black, opaque, well formed hex., thick, glassy lustre)	100	3.30	1750.0
	200	4.30	1581.0
		d in mm x30	
Swiss 5	10	1.0	747.8
(Dark green, not so well formed rhom., less brill. than swiss 1)	20	1.2	865.4
	50	1.5	1108.0
	100	1.9	1090.0
	200	2.3	1229.0
	500	3.1	1255

(\*Phase contrast 4 mm objective was used and  $d$  is the mean of six observations in each case).

To study the apparent hardness variation with load for higher loads a commercial indenting machine, the Penetrascop was used; but as with it no accurate estimation could be made of loads below 5 kg it was discarded. Then a robust model of the indentation apparatus made in the laboratory was used. Even at higher loads the choice of the indenter presented some difficulty. Vickers pyramid impressions continued to be too small to permit of accurate measurement even at loads of 2 kg. Much more important, they shattered the surface of the crystals such that fractures extended from the highly stressed corners of the indentations. Even the diamond indenter itself was badly damaged after a few indentations as seen in figure 56. Figure 57, shows a Vickers pyramid indentation for a load of 500 gm. Figure 58 shows the Vickers pyramid indentations for loads of 1,2 and 3 kg. along with double-cone indentations for loads of 2,3,4 and 5 kg. From the picture it is easy to see that the Vickers pyramid indentations damage the surface severely whilst the double-cone indentations are well defined without any damage to the surface. Figure 59 shows again the 2 kg Vickers indentation along with a 4 kg double-cone indentation, figure 60 shows the Fizeau fringes on them under low dispersion and Figure 61



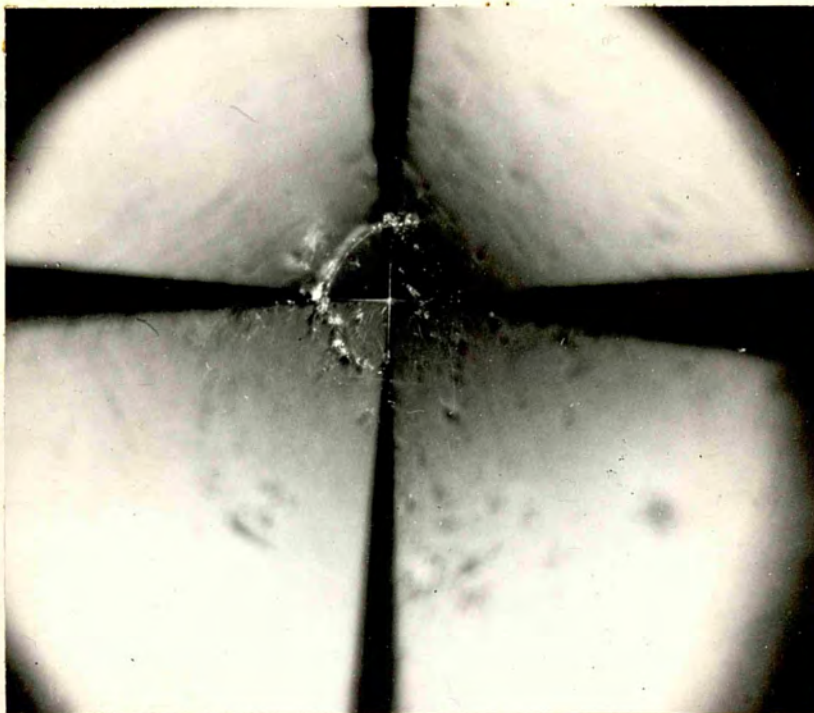


FIG. 56

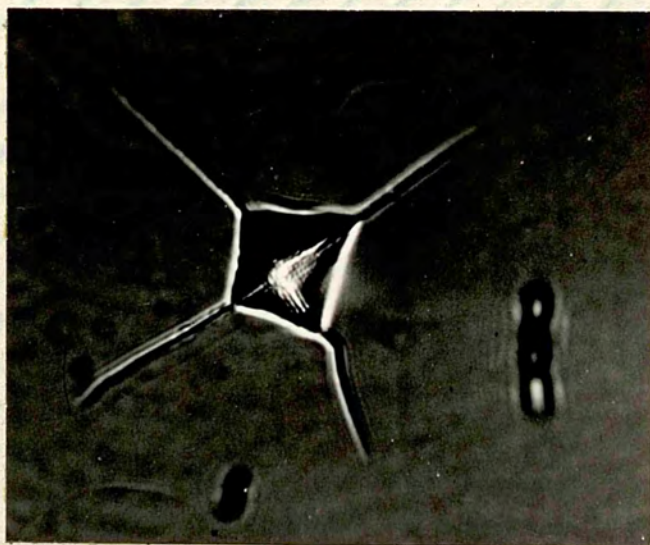


FIG. 57  
x750





FIG.58  
x50

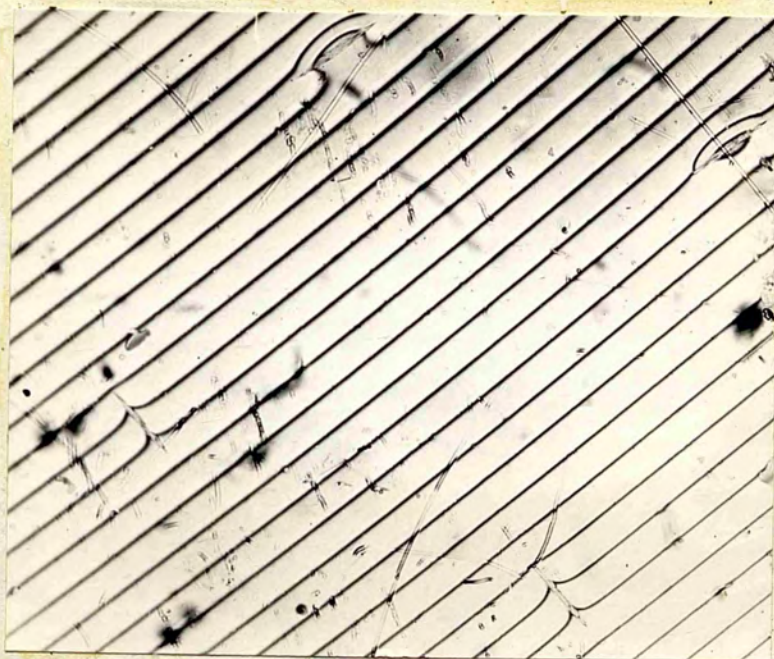


FIG.58a  
x50





FIG. 59  
x120

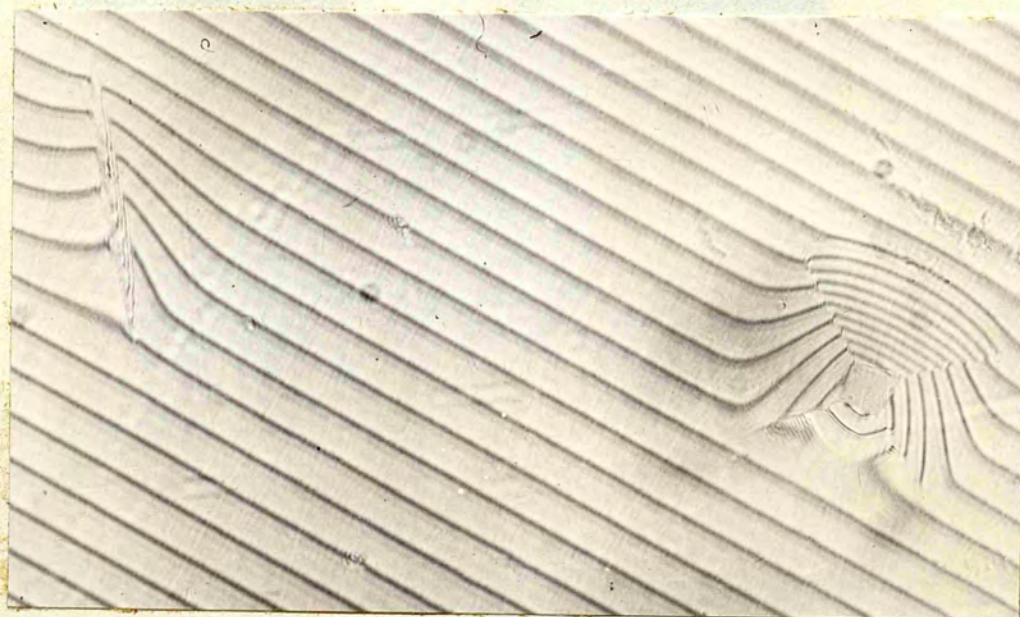


FIG. 60  
x120



FIG. 61  
x120



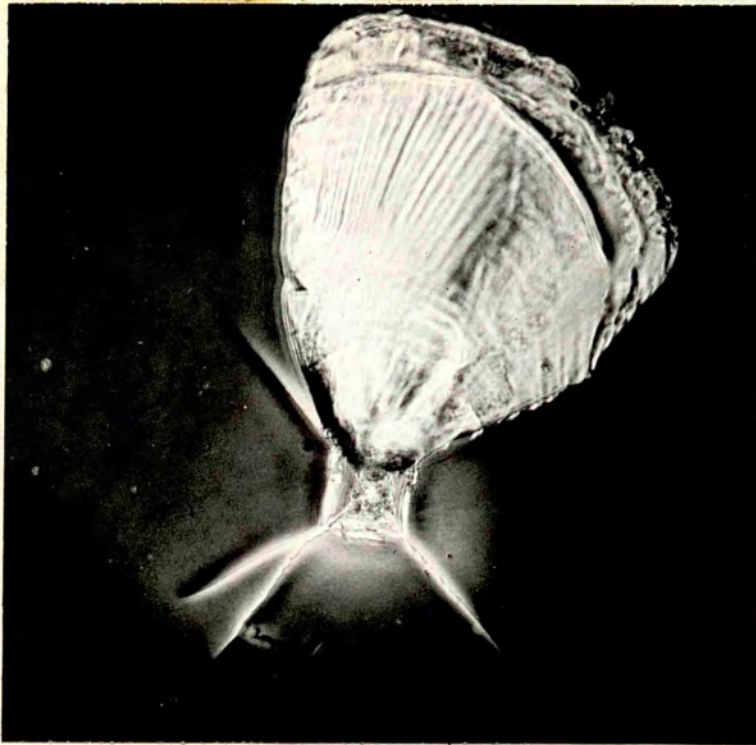


FIG. 62  
x360

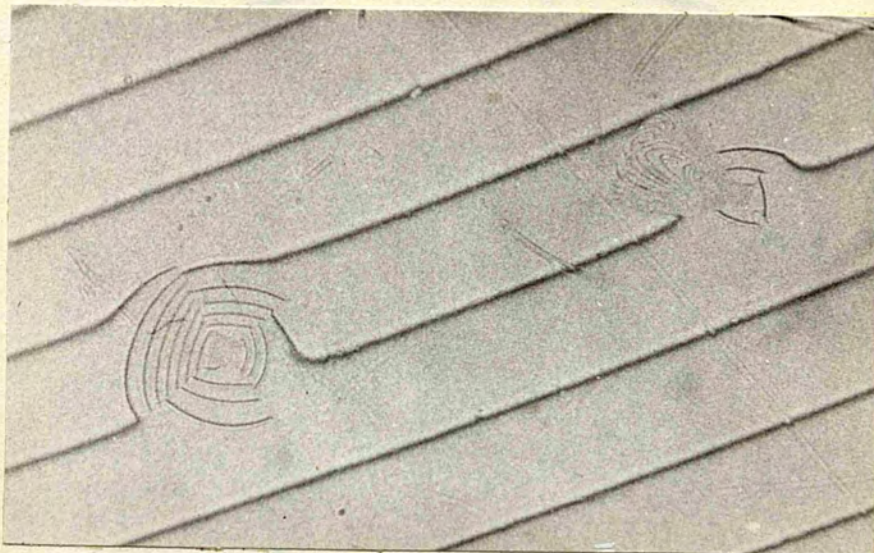


FIG. 62a  
x90



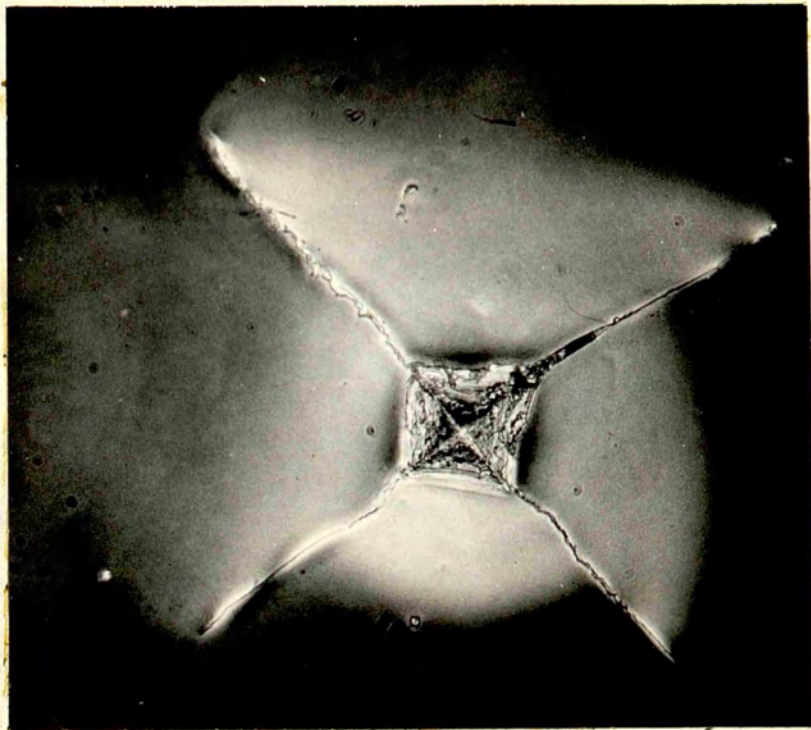


FIG.63  
x360

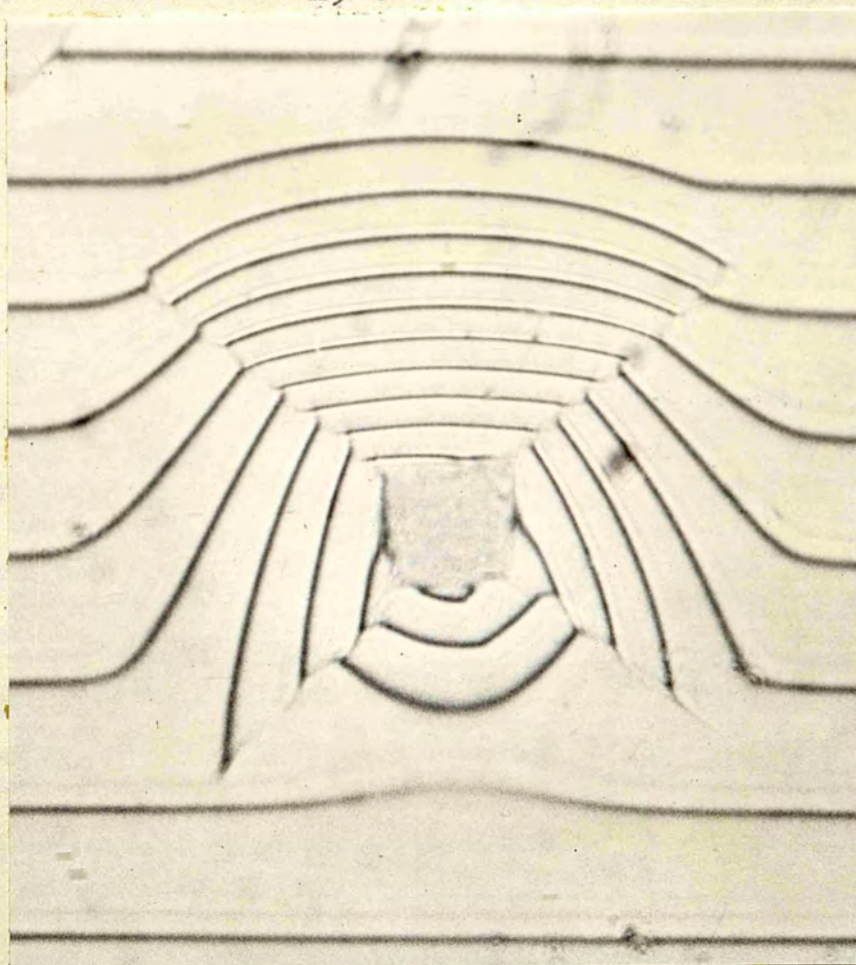


FIG.63a  
x360

shows Fizeau fringes on them with larger dispersion. The fringes show that much more material is disturbed with a 2 kg Vickers pyramid indentation than with a 4 kg d-c indentation. Figure 58a shows the Fizeau fringes on some double-cone indentations.

Figures 62 and 63 are the phase-contrast pictures of the 1 kg and 2 kg Vickers indentations taken with an Olympus Microscope. In figure 63 the areas between the corner cracks which appear white represent the actual region of disturbance of the material. This is indeed confirmed by figure 63a which illustrates a low dispersion fringe picture taken with the same indentation. The two pictures have been placed such that it is easy to see the amount of disturbance in the material on each side of the indentation. To see whether this disturbance is a 'piling-up' or a 'sinking-in', fringes of equal chromatic order were employed to each side of the indentation as shown in figure 63b. In the figure the photographs of the fringes are shown correctly oriented with respect to the Fizeau fringes on the indentation.  $AB_1$ ,  $AB_2$ ,  $AB_3$  and  $AB_4$  are respectively the fringes obtained when the slit of the spectrograph was placed parallel to AB and at different positions from AB to A'B'. Similarly  $BC_1$  and  $BC_2$  are respectively the fringes for the positions of the slit of the spectrograph from BC to B"C".  $DC_1$  and  $AD_1$  are the fringes when the slit was



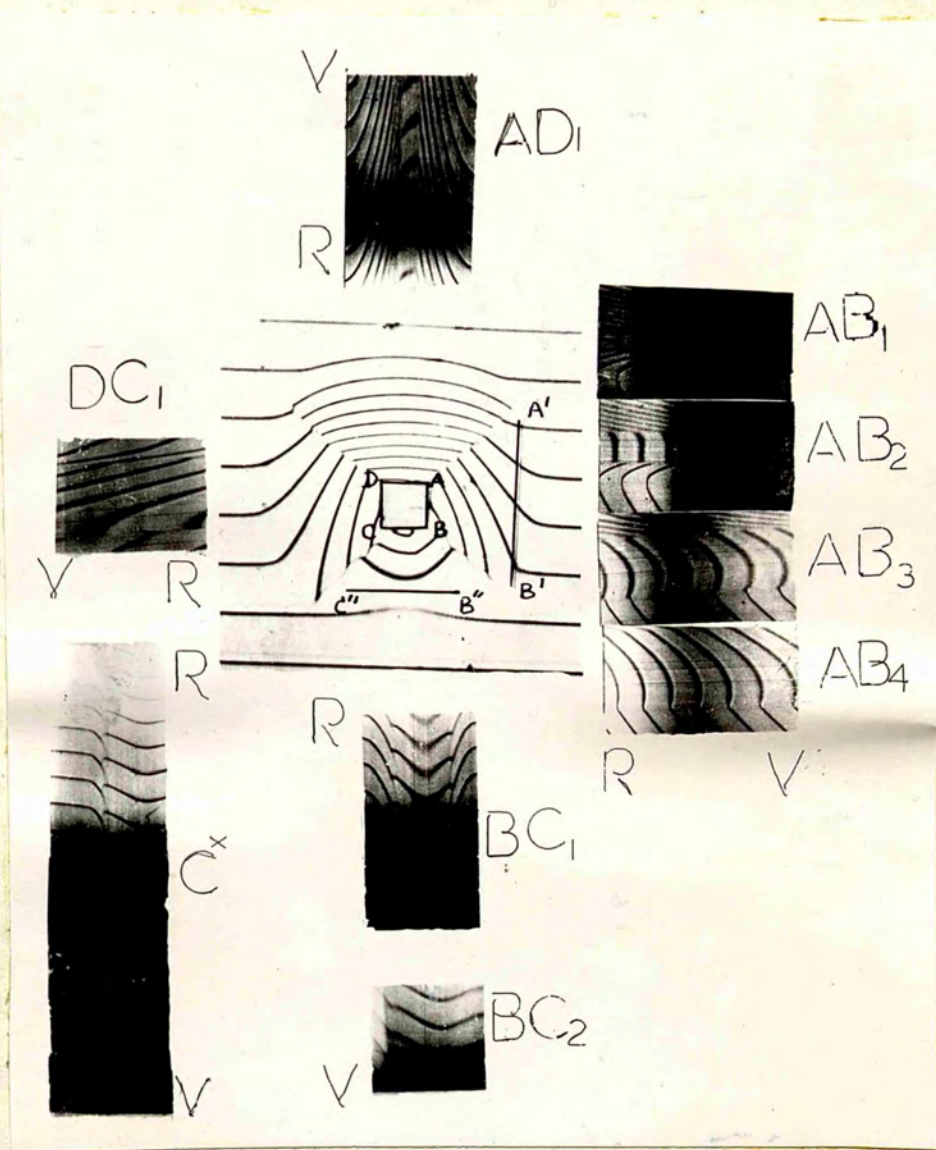


FIG. 63b.

placed in the disturbed regions parallel to DC and AD respectively.  $C^*$  shows the whitelight fringes at the corner crack C.

The fringes in all the cases, except  $AB_1$  and  $AB_2$  are convex towards the violet indicating that the disturbed material on each side is a 'pile-up'.  $AB_1$  shows a slight 'sinking-in' near AB and  $AB_2$  shows the surface flat before 'piling-up' as shown in  $AB_3$ . The Fizeau fringes on the indentation show the inequality of the amount of 'pile-up' on each side demonstrating the directional nature of the hardness of the crystal face. Figure 63c shows the Fizeau fringes on the same indentation taken with a large dispersion. The 'pile-up' is four half-wavelengths on the left and the right side and seven and three half-wavelengths respectively on the top and bottom side of the indentation. The corner cracks on the indentation are sharp assymetrical ridges as seen by the whitelight fringes on them. Right side of figure 62a shows the Fizeau fringes on a 1 kg indentation; the left side of the same figure shows the fringes on a 2 kg indentation. The surface of the crystal on one side of the 1 kg indentation has chipped off; on the 2 kg indentation the corresponding side shows a maximum 'pile-up', indicating the weakness of the surface in that direction. Opposite to the chipped off side of the indentation (figure 62) an additional crack is seen



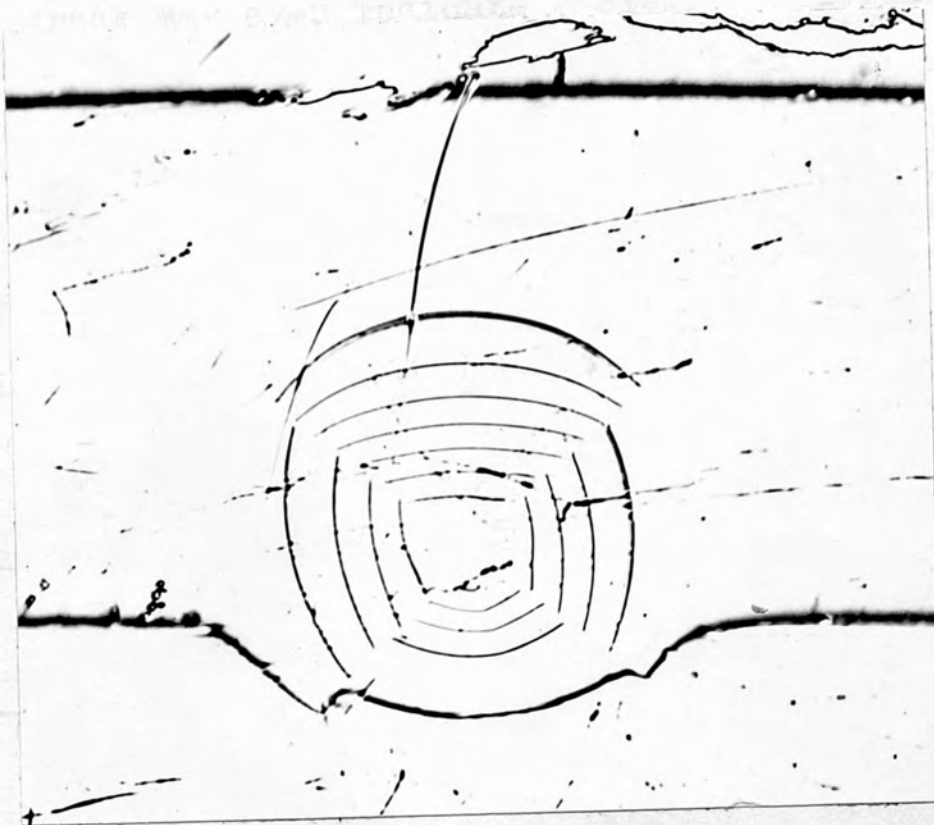


FIG. 63c

x200



FIG. 64

showing again the weakness of the surface; this additional crack may even indicate a cleavage direction of the crystal. The 'pile-up' on the sides of the 1 kg indentation on the sides is much less than on the 2 kg indentation. Table (2) gives the hardness values computed for different loads using Vickers pyramid indenter for two different crystals.

TABLE 2

Sample	Load gm or kg	d in mm x31	$H_{vk}$ in $kg/mm^2$	$H_{dc}$ in $kg/mm^2$
Swiss 1	1 kg	1.05	1616	2068 for a load of 2 kg.
	2 kg	1.5	1584	
Westinghouse 6 (Sample 8)	200 gm	0.45	1760	2185 for a load of 2 kg
	500 gm	0.70	1819	
	1 kg	1.00	1782	
	2 kg surface of the crystal was completely smashed.			

For the sake of comparison the double-cone hardness obtained on the same samples with comparable loads are shown in the last column of the table.

Further study of the Vickers hardness could not be made on the crystals because of the damage done to the indenter twice.

Double-cone indentation hardness with heavier loads

The double-cone indenter proved far more durable than the Vickers pyramid indenter. 38 silicon carbide crystals were indented with this indenter, with each crystal having at least 70 to 80 indentations yet its edge has still remained undamaged. Figure 64 shows a photograph of the working edge of the indenter after indenting 34 crystals. This indenter was used with the robust model of the indentation apparatus. Indentations were made on the crystals with loads ranging from 5 gm to 6 kg, making sure that all indentations on any one crystal, were parallel to one another. Most of the crystals showed no indentation marks with loads less than 200 gm even when seen through a 4 mm objective using phase-contrast. At 500 gm loads, indentations were just visible in some cases but were difficult to measure because the ends of the indentations were not clearly marked on the surface of the crystals. Clear indentations were however obtained over the range 1 kg to 5 kg for most of the crystals available. The crystals usually shattered when loads higher than 5 kg were applied and in some cases even with lower loads. Minute cracks were observed on either side of the length of the indentation in the higher load range for some crystals. Figure 65 top shows a crack on one side of an indent and figure 65a bottom shows a crack on the other side of the same indent.





FIG.65  
x360



FIG.65a  
x360

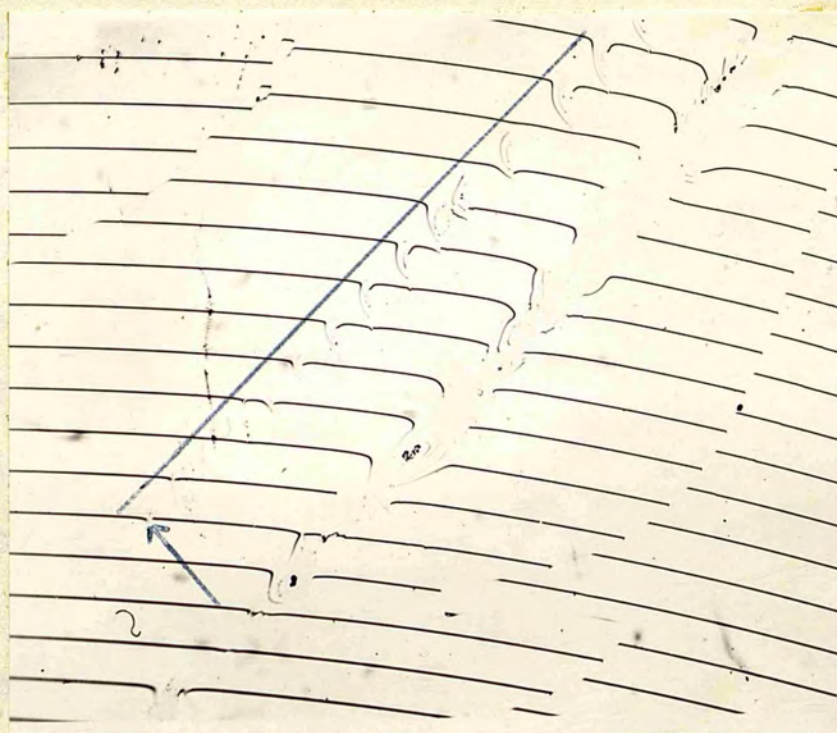


FIG.66  
x50



Figure 54 referred to already, shows a picture of the visible indentations. Figure 66 shows the Fizeau fringes obtained on the indentations; row of indentations parallel and nearest to the line drawn, is a series representing loads from 5 gm to 5 kg. The first visible indentation, marked by an arrow, is for a load of 1 kg and indentations with loads below this value have shown no visible change in the Fizeau fringes indicating that they have completely recovered. Table (3) gives the apparent double-cone hardness for different loads in the case of one crystal. This hardness calculated from the length of indentation measured after recovery, may be called the 'recovered hardness' or the 'plastic hardness'. Figure 67 shows graphically its variation with load. It is seen from the graph that the apparent recovered hardness decreases with increase of load upto 3.5 kg and then for higher loads maintains approximately a constant value for this specimen. Similar results have been obtained in the case of other crystals also; only the load above which constancy of hardness has been noted is different from 3.5 kg for other crystals.

To obtain the value of real hardness before the elastic recovery of the indentation, the length of the indentation should be measured whilst the indenter is in contact with the surface of the crystal. Since we have not yet achieved this the crystals being either translucent

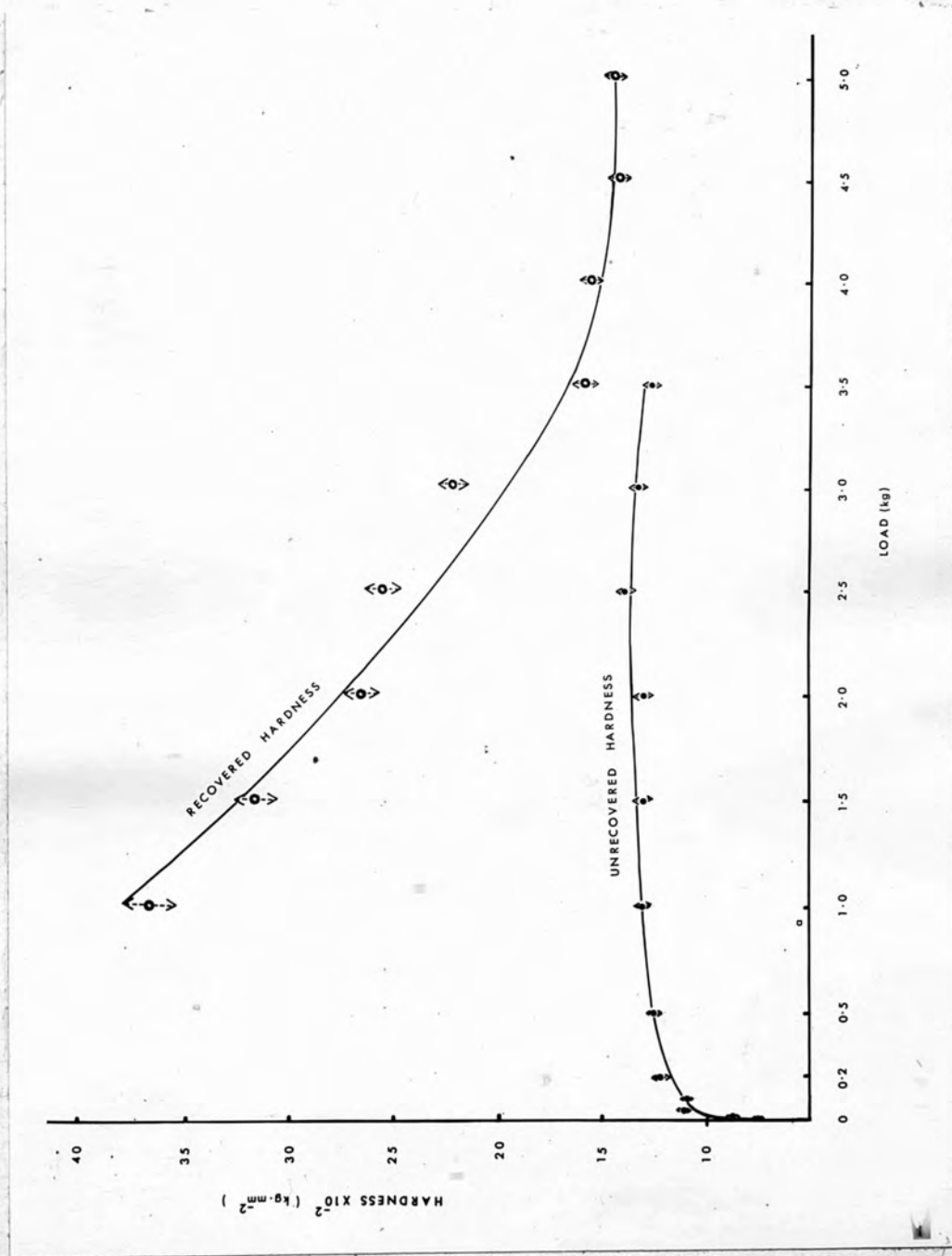


FIG. 67

or opaque, they were given a thin coating of silver and indentations were made on them with loads from 10 gm to 5 kg. For reasons given already, the measured lengths of the indentations on the silvered surface would be the same as the length one would get if the indenter were in contact with the surface. The hardness calculated from this value of the length may be called the 'unrecovered hardness' or the 'elasto-plastic hardness' of the crystal. Table (4) gives this hardness

TABLE 3

( Sample 5, unsilvered to give recovered hardness)

No.	Load in kg.	d in mm x30	Hardness in kg/mm <sup>2</sup>	Log(load in gm)	Lod(d in mm x30)
1	1.0	2.7	3687	3.0000	0.4314
2	1.5	3.25	3200	3.1761	0.5119
3	2.0	3.8	2688	3.3010	0.5798
4	2.5	4.1	2598	3.3979	0.6128
5	3.0	4.6	2254	3.4771	0.6628
6	3.5	5.45	1613	3.5441	0.7364
7	4.0	5.7	1593	3.6021	0.7559
8	4.5	6.1	1456	3.6532	0.7853
9	5.0	6.8	1485	3.6990	0.8325

for different loads on the same crystal for which the recovered hardness is given in table (3). Figure 67 also shows the graph between the load and unrecovered hardness, according to which the unrecovered hardness increased with load upto 500 gm and then at higher loads

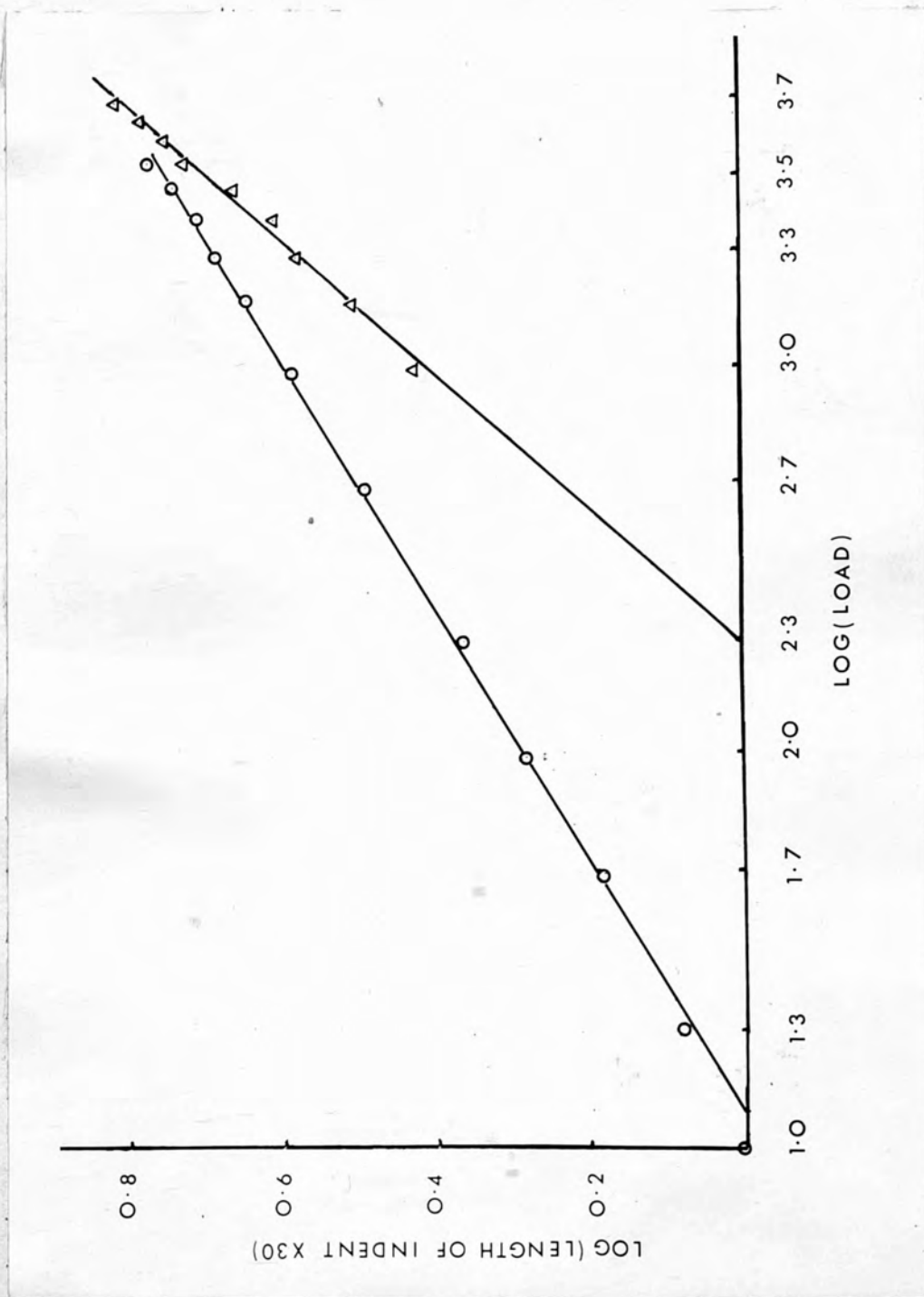


FIG. 68

○ Unrecovered length

△ Recovered length



has more or less the same value. In some crystals a slight decrease in this hardness is noted at still higher loads; in the case of this crystal also the hardness at 3.5 kg is less than at 3 kg. Observations beyond 3.5 kg could not be taken on this crystal as there was not enough space on the surface for further indentations. The last two columns of tables (3) and (4) give the log (load) and the log (length of indentation) from which the graphs shown in figure 68 have been drawn. The logarithmic index  $n$  can be calculated from the gradient of the log-log graphs.

TABLE 4  
(Sample 5, thinly silvered to give unrecovered hardness)

No.	Load in gm. or kg.	d in mm x30	Hardness in kg/mm <sup>2</sup>	Log(load in gm)	Log(length of ind. in mm X30)
1	10 gm	1.0	747.8.	1.0000	0.0000
2	20 "	1.2	865.4	1.3010	0.0792
3	50 "	1.5	1108	1.6990	0.1761
4	100 "	1.9	1090	2.0000	0.2788
5	200 "	2.3	1229	2.3010	0.3617
6	500 "	3.1	1255	2.6990	0.4914
7	1 kg	3.85	1310	3.0000	0.5855
8	1.5 "	4.4	1316	3.1761	0.6435
9	2.0 "	4.85	1311	3.3010	0.6857
10	2.5 "	5.1	1409	3.3979	0.7076
11	3.0 "	5.5	1348	3.4771	0.7404
12	3.5 "	5.9	1275	3.5441	0.7709

From figure 68 the value of  $n$  for 'recovered hardness' is 1.72 and for 'unrecovered hardness'  $n = 3.31$ .

Table (5) shows the double-cone 'recovered hardness' for sample 8 of the crystals. Figure 69a is the hardness-load graph and figure 69b is the  $\log(\text{length of indent}) - \log(\text{load})$  graph for the same. The log-log graph gives 1.71 as the value for the logarithmic index  $n$ . The Vickers hardness for the sample is already given in table (2), from which, using the formula  $L = hd^n$ , the logarithmic index  $n$  works out to be 1.94.

TABLE 5

(Sample 8, unsilvered to give recovered hardness)

No	Load in kg.	d in mm x22	Hardness kg/mm <sup>2</sup>	in. Log(load in gm)	Log(d in mm x22)
1	1.0	2.1	3189	3.0000	0.3220
2	1.5	2.5	2832	3.1761	0.3979
3	2.0	3.0	2185	3.3010	0.4771
4	2.5	3.35	1962	3.3979	0.5250
5	3.0	3.85	1550	3.4771	0.5855
6	3.5	4.15	1445	3.5441	0.6180
7	4.0	4.5	1295	3.6021	0.6532
8	4.5	4.9	1128	3.6532	0.6902
9	5.0	5.15	1080	3.6990	0.7118

Figure 70 shows the Fizeau fringes on the 5 and 4.5 kg indentations; figure 71 shows the same for 4 and 3.5 kg indents and figure 72 for 3, 2.5, 2, 1.5 and 1 kg indents. These have been taken with a 16 mm

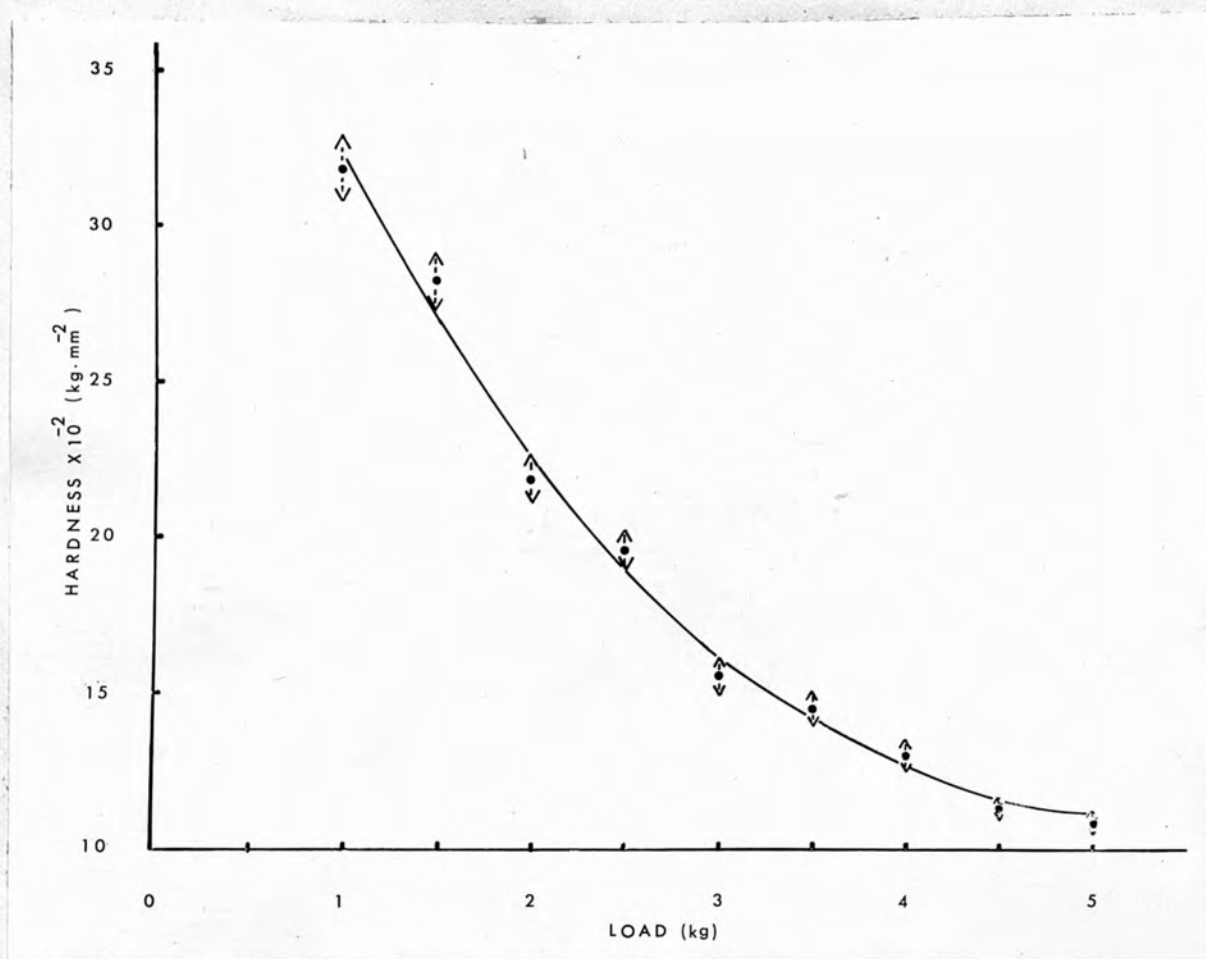


FIG. 69a

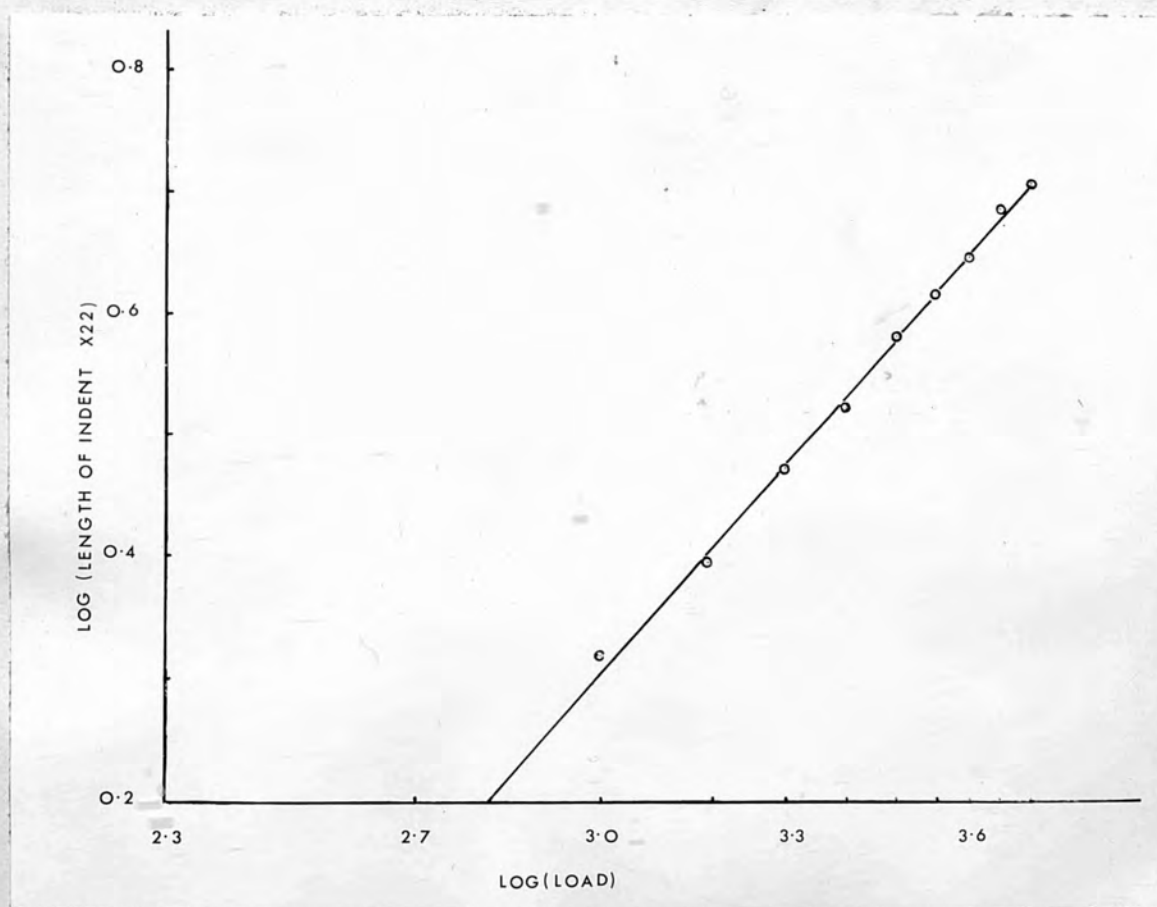


FIG. 69b

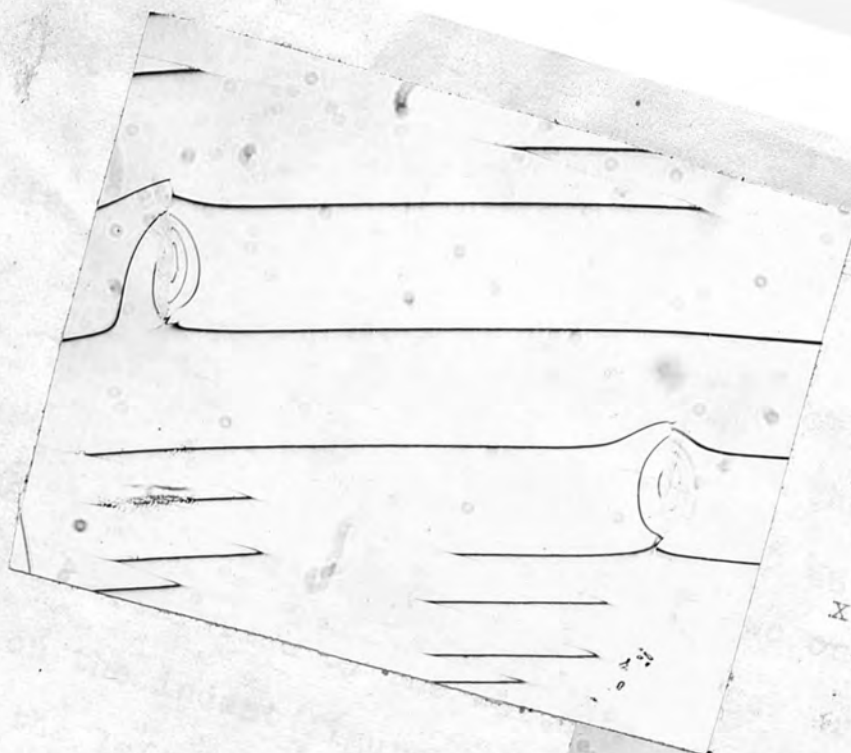


FIG. 70  
x75

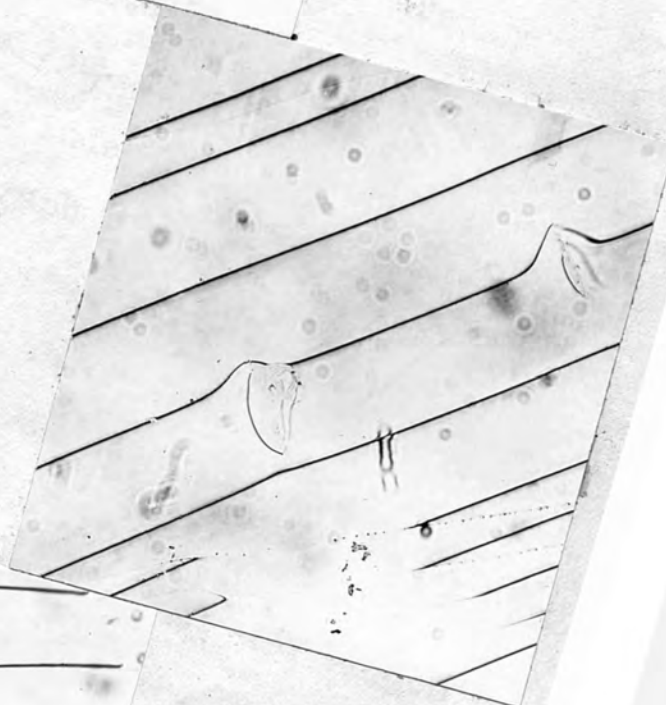


FIG. 71  
x75



FIG. 72  
x75



objective. Fringes on the same indents were obtained using a 8 mm objective for the purpose of calculating the displacement of the material around them and also for determining the radius of curvature of the indents. Figure 73 shows the Fizeau fringes on the 5 kg indent; there are three fringes on the right and two on the left side of the indent. That these fringes are 'pile-ups' is confirmed by the white light fringes (F,E,C.O) on the indent (figure 73a).  $L_1$  is the fringe pattern on the left side of the indent obtained through the constant deviation spectrograph using mercury light;  $L_2$  and  $L_3$  represent respectively the FECO near and away from the indent, with the slit of the spectrograph parallel to the indent in both the cases.  $R_1$ ,  $R_2$  and  $R_3$  represent similar fringes on the right side of the indent. The cracks at the end of the indent, are ridges as seen by the FECO  $T_2$  (fig.73a) on one of the cracks;  $T_1$  shows the fringes on the crack as seen through the spectrograph using mercury light. The Fizeau fringes inside the indent are not very clear. Using Hilgers Comparator the distance of these fringes from the centre was measured and treating them as Newtons rings, the radius of curvature of the indent was calculated.

Figures (74,75,76,77,78,79,80 and 81) represent respectively the Fizeau fringes on 4.5,4,3.5,3,2.5,2,1.5 and 1 kg indentations. The magnitude of the 'pile-ups'



FIG. 73  
x225

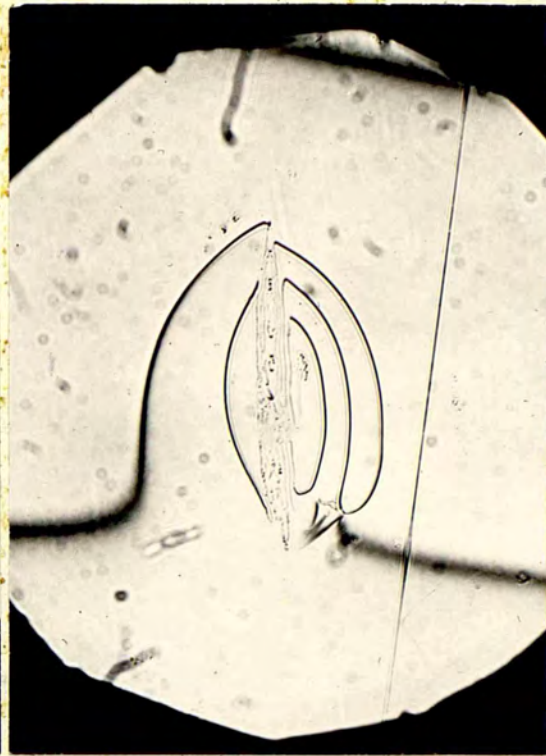


FIG. 74  
x225



FIG. 75  
x225

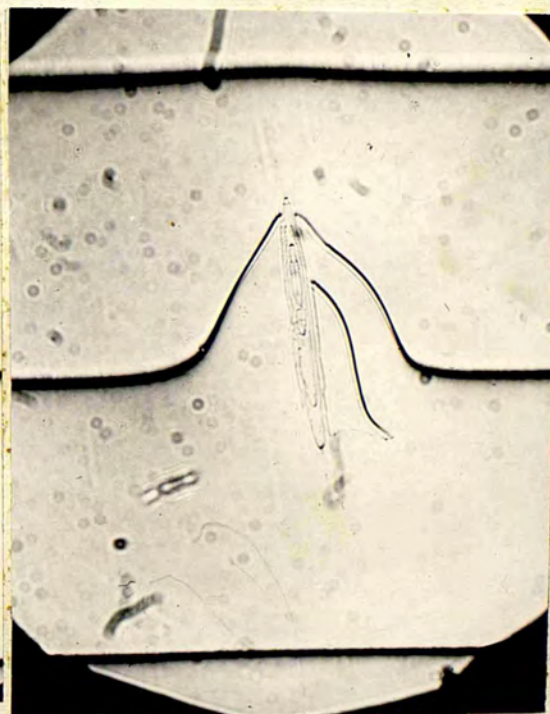


FIG. 76  
x225



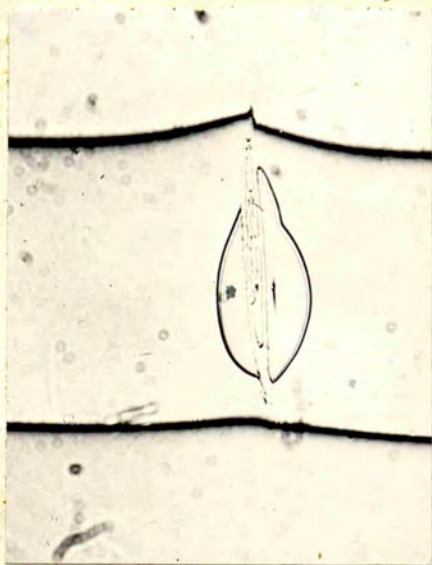


FIG.77  
x225



FIG.78  
x225



FIG.79  
x225



FIG.80  
x225



FIG.81  
x225



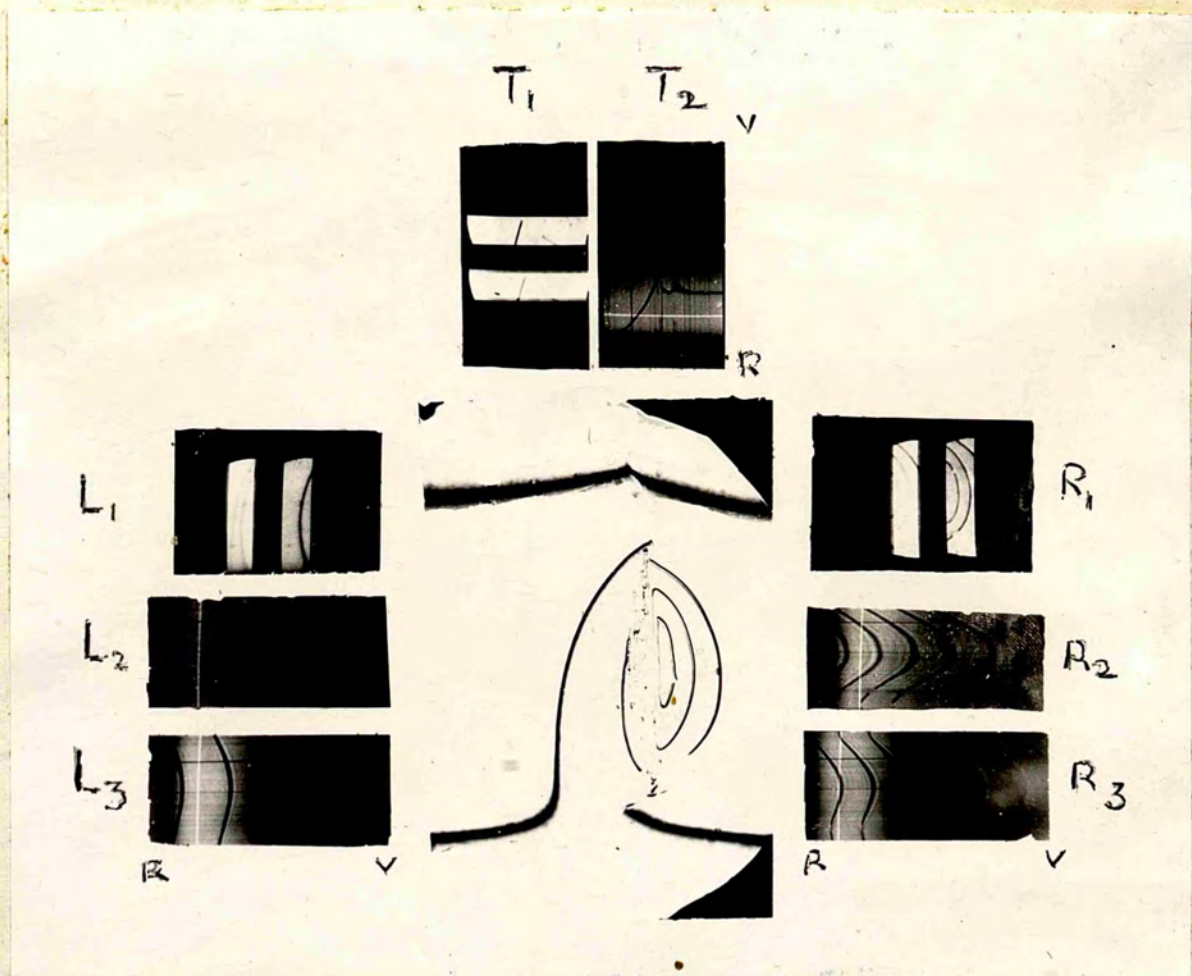


FIG. 73a.

So the observations are in agreement with this analysis. The dimensional analysis holds good whether the material shows work-hardening characteristics or not; an ideally plastic material shows no work-hardening properties which means that its tensile yield stress is constant.



and the radii of curvature of the indents have been shown in table (6);  $d_1, d_2$  and  $d_3$  represent the distance in cm of the first, second and third fringe from the centre of the indent on its right side measured at a magnification of 450;  $d'_1$  and  $d'_2$  are similar quantities for the left side.  $dm/m$  gives the 'pile-up' parallel to the indent as the fraction of the fringe separation;  $R$  is the average radius of the indent;  $R_1$  and  $R_2$  are the radii at the centre and away from the centre of the indent, calculated only for those indents which had enough fringes in both regions for the purpose of calculation.

#### Discussion of the results

(1) The Vickers hardness (recovered) for silicon carbide given in table (2) may be taken as constant; this is justified on the ground that the measurement of the diagonal length alone contributes a 4% error in value of the hardness ( $H_{vk}$ ). A dimensional analysis (1954) shows that  $H_{vk}$  should be independent of the recovered diagonal length ( $d_R$ ), which means that  $H_{vk}$  should be independent of the load. So the observations are in agreement with this analysis. The dimensional analysis holds good whether the material shows work-hardening characteristics or not; an ideally plastic material shows no work-hardening properties which means that its tensile yield stress is constant.

The formula for  $H_{vk}$  is  $H_{vk} = \frac{1.854L}{d_R^2}$  and as stated in the beginning of this chapter if  $H_{vk}$  is to be independent of the load,  $\sqrt{L}$  must be proportional to  $d_R$ ; that is  $\sqrt{L}$  must be proportional to  $(d_U - d_E)$  where  $d_U$  is the unrecovered diagonal length and  $d_E$  is the elastic recovery in it. A dimensional analysis further shows that  $H_v(\text{unrecovered})$  is also independent of  $d_U$  for all types of material; this means that unrecovered Vickers hardness should also be independent of the load. It can be shown that

$$H_{vk}(\text{recovered}) = H_{vk}(\text{unrecovered}) + 2H_{vk}(\text{unrec.}) \frac{d_E}{d_U},$$

when  $d_E$  is very small as compared to  $d_U$  which is the case here. Since both the unrecovered and the recovered hardness are independent of their indentation diagonal lengths, from the above relation it is easy to see that  $d_E$  is proportional to  $d_U$ . This was noted by Winton and Grodzinski (1956) and it may be true in the case of silicon carbide although  $d_U$  obtained by silvering the surface thinly showed no measurable difference from  $d_R$ . This method, however appears unsuitable for estimating the unrecovered diagonal length of Vickers indentations on hard materials.

(2) From figure 55 it is seen that the double-cone 'unrecovered hardness' for loads from 10 gm to 200 gm, increases with load. In some cases this increase is followed by a decrease in hardness as shown for a sample

in the figure.

(3) Figure 67 shows the variation of 'unrecovered hardness' with load for loads ranging from 10 gm to 3.5 kg. The apparent hardness increases with load upto 500 gm and then for higher loads has a constant value. In some crystals a slight decrease in apparent hardness is noted for still higher loads.

(4) Figure 67 also shows the variation of 'recovered hardness' with load for the same specimen, the load range being 1 kg to 5 kg. Although indents were made with lower loads, they were not visible except the 500 gm indent; this indent was just visible but was not clear enough for measurement. The graph shows that the 'recovered hardness' decreases with load upto a certain load ( in this case 3.5 kg) and then for higher loads has a constant value. In this sample the apparent hardness at 1 kg is  $3189 \text{ kg/mm}^2$  but for a load of 5 kg it is  $1080 \text{ kg/mm}^2$ . As seen in figure 67 the recovered and the unrecovered hardness tend to acquire the same value as the load is increased. At any particular load the 'recovered hardness' is greater than the 'unrecovered hardness'; the difference between the two reduces as the load is increased. This has been noted in all the crystals studied. Since the load required to produce an indent of a given 'unrecovered length' is lower than that for producing the same 'recovered length' of the



indent, one would expect the 'recovered hardness' to be greater than the 'unrecovered hardness' as indeed it is.

(5) Figure 68 gives the  $\log(\text{length of indent}) - \log(\text{load})$  graph for the same sample under discussion. The graphs for both the recovered and the unrecovered lengths are nearly straight lines but they appear to meet at higher loads. It is clear that elastic recovery of the indent plays an increasingly important part as the size of the indentation decreases. At higher loads the contraction in the length of the indents due to elastic recovery becomes less. In this case the two lines tend to meet above 3.5 kg load, and it is such a load which gives the real hardness.

(6) The logarithmic index calculated from figure 68 is 1.71 for recovered hardness and 3.31 for 'unrecovered hardness'. Figure 69a and 69b are respectively the hardness-load and  $\log(\text{length of indent}) - \log(\text{load})$  graphs for another sample of silicon carbide. The value of  $n$  for this specimen comes out to be 1.72.

(7) The value of  $n$  for recovered hardness for all the specimens tested varies from 1.68 to 1.74. Considering the errors involved in loading and measuring the length of the indents, the value of  $n$  shows remarkable constancy. The difference between the values of  $n$  for the 'unrecovered' and the 'recovered' hardness is a measure of

the degree of elastic recovery in the material.

Although  $n$  for Vickers hardness is associated with the work-hardening of the surface of the specimen (1956), it is difficult to extend the argument for d-c hardness until more data becomes available as to the relation between the work-hardening capacity and the d-c hardness of a material.

(8) Tarasov and Thibault (1947) have observed elastic recovery in silicon carbide using a Knoop indenter; surprisingly Grodzinski (1952) did not notice any elastic recovery effect in d-c indentations on the (0001) face of silicon carbide crystals as we do here.

(9) Although it is useful to distinguish between the 'recovered' and the 'unrecovered' hardness of a material to study its elastic and plastic properties, as a general definition hardness should imply only 'unrecovered' hardness. In a material like rubber an indenter may not leave any 'recovered' impression even at high loads; in such a case its 'recovered hardness' will be infinite, which cannot be the case. The 'unrecovered' hardness will always have some definite value even at low loads. Hence 'unrecovered' hardness appears to be a more practical and theoretically sound concept, and the limit value could be well adopted as the measure of real hardness.

TABLE (6)

No	Load in kg.	$d_3$ (cm)	$d_2$	$d_1$	$d_1'$	$d_2'$
1	5	2.7	1.8	1.1	0.8	2.6
2	4.5	2.5	1.8	1.2	1.1	3.0
3	4	-	2.0	1.1	0.8	2.8
4	3.5	-	2.1	1.0	2.2	-
5	3	-	-	1.2	0.9	-
6	2.5	-	1.2	0.6	1.1	-
7	2	-	-	0.1	-	-

TABLE (6)

Fringe sep. m (cm)	dm	dm/m	R (mm)	R1 (mm)	R2 (mm)
12	10.5	0.875	3.88	-	-
11.5	7.5	0.652	4.07	-	-
7.5	5.0	0.666	-	-	-
8.2	3.8	0.463	4.01	3.15	4.84
9.0	4.5	0.500	3.69	3.29	4.16
6.1	3.1	0.508	3.94	-	-
5.5	1.6	0.29	4.06	-	-

From table (6) it is seen that the radius of curvature of all the indents is about 4 mm; since the radius of curvature of the d-c indenter is 2mm, there has been approximately a 50% recovery in depth. From the table it is also clear that the recovery in depth is less at the centre of the indent than at its ends.



CHAPTER IXDIRECTIONAL VARIATION OF HARDNESSIntroduction

The plastic properties of a substance play a very important part in hardness testing by static indentation. Plastic deformation of a crystalline material occurs by either (a) slip on a set of planes in given crystallographic directions or (b) twinning, involving a definite shear on a given plane. Changes in the twinning pattern around the indentations, with changes in orientation of the crystal grain, have been found to conform to appropriate crystallographic relations in the case of many anisotropic metals (1956). Variations with grain orientation are apparent not only in the form of the twins, but also in the shape of the outline of the indentations. The precise shape of a recovered Vickers pyramid impression, will depend on the degree of 'sinking-in' or 'piling-up' that might take place as the indentation is made and on the amount of the elastic recovery that takes place as the indenter is removed. Workers (1956) have attributed a convex edge to the bulging associated with a 'piling-up' and a concave edge with a 'sinking-in'. Tolansky and Nichols (1952) have, however, found that concavity can be associated with both piling-up and sinking-in.

Schulz and Hanemann (1941) studying hardness in

different directions on a crystal found a maximum hardness variation of about 7% in aluminium; Perryman (1950) also reported directional variation in hardness in aluminium, copper and lead. There is no evidence in literature, of any attempt to study the variation of hardness with crystallographic direction of hard materials using multiple-beam interferometry. Daniel and Dunn (1949) investigated the effect of crystal orientation on measured Knoop hardness for single crystals of silicon ferrite and zinc. The hardness variation in zinc was quite marked. They suggested that the average hardness values for all body-centred cubic metals may be independent of the plane tested. Tolansky and Williams (1955) studied the directional hardness variations in tin and bismuth crystals using a double-cone indenter. They found the ratio of maximum and minimum hardness as 1.6:1 for a (311) face and 4.5:1 for a (554) face. For the first time they demonstrated by interferometry that slip mechanism plays a primary part in producing directional variation in hardness.

Several authors (1956) have drawn attention to the variation of hardness with orientation of the surface tested, for minerals and synthetic stones. Robertson and Van Meter (1951) reported  $H_k$  variation of nearly 500 per cent for molybdenite and of values ranging from 633 to 1148 kg/mm<sup>2</sup> for arsenopyrite. Stern (1952) found

that the double-cone hardness varied from about 950 to 2070 in the case of synthetic corundum.

### Choice of Indenter

The various methods and types of indenters used for hardness studies have already been described in Chapter II. It is worthwhile considering the characteristics of the various methods to see the effects produced on crystal surfaces which show hardness variation in different directions. Scratching by a diamond (1950) reveals directional hardness but the technique is difficult to apply and liable to serious systematic error. According to Bierbaum the relatively strong corners of a diamond cube are the best scratching points. The scratches formed are always narrow and the width, which is the required dimension, is difficult to measure accurately, partly because of the scale and partly of irregularity and distortion of the edges due to plough-up of material (1955). There is also the serious difficulty of recognizing and allowing for recovery effects. Tolansky and Williams (1955) established that long narrow indents reveal big recovery effects in their width dimensions and as scratches have similar characteristics, errors of even 100% may arise through recovery defects. So, although capable of revealing qualitative differences, scratch method is unsatisfactory for quantitative estimation of hardness variation.



The ball and the cone indentations produce slightly elliptical impressions on an anisotropic material but these are not easily amenable either to exact measurement or to clear interpretation. The diamond chisel suggested by Meincke (1951) is also unsatisfactory; in it the width of a long narrow indent is measured and this involves serious end effects in addition to recovery defects. The method is also used for indents of large dimensions.

As stated earlier Vickers diamond pyramid indenter gives non-symmetrical indents on anisotropic materials; the indentations do reveal qualitatively directional differences (1949,1952) but are again difficult to interpret quantitatively. In view of the fourfold symmetry of a Vickers indenter, it is less suitable for a study of directional hardness than a Knoop or a d-c indenter in which the hardness is expressed in terms of a single measurement. In Knoop indenter it is assumed with some justification that the recovery will effect the minor diagonal rather than the major one, which is an important advantage.

The double-cone indenter, also described in chapter II, appears to be the best instrument for studying directional hardness. In the case of silicon carbide crystals it does show recovery effects, but by studying both its recovered and unrecovered hardness, it is

possible to estimate the recovery for a particular load as has been done in chapter VIII. It gives elongated, shallow boat-shaped impressions which are ideal in shape for showing directional hardness.

### Present Investigations

In this chapter a description is given of the directional hardness studies made on the (0001) face of silicon carbide crystals. Observations were made with both double cone and a Vickers indenter. The load chosen for the Vickers indenter was 500 gm, since a lower load gave very small impressions and a higher load resulted in damage to the surface of the crystal. Indentations made with a double-cone indenter on a thinly-silvered surface of SiC crystal, using a load of 200 gm were too small to reveal any directional variation in hardness. So a load of 2 kg or 3 kg was chosen to make this study as it has been seen (chapter VIII) that with such loads the indentations showed enough permanent deformation to permit of their study by interferometry. Therefore the hardness referred to in this chapter will be 'recovered' hardness, so that any interpretation of the same will involve only the plastic properties of the crystal. It is, however, possible to estimate the 'unrecovered' hardness along any particular direction by making proper allowance for the elastic recovery associated with that load.

### Vickers Indents

Vickers pyramid and double-cone indentations were made at  $10^{\circ}$  interval in direction on the surface of the crystals; the robust model of the indentation apparatus was used for this purpose. Sufficient space was left between successive indentations to ensure that the range of deformation due to one indentation was not affected by neighbouring indentations. The direction of the indents was altered by rotating the crystal on the stage of the microscope and the angle of rotation was read by the scale and vernier attached to the stage. The indentations were made away from the edge of the crystal so that the distortion of material surrounding the indentation was itself surrounded by the undeformed surface of the crystal.

Figure 82, shows a group of Vickers pyramid indentations made on the (0001) face of a SiC crystal. All the eleven indentations seen in the figure were made in such a way that after each indentation the crystal was rotated through  $10^{\circ}$  with respect to the Vickers pyramid indenter itself. Figure 83 shows the Fizeau fringes on the same indentation. To see the variation in the shape of the indentations with orientation of the crystal, figure 82 has been further magnified. Figure 84 shows the Vickers indentation for  $0^{\circ}$  and  $10^{\circ}$ ; figures 85, 86 and 86a show the indentations for other angles. All



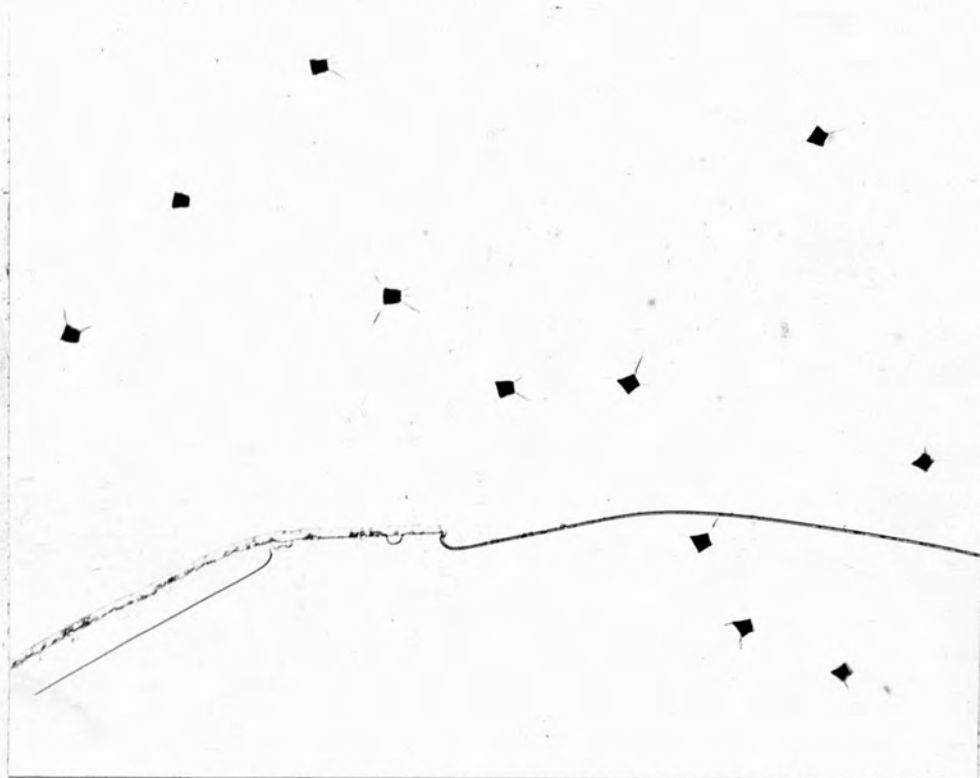


FIG.82  
x110



FIG.83  
x85



FIG.84  
x350

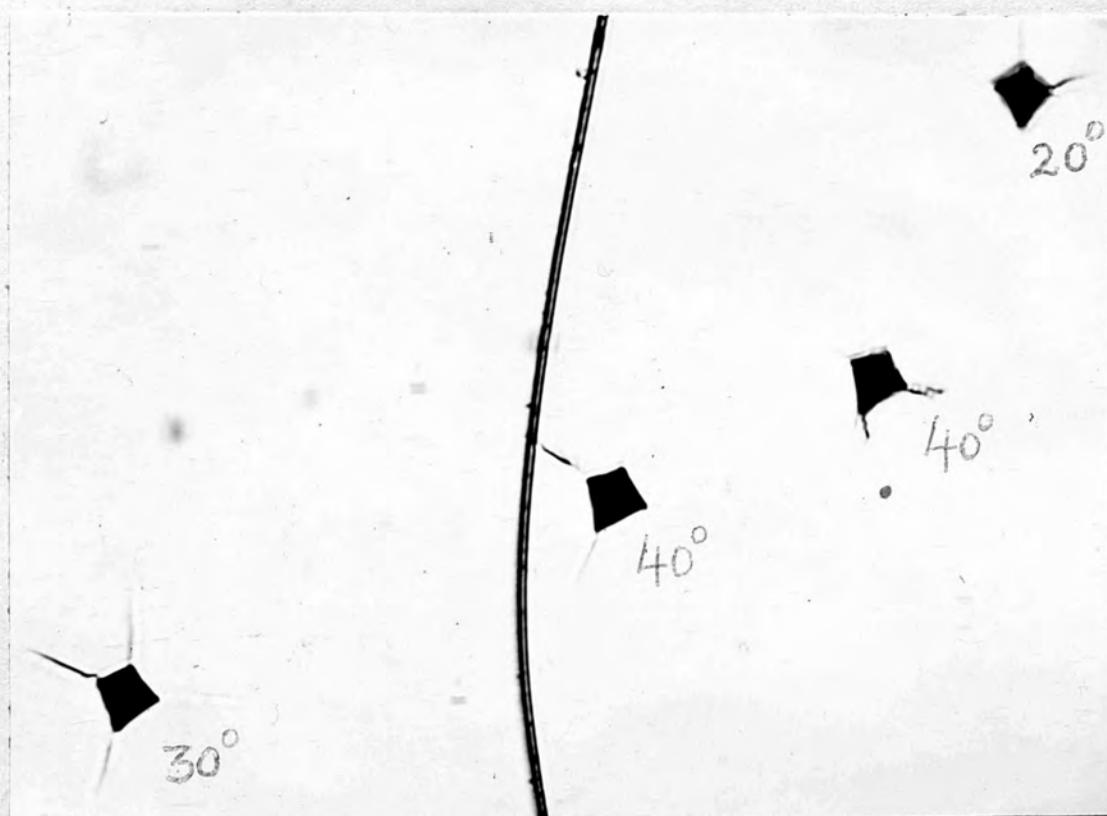


FIG.85  
x350

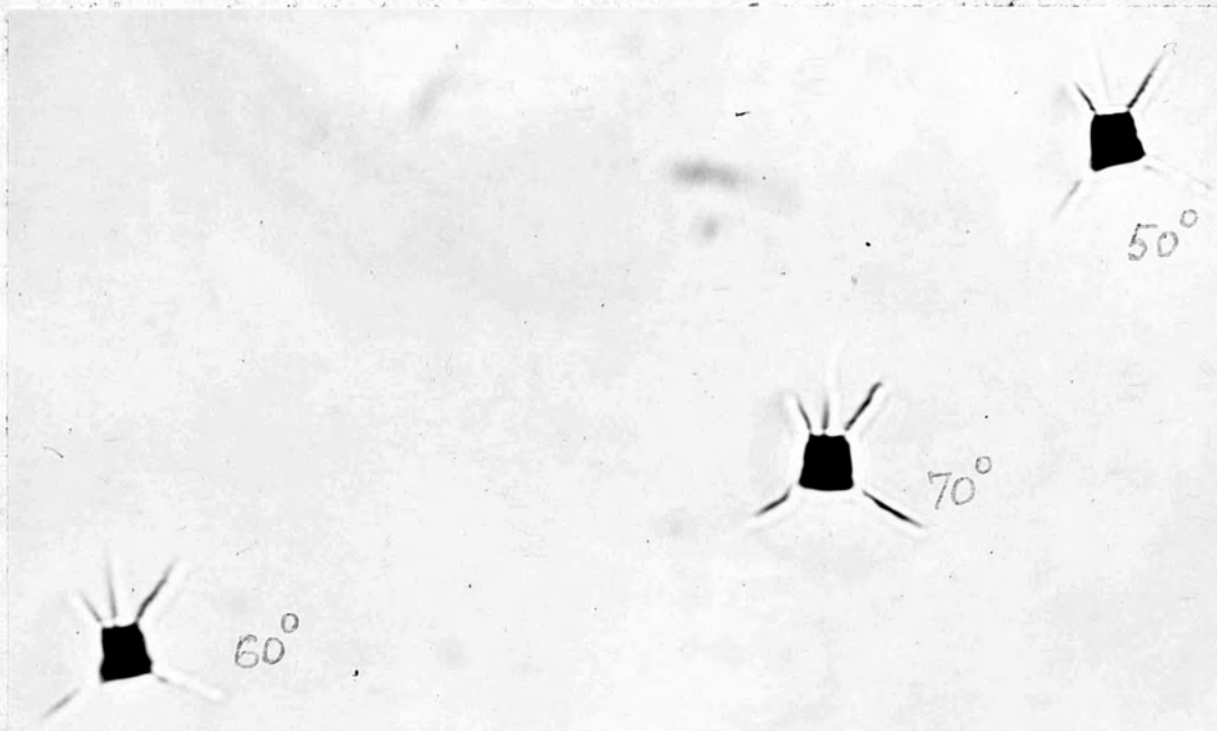


FIG.86  
x350

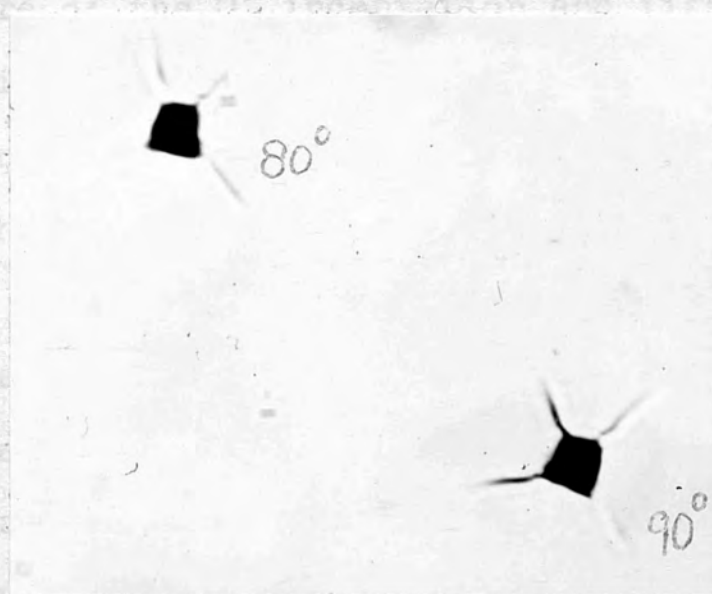


FIG.86a  
x350



the indentations show cracks at their corners. The shape of the indents changes gradually from a kite at  $0^\circ$  to that of a trapezium at  $60^\circ$  and again it tries to acquire the shape of a kite as the angle increases. Over the range  $40^\circ$  to  $70^\circ$ , an additional crack is seen, which is approximately parallel to the  $[11\bar{2}0]$  direction of the crystal face indicating that it could be one of the cleavage directions of the crystal. The cracks leaving the corners tend to proceed in the same directions on the crystal, no matter what the orientation of the pyramid indenter itself. Figures 87, 88 and 89 show the Fizeau fringes on the indentation marked with their appropriate angle. These fringes help in noting the shape of the distortion around the indentations and in locating the additional crack. Figure 90 shows the phase contrast picture of the  $0^\circ$  indentation and figure 90a gives a magnified picture of Fizeau fringes contouring the indentation. Figures 91 and 91a are similar pictures for the  $60^\circ$  indentation. These figures further help in noting the change in shape of the indentation. Figure 92 shows the Vickers indentation obtained at  $60^\circ$  orientation when the time of indentation was increased from 15 seconds to 60 seconds. The hardness calculated from the mean values of the diagonal lengths of each indentation lies between 1819 and 1860  $\text{kg/mm}^2$ . Considering that a 2% error is noted in the measurement of the



FIG. 87  
x250

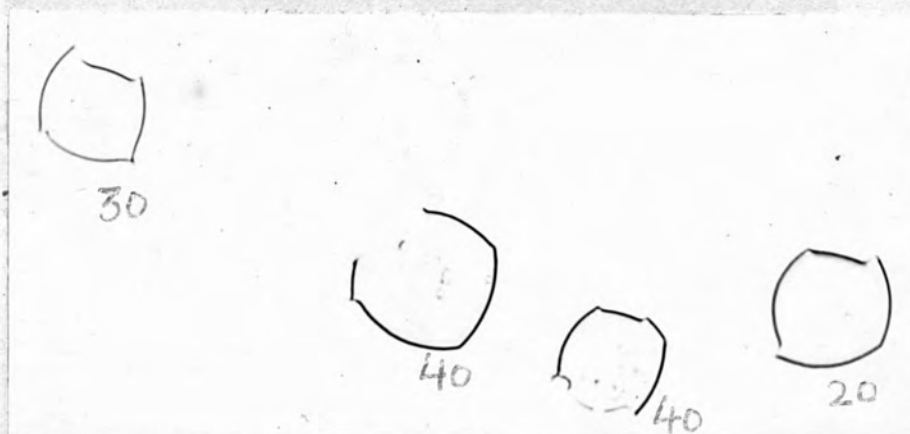


FIG. 88  
x250

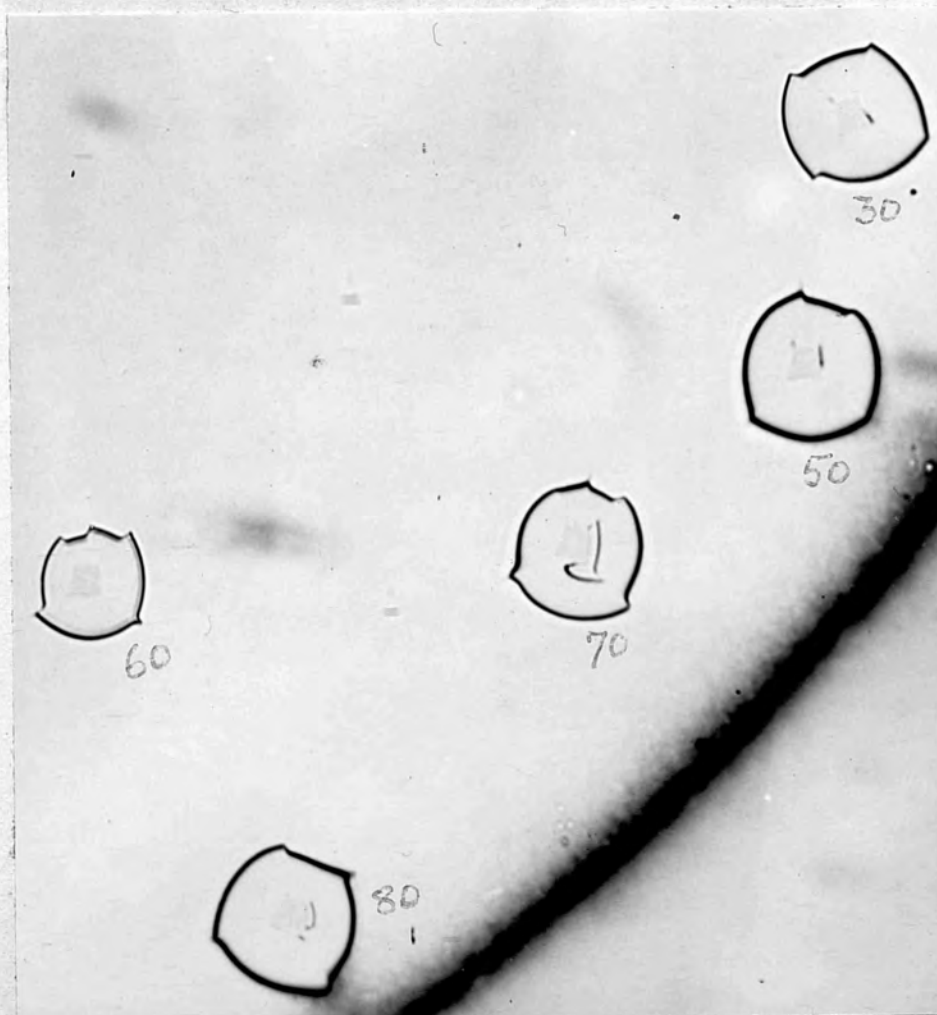


FIG. 89  
x250



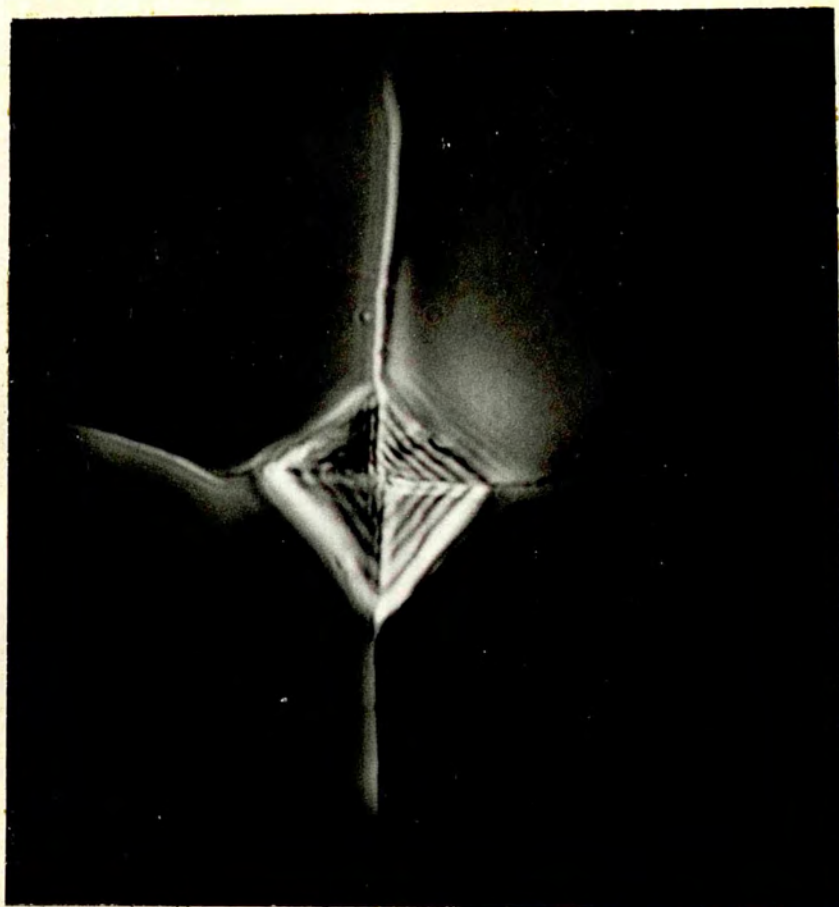


FIG. 90  
x1200

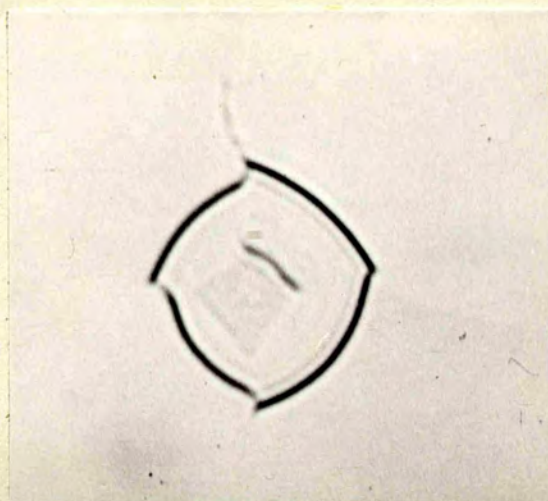


FIG. 90a  
x575



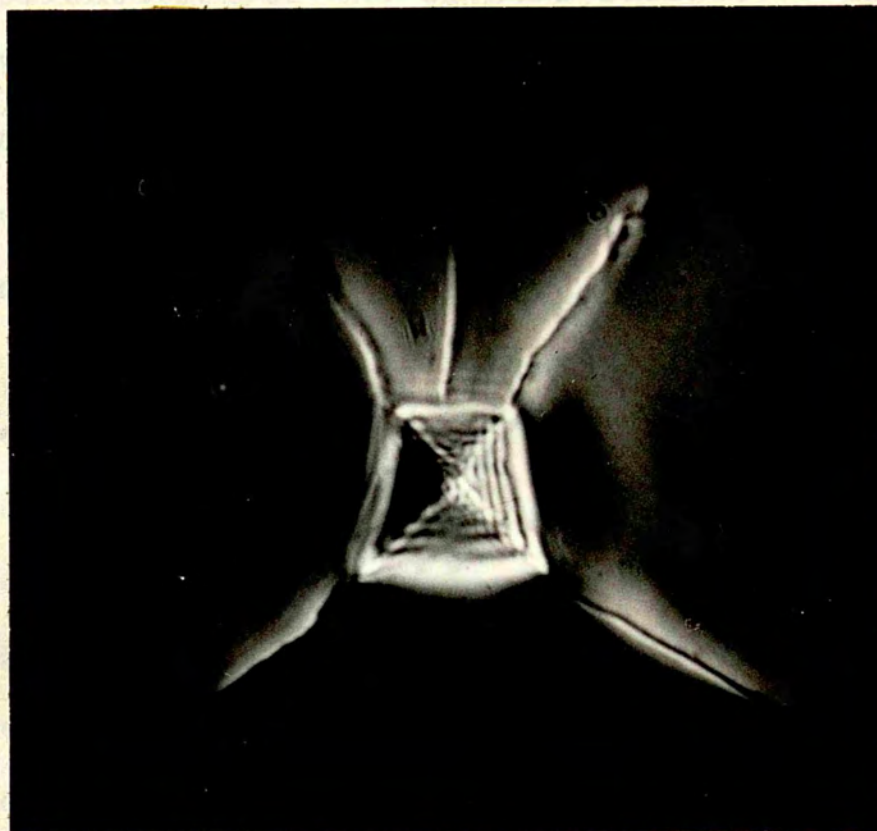


FIG.91  
x1200

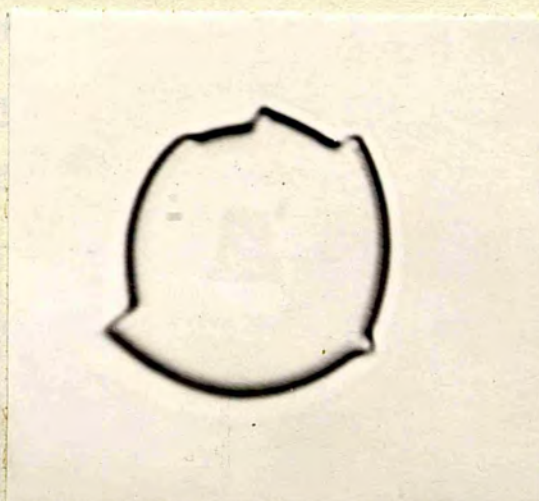


FIG.91a  
x575

diagonals involving a 4% error in hardness, the calculated value of the hardness does not show much effective variation with orientation of the crystal surface. In other words the Vickers indenter is not responsive to directional variations.

Figure 93 shows again Fizeau fringes on some of the Vickers indentations; in the picture one of the fringes is made to pass through the  $60^\circ$  and  $70^\circ$  indentations to estimate the pile-up around them in terms of fringe separation. Figure 94 (top) shows the FECO on the additional crack; calculations show that it is a slope-up of 120 A. Figure 94 (bottom) also shows the FECO on one of the edges of a Vickers indentation; it is found to be a pile-up of the order of 450 A. Although some of the indentations appear to have concave sides, the FECO shows them to be 'piling-ups' and not 'sinking-ins'. This confirms the observations of Tolansky and Nickols and goes against the general impression of many workers (1956) that a concave shape implies a 'sinking-in'.  
Directional Hardness Studies with the Double-Cone Indenter

Indentations were made with the double-cone indenter at  $10^\circ$  interval in direction on the (0001) plane of a number of SiC crystals, using the robust model of the indentation apparatus. In the case of some crystals the interval was changed to  $20^\circ$  due to the smallness of the size of the crystal. All the precautions





FIG.92  
x900

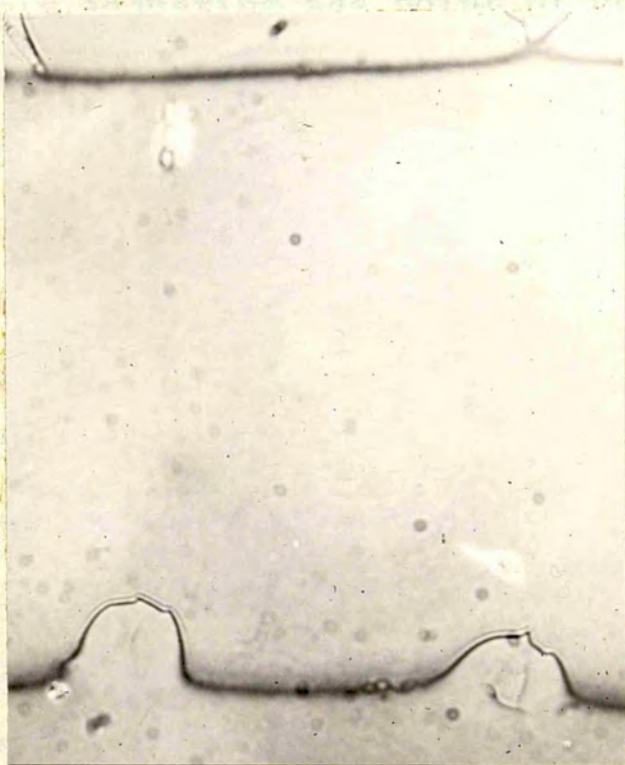


FIG.93  
x250

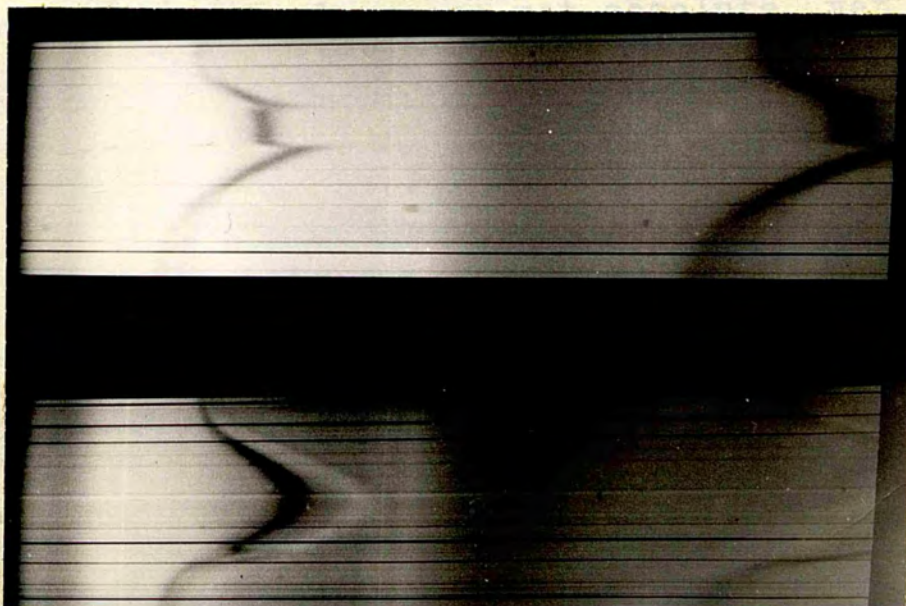


FIG.94



mentioned regarding the spacing of the indents were also taken in this case. Figure 95 shows a group of indentations made after every  $20^\circ$  rotation of the crystal surface with a load of 2 kg. To obtain a general idea of the distortion accompanying the indents, a convex lens of suitable curvature was silvered and matched against the indented surface of the crystal after silvering it. By properly adjusting the point of contact a multiple-beam Newton's ring pattern was obtained in such a way that a single ring passed through all the indentations. Figure 96 shows such a picture in which the second ring passes through all the indentations. Figure 96a shows a similar pattern in which the first ring passes through all the indentations. These indents were made along the circumference of a circle with the  $[11\bar{2}0]$  direction as one of its diameters. Table (1) shows the hardness values with different directions. Figure 97 gives the polar graph for the same. It should be noted that even if the d-c hardness values are not absolute, yet the relative hardness in different directions is still revealed.

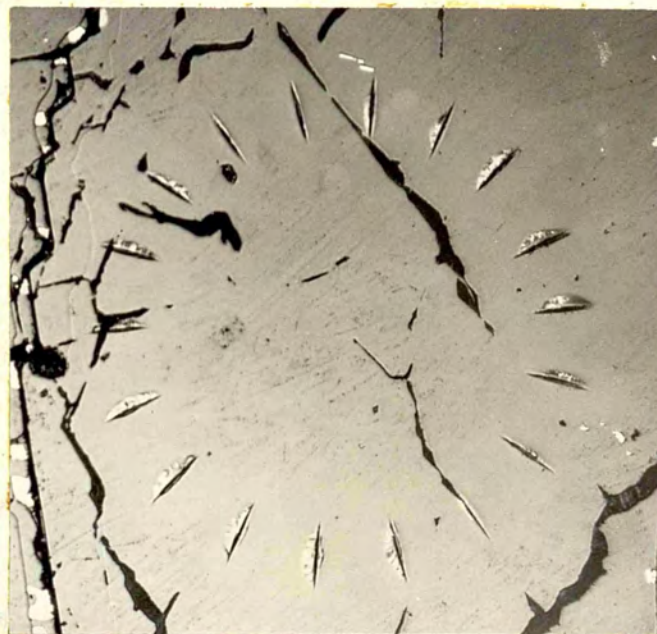


FIG.95  
x50

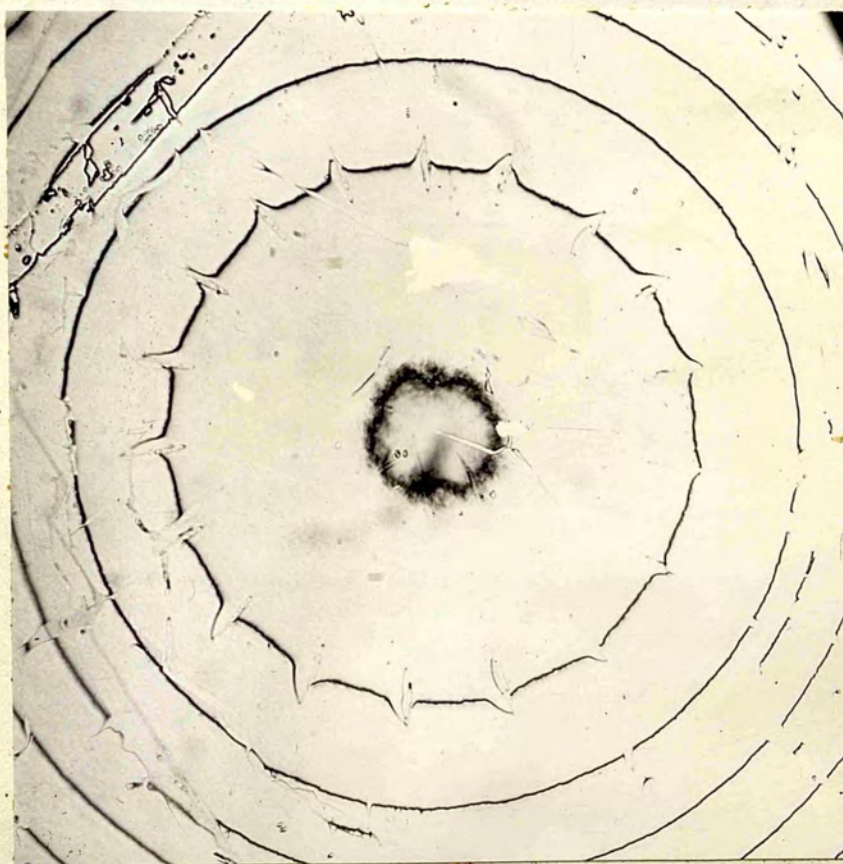


FIG.96  
x60



TABLE 2  
Hardness values (kg/mm<sup>2</sup>) for different directions

No.	Angle of indentation with [110]	Hardness (kg/mm <sup>2</sup> )	Hardness (kg/mm <sup>2</sup> )
1	0	2.3	3307
2	30	2.0	2836
3	60	2.0	2836
4	90	2.0	2836
5	120	2.1	2450
6	150	2.15	2288
7	180	2.15	2288

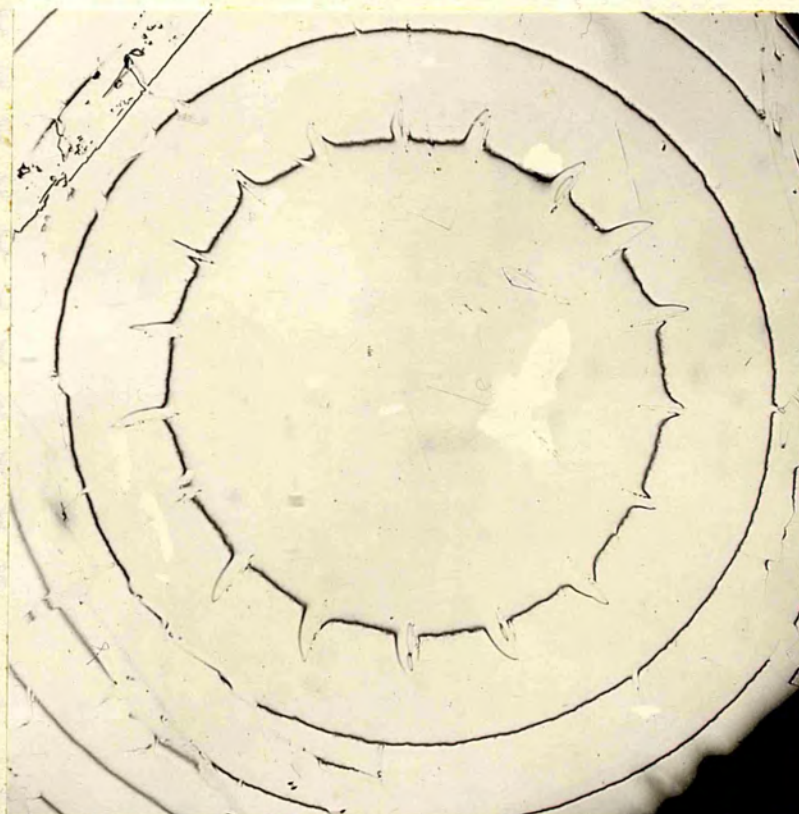


FIG. 96a  
x60

In the indentations were made as shown schematically in figure 96. Figures 97 to 105 show interferograms on each individual indentation starting from  $[11\bar{2}0]$  direction to  $[1\bar{1}20]$  direction. The angle between successive indentations is  $10^\circ$ . Table (2) gives the hardness values for different directions. Figure 107 is the polar graph for the



TABLE (1) (load of 2 kg.)

No	Angle of d-c indenter with $[11\bar{2}0]$ direc.	Length of indent(d) in mm. x16	Hardness in kg/mm <sup>2</sup>
1	0	1.9	3307
2	20	2.0	2836
3	40	2.0	2836
4	60	2.0	2836
5	80	2.1	2450
6	100	2.15	2288
7	120	2.15	2288
8	140	2.25	1992
9	160	2.1	2450
10	180	1.9	3307
11	200	2.15	2283
12	220	2.2	2131
13	240	2.2	2131
14	260	2.2	2131
15	280	2.15	2283
16	300	2.1	2450
17	320	2.1	2450
18	340	2.0	2836

In the case of very well formed crystals, indentations were made as shown diagrammatically in figure 98. Figures 99 to 105 show the interferograms on each individual indentation starting from  $[11\bar{2}0]$  direction to  $[\bar{1}2\bar{1}0]$  direction. The angle between successive indentations is  $10^\circ$ . Table (2) gives the hardness values for different directions. Figure 107 is the polar graph for the

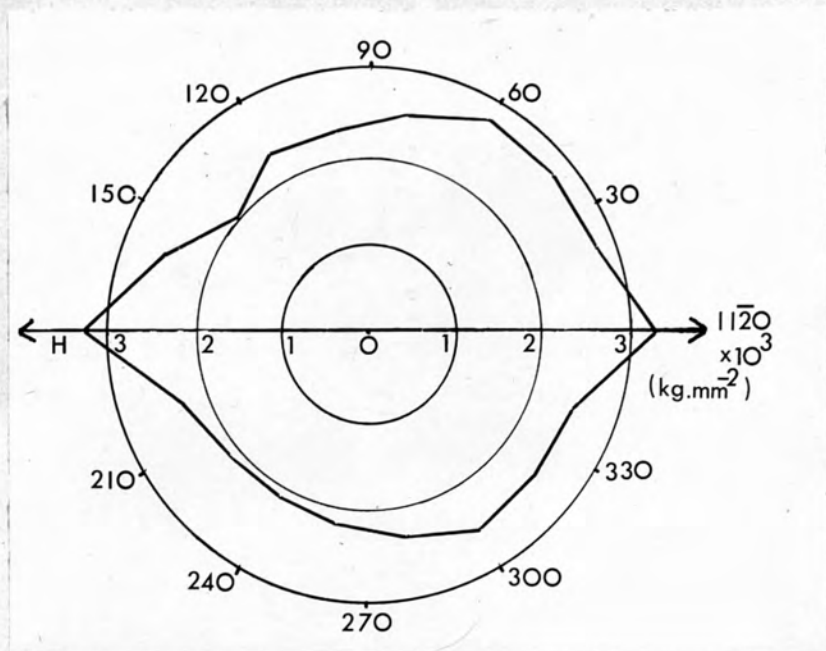


FIG. 97

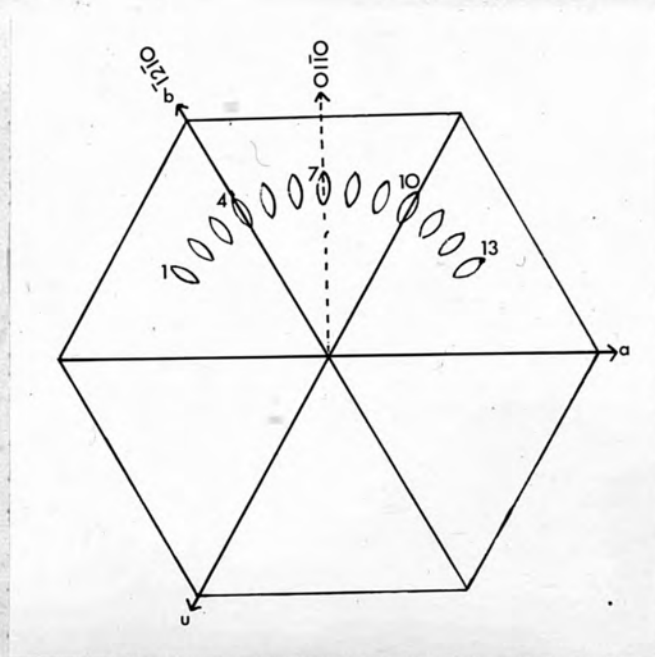


FIG. 98



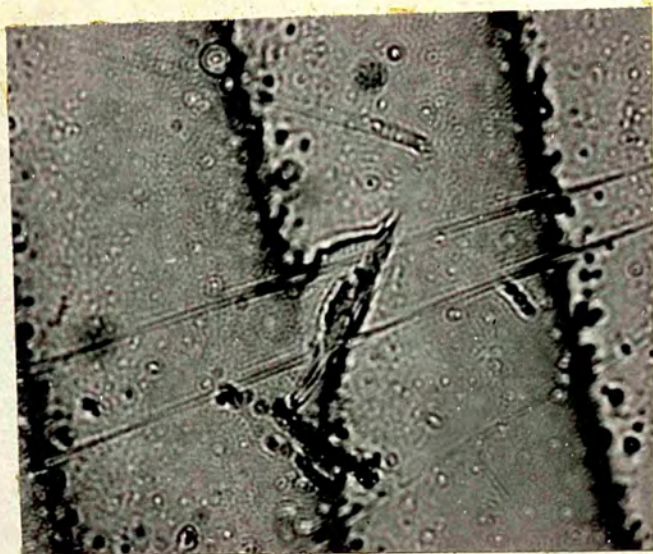


FIG. 99  
x210



FIG. 100  
x210



FIG. 101  
x210



FIG. 102  
x210





FIG. 103  
x210

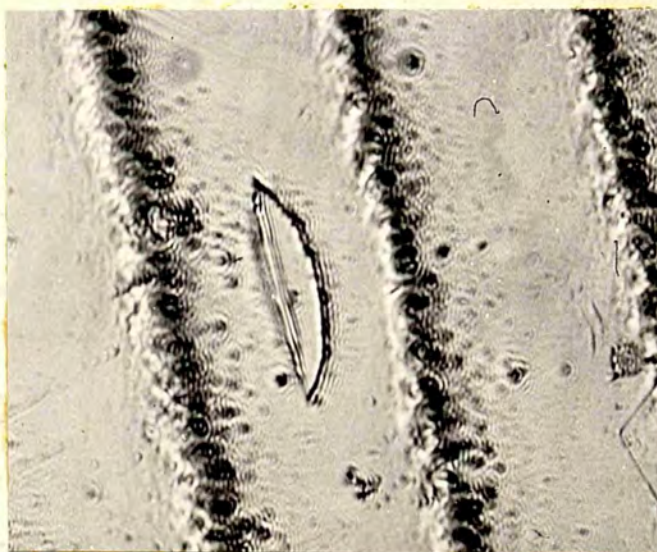


FIG. 104  
x210

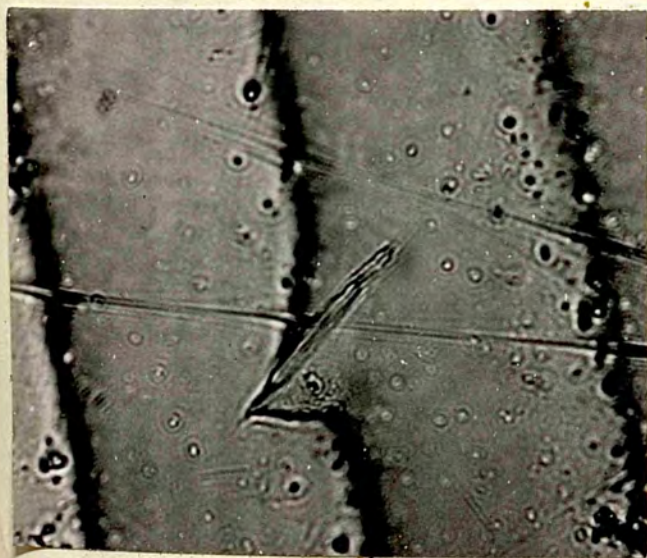


FIG. 105  
x210

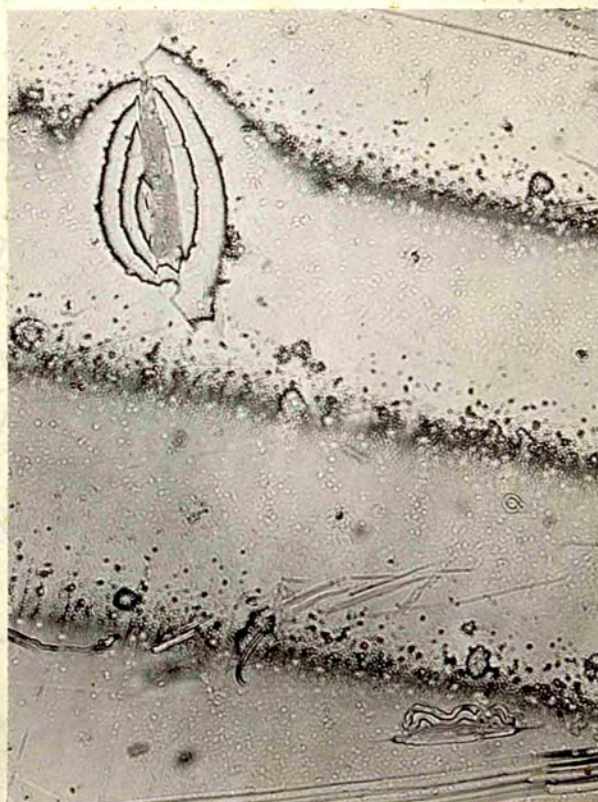


FIG. 106  
x210



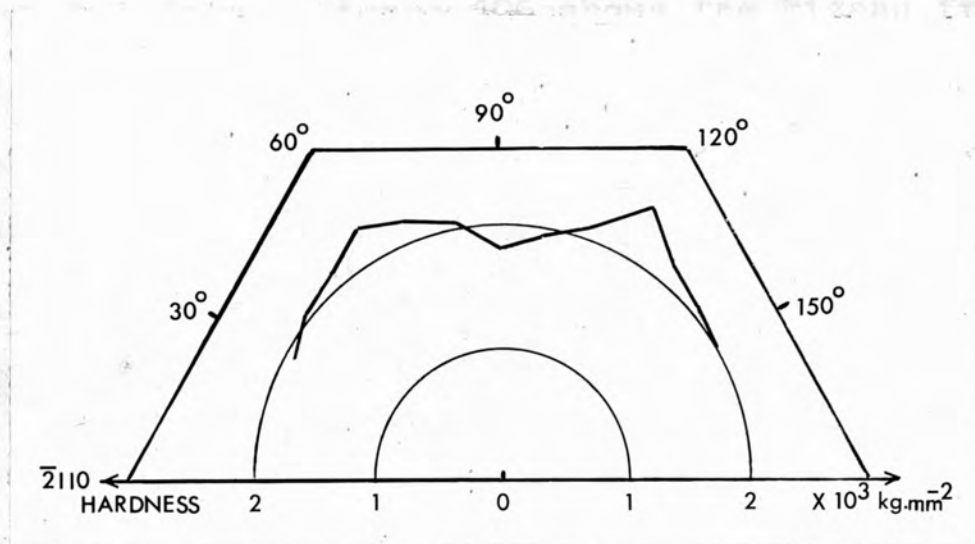


FIG.107

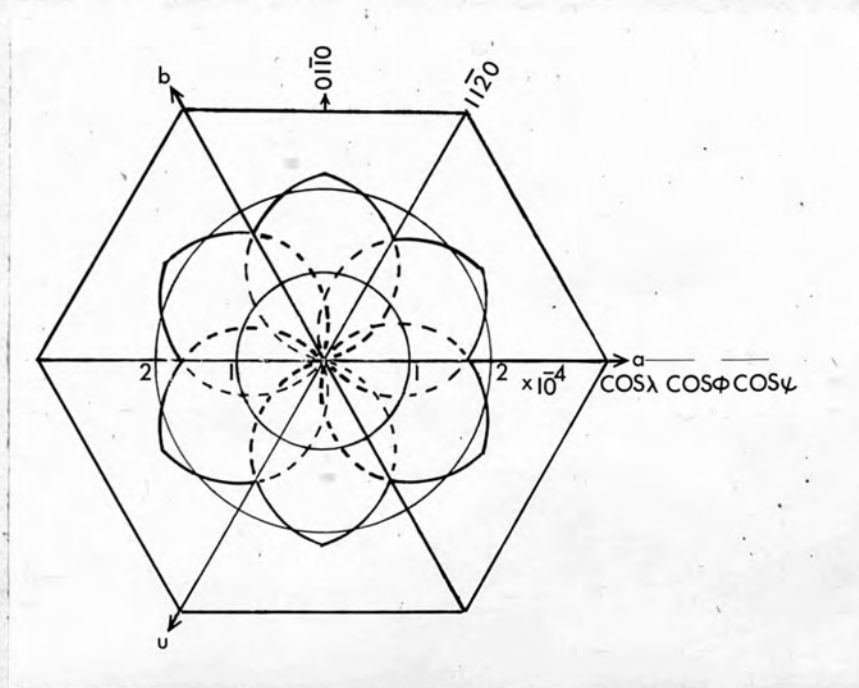


FIG.108

same; the radial distance from the centre in the graph gives the hardness value corresponding to that direction of the crystal face. Figure 106 shows the Fizeau fringes obtained on the indentations made parallel (bottom left corner of the figure) and at right angles (top right hand corner of the figure) to a  $[11\bar{2}0]$  direction. The calculated values of hardness in the two directions come out respectively to be 2268 and 1650 Kg/mm.<sup>2</sup>.

TABLE (2) (load 3 kg.)

No.	Angle of d-c indenter with $[\bar{2}110]$ direc.	Length of indent(d) in mm. x24	Hardness kg/mm. <sup>2</sup>
1	30	3.9	1922
2	40	3.85	2012
3	50	3.8	2093
4	60 $[\bar{1}2\bar{1}0]$	3.7	2268
5	70	3.75	2179
6	80	3.8	2093
7	90	4.0	1795
8	100	3.9	1922
9	110	3.8	2093
10	120 $[11\bar{2}0]$	3.6	2462
11	130	3.75	2179
12	140	3.8	2093
13	150	3.85	2012



### Discussion of the results

(1) As has been stated earlier, the Vickers pyramid indentations do reveal qualitatively the directional variation in hardness by the change in shape of the indentations but quantitatively they do not show any variation in hardness. X-ray analysis showed that the crystal (crystal 3) on which Vickers indentations were made is of  $\alpha$ -SiC II type 6H.

(2) In the case of very shining SiC crystals, it has been noted that the hardness variation shows a two-fold symmetry as seen by the polar graph (figure 97). The graph shows that the crystal has maximum hardness in  $[11\bar{2}0]$  direction and minimum hardness at  $40^\circ$  to this direction on one side and  $20^\circ$  on the other side. An X-ray analysis shows this crystal (crystal 1) to be of type 6H with a strong component of  $\alpha$ -SiC I 15R rhombohedral type; therefore one would expect the hardness variation to show a six-fold or a three-fold symmetry. Since a large number of crystals have shown observations of this type, it is difficult to rule them out completely. It may however, be stated that X-ray diffraction methods do not reveal completely information about the very outer layer of atoms, where the strain related to surface tension produces some variation in spacing of atomic planes. Perhaps this could be the reason for the above observations.

(3) A large number of well formed crystals which in general were not very shining gave hardness variation as shown in the graph figure 107. An X-ray analysis showed that the crystal (crystal 2) whose observations are given, is of hexagonal  $\alpha$  - SiC II 6H type. The polar graph shows clearly that the maximum value of hardness is along  $[11\bar{2}0]$  directions which happen to be the closed packed directions for hexagonal crystals. The line of argument followed by Daniel and Dunn (1949) and Tolansky and Williams (1955) can be extended to interpret these results. Daniel and Dunn assumed that the force exerted by the Knoop indenter was acting parallel to the line of greatest slope of the facet of the indenter. Based on this assumption they calculated the resolved shear stress on the slip plane along the slip direction and found that the reciprocal of the hardness value and the calculated shear stress for different orientations of the indenter were in fair agreement for all planes of silicon ferrite and zinc except the (0001) plane of zinc. Mebs in a written discussion suggested that each facet of the indenter produced a compressive stress in a direction normal to the contact plane. Tolansky and Williams, using a d-c indenter, found close agreement between the reciprocal of the hardness value and the shear stress when the force direction is taken normal to the faces of the indenter.

## Resolved Shear Stress

The deformation of a crystal surface can be considered as the result of compression of a number of very small cylinders parallel to the deforming force  $F$ , each cylinder tending to elongate towards the surface.  $F$  is assumed to act at right angles to the cone face. The direction  $H$  (figures 109 a & b) is parallel to the length of the indenter and at right angles to  $F$ .  $SP_n$  is the normal to the slip plane  $SP$  of which  $SD$  is the slip direction lying in the slip plane.  $AR$  is drawn perpendicular to  $SD$  in the slip plane.  $\phi$  is the angle between  $F$  and the normal to the plane  $SP_n$ ;  $\lambda$  is the angle between  $F$  and the slip direction  $SD$ ; and  $\psi$  is the angle between  $AR$  and  $H$ . It can be shown that the resolved component of the force  $F$  in the slip plane along the slip direction is  $F/A \cdot \cos \lambda \cos \phi$ , where  $A$  is the cross-sectional area of the cylinder. Daniel and Dunn introduced a factor in this to account for effects due to constraints.

Constraints modify the tendency to slip according to the position of the axis of rotation of the slip plane. As each cylinder elongates by slip and lattice rotation, the cross-sectional area must reduce and change from a circular to an elliptical shape. A particular slip plane will tend to rotate about an axis  $AR$  in the slip plane  $SP$  and perpendicular to the slip direction  $SD$ . Due to



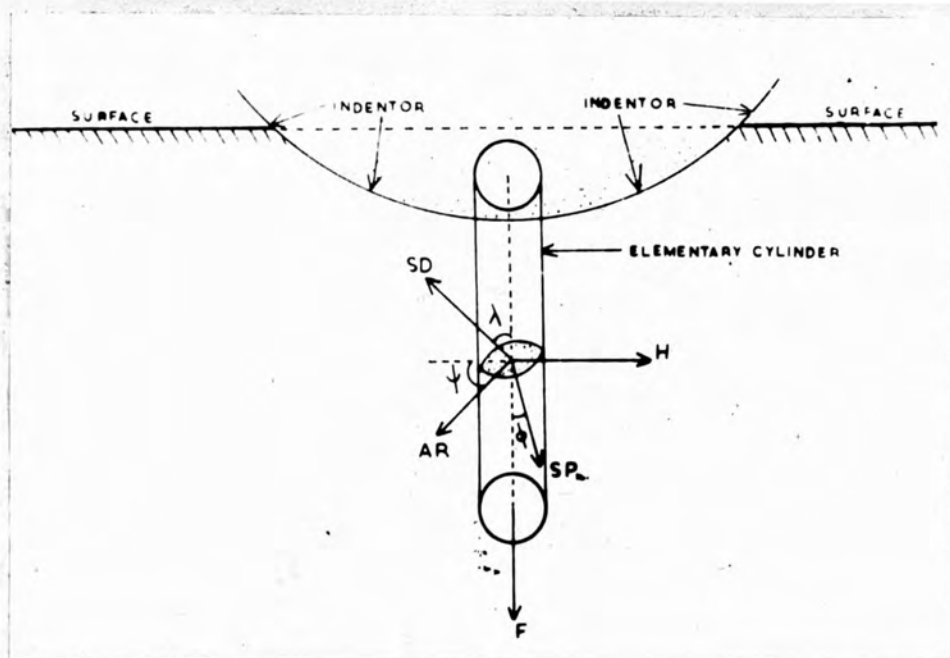


FIG.109

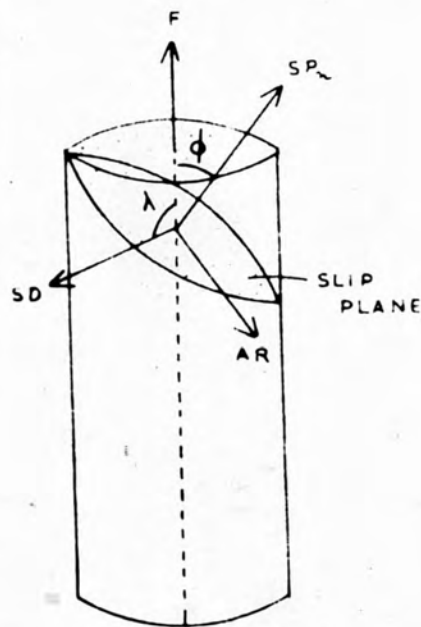


FIG.110

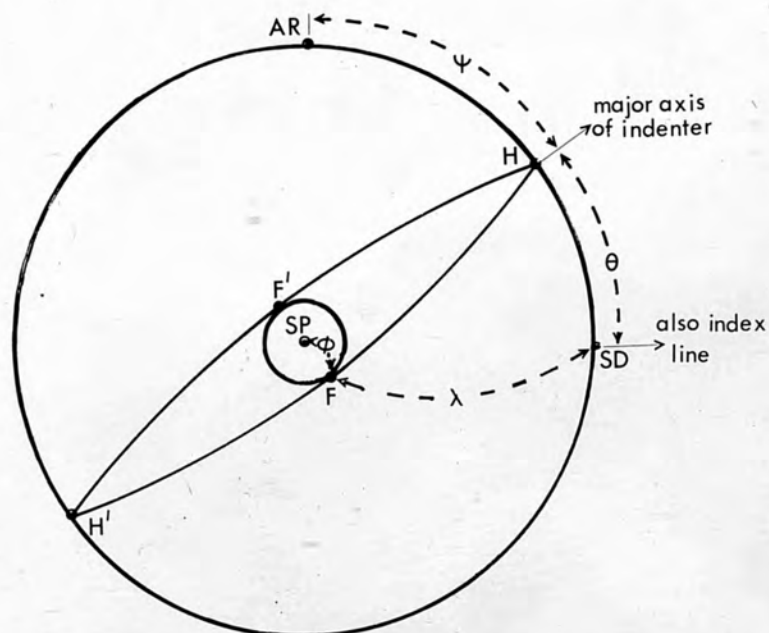


FIG.111

constraints, the force  $F$  has a maximum rotational effect about an axis  $H$  perpendicular to  $F$  and parallel to the length of the indenter. The larger the angle (between the two axes  $AR$  and  $H$ ), the lesser will be the resolved shear effective in promoting deformation. A modifying function which would decrease the resolved shear as  $\psi$  increases from 0 to 90 degrees, is  $\cos \psi$ . Therefore the effective resolved shear stress, after allowing for constraints, becomes

$$E.R.S. = F/A \cdot \cos \lambda \cdot \cos \phi \cdot \cos \psi .$$

The value of  $\cos \lambda \cdot \cos \phi \cdot \cos \psi$  varies as the angle  $\theta$  between the major axis of the d-c indenter and an index line on the crystal face changes. Since the load is the same  $F/A$  is constant. The angles  $\lambda$ ,  $\phi$  and  $\psi$  for each position of the indenter have been measured by drawing a stereographic projection (figure 111) of the crystal and the indenter using the (0001) plane of the crystal as the plane of projection. The measurement was done with the help of a Wulff net. The angle of the d-c indenter in the width direction is  $154^\circ$ , so the angle between  $F$  and  $F'$  directions is  $26^\circ$ . It means that as the indenter rotates  $F$  and  $F'$  move along the circumference of a circle with the centre of projection as its centre and radius equivalent to  $13^\circ$  on the Wulff net. The angle of the indenter along the major axis is  $177^\circ$  (from the measurement of fringes), so there will

be a negligible error if the ends of the major axis Hand H', are taken at the ends of the diameter of the projection. For the purpose of calculation the initial position of the major axis of the indenter is taken normal to one of the slip directions  $[11\bar{2}0]$  so that initially AR is along that particular slip direction. The angles  $\lambda$ ,  $\phi$  and  $\psi$  were measured for every  $10^\circ$  rotation of HH' and FF'. Table (3) gives the observations and also the mean value of  $\cos \lambda \cos \phi \cos \psi$  calculated from the positions of F and F'. It may be stated that the slip plane for hexagonal crystals is the crystal plane (0001) itself.

Since there are six slip directions in this case each one will give similar observations. Figure 108 is a polar graph showing the variation of E.R.S with different orientations of the d-c indenter, for all the slip directions. If two slip directions give values for E.R.S for a particular position of the indenter, then it is assumed that the slip direction giving a higher value of E.R.S. (shown by continuous line) is effective to bring about plastic deformation and not the one giving a lesser value (shown by dotted line). In this way it is seen in the figure that E.R.S. is maximum in the  $[01\bar{1}0]$  directions and gradually acquires a minimum value along  $[11\bar{2}0]$  directions. If this is compared with figure 107, it is noticed that the directions  $[01\bar{1}0]$  for which E.R.S.



is maximum are also the directions of minimum hardness; and the directions  $[11\bar{2}0]$  of minimum E.R.S. values are the directions of maximum hardness. This explanation is based on the assumption that a large indentation accompanies high resolved shear on the slip planes.

Considering that factors such as twinning, work-hardening and friction have not been taken into account in this explanation, the agreement between theory and experiment is fairly satisfactory.

TABLE (3)

No.	$\theta$ in deg. from a $[11\bar{2}0]$ direction	$\lambda_F$ in deg.	$\lambda_{F'}$	$\psi$	mean $\lambda$	$\cos \phi \cdot \cos \lambda$ ( $\phi_F = \phi_{F'} = 13^\circ$ )
1	-90	77	77	0	77	0.2192
2	-80	78	78	10	78	0.1995
3	-70	78 40'	78 16'	20	78 28'	0.1826
4	-60	79	79	30	79	0.1610
5	-50	80 16'	80	40	80 8'	0.1287
6	-40	82	82	50	82	0.0871
7	-30	84	83 48'	60	83 54'	0.0517
8	-20	85 48'	86	70	85 54'	0.0238
9	-10	87 30'	88	80	87 45'	0.0067
10	0	90	89 48'	90	89 54'	0.0000
11	10	87 46'	87 30'	80	87 38'	0.0070
12	20	86	85 30'	70	85 45'	0.0252
13	30	83 45'	84	60	83 53'	0.0593
14	40	82	82	50	82	0.0871
15	50	80 10'	80 10'	40	80 10'	0.1283
16	60	79 20'	79 10'	30	79 15'	0.1588
17	70	78 15'	78 30'	20	78 23'	0.1880
18	80	78	78	10	78	0.1995
19	90	77	77	0	77	0.2192

CHAPTER X

INTERFEROMETRIC STUDY OF RING CRACKS ON SILICON CARBIDE

Introduction

According to Hertz (1881) hardness is essentially related to the irreversible phenomena occurring when the elastic limit of the material is exceeded in any part of the applied stress system. This concept of hardness is very useful in the case of brittle materials where the irreversibility occurs suddenly in the form of fracture. His criterion for the hardness of a body is that it is measured by "the least value of the (central) pressure per unit area necessary to produce permanent set (or rupture) at the centre of the impressed surface." In other words he reduces hardness to a quality of elasticity; that is he measured hardness by the force just necessary to produce the initial permanent deformation.

Hertz considered the deformation of an 'ideal' plastic material of yield stress  $Y$ , by a hard spherical indenter of radius  $r$ . When a load  $W$  is applied to the indenter, the material and the indenter will both deform elastically and the region of contact is a circle of radius  $a$ , given by

$$a = \left\{ \frac{3}{4} Wgr \left( \frac{1-\sigma_1^2}{E_1} + \frac{1-\sigma_2^2}{E_2} \right) \right\}^{1/3} \quad (1)$$

where  $E_1$  and  $E_2$  are Young's moduli of the indenter and the material respectively and  $\sigma_1$  and  $\sigma_2$  are the corres-

ponding values of Poisson's ratio. The average pressure ( $P_m$ ) and the maximum pressure ( $P_o$ ) at the centre of the circle are given by

$$P_m = \frac{Wg}{\pi a^2}$$

$$P_o = \frac{3}{2} P_m$$

Applying the Tresca or Huber-Mises criterion to the stresses in the material it can be shown (1934,1949) that the shear stress is maximum at a point about  $0.5a$  below the centre of the circle of contact. For materials with Poisson's ratio  $\sigma = 0.3$  it has a value of  $0.47P_m$ . Since at the point of maximum shear stress the two radial stresses are equal, the Tresca and the Huber-Mises criterion both indicate that plastic flow will occur when the shear stress equals  $1/2 Y$ ; that is when  $0.47P_m = 0.5 Y$ . This means that plastic deformation commences at this region when  $P_m \approx 1.1Y$ . The maximum tensile stress is at the perimeter of the circle of contact and is given by

$$\text{Maximum Tensile Stress(M.T.S.)} = \frac{1-2\sigma}{3} P_o.$$

In brittle materials fracture or cracks are caused by these tensile stresses which decrease least rapidly in a downward direction from the plane surface and away from the region of contact. This decrease in the tensile stress from its maximum value at the perimeter of the circle of contact, is along a conical surface, frequently called a Hertzian cone. Preston (1921) and



Bailey (1937) have made studies on these ring cracks. It has been shown by sectioning that a circular crack has a conical split in depth. Bailey, without reporting specific measurements, proposed schematically a section as illustrated in figure 112 and also considers that severe strains arise due to lodgement of particles in the open cracks. Raman (1926) examined percussion figures interferometrically. The surface distortions accompanying such ring cracks have been studied by Tolansky and Howes (1955) in the case of glass and diamond.

#### Present Work

In this chapter the ring cracks formed by steady pressure made by a diamond ball on silicon carbide crystals are described. The distortions round the cracks and the profiles of sections through their diameters, are studied by multiple-beam interferometry. Steady pressures were applied to the (0001) plane of the crystals using a diamond ball of radius 0.39 mm. The crystal specimen was mounted on a duraluminium cylindrical block which just fitted into the collet of the hardness tester, the description of which has already been given. While mounting it was ensured that the (0001) plane of the crystal was horizontal to the vertical axis of the cylinder. This was done by viewing the image of a lamp reflected from the surface of the crystal and placing the cylinder on a glass plate from which the

image was also reflected. The crystal surface was assumed to be horizontal when the two images appeared to be at the same angle. The cylinder, with the specimen, was inserted in the collet of the hardness tester and firmly fixed in the holder by tightening the milled ring. The collet was then introduced into the V slideway and locked with the aid of a clamp screw. By adjusting the counterweight on the screw spindle, the beam was balanced to the position when it just made an electrical contact, which could be seen by the flickering of the indicator lamp. The load selected was then placed on the circular plate so that the centre of the load was immediately over the centre of the diamond ball. The diamond ball, which was mounted like the diamond indenter objective, was put in the magnetic chuck of the illuminator box of the microscope. Before making the impact the surface of the crystal was seen through an 8 mm objective.

The stage of the microscope was lowered by the coarse motion mechanism until the surface of the crystal approached the diamond ball. Then with the help of the fine motion screw the ball was raised until it made a contact with the surface of the crystal and lifted it sufficiently. This took place when the red light was extinguished due to a break in the electrical contact. The movement of the diamond ball when the impact was made, was kept at about 10 microns per sec. The period of

impact was 15 seconds. By reversing the fine motion screw the ball was then separated from the crystal surface.

Impacts made with loads of 1 kg and below did not give any visible ring cracks. A load of 2 kg gave a primary crack and 3,4 and 5 kg loads gave rise to multiple ring cracks. Loads above 5 kg, when applied, shattered the surface of the crystal. After making the impacts the crystal surfaces were silvered by vacuum deposition. The cracks were examined by phase-contrast microscopy and then by matching them with a silvered flat, Fizeau and FECO fringes were obtained on the ring cracks, which permitted an examination of surface distortions to be made.

#### Observations

Figure 113 is a phase-contrast picture of a ring crack obtained when a load of 2 kg was applied. All the phase-contrast pictures were taken with the Olympus Microscope; positive phase-contrast was used for taking these pictures. Figure 114 represents the Fizeau fringes obtained on two ring cracks, dispersion being arranged such that a fringe passes across a diameter of each crack. The Fizeau fringes are not linear profiles, but are mixed patterns determined both by the profile section and by the circular shape of the cracks. To obtain linear profiles of the cracks it is advantageous to use precision fringes of equal chromatic order.



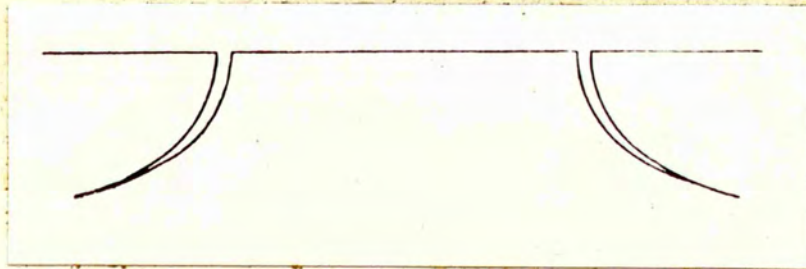


FIG.112



FIG.113  
x1400

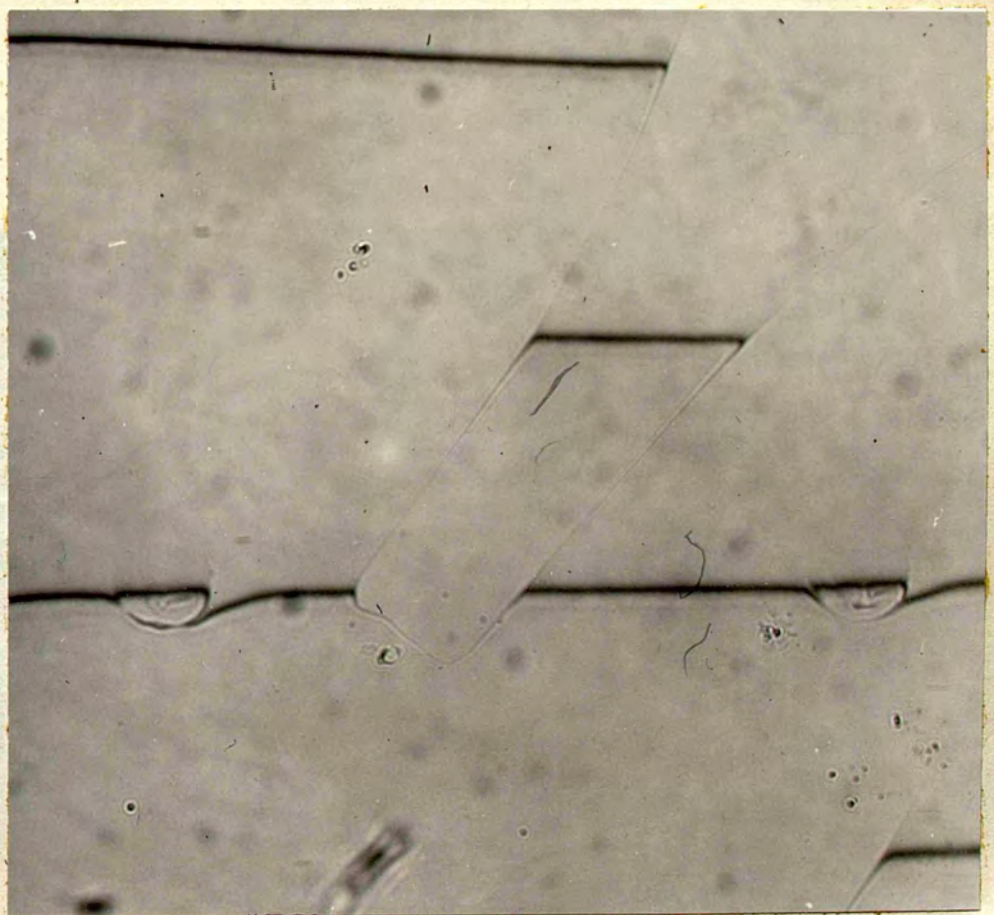


FIG.114  
x250





FIG.115

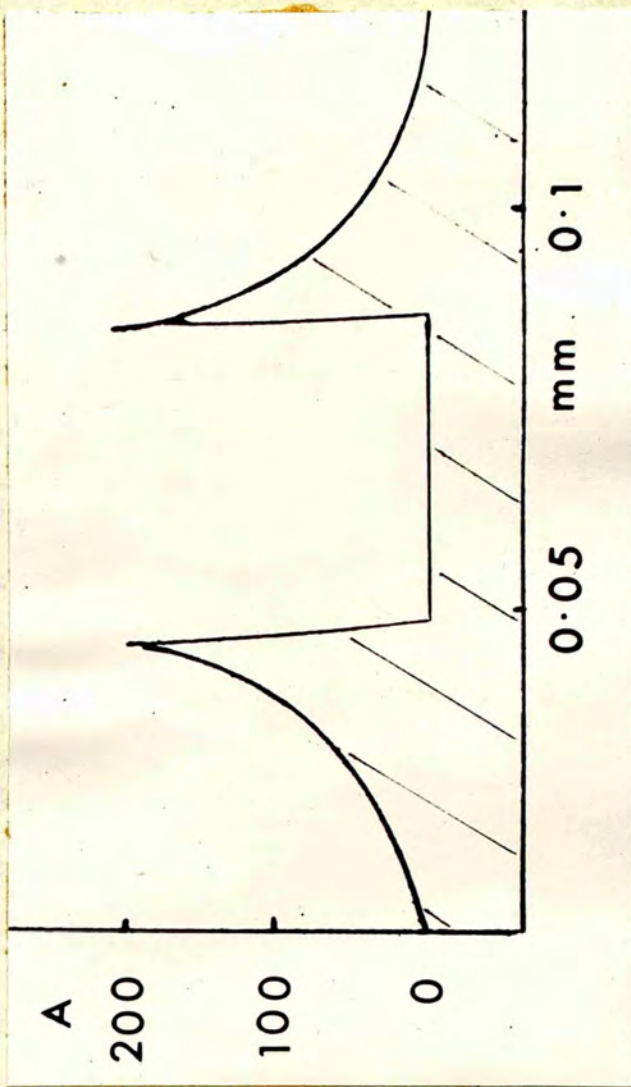


FIG.116

Figure 115 shows these fringes obtained on the same ring crack across a diameter; the photograph shown has been magnified many times. The fringes have been obtained with quite a high dispersion. The interferogram has been calibrated using the chromatic dispersion of the spectrograph. For comparison with Fizeau fringes the white light fringes have been placed with chromatic dispersion vertical so that they act as topographical sectionings. Figure 116 is a scale drawing of figure 115 giving an exact vertical section through the ring crack.

The following information about the ring crack can be obtained from the white light fringes. The ring crack is single. It is almost circular having a ring of radius 0.023 mm. The central area of the crack is flat. The fringe shows that there is a smooth steep rise upto 200 Å, as the ring crack is approached from the left; on reaching the crack there is an abrupt fall to the same level as the undisturbed surface of the crystal away from the crack. If this level is called the zero level then the entire area inside the ring crack is at zero level. On the right side of the crack an equal rise is indicated. The "circular" crack shows slight indications of a octagonal character.

Figure 117 shows the multiple ring crack obtained when a load of 3 kg was applied. Figure 118 shows the Fizeau fringe pattern on the same. The white light



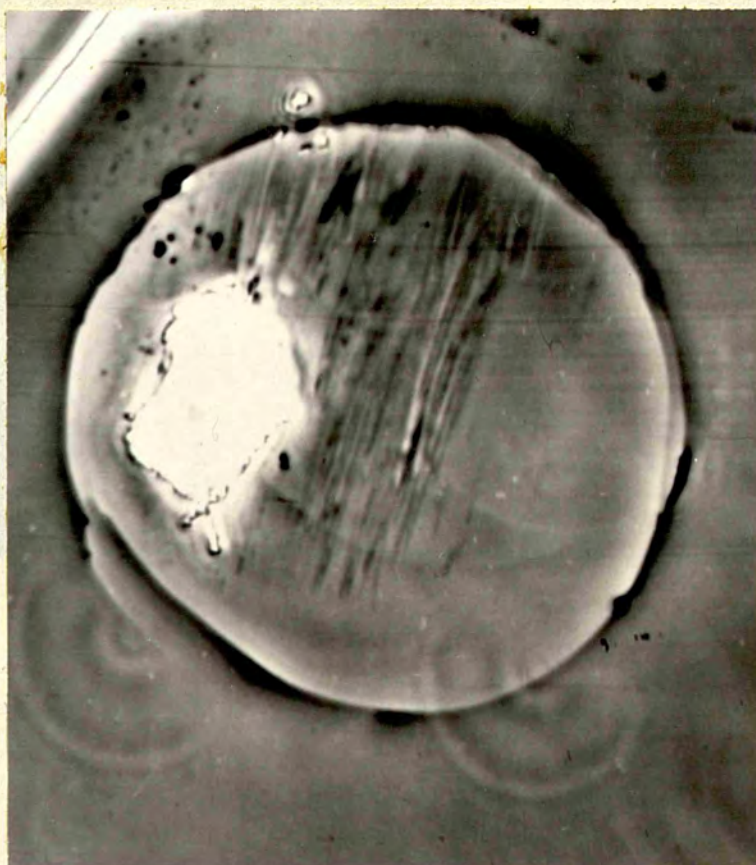


FIG.117  
x1200

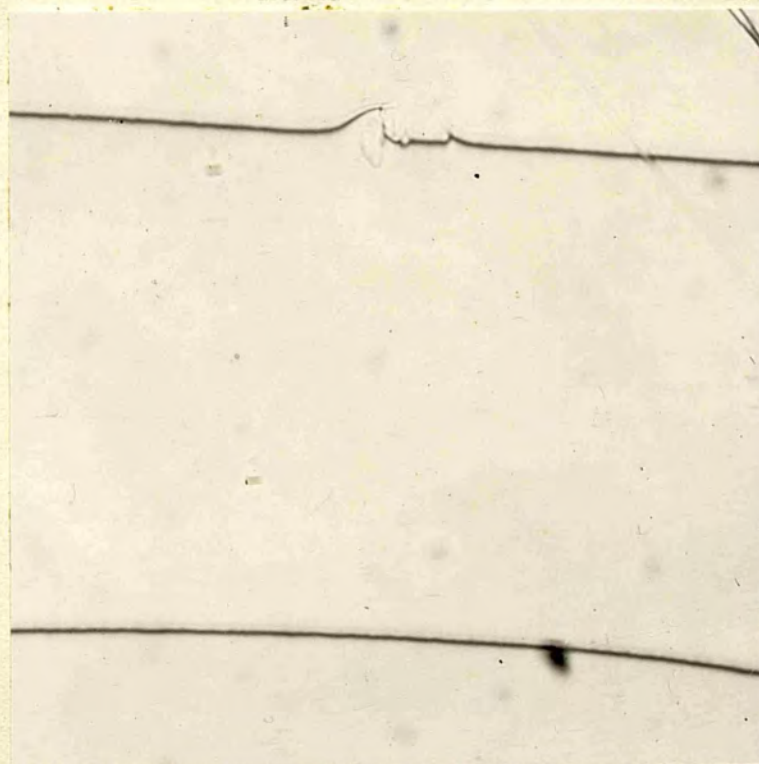


FIG.118  
x250



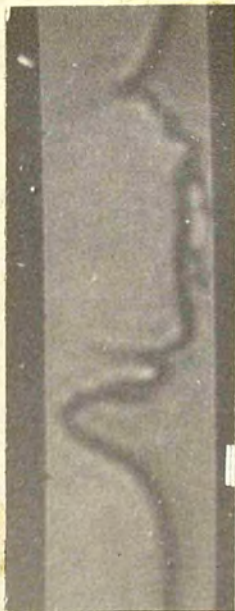


FIG. 119b

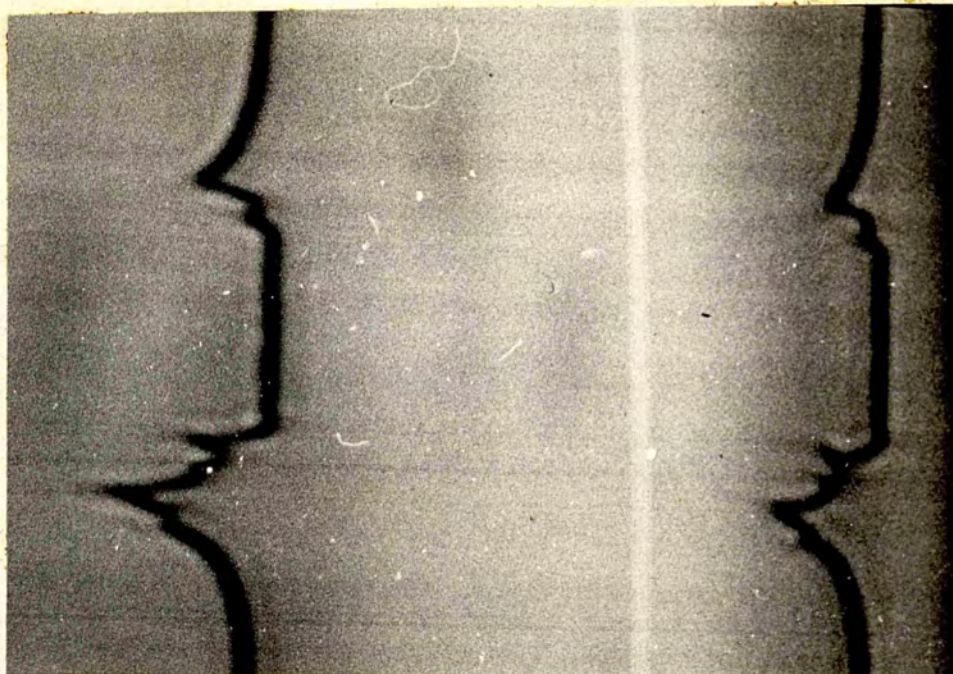


FIG. 119a

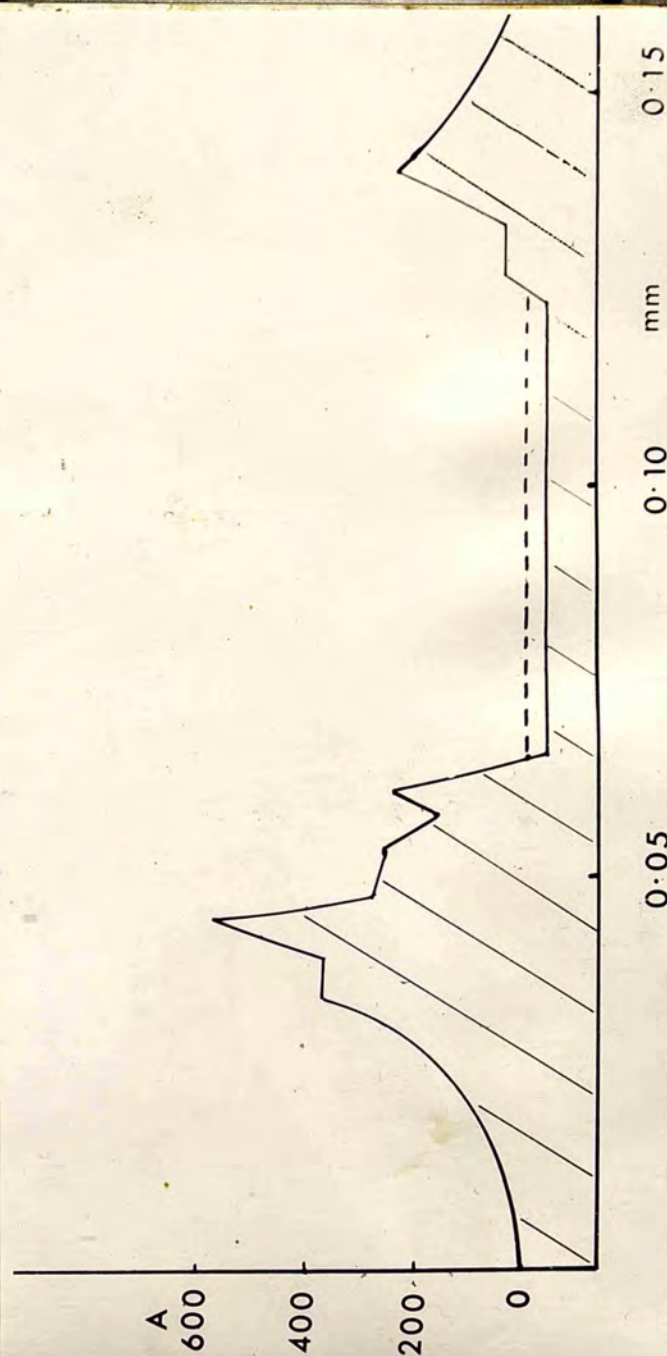


FIG. 120

fringes across a diameter of the ring crack are seen in figure 119a of which figure 119b is the fringe due to mercury green. It shows that on the left side of the ring crack there are two major and two minor cracks and on its right side one major and one minor crack. The area within the crack is flat. Figure 120 is a scale drawing of fig.(119a). On approaching the ring crack from the undisturbed region on the left, the surface exhibits a smooth slope up of 600 Å preceded by a minor crack. A similar distortion, though to a lesser extent, is observed on the right side of the ring crack. The photograph of the ring crack is not able to show this assymetry in the displacement of the material but the Fizeau fringes are still more the white light fringes show very clearly the nature of the cracks and the assymetry in the amounts of the displaced material on the sides of the ring crack. In this ring crack the flat area within the crack is 30 Å below the outside undisturbed surface of the crystal. Again the "circular" crack shows some octagonal character.

Figure 121 is the phase-contrast photograph of a multiple ring crack with a load of 4 kg. The right half of the figure is almost a semi-circle but the left half simulates half an octagon. Figures 122 and 123 are the Fizeau and the white light fringes on the same. Figure 124 is a scale diagram of figure 123. In this



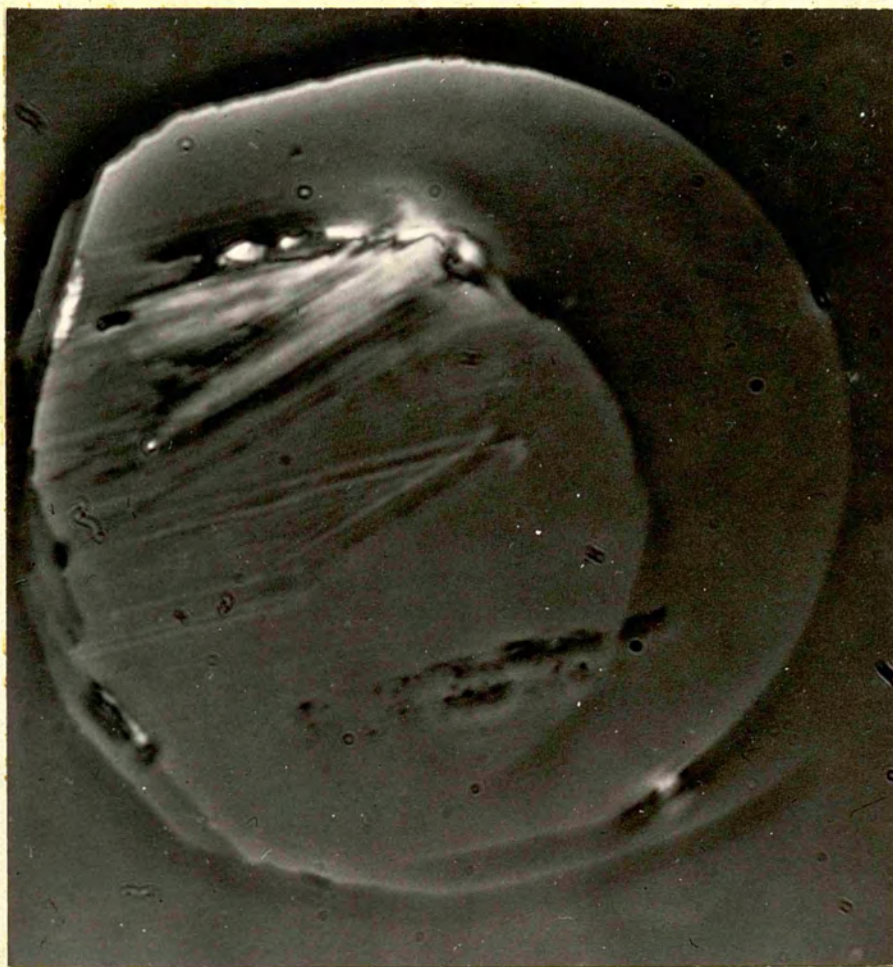


FIG.121  
xl400

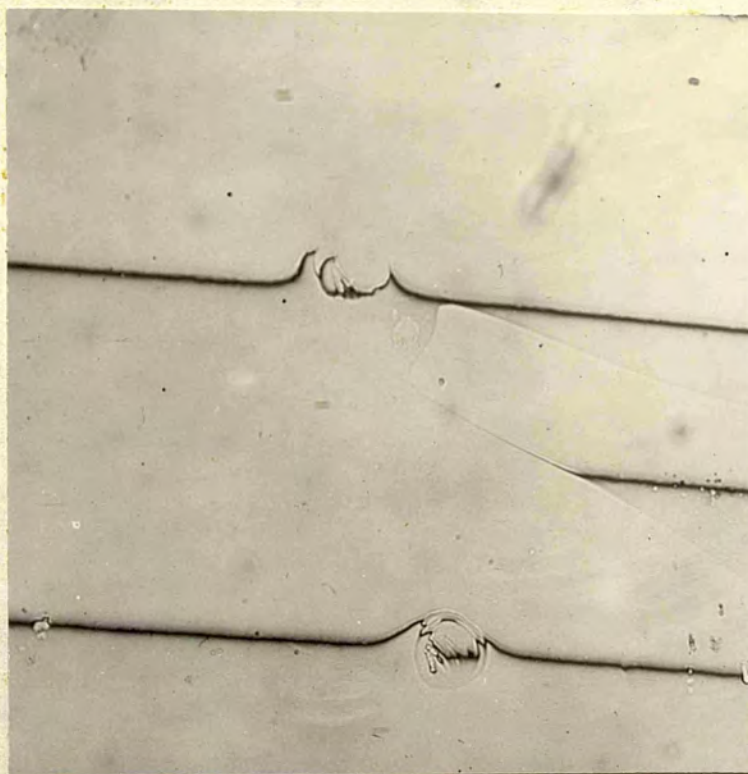


FIG.122  
xl50



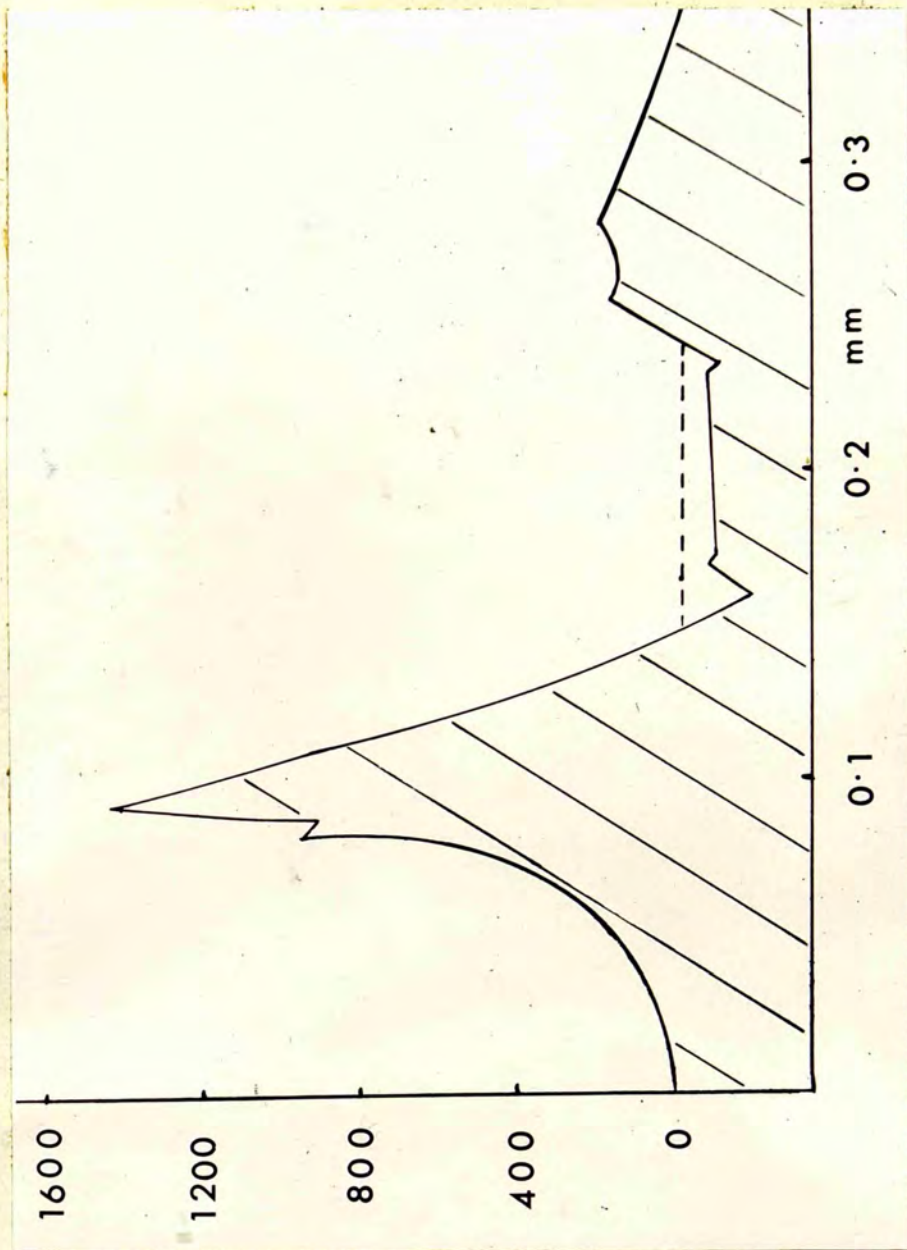


FIG.124

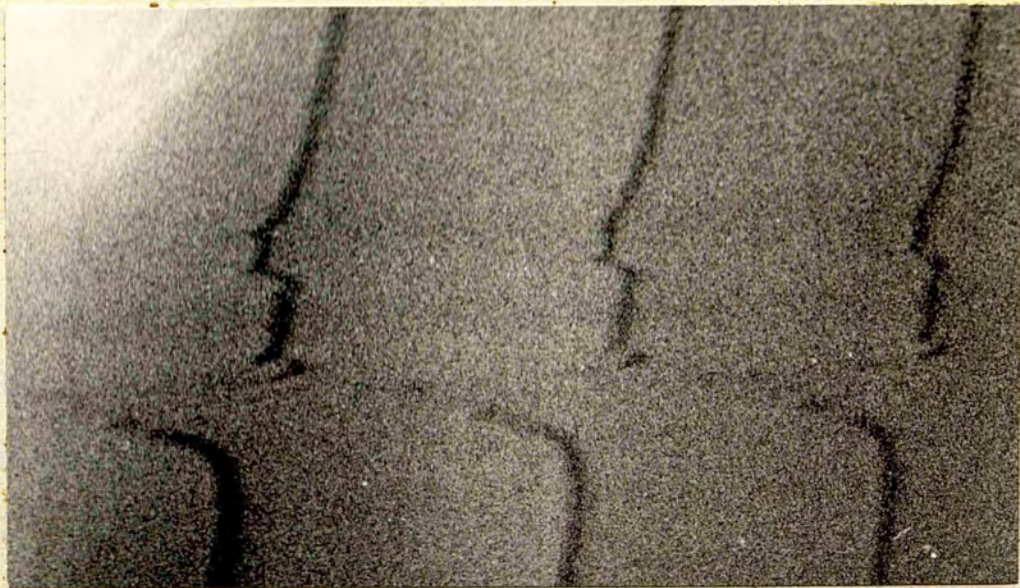


FIG.123

case on the left side of the ring crack there is a major crack and two minor cracks. The maximum slope up as the ring crack is approached from the left is 1500 Å preceded by a minor crack. The displacement of the material on the right side of the ring crack is much less. The area within the ring crack is still flat but on either side of the flat area there is a crack which goes below the level of the flat area, which itself is 50 Å below the undisturbed level of the crystal surface. The left and right end-cracks are respectively 160 Å and 80 Å below the undisturbed level.

Figure 125 is a multiple crack obtained when a load of 5 kg is applied while impacting the surface with the diamond ball. Figures 126 and 127 are the Fizeau and FECO fringes on the same. Figure 128 is a scale diagram of figure 127 corrected for the inclination of the fringe system. The slope up of material on the left side of the ring crack in this case is 1650 Å from the undisturbed level; the slope up is again preceded by a minor crack, there being a major and minor crack on this side. On the right side, the slope up of material is nearly the same as on the left side of the ring crack but there are two major cracks and one minor crack. A point to be noted is that the area within the ring crack is no longer flat. It is curved and depressed at the ends to the extent of 180 Å on the left side and 230 Å on



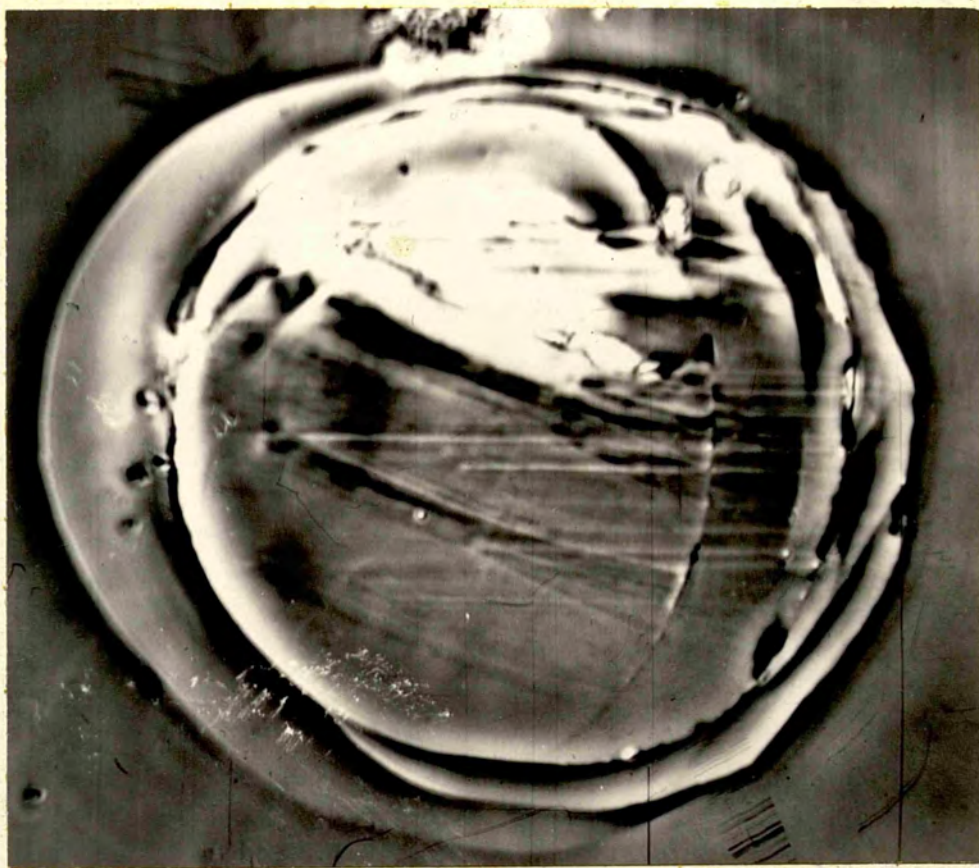


FIG.125  
x1200

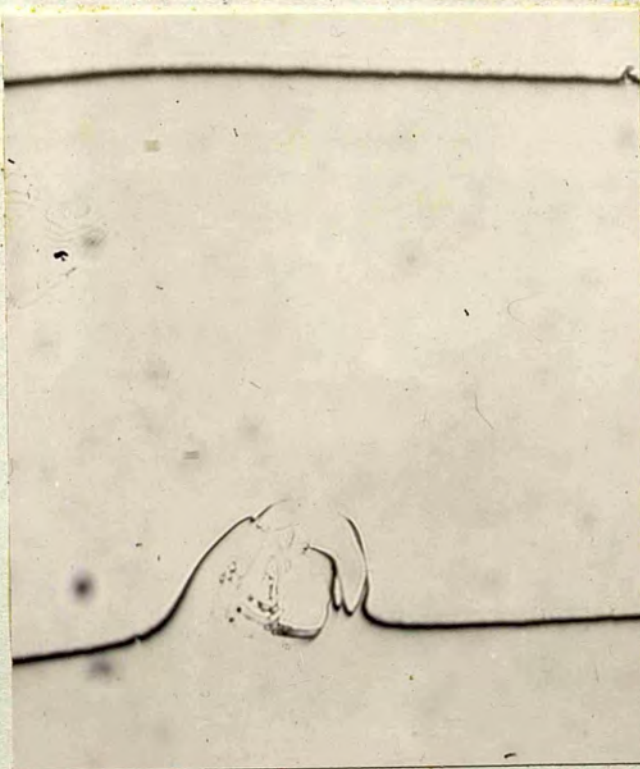


FIG.126  
x250



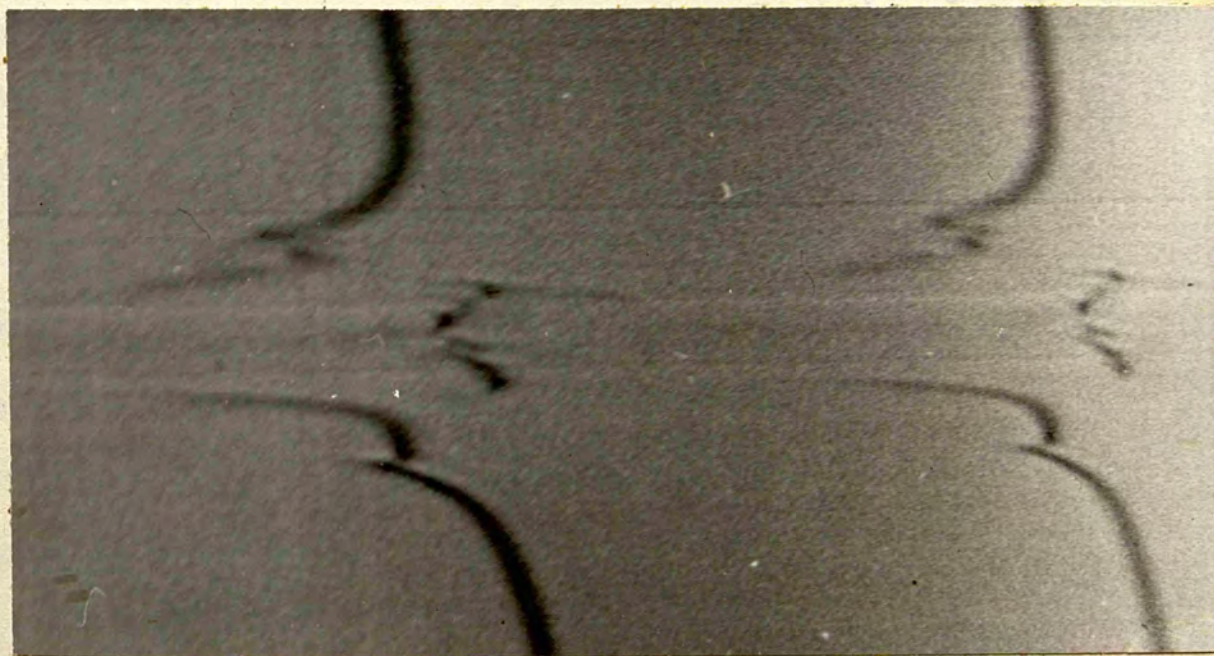


FIG.127

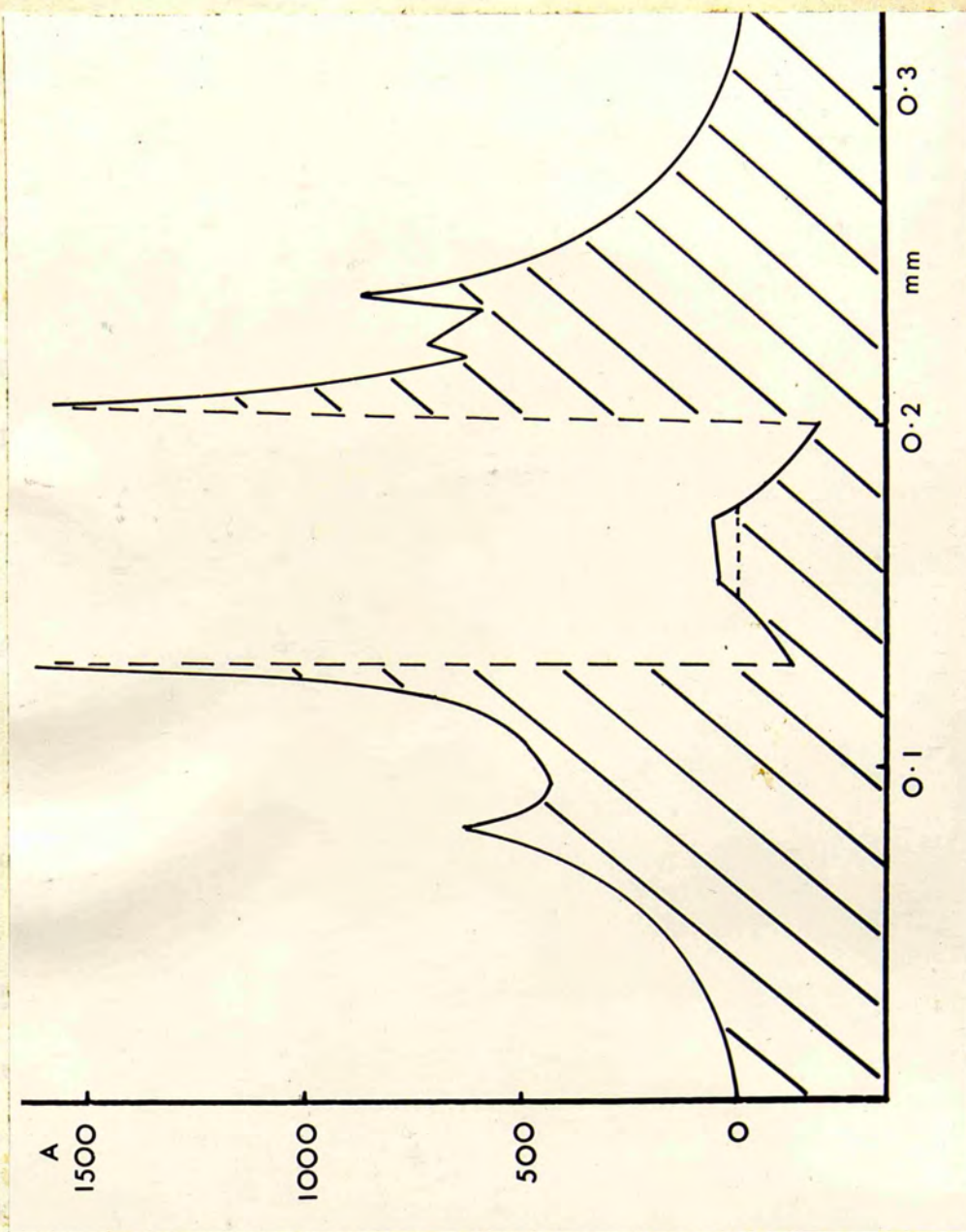


FIG.128

the right side. In fact the centre of this area is 70 Å above the zero level. Figure 129 shows the Fizeau fringes taken on this ring crack to detect the surface distortions around it; figure 130 shows the white light fringes on the same area. Figure 131 is the scale diagram of figure 130 from which it is easy to see that the pile up in that region is 600 Å and that it is smooth.

In all the ring cracks there is a sharp discontinuity at the actual crack, the level drops abruptly inside, while there is a smooth decline away from the crack towards the undisturbed level with a minor crack within this smooth decline for loads of 3,4 and 5 kg. This observation is similar to the one found in glass and diamond by Tolansky and Howes (1954,1955) except for the occurrence of a minor crack within the smooth decline in the case of silicon carbide.

As a matter of interest, the radius of the circle of contact was calculated by using Hertz's classical equation (1). Assuming Poisson's ratio to be 0.3 for SiC the equation reduces to

$$a = 1.1 \left\{ \frac{Wgr}{2} \left( \frac{1}{E_1} + \frac{1}{E_2} \right) \right\}^{1/3} \quad (1a)$$

For the diamond ball  $E_1 \approx 10 \times 10^{12}$  dynes/cm<sup>2</sup> and for silicon carbide  $E_2 \approx 4 \times 10^{12}$  dynes/cm<sup>2</sup> (1951). Substituting for the radius of the diamond ball ( $r=0.039$ cm) and taking  $g = 980$  cm/sec<sup>2</sup> equation (1a) works out to

$$a = 2.072 \times 10^{-4} W^{1/3}$$





FIG. 129  
x250



FIG. 130

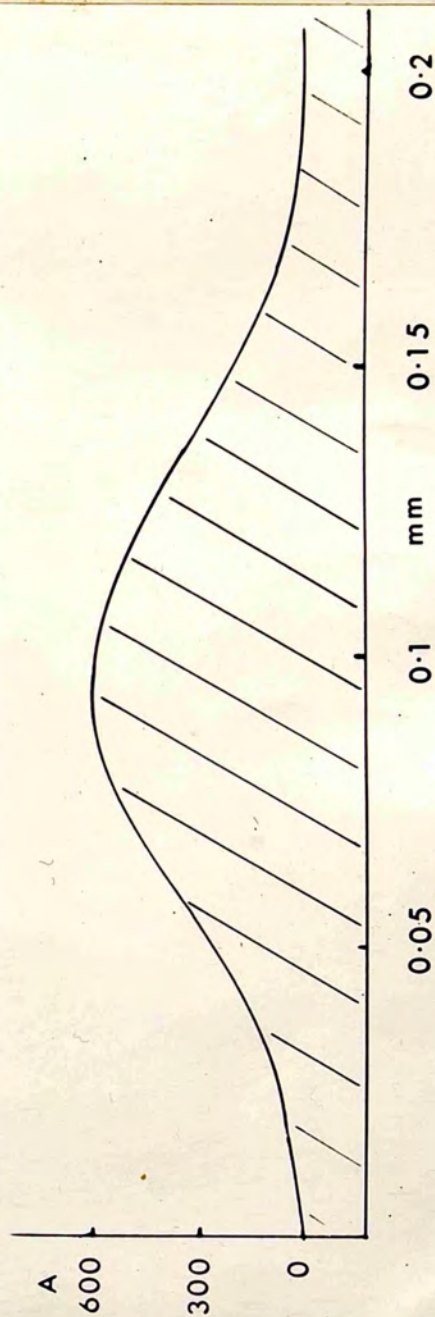


FIG. 131

The following table shows the calculated values of 'a' for different loads (taking  $a=2.0 \times 10^{-4} W^{1/3}$ ) along with measured values. The same table also shows the values of the average pressure ( $P_m$ ), the maximum pressure ( $P_o$ ) and the maximum tensile stress calculated from the measured values of 'a'.

TABLE

Load' in kg.	a(measured)' in mm	a(cal.) in mm	' $P_m \times 10^{-11}$ dynes/cm <sup>2</sup>	' $P_o \times 10^{-11}$ dynes/cm <sup>2</sup>	M.T.S. $\times 10^{-11}$ dynes/cm <sup>2</sup>
2	0.023	0.025	1.14	1.71	0.22
3	0.029	0.028	1.05	1.57	0.20
4	0.033	0.031	1.09	1.63	0.21
5	0.038	0.034	1.04	1.56	0.20

The agreement between the calculated and measured values of 'a' is reasonably good particularly when the values of Young's moduli taken, for diamond and silicon carbide, are not very reliable and also there can be a slight error in the measured value of 'a'.

It should, however, be stated that in Hertz's equation 'a', is the radius of the circle of contact as long as the material is within elastic limits. To get this value of 'a' it is essential to apply only such loads as would deform the material elastically only and 'a' should be measured during the actual contact of the



spherical ball with the surface of the material. In other words 'a' is the radius of the circle of contact before recovery of the impacted surface. In the present observations the area within the ring crack of only 2 kg load has completely recovered after impact; so that it can be said to be within elastic limits of the material. Secondly the measured value of 'a' should normally be greater than the Hertzian value because the observations have been taken after recovery of the material. Thirdly Hertz's equation is true for an 'ideal' plastic material. These factors need to be considered more thoroughly before interpreting the results given in the table.

The Vickers hardness of this specimen is  $1819 \text{ kg/mm}^2$  for a load of 500 gm and X-ray analysis shows that the crystal is  $6H \propto \text{-SiC II type}$ .

#### Discussion of the results

(a) Tolansky and Howes (1955) established that "ring cracks do not automatically run to completion once initiated but require application of pressure for a specified period before completion occurs. It implies that there is some specified single point of initiation from which a crack develops travelling at a finite velocity—this must be some sort of highly localized surface weakness". This perhaps explains why the ring cracks observed on SiC crystals do not have a complete octagonal character. Since the time of impact was kept fixed and



so also the load, the cracks may not have had time to complete into a octagonal shape.

(b) Although glass and diamond have not shown conical split in depth the ring cracks on SiC with loads of 4 and 5 kg, show such splits confirming the conjecture of Bailey (1937).

(c) The average pressure to produce a ring crack with a load of 2 kg. for SiC is  $1.14 \times 10^{11}$  dynes/cm<sup>2</sup>. For a load of 5 kg the value of the same for diamond (1955) was reported to be  $1.4 \times 10^{11}$  dynes/cm<sup>2</sup> (1955) and for the onset of ring crack in glass the average pressure was found to be  $1.4 \times 10^{10}$  dynes/cm<sup>2</sup> (1954).

Diamond ball impacts on the Trigonal pyramid face of SiC crystal

Using the same diamond ball, impacts were made on the rare trigonal pyramid face (1011) of a different SiC crystal with loads of 1, 2 and 3 kg. Higher loads damaged the surface completely. Figure 132 shows the photograph of the cracks taken with a Vickers microscope. Higher magnifications could not be used while photographing the impacted regions as the difference in height between the piled up material and the bottom of the ring cracks was so pronounced that they could not be brought into focus at the same time; for the same reason phase contrast picture 132a does not show the actual area of impact properly. Figures 133, 134, and 135 show the



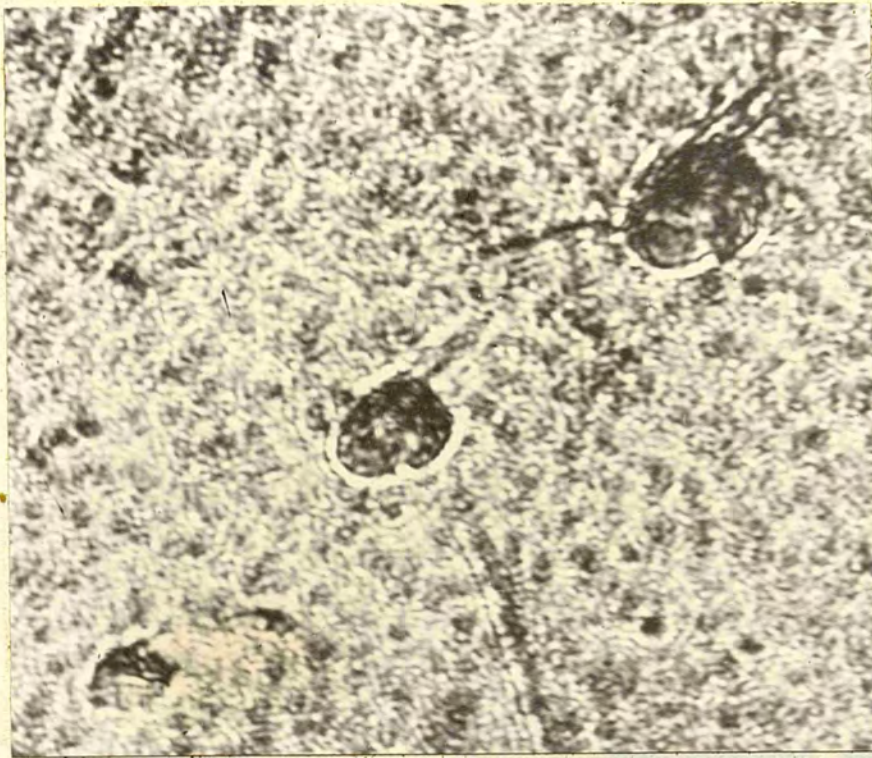


FIG.132  
x180



FIG.132a  
x200



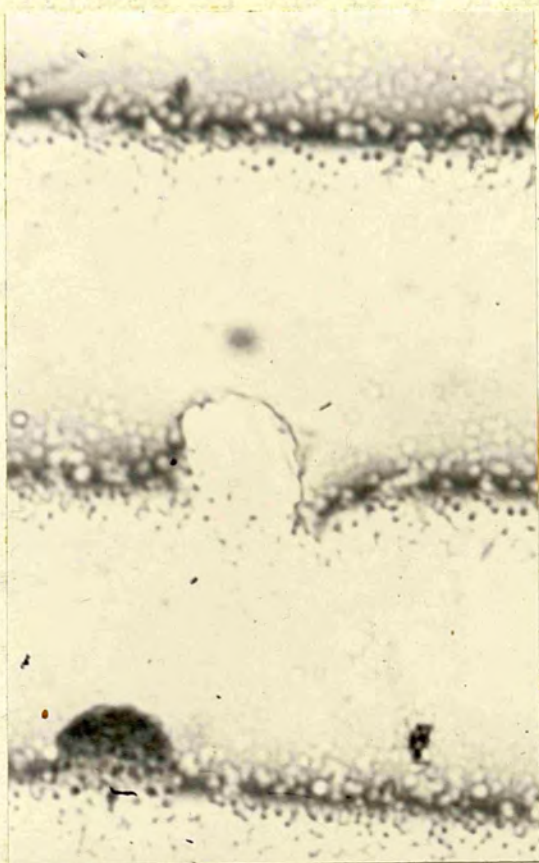


FIG.133  
x360

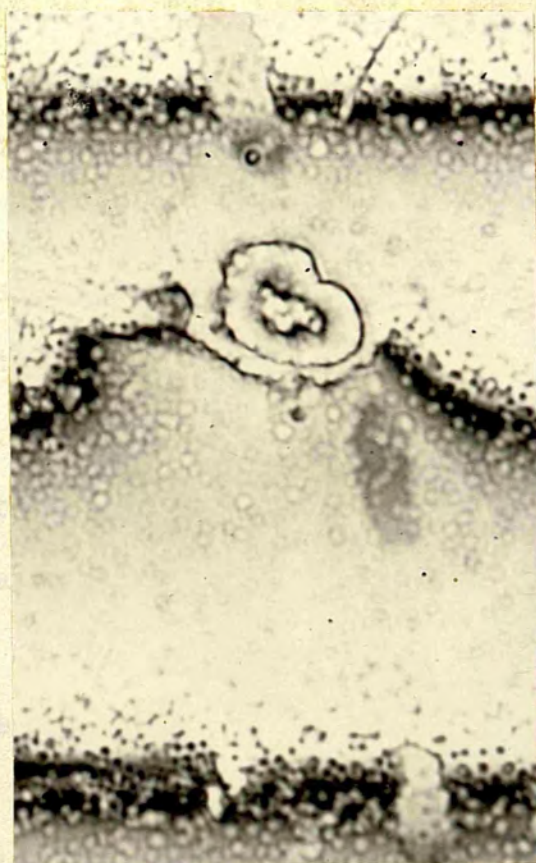


FIG.134  
x360

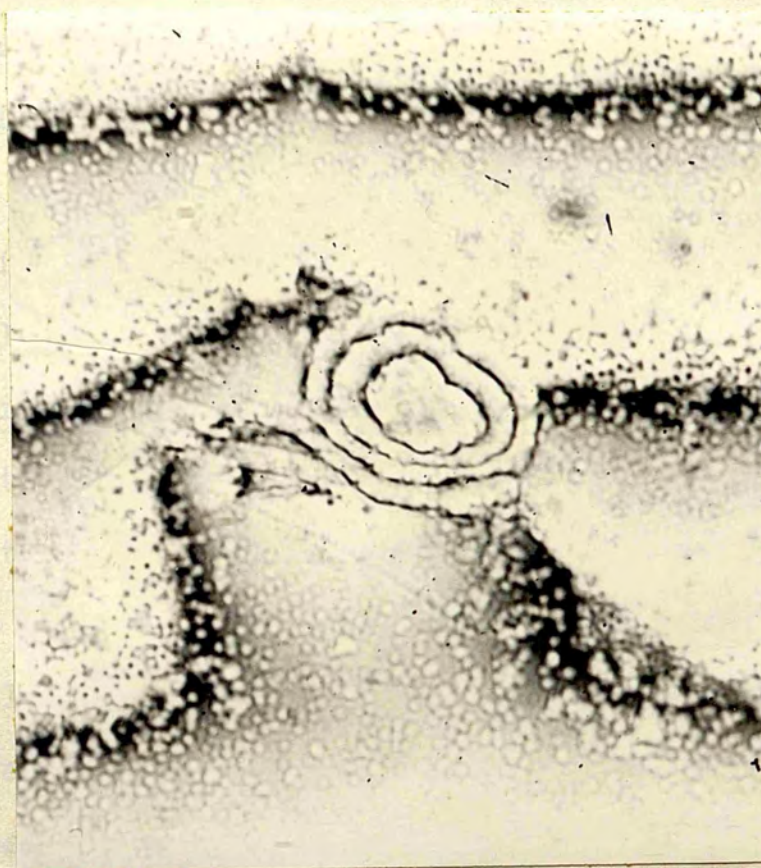


FIG.135  
x360



Fizeau fringes on the ring cracks of loads 1,2 and 3 kg respectively. They show that the surface within the ring cracks is depressed as much as 2 fringes for 2 kg and 3 fringes for 3 kg. and the corresponding rise of material outside the ring cracks is 2200 A and 1500 A. For 1 kg the rise of material outside the ring crack is 700 A.

Figure 136 is a phase contrast picture of the piled up area surrounding the ring crack for the load 1 kg. It shows clearly that there are linear micro-slips which in fact are parallel to the sides of the trigonal pyramid face. Figures 137 and 138 are similar pictures for loads 2 and 3 kg respectively, in which the micro-slip lines become more prominent. Figure 139 shows schematically the shape of the trigonal pyramid face and the orientation of the microslips with respect to it along with the area of impact of the diamond ball. A closer observation of the micro-slip lines shows that the slip lines parallel to AB have appeared first and later the slip lines parallel to BC and AC (side-edge of the basal plane) respectively. The number of slip lines also increases in the same order. Alternately, it maybe that the slip lines parallel to AB have come out of the surface and slip lines parallel to BC and AC have gone into the surface. As interferometry has not revealed any slip steps, the slip lines must be very shallow.



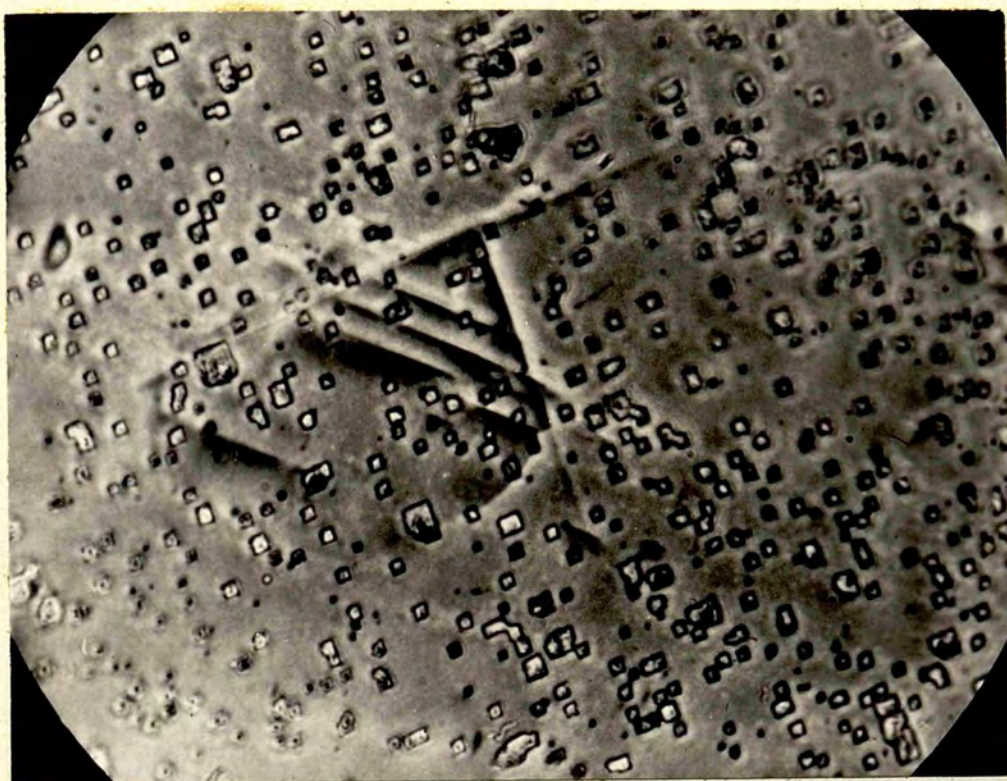


FIG.136  
x800

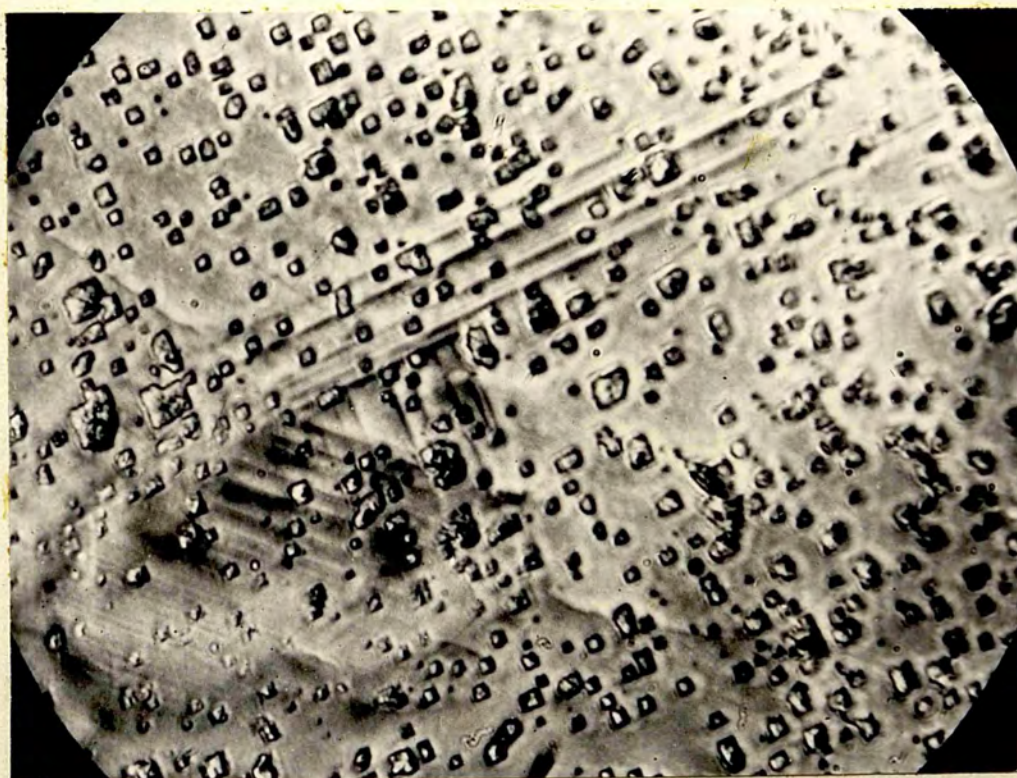


FIG.137  
x800



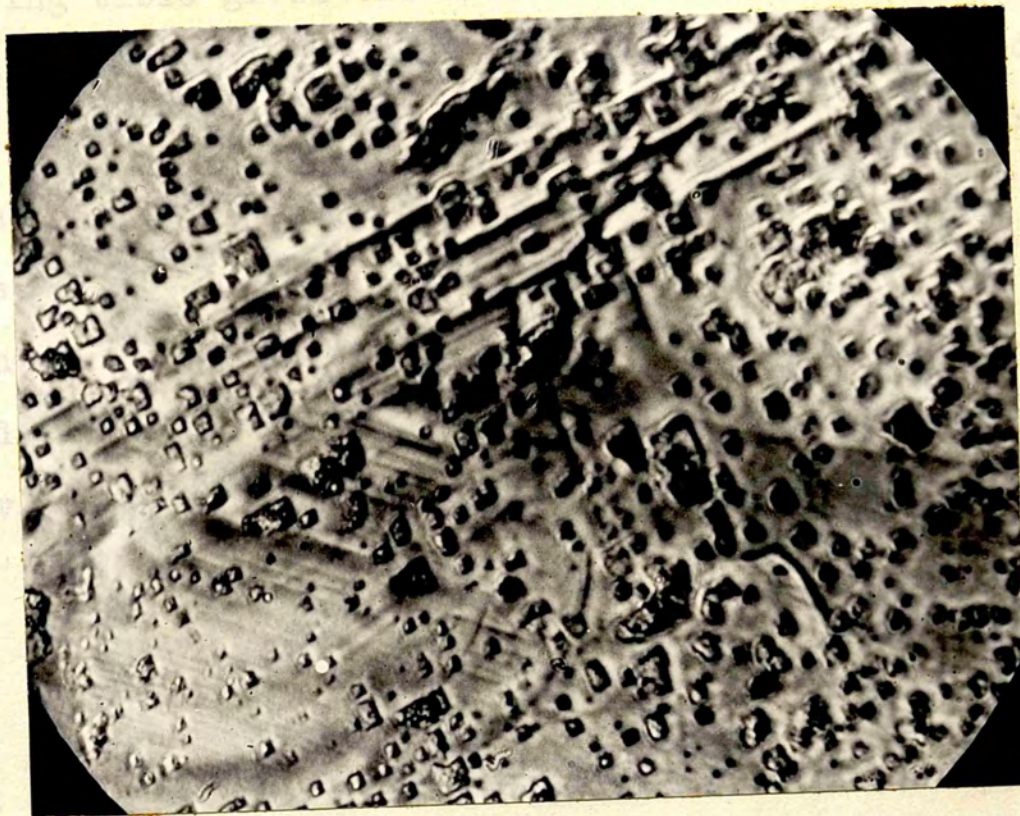


FIG. 138  
x800

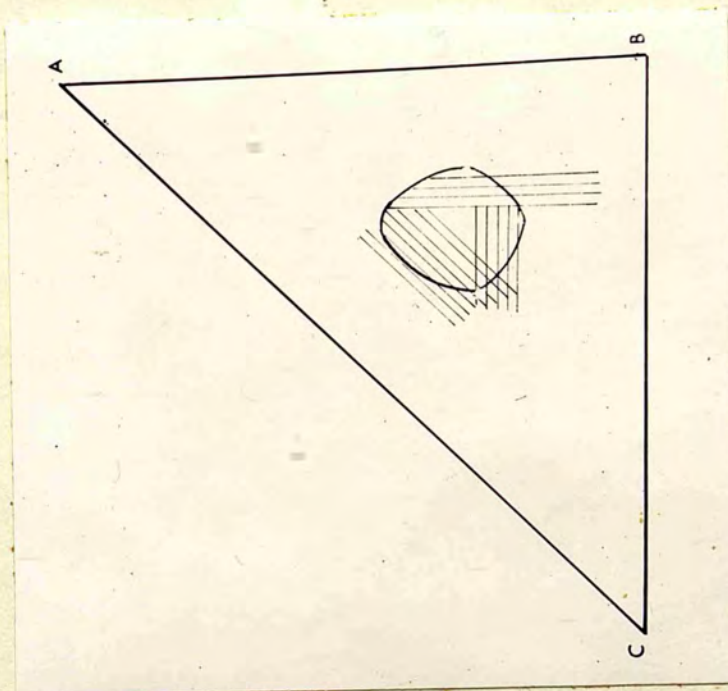


FIG. 139



The following table gives the mean value of the measured radii of the ring cracks and the mean pressure calculated therefrom. Since the area within these cracks is depressed very much below the undisturbed level of the crystal surface permanently, the impacted surface has deformed much beyond elastic limits; hence the measured values of the radii of the ring cracks will have no relation with the value of the same obtained from Hertz's equation.

TABLE

Load in kg	a(measured) in mm.	P <sub>m</sub> in dynes/cm <sup>2</sup>
1	0.027	0.41x10 <sup>11</sup>
2	0.040	0.39x10 <sup>11</sup>
3	0.055	0.30x10 <sup>11</sup>

CHAPTER XI

X-RAY ANALYSIS OF SILICON CARBIDE CRYSTALS

Experimental Details

A Unicam single crystal goniometer was set up. The crystallographic axes of the crystal were determined by its symmetry. The crystal was, then, mounted on the arc of the goniometer head, with its basal plane parallel to one of the arcs and its  $[11\bar{2}0]$  axis parallel to the oscillation axis. The X-ray beam hit the crystal face near the point where indentations were made. This was achieved in the following way. A beam of light was passed through the collimator and the spindle of the X-ray camera was rotated till half the circular patch of light was cut off by one edge of the crystal. The crystal was then, turned through  $180^\circ$  about the oscillation axis and the collimator was again viewed through a low power microscope. By making successive adjustments, the crystal was set such that half the circular patch of light was cut off by the two edges of the indented face of the crystal in its two positions.

The final setting of the crystal was made by taking a photograph consisting of two  $15^\circ$  oscillations on the same film, with the arcs at  $45^\circ$  to the incident X-rays. This was done as follows:

- (i) The arcs were set at  $45^\circ$  to the incident X-ray beam; the cylindrical camera was loaded with the film. The

film was exposed for 20 minutes to unfiltered copper radiation at 30 KV. 20 m.a.

(ii) The crystal was then turned through  $180^\circ$  about the vertical axis and a further photograph was taken on the same film for 5 minutes. Figure 140a shows such a photograph for crystal (1),

(iii) The corrections needed for the arcs were calculated from the photograph and applied.

(iv) Another double oscillations photograph was taken to ensure that the crystal was properly set. Figure 140b shows such a photograph for crystal 1 .

To set the crystal with  $[0001]$  axis as oscillation axis, it was essential to take out a tiny chip of the crystal; the chip was mounted on a glass fibre using an adhesive. The adhesive used was either seccotine or shellac. As far as possible it was seen that the glass fibre was parallel to  $[0001]$  direction of the crystal. The glass fibre was later mounted on the arc of the goniometer with  $[0001]$  direction parallel to the oscillation axis. The final setting, however, was done as in the earlier case.

After setting the crystal with its  $[11\bar{2}0]$  direction parallel to the oscillation axis, the indented face of the crystal was so adjusted, by turning the spindle, that it was making an angle of  $5^\circ$  with the direction of the incident X-ray beam; it was ascertained that the crystal





FIG.140a

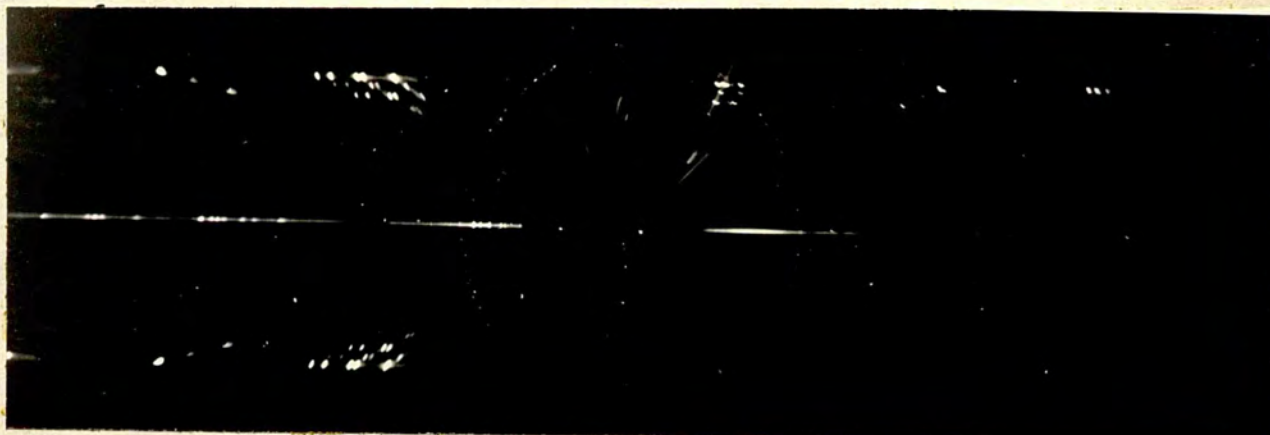


FIG.140b

turned a further  $15^\circ$  during its oscillation. It is easy to see that in this setting the  $[0001]$  axis of the crystal lies in the horizontal plane.

### Experimental Observations

Figures 141, 142, 143 and 144 are the  $15^\circ$  oscillation photographs of the crystal. In each of the photographs the X-ray beam makes different angles (shown on the figures) with the indented face at the beginning of its  $15^\circ$  oscillation. Figures 145 and 146 are the oscillation photographs with the  $[0001]$  axis as oscillation axis. In figure 145 the incident X-ray beam makes an angle of approximately  $-22^\circ$  with the  $[11\bar{2}0]$  axis at the start of the oscillation and in figure 146 it makes an angle of approximately  $-8^\circ$ . By means of the Bernal chart  $\zeta$  was measured on each film from the highest suitable layer and the values of the Bravais lattice and the reciprocal lattice unit-cell dimensions calculated. In the hexagonal system  $c$  ( $[0001]$ ) axis is parallel to  $c^*$  axis and  $a$  ( $[11\bar{2}0]$ ) axis makes an angle of  $30^\circ$  with  $a^*$  axis; therefore

$$\begin{aligned} c^* &= \frac{\lambda}{d_{001}} = \frac{\lambda}{c} \quad \text{and} \\ a^* &= \frac{\lambda}{d_{100}} = \frac{\lambda}{a \cos 30} \quad (\text{Figure 148}) \end{aligned}$$

Table 1 gives the calculated values of the unit-cell dimensions for SiC crystal (2).

TABLE (1)

Oscillation axis	Average value of for the $n^{\text{th}}$ layer line	Reciprocal lattice unit-cell dimensions	Bravais lattice unit-cell dimen.(in A.)
$[11\bar{2}0]^a$	0.510 (first)	$a^* = 0.588$	$a = \frac{1.5418}{0.51} = 3.023$
$[0001]^c$	0.515 (fifth)	$c^* = 0.103$	$c = \frac{1.5418}{0.103} = 14.965$

Tabulation of  $\zeta$  and  $\xi$  for each spot.

The  $\zeta$  and  $\xi$  values for each spot were read by means of the Bernal chart and tabulated as shown below, the indices being added after following the procedure described later. For the sake of convenience the third of the indices, u, has been omitted while indexing the spots.

TABLE (2)

Right side of photograph (figure 141)				Left side of photograph (figure 141)			
$\zeta$	'k,1	'h=0	'h=1	$\xi$	'k,1	'h=0	'h=1
0.635	0 6	s		0.45	0 <u>3</u>		s
0.81	0 7		s	0.54	0 <u>4</u>		s
0.91	0 8		s	1.125	1 <u>7</u>		s
1.22	1 10	m		1.41	2 <u>7</u>	w	
1.300	1 11	m		1.46	2 <u>8</u>	m	
1.650	2 11	m		1.52	2 <u>9</u>	w	
1.680	2 8		vs	1.55	2 <u>5</u>		w
1.730	2 9		vs	1.575	2 <u>6</u>		w
1.780	2 10		vs	1.86	3 <u>5</u>	vw	

vw- very weak; w- weak: m- medium: s- strong: vs- very strong.



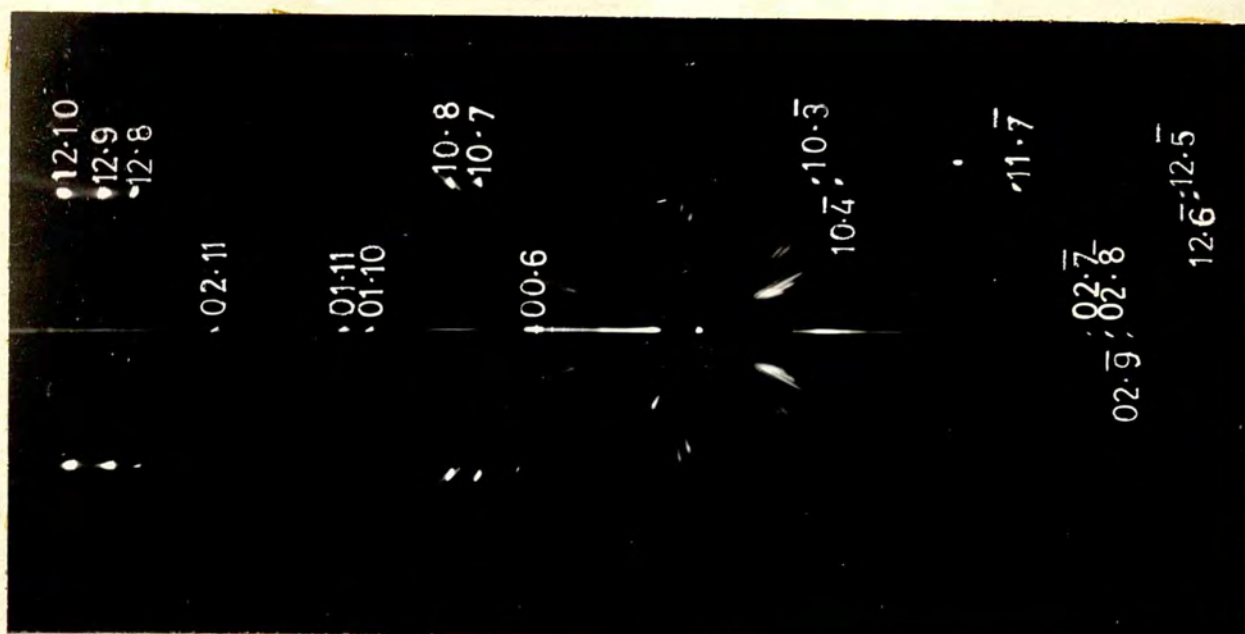


FIG.141 Oscillation Photograph(indexed)  
Specimen: SiC crystal(2), oscillated  $150^\circ$   
clock-wise from position where the X-ray  
beam makes an angle of  $50^\circ$  with c-axis and  
with 1120 axis as oscillation axis.  
Camera: cylindrical,  $r=3$  cm.  
Radiation: Cu K (filtered).

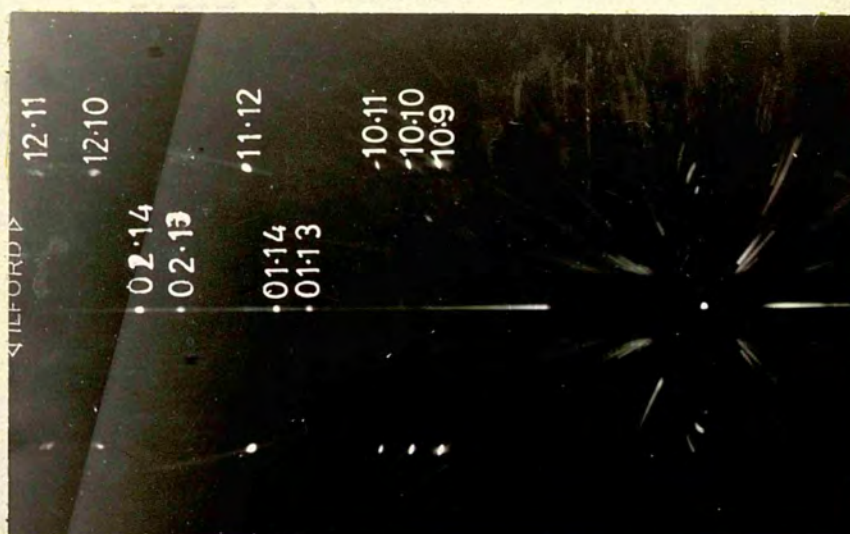


FIG.142 Same as fig.141 but with the  
X-ray beam at an angle of  $19^\circ$  with  
c-axis at the beginning of oscillation.

TABLE (3)

Right side of Photograph (fig.142)

$\zeta_y$	' k,l	' h=0	' h=1
0.99	0.9		s
1.09	0 10		s
1.18	0 11		m
1.48	1 13	m	
1.53	1 12		vs
1.55	1 14	s	
1.78	2 13	m	
1.79	2 10		vw
1.84	2 11		vw
1.85	2 14	s	

(No spots have been obtained on the left side of the photograph)

TABLE (4)

Right side of photograph (fig.143)

$\zeta_y$	' k,l	' h=0	' h=1
1.25	0 12	s	
1.375	0 13		m
1.475	0 14		s
1.650	1 15	s	
1.751	1 16	s	
1.820	2 14	vs	

(No spots have been obtained on the left side of the photograph)



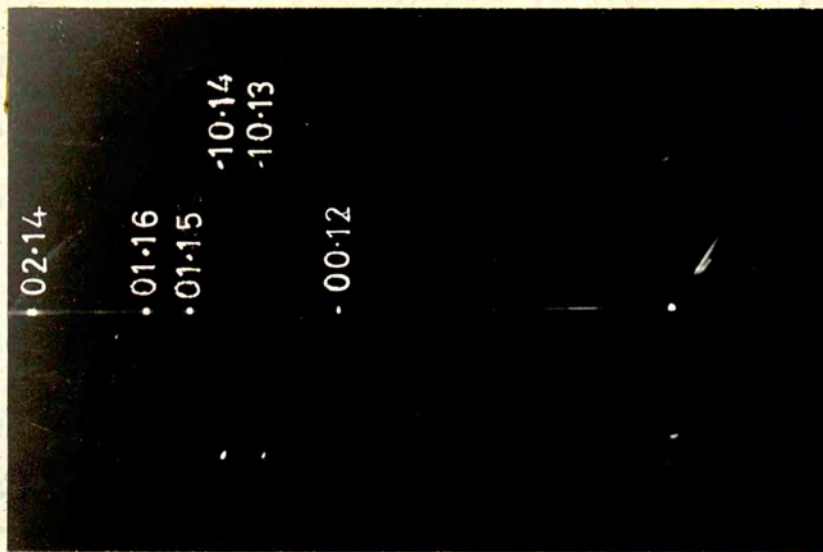


FIG.143 Same as fig.141 but X-ray beam at an angle of  $33^{\circ}$  with c-axis at the beginning of oscillation.

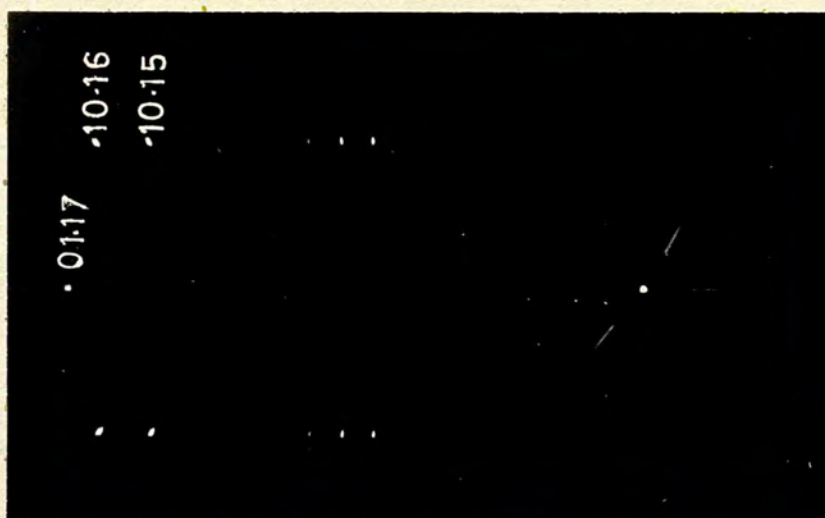


FIG.144 Same as fig.141 but with the X-ray beam at an angle of  $47^{\circ}$  with c-axis at the beginning of oscillation.



TABLE (5)

Right side of photograph (fig.144)

$\zeta$	k, l	h=0	h=1
0.985			m
1.080			m
1.175			w
1.570	0 15		s
1.670	0 16		s
1.840	1 17	s	

No spots have been obtained on the left side of the photograph.

TABLE (6)

Right side of photograph (fig.145)

$\zeta$	'h,k	' l=0	l=1	l=2	l=3	l=4	l=5	l=6	l=7	l=8
0.590	0.1		vw	vw	vw					
1.050	1 1							w		
1.535	2 1		s	s	s	s	s			
1.375	3 0							vs		

Left side of photograph (fig.145)

0.585	1 1									m
1.170	2 2			m	m	m	m			
1.540	3 2						m		m	

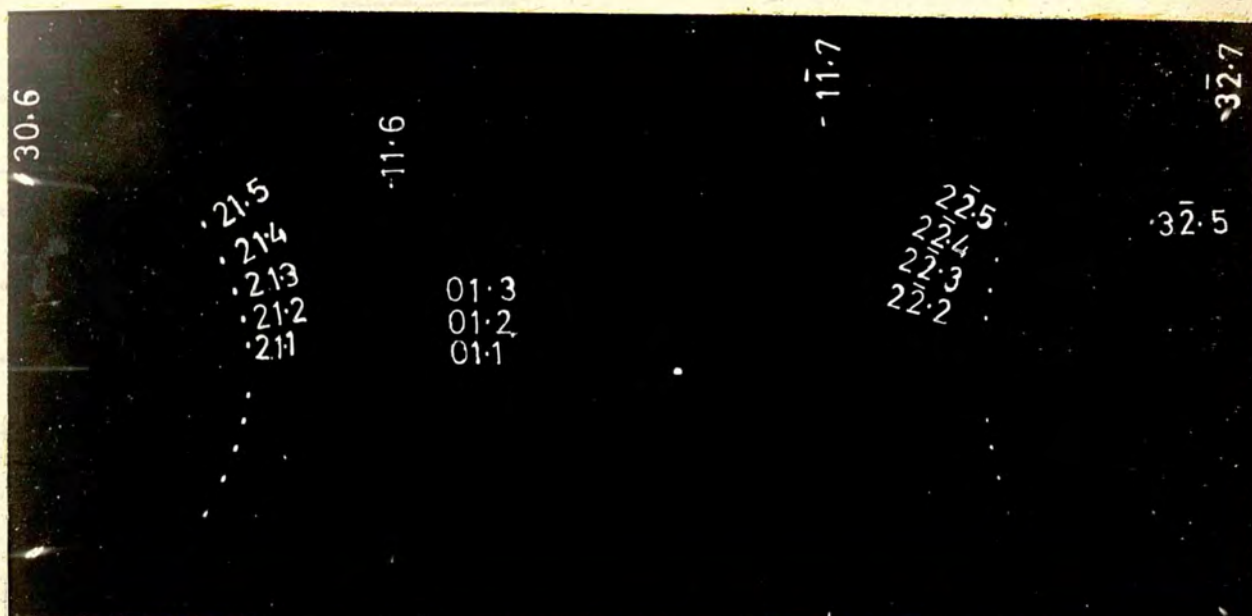


FIG.145 Oscillation Photograph(indexed)  
 Specimen: SiC crystal(2), oscillated 15°  
 clock-wise from position where the X-ray  
 beam makes an angle of 22° with 1120 axis  
 and with c-axis as oscillation axis.

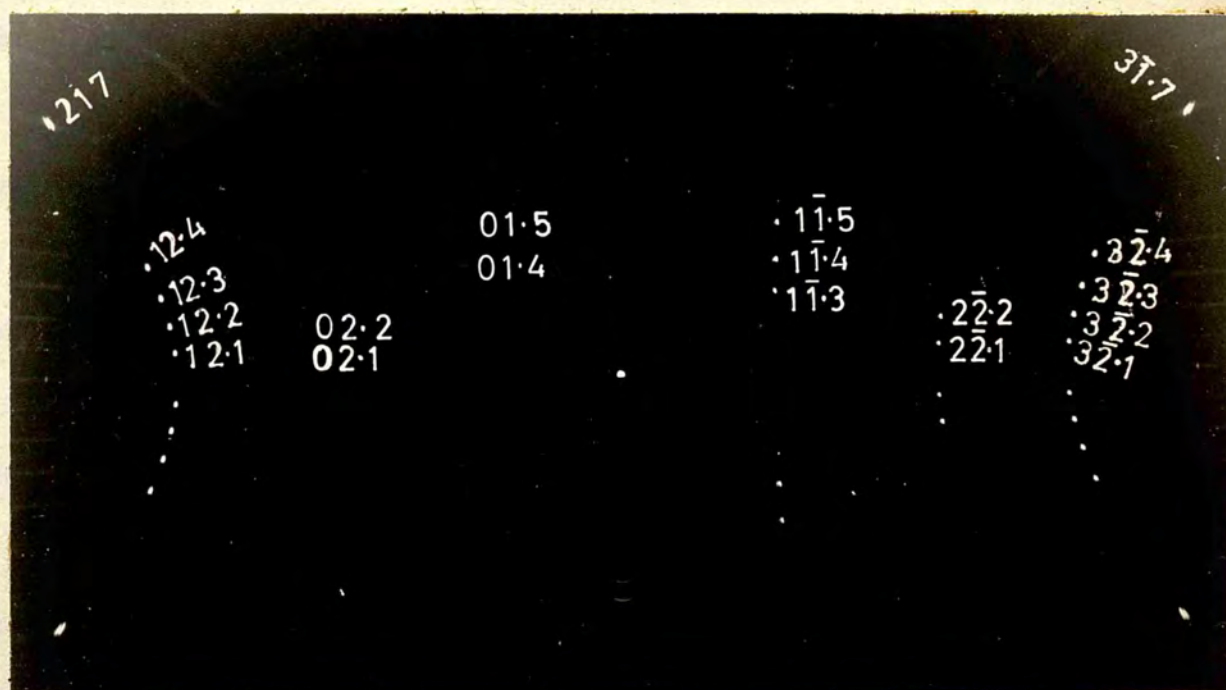


FIG.146 Same as fig.145 but with the  
 X-ray beam at an angle of 8° with 1120  
 axis at the beginning of oscillation

TABLE (7)

Right side of photograph (fig.146)										
$\ell_g$	$h, k$	$\ell=0$	$\ell=1$	$\ell=2$	$\ell=3$	$\ell=4$	$\ell=5$	$\ell=6$	$\ell=7$	$\ell=8$
0.590	0 1					VW	VW			
1.165	0 2		VW	VW						
1.535	1 2		s	s	s	s				
1.535	2 1								s	w
Left side of photograph (fig.146)										
0.600	1 1				s	s	s			
1.175	2 2		s	s						
1.545	3 2		s	s	s	s				
1.545	3 1								s	s

When the a-axis is the oscillation axis, all spots on the zero layer-line correspond to reflections of the type  $0, k, \ell$ ; similarly all spots on the first layer-line are of the type  $1, k, \ell$  and so on. For the photographs with a-axis as oscillation axis a reciprocal lattice was constructed for the  $b^*$  and  $c^*$  plane as shown in figure 149. The reflecting circles corresponding to the two limits of the oscillation were drawn on tracing paper. This was placed over the reciprocal lattice in the correct position as is shown for the zero and first layers in figure 149. During oscillation as the crystal was moved clockwise from its original position, the reflecting circle must be moved in the anti-clockwise direction.





FIG.147

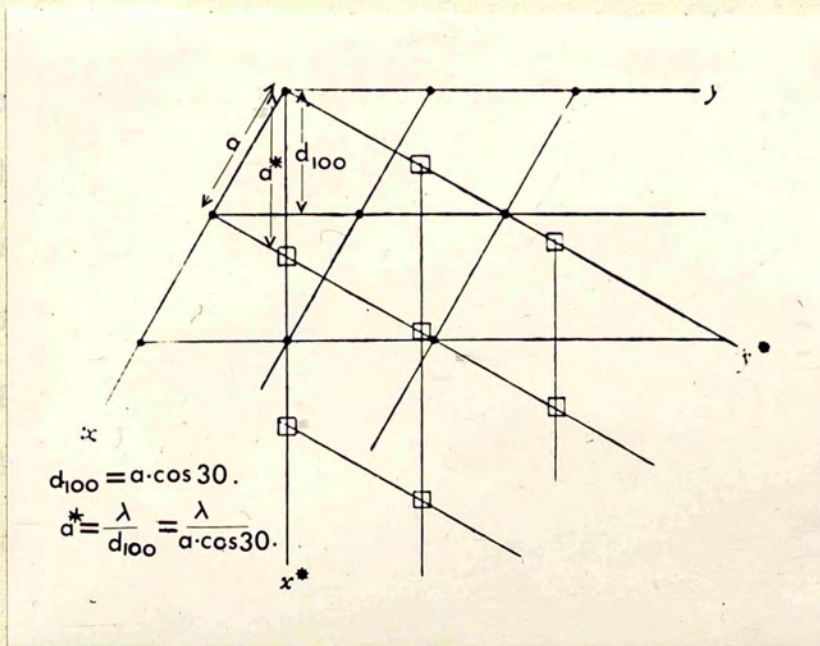


FIG.148

For the first layer the radius of the reflecting circle must be equal to  $\sqrt{1 - \zeta^2}$ , which in this case works out to 0.86, since  $\zeta_1$  is 0.51. As the  $a^*$ -axis is oblique to the  $b^*c^*$  plane, for the first layer, the zero point of the  $\zeta$  co-ordinate does not coincide with the zero point of the reciprocal co-ordinates. The required zero point for the  $\zeta$  co-ordinate is the point at which the oscillation axis intersects the particular plane of the reciprocal lattice. The oscillation axis is, of course, perpendicular to these planes of the reciprocal lattice. Thus the zero point should be shifted from O to O' (figure 149) by an amount equal to  $a^* \cos 60$ , which works out to 0.294.

A pair of compasses was set to each value of  $\zeta$  in turn and with centre at the point where the oscillation axis cuts the plane of the reciprocal lattice, (O for zero layer and O' for first layer) arcs were drawn through the lunes. Each of these passes through or close to a reciprocal point which is the one corresponding to the reflection in question. The indices of this point were assigned to the spot with that  $\zeta$  value. In this way all the spots were indexed. For the photographs with the c-axis as oscillation axis, a reciprocal lattice for the plane  $a^*b^*$  was constructed as shown in figure 150. The process of indexing the spots for these photographs was carried out as before. Figure 150 shows clearly



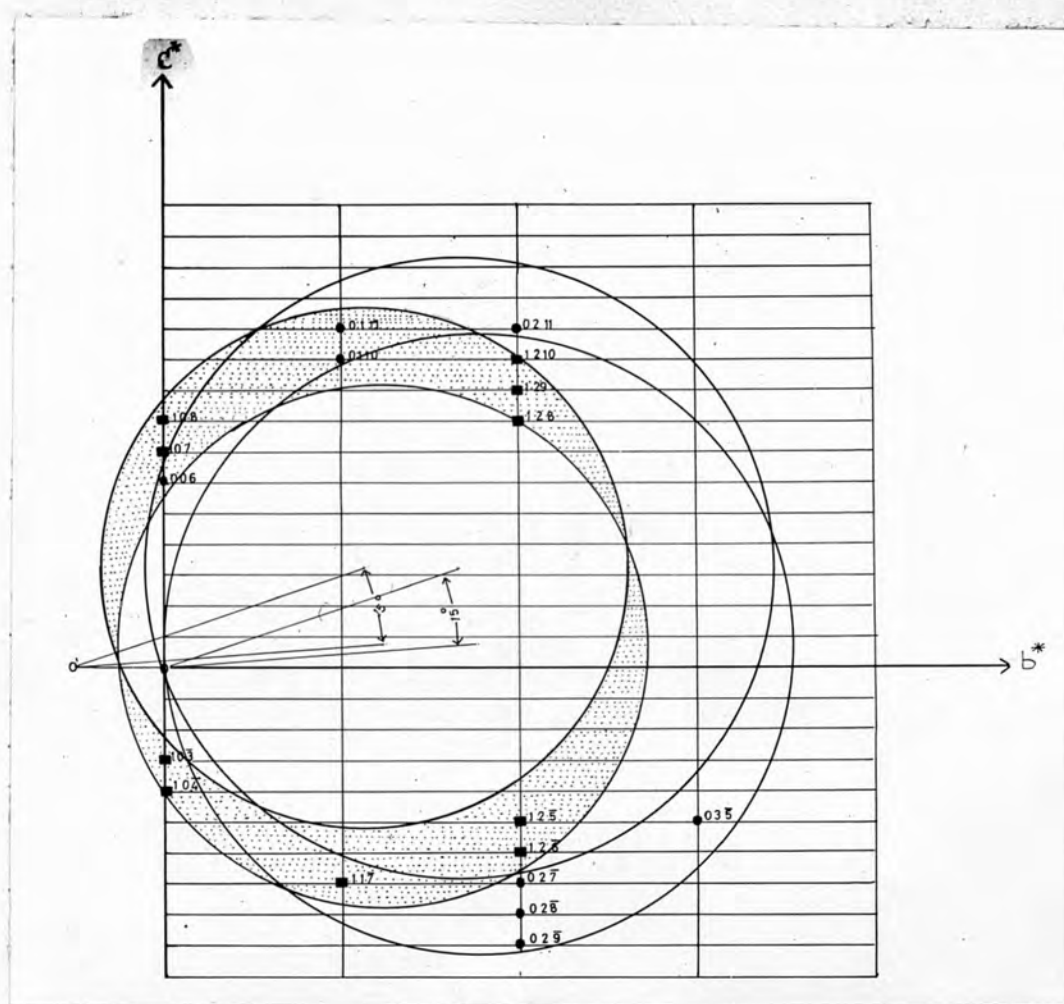


FIG.149

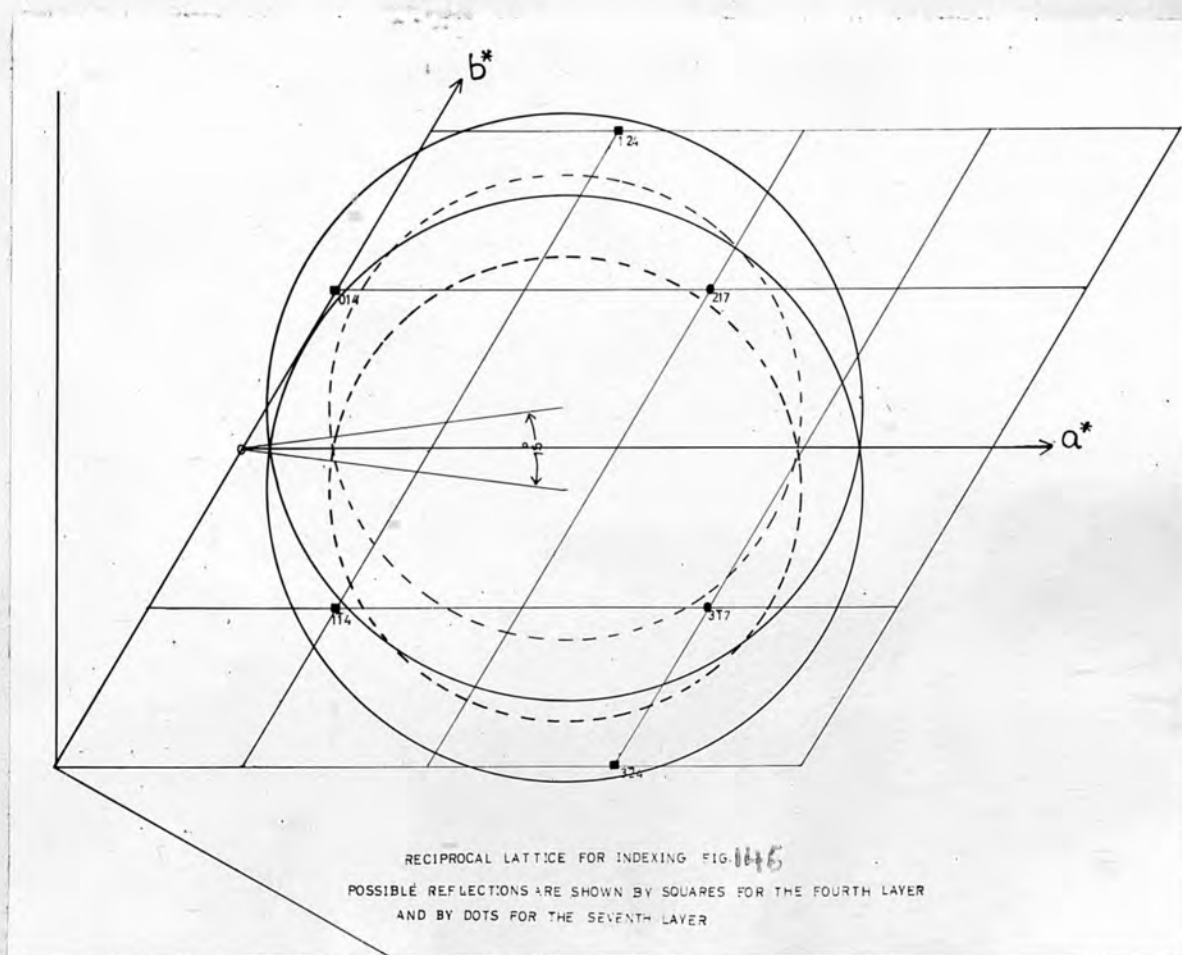


FIG.150



how the fourth and the seventh layer lines were indexed by drawing circles of reflection and obtaining the proper lunes.

Alternate method of obtaining the lattice constant c

To verify the value of the lattice constant c, obtained earlier, the following method suggested by Dr. Jeffery of Birkbeck College was followed. Stacking faults in this crystal produced weighted rods on reciprocal space passing through the R.L. points parallel to  $\mathbf{c}^*$ . For the first layer such rods produced horizontal streaks on the photograph which enabled the position of the rod in reciprocal space to be determined by the  $\rho\phi$  chart in a manner similar to that employed with Laue streaks for the zero layer. This method was particularly useful for crystal (3) where no normal Laue streaks were present on the first layer to fix the orientation. The  $\phi$  values of the end of the horizontal streaks of the zero and the first layers of figure 141 were measured by using the  $\rho\phi$  chart; they were  $20^\circ$  and  $38^\circ$  respectively. The zero layer rowline OC (figure 151) will, therefore, make an angle of  $70^\circ$  ( $\frac{\pi}{2} - \phi_0$ ) with the X-ray beam at the point O. The first layer row line (10.l) will be parallel to that of zero layer and pass through P, a point on the circle of reflection for the first layer. The position of P is determined by drawing OP at an angle of  $52^\circ$  ( $\frac{\pi}{2} - \phi_1$ ) to the X-ray beam. O', the zero point

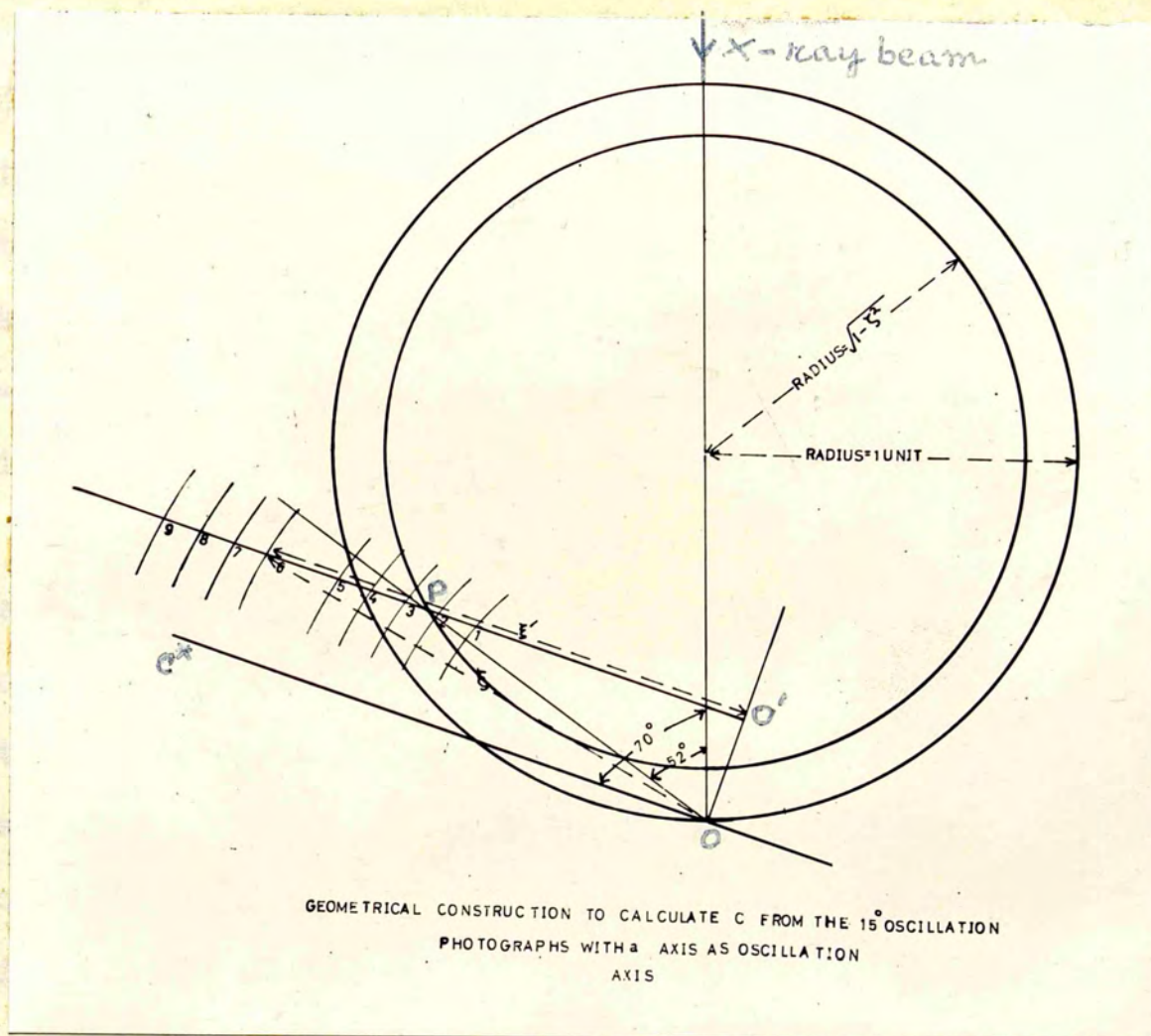


FIG.151



FIG.152



for the  $\zeta'$  co-ordinate of the first layer, is obtained by drawing a perpendicular from O on to the row line. In the absence of any visible streaks in the photograph on the first layer the same construction could be drawn by knowing the  $\phi$  angle for the zero layer and choosing  $OO' = a \cos 60$ . The row line 10·l was followed through a series of oscillation photographs and the  $\zeta$  values of the reflections measured over as wide a range as possible. These  $\zeta$  values were then used to locate the R.L. points along 10·l as shown in figure 151. It is easy to see that  $\zeta'$ , the distance of the points from O', will be some integral multiple of  $c^*$ . Table (8) gives the calculated values of  $c^*$  from the construction. The indices shown in the table have been added by indentifying the spots from the corresponding reciprocal lattice.

TABLE (8)

NO	hki			n	c* =
1	10.7	0.81	0.750	7	0.107
2	10.8	0.91	0.855	8	0.107
3	10.9	1.00	0.945	9	0.105
4	10.10	1.09	1.040	10	0.104
5	10.11	1.18	1.135	11	0.103
6	10.13	1.38	1.340	13	0.103
7	10.14	1.48	1.440	14	0.103
8	10.15	1.57	1.530	15	0.102
9	10.16	1.67	1.640	16	0.102



Taking the mean of the last three values of  $c^*$  from table 8, the lattice constant  $c$  works out to be 15.069A. Similarly it is possible to calculate the axial constant  $a$  more accurately from the oscillation photographs with  $c$ -axis as oscillation axis. From figure 150 the distance of the reciprocal point 21.7 from the origin is given by

$$\begin{aligned} d_{21.7}^* &= \sqrt{4a^{*2} + b^{*2} + 4a^*b^*\cos\gamma^*} \\ &= \sqrt{7}a^* \text{ since } \gamma^* \text{ is } 60^\circ \text{ and } a^*=b^* \end{aligned}$$

The value of  $d_{21.7}^*$  ( $\zeta_{21.7}$ ) from table 7 is 1.535, using the relation  $a = \frac{\lambda}{a^*\cos 30}$ , the axial constant works out to be 3.07A.

#### Space group determination

The indexing of reflections is necessary to fix the space group of the crystal. For a further investigation of the crystal structure, the knowledge of the relative intensities of reflections of definite index is of great importance; because these intensities are a function of the positions of the atoms in the crystal. It should, however, be noted that some reflections may be missing from the oscillation photographs taken, on account of certain symmetries in the atomic arrangement; others because they are so weak that they do not produce a perceptible blackening in the film; still others are absent because the crystal planes have not been in reflecting positions.

The systematic absence of certain kinds of indices among special reflections is produced by the presence of certain elements of symmetry in the space group. For example for a six-fold axes of the type  $6_1$  and  $6_5$ , the absent reflections are  $00\ell$ , when  $\ell$  is not divisible by 6. From the different oscillation photographs of crystal (2), it is seen that the only  $00\ell$  reflections present in them are  $00.6$  and  $00.12$  indicating that the crystal has six-fold symmetry of the type stated above. Figure 147 is a Laue photograph of the same crystal, taken on a flat plate camera at a distance of 3cm., with the incident X-ray beam parallel to c-axis. It clearly shows the crystal to be of hexagonal form. From the values of  $a$  and  $c$  and its hexagonal form, it is evident that crystal (2) is  $\alpha$ -SiC  $\overline{II}$  type 6H. The specifications of this type of crystal obtained from literature are as follows;  $a=3.0817\text{\AA}$ ,  $c=15.1183\text{\AA}$ , space group  $C_{6v}^4$  -  $C6$  mc, axial ratio  $c/a= 3.0 \times 1.63529$ , and molecules per hexagonal cell = 6.

Figure 152 is an oscillation photograph of crystal (1) with its  $a$ -axis as oscillation axis; figure 153 is its oscillation photograph with its  $c$ -axis as oscillation axis. A calculation of the axial constants show that the crystal is a 6H type with a strong component of  $\alpha$ -SiC  $\overline{I}$  15R. Hence its Laue photograph (figure 154) shows a three-fold symmetry, indicating that it is of

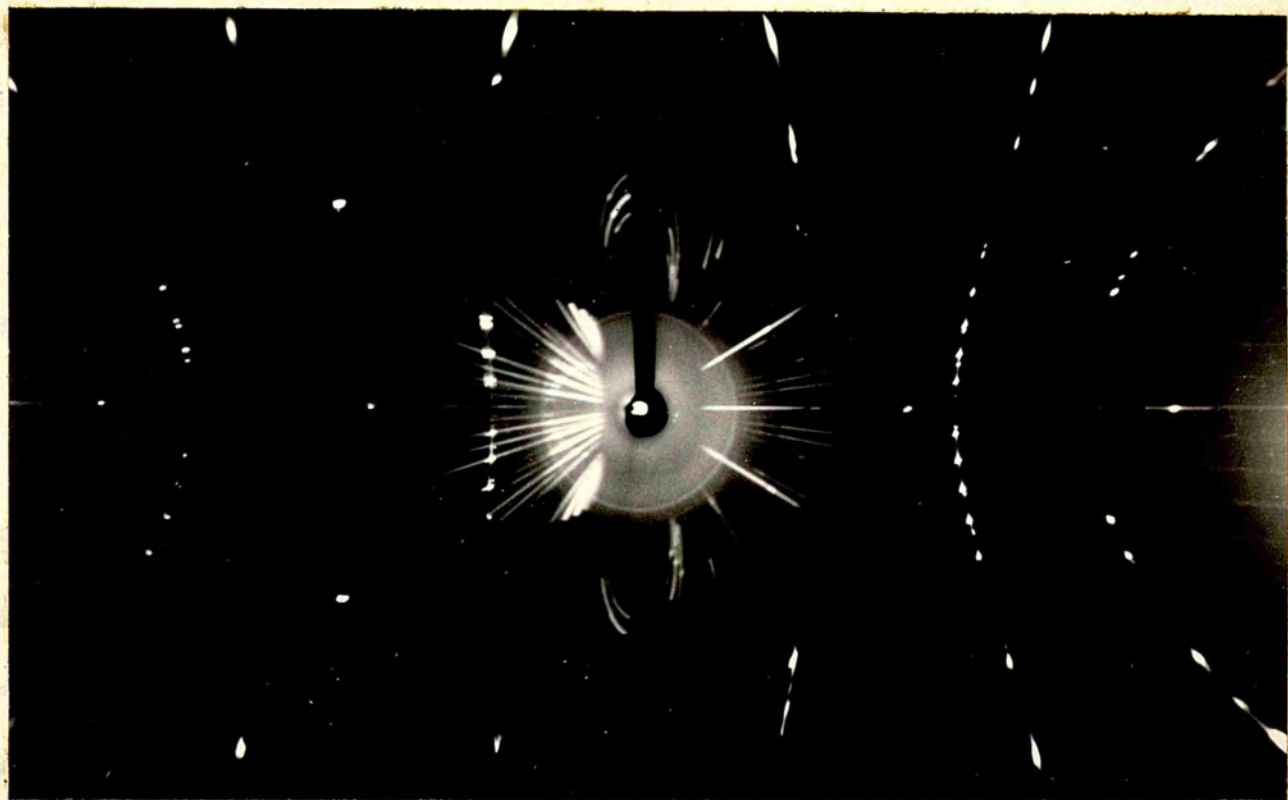


FIG.153

Figures 157 and 158 represent the oscillation photographs of crystal (4) with its  $a$  and  $c$  axis respectively as oscillation axis. The volume of the unit cell dimensions calculated from the photographs, came out to be  $a = 10.84$  and  $c = 15.12$  Å, identifying it to be similar to crystal (2); the  $h$  k photograph (figure 159) shows the

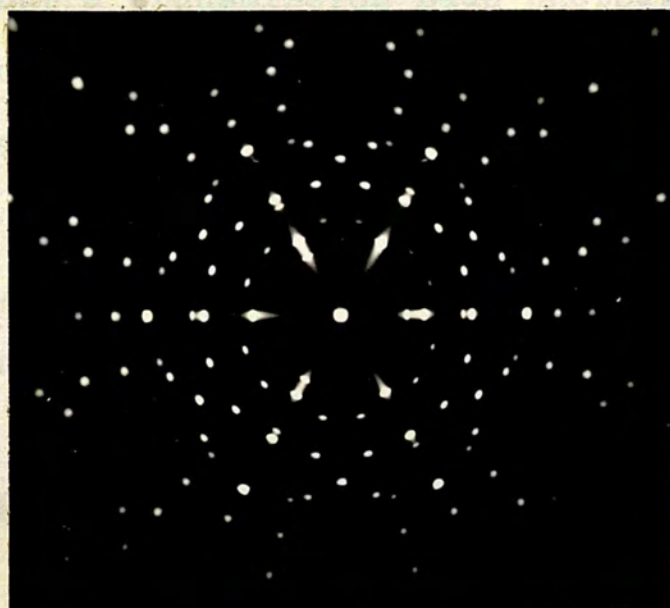


FIG.154

crystal form. Figure 160 is a photograph taken from the front face of the crystal (see features) of the crystal. It shows a fourfold symmetry; this is thus in agreement with the photographs taken with the  $a$  and  $c$  axis. Figure 161 is a photograph of the crystal taken from the back face. It also shows a fourfold symmetry. It appears that the crystal



rhombohedral form. Figure 153 also shows clearly that there is no proper horizontal matching of the position of spots above and below the zero-layer line as there is in crystal (2); this is a feature observed in rhombohedral specimens.

Figure 155 represents an oscillation photograph of crystal (3) with a axis as oscillation axis. Figure 156 is its Laue photograph. The calculated values of the unit cell dimensions come out to be  $a = 3.078\text{\AA}$  and  $c = 15.13\text{\AA}$ ; so that the crystal is of the same type as crystal (2).

Figures 157 and 158 represent the oscillation photographs of crystal (4) with its a and c axis respectively as oscillation axis. The values of the unit cell dimensions calculated from the photographs, came out to be  $a = 3.08\text{\AA}$  and  $c = 15.12\text{\AA}$ , identifying it to be similar to crystal (2); but a transmission Laue photograph (figure 159) shows the crystal to be partly of rhombohedral form. Figure 160 is a back-reflection photograph taken from the front face (face with the observed surface features) of the crystal. This clearly shows a six-fold symmetry; this is thus in agreement with the oscillation photographs taken with the same face exposed to incident radiation. Figure 161 is a back-reflection photograph of the crystal taken from the bottom face of the crystal. It also shows a six-fold symmetry. So it appears that the crystal



FIG.155

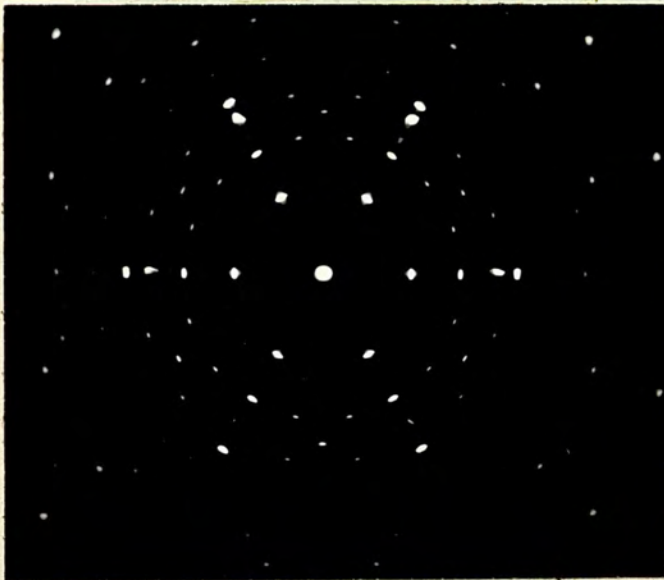


FIG.156





FIG.157

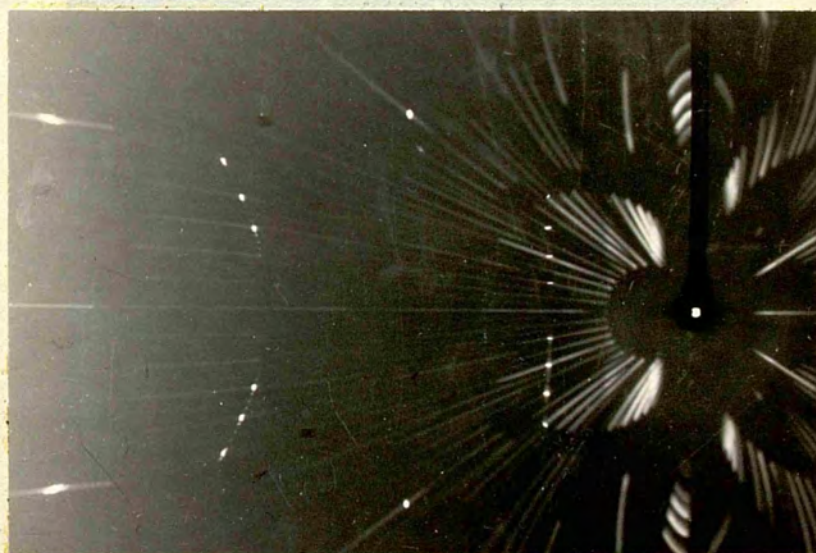


FIG.158





FIG.159

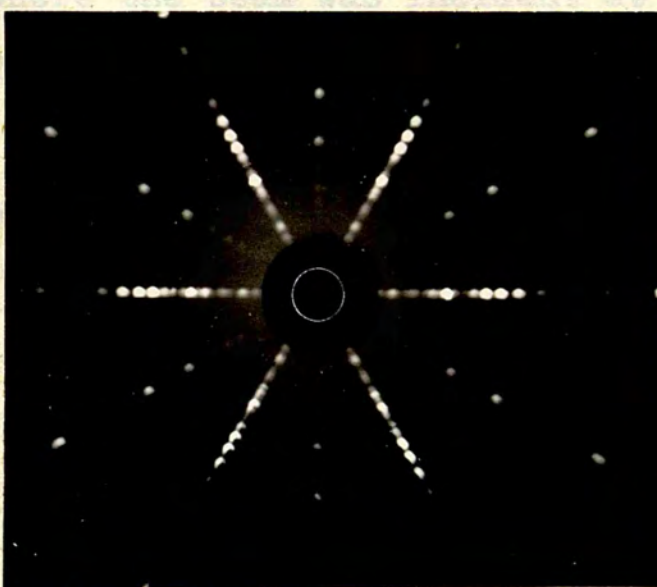


FIG.160

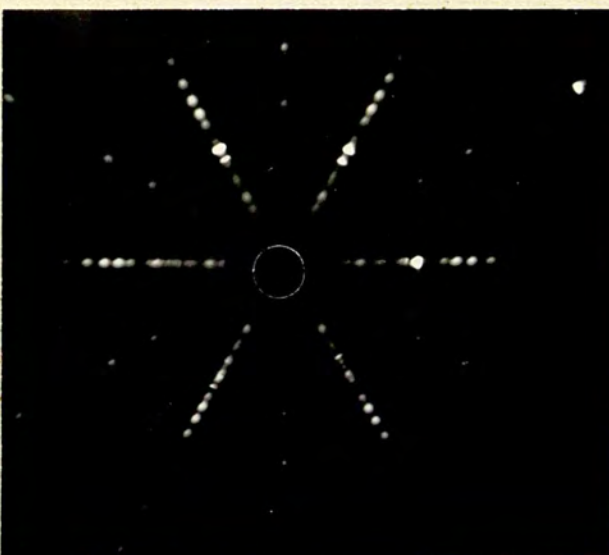


FIG.161

has a rhombohedral component inside it although the faces of the crystal have a hexagonal form. Close inspection of the oscillation photographs with  $c$  as the rotation axis (figure 158) shows faint subsidiary reflections between some of the main ones corresponding to  $6H$ . These indicate a  $c$  spacing of about 4 times that of  $6H$  and the lack of a horizontal plane of symmetry for these reflections indicate a rhombohedral lattice. For this photograph the plate was parallel to the beam. In figure 157 where the beam was incident at a glancing angle of  $5-20^\circ$  to the surface of the plate no subsidiary reflections can be seen. This supports the evidence of the Laue photographs that the rhombohedral form is in the interior of the crystal, and the small size of the subsidiary reflections suggest that it may be a central core.

In 1956 Cabrera and Levine extended the dislocation growth theory to the evaporation of crystals. Except for the work of Axelrod and Votava (1953, 1954) and Lohsain, Mukoyama and Chernov (1959, 1961), there is little experimental evidence to support this theory. The cinematographic study of the transformation of a growth spiral into an evaporation spiral in the case of the  $\beta$ -toluidine crystals by Lohsain and his associates (1961) leaves no doubt as to the broad validity of the present dislocation theory of evaporation. These authors

## CHAPTER XII

### OPTICAL AND INTERFEROMETRIC STUDIES ON SILICON CARBIDE CRYSTALS

#### Introduction

Since 1949, when Burton, Cabrera and Frank proposed the screw dislocation mechanism for the growth of crystals from the vapour, a number of workers have reported the existence of growth spirals in various materials. Apatite, beryl, biotite, cadmium, cadmium iodide, cadmium sulphide, cadmium fluorite, diamond (synthetic), fluorite (synthetic), gold, graphite, haematite, ice, magnesium, organic long-chain compounds (at least 20), pyrite, rocksalt, silicon, silicon carbide, silver, titanium, zinc, zinc sulphide and quartz (synthetic) are included in the long list of crystals on which growth spirals have been observed.

In 1956 Cabrera and Levine extended the dislocation growth theory to the evaporation of crystals. Except for the work of Amelinckx and Votava (1953,1954) and Lemmlein, Dukova and Chernov (1957,1961), there is little experimental evidence to support this theory. The cinemicrographic study of the transformation of a growth spiral into an evaporation spiral in the case of the p-toluidine crystals by Lemmlein and his co-workers (1957), leaves no doubt as to the broad validity of the proposed dislocation theory of evaporation. There is, however,



no evidence from the use of such sensitive techniques as multiple-beam interferometry and phase-contrast microscopy to make possible a more detailed analysis of the mechanism of spiral-layer evaporation.

In the course of our microtopographical studies of the surfaces of silicon carbide crystals, we came across a sample of these crystals (supplied by Phillips, Hollond), with pits having some of the characteristics of the evaporation pits referred to above. In this chapter a description will be given of the observations made on such crystals with the help of multiple-beam interferometry and phase-contrast microscopy.

#### Description of the crystals

The crystals studied are different from those described by Verma (1951) both in colour and size. The silicon carbide crystals studied by Verma were pale green, dark green, blue and black. They were in the form of hexagonal plates, with the basal pinacoid predominantly developed. The opposite faces of the crystals differed in appearance in all modifications; one face was planar and the other often stepped and it is on these planar faces that he observed the growth spirals.

The crystals described here are thin, transparent and colourless parallel plates. The two sides of the plates, which are very plane and shining, are the (0001) pinacoid faces. Most of the crystals are either hexagonal

or approximately square plates, about 2 mm across and 0.25 mm thick. It is on one of these faces that the features were observed. These commercial samples were grown at a temperature of 2500<sup>oC</sup> on graphite.

#### Description of the features

Figures(162a,b,c,d) show these features on some of the crystals photographed under transmitted light. Figure 163 shows the same for another crystal photographed under reflected light without silvering the crystal. Figure 164 shows the double-beam Fizeau fringes on one face of a crystal and figure 164 shows similar fringes on the other face of the same crystal. The corresponding corners in both the figures have been marked to show one to one correspondence between the two faces. The parallel nature of the fringes clearly indicates that the two faces of the crystal are plane; the brightness of the fringes shows that the surfaces are sufficiently reflecting.

Surface features on a very large number of these crystals were studied and in the light of this study, the crystals were classified under the following four categories:

- (a) Crystals with isolated features.
- (b) Crystals with overlapping features.
- (c) Crystals with both overlapping spiral-like features and isolated features.



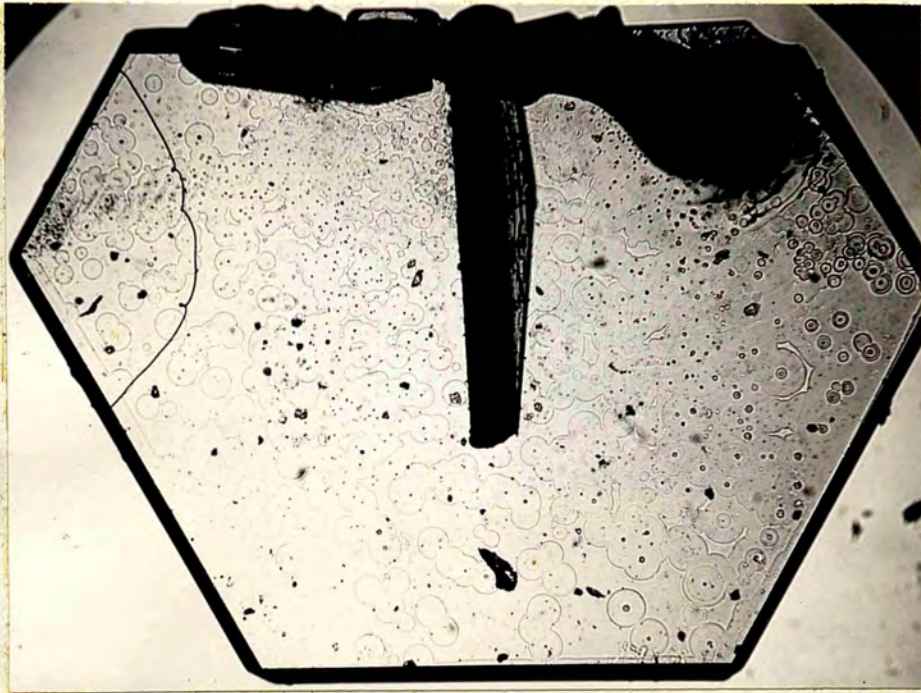


FIG.162a  
x45

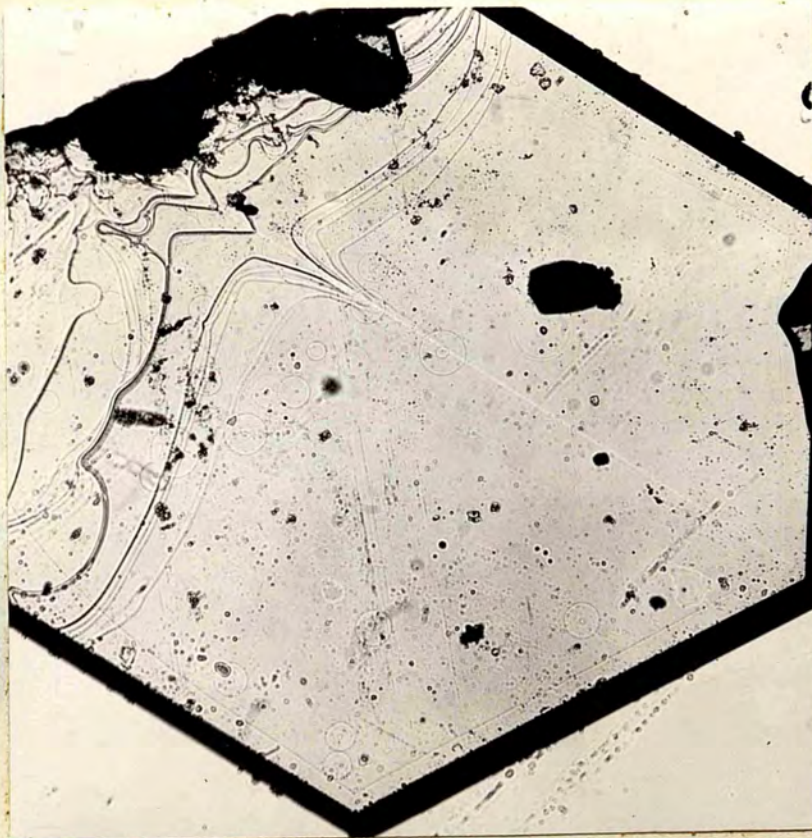


FIG.162b  
x45



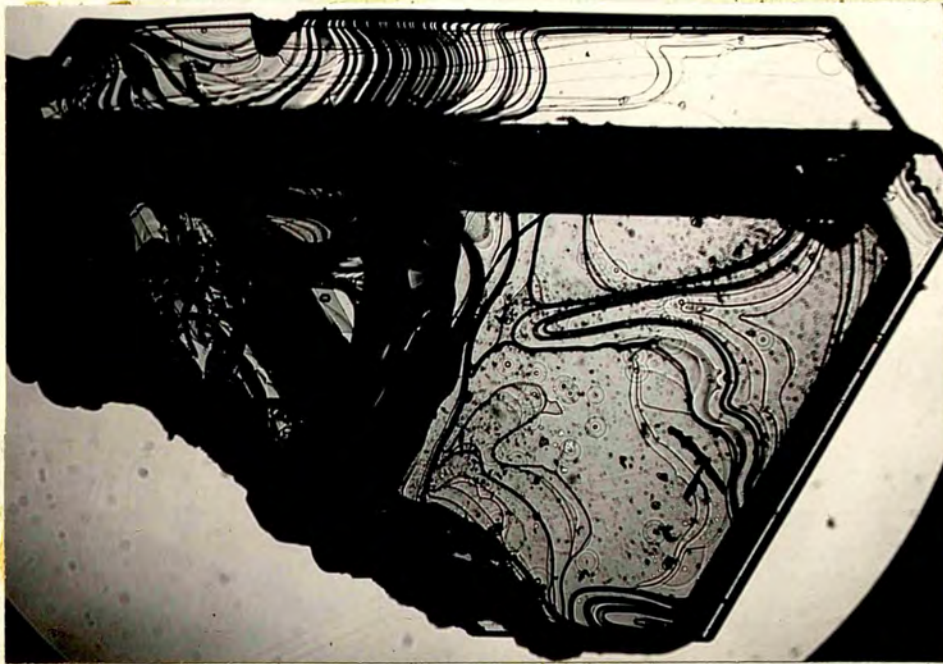


FIG.162c  
x45

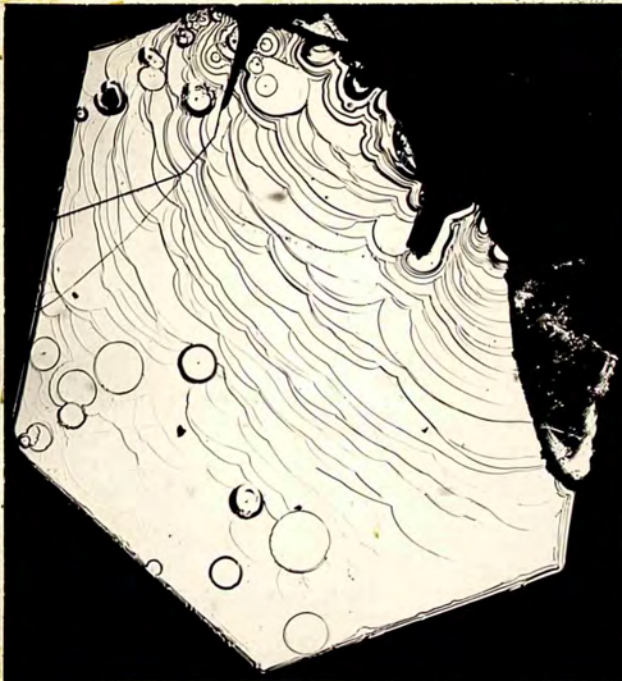


FIG.162a  
x45

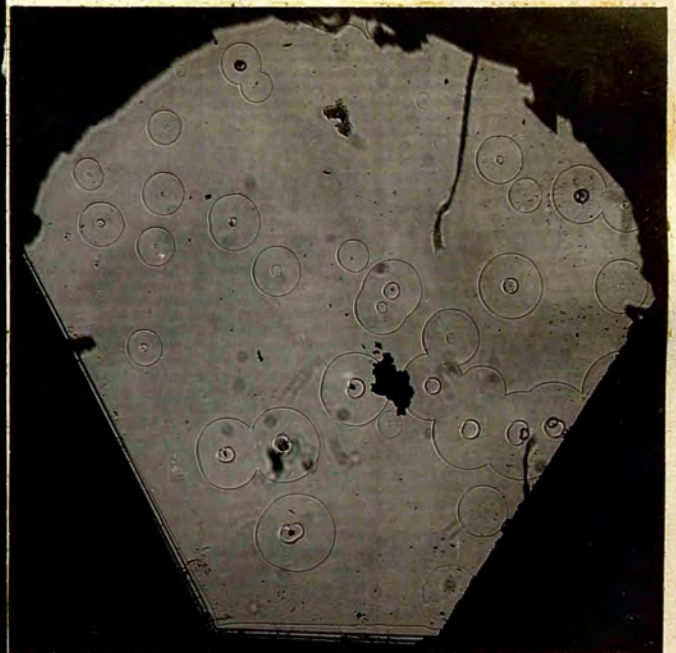
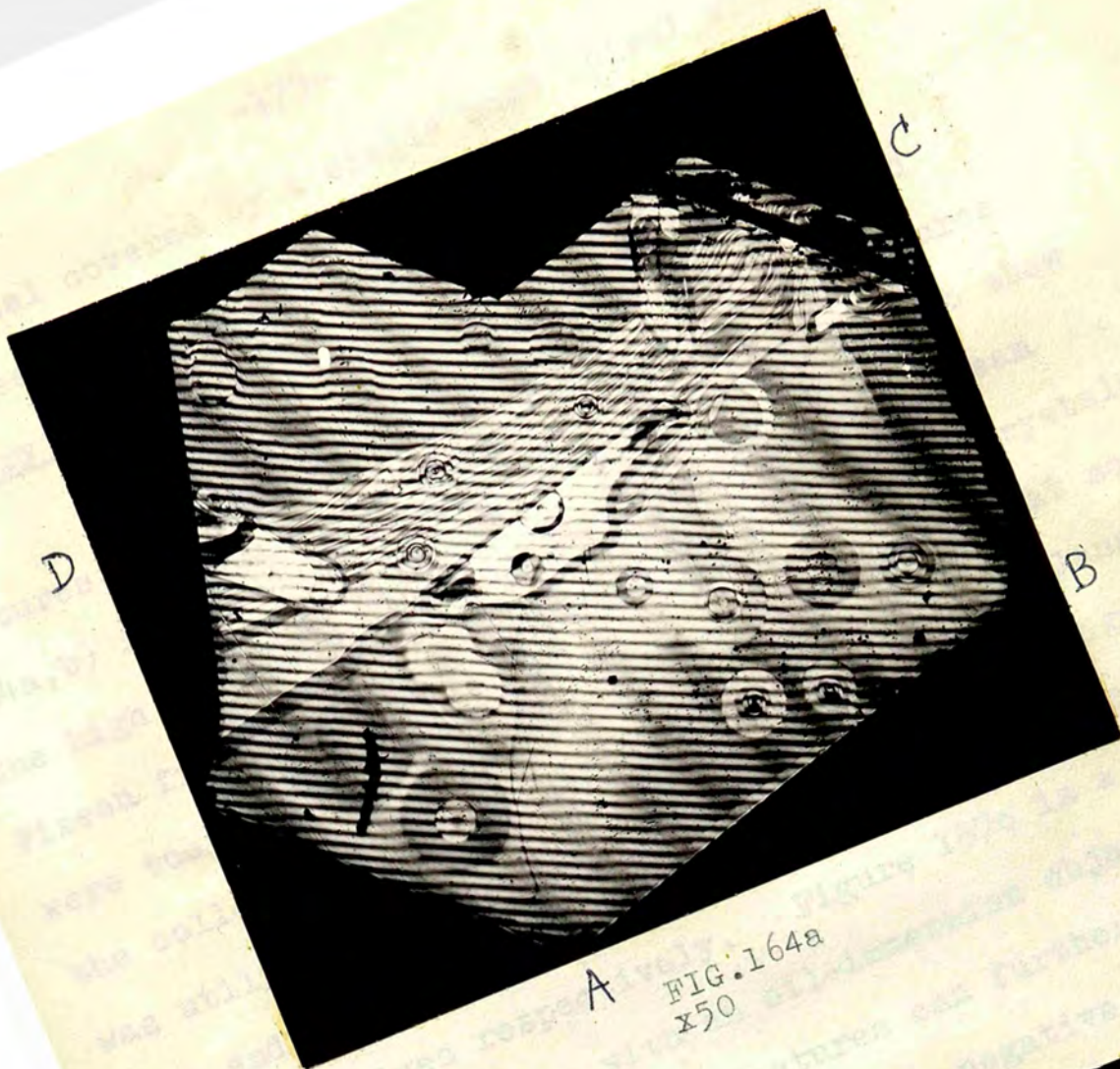


FIG.163  
x45





A FIG. 164a  
x50

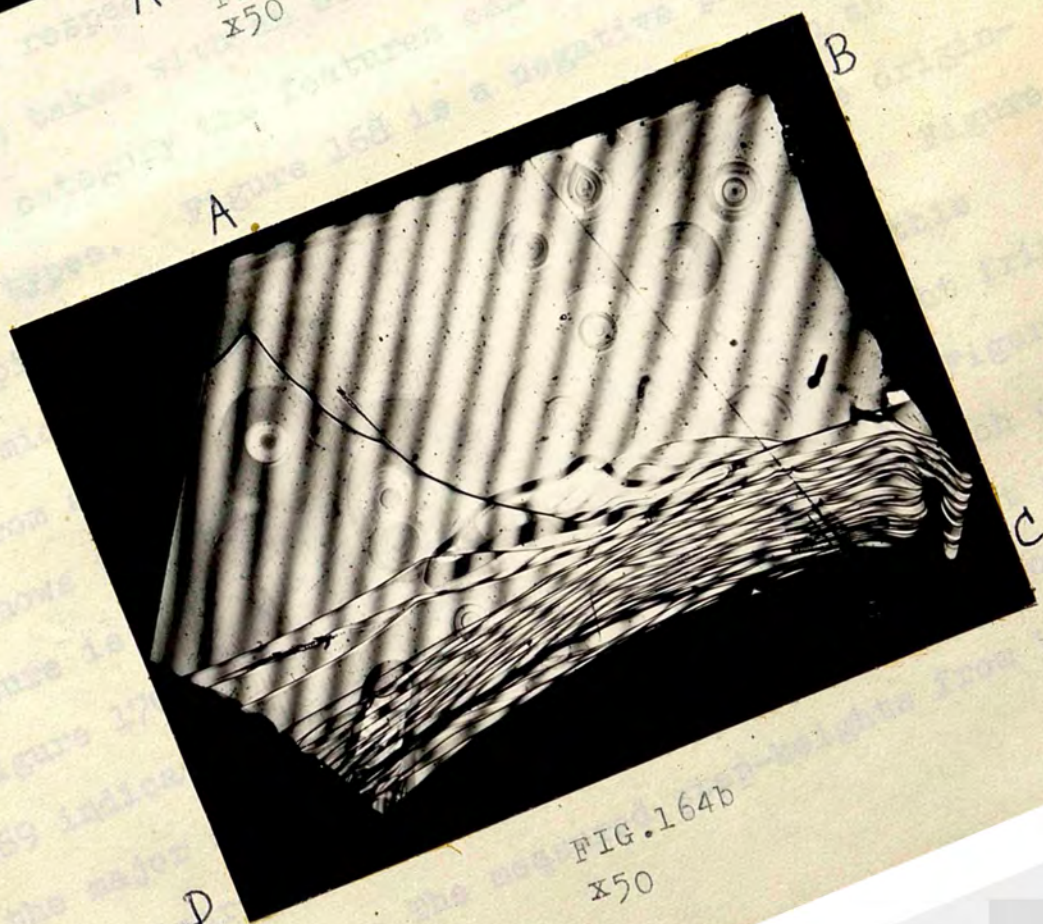


FIG. 164b  
x50



(d) Crystal covered by a single huge spiral with pits in between steps.

Category (a)

Figure 165 shows a crystal with isolated features. The double-beam fringe pattern in figures (164a,b) is on this crystal. Figures 166a and 166b show the high dispersion and low dispersion multiple-beam Fizeau fringes on these features. Some of the crystals were too small for matching against a silvered flat so the collodion thin-film technique developed by Tolansky was utilized to obtain Fizeau fringes on them; figures 167a and 167b show such fringes obtained using 8 mm and 4 mm objectives respectively. Figure 167c is a similar fringe pattern taken with an oil-immersion objective. Even in this category the features can further be divided into three types. Figure 168 is a negative phase-contrast picture of a circular feature, taken with an Olympus microscope. This feature appears to have originated from a pair of opposite handed dislocations. Figure 169 shows the Fizeau fringes on the same. That this feature is a depression, is seen by the white light fringes (figure 170) which are convex towards the red. Figure 169 indicates the existence of a minor step in each of the major steps. The white light fringes make it still more clear that the two major steps are in fact four unequal steps. The measured step-heights from the centre



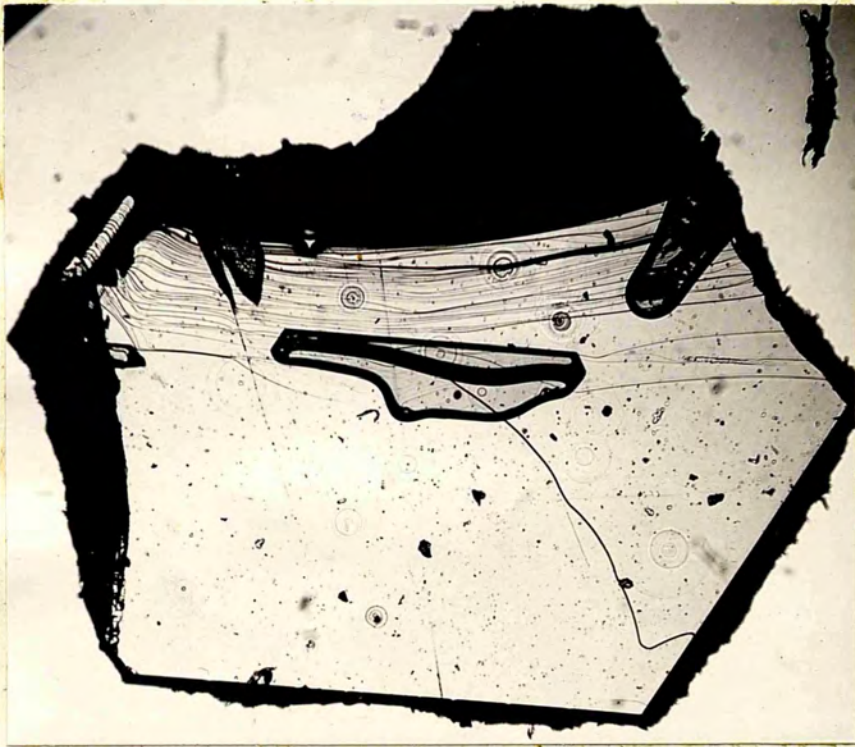


FIG.165  
x45



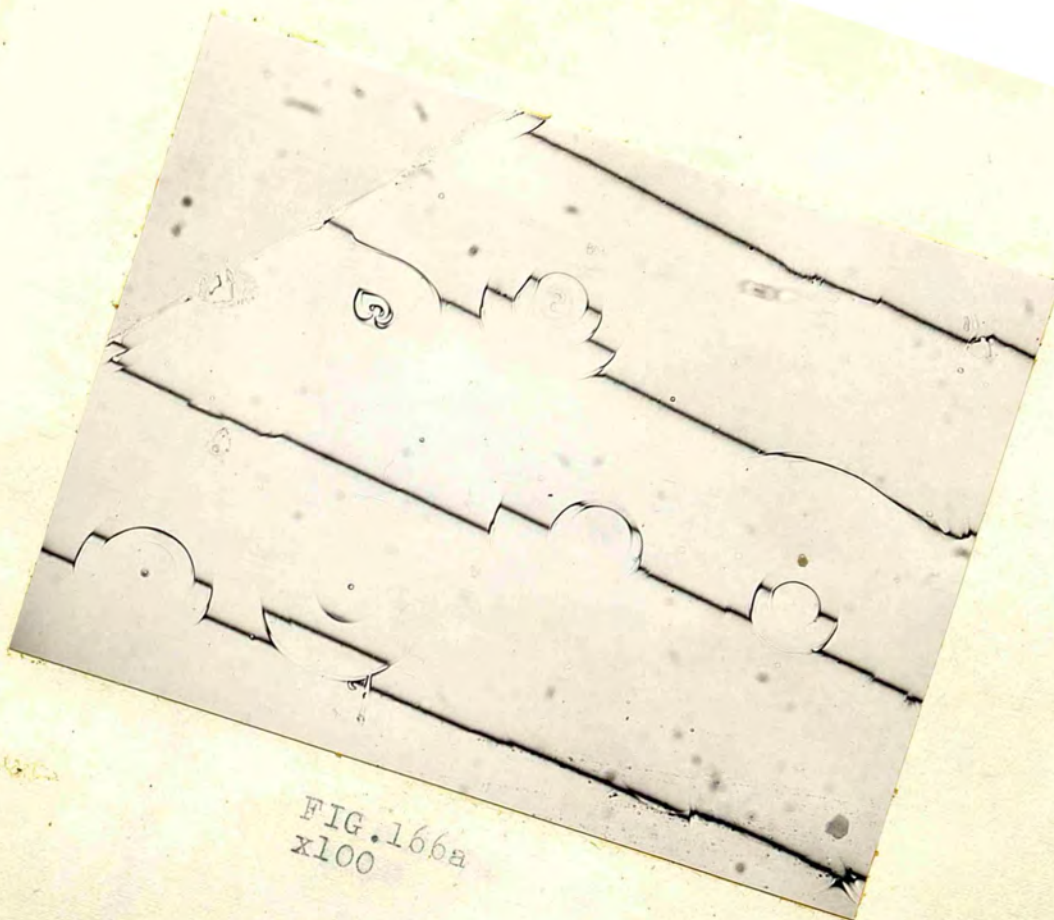


FIG. 166a  
x100

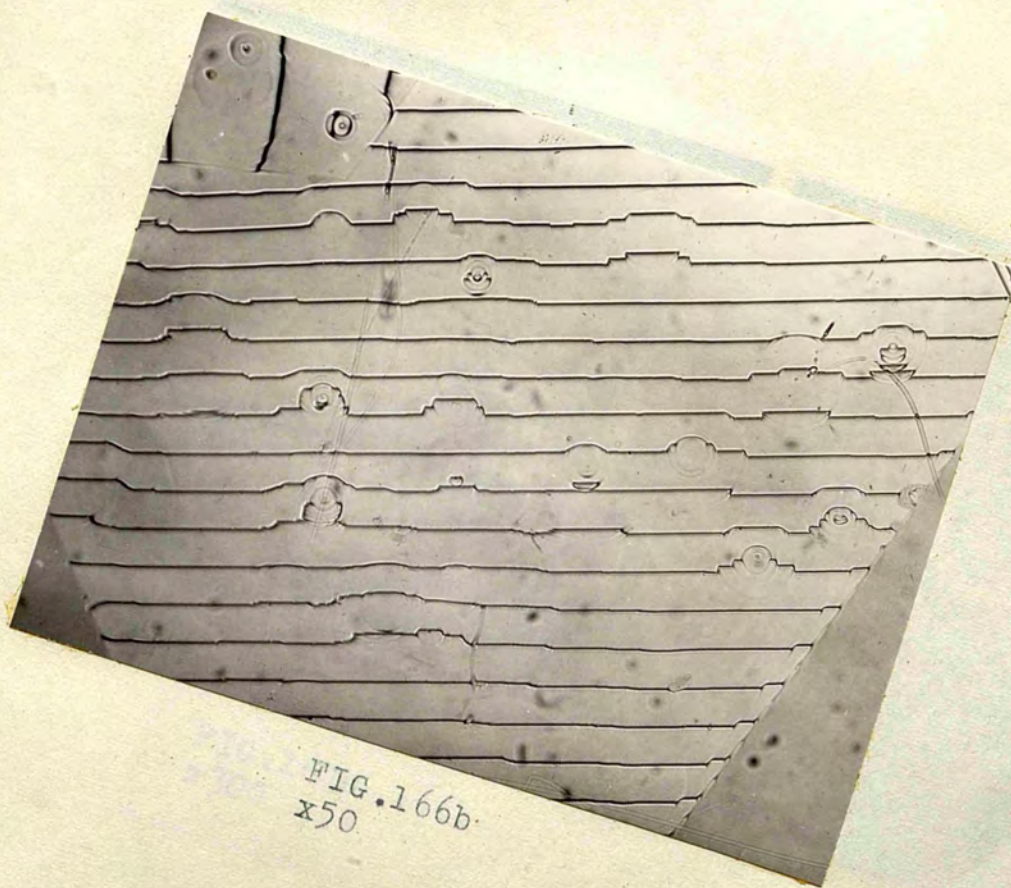


FIG. 166b  
x50





FIG. 167a  
x150



FIG. 167b  
x300



FIG. 167c  
x600 (reduced)



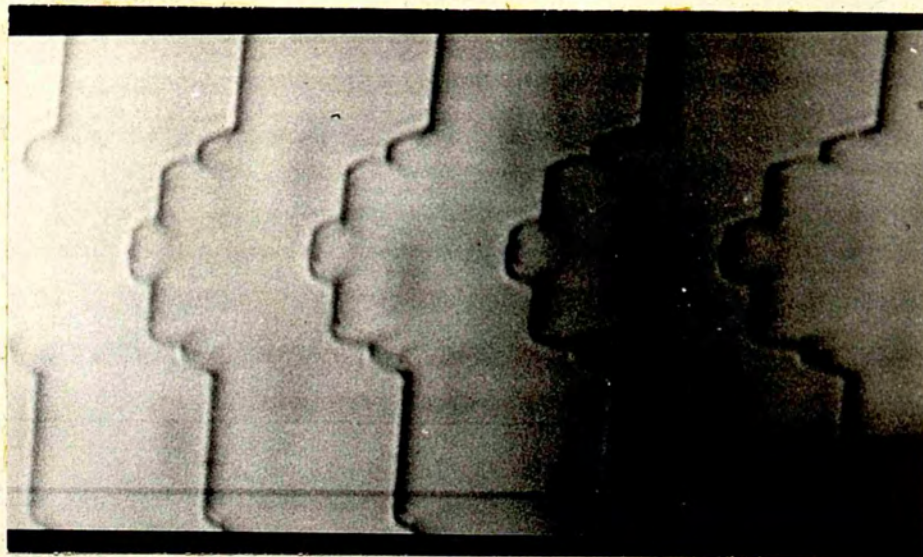


FIG.170  
x300

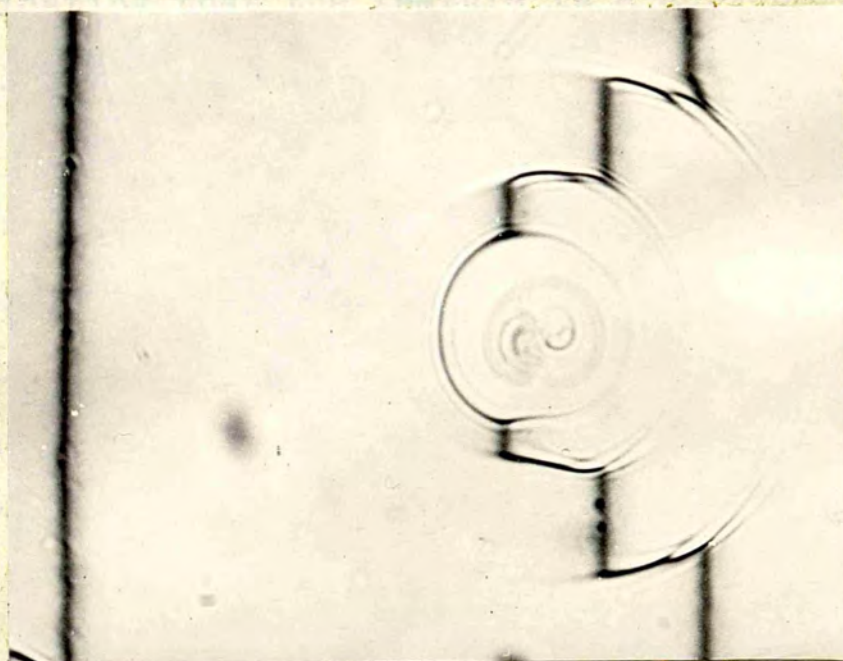


FIG.169  
x350



FIG.168  
x300(reduced)

are 279A, 279A, 159A, 299A and 159A.

Figure 171 is a negative phase-contrast picture of a feature which looks like a stack of unequal circular discs; the point of emergence of the dislocation is at the centre of this feature. Figure 172 gives the Fizeau fringes on the feature from which the step-heights come out to be 450A, 450A, 257A and 193A. Figure 173 gives the white light fringes, which are convex towards the red, indicating that the feature is a depression.

Figure 174 is positive phase-contrast picture of a heart-shaped feature found at the edge of a crystal. Figure 175 is a Fizeau fringe pattern on the feature from which the step heights come out to be 449A, 481A, 257A and 192A. The white light fringes (figure 176) show that the feature is a depression. A close look at figure 176 shows that although the feature is a depression, its central core is an elevation, as at that point the fringes are convex towards the violet.

The first two features are the more common type seen; the heart-shaped feature is a very rare one and found at the edge of the crystal.

An X-ray back reflection c-axis Laue photograph from both the faces of this crystal (crystal 4) shows a hexagonal symmetry; but a transmission c-axis Laue photograph shows a trigonal symmetry. The a-axis oscillation photographs show only reflections corresponding to



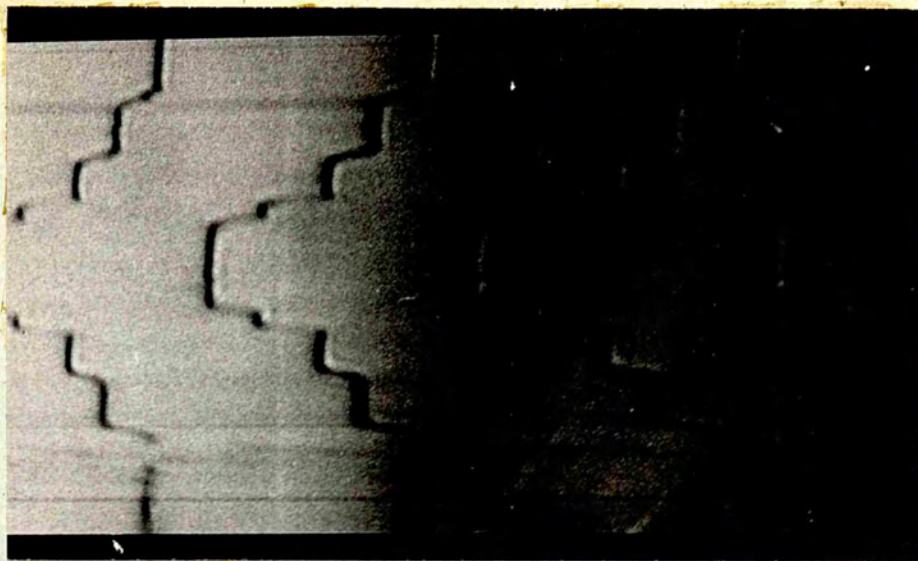


FIG. 173  
x300

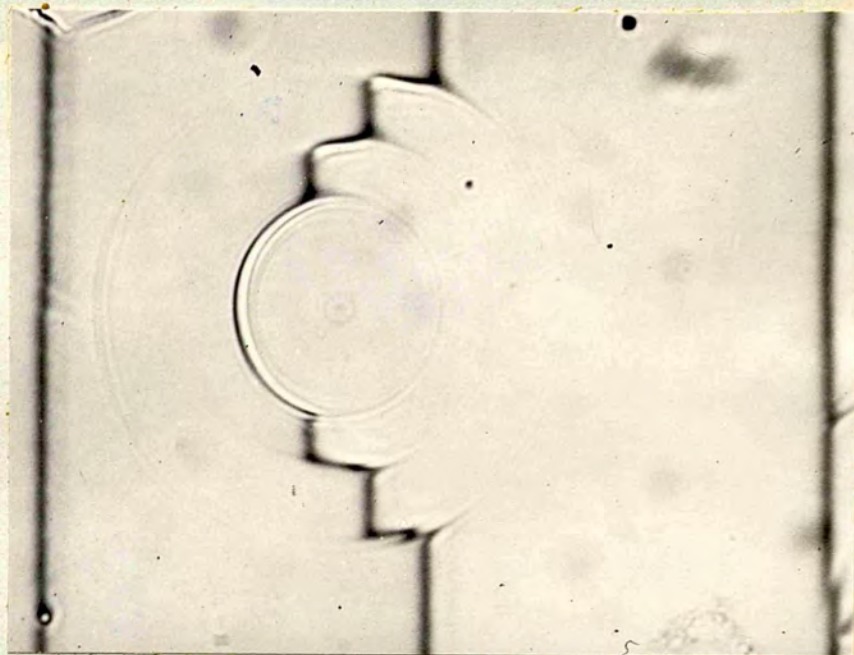


FIG. 172  
x375

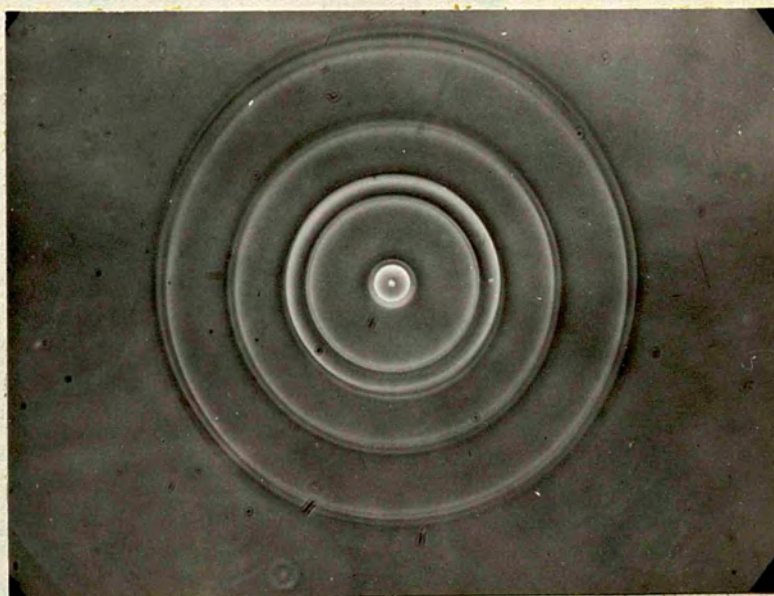


FIG. 171  
x375



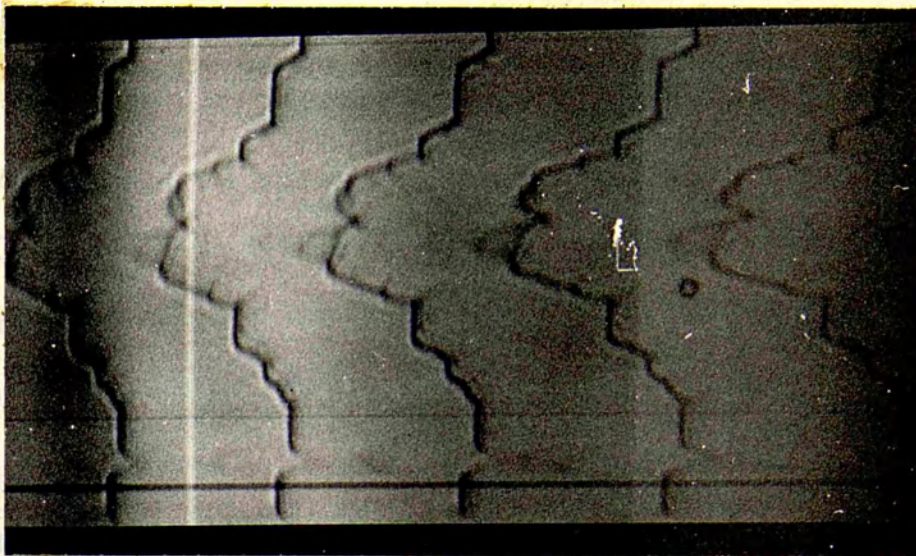


FIG. 176  
x300

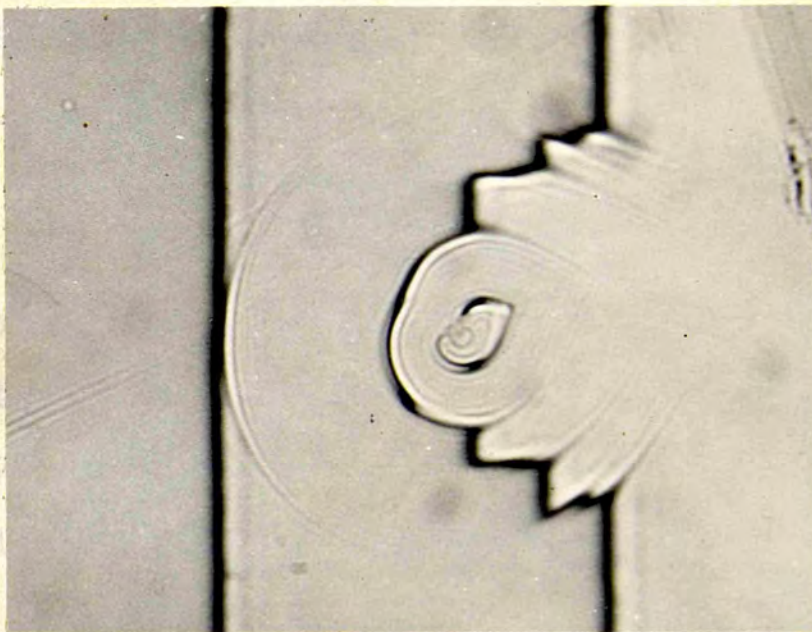


FIG. 175  
x375



FIG. 174  
x375



6H cell but a c-axis oscillation photograph shows faint subsidiary reflections between some of those corresponding to 6H; these indicate a spacing just over 4 times that of 6H and are not symmetrical about the horizontal plane. (A full X-ray analysis of this crystal is given in chapter XI). This suggests that the crystal has a rhombohedral central core surrounded by 6H in parallel orientation. Figures 176a,b,c are phase-contrast pictures of other isolated features observed. The photographs were taken without silvering the crystal surface.

#### Category (b)

The overlapping features on crystals of this category are either straight depressions below the crystal surface or raised pits with the bottom of the pits in level with or sometimes below the surface of the crystals. Figure 177 is a picture of some of these features taken with reflected light. Figures 178a,b are phase contrast pictures of these features. Figures 179 and 181 show the Fizeau fringes taken with high dispersion. The white light fringes shown in figure 180 are convex towards the red and hence the features are depressions. A close study of these fringes reveals that the pits are in between the unequal surface levels of the crystal; the bottom of these pits is rounded and is either in level with or slightly lower than the surface of the crystal.

Figure 182 shows Fizeau fringes on another crystal.

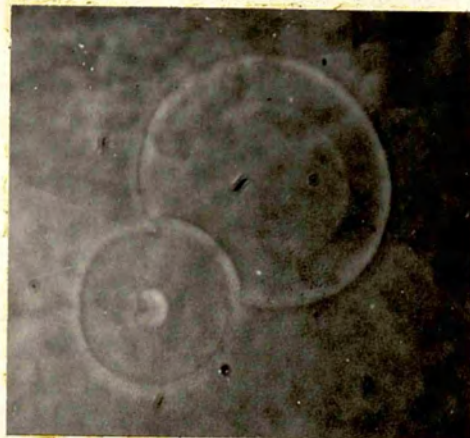


FIG.176a  
x600

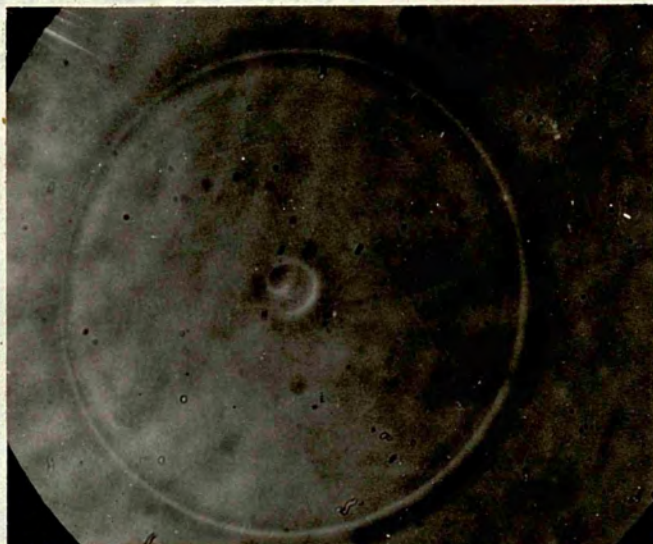


FIG.176b  
x600

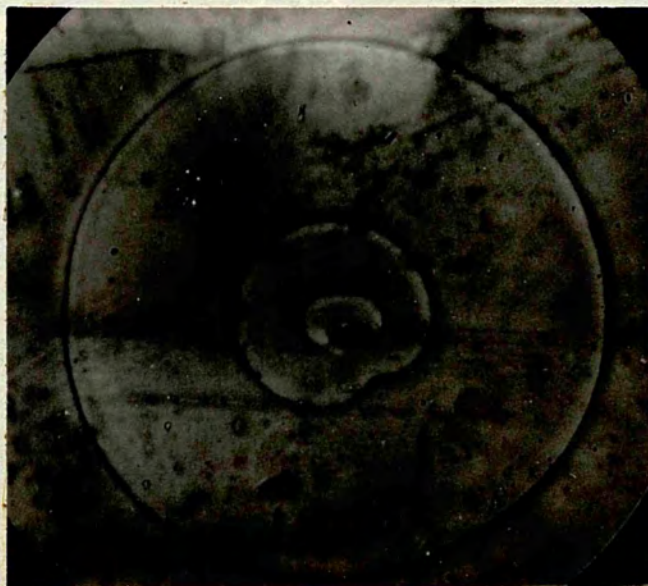


FIG.176c  
x600



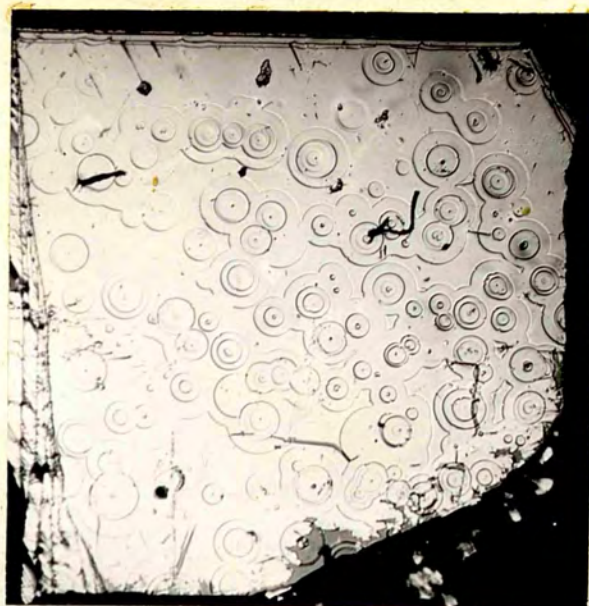


FIG.177  
x100

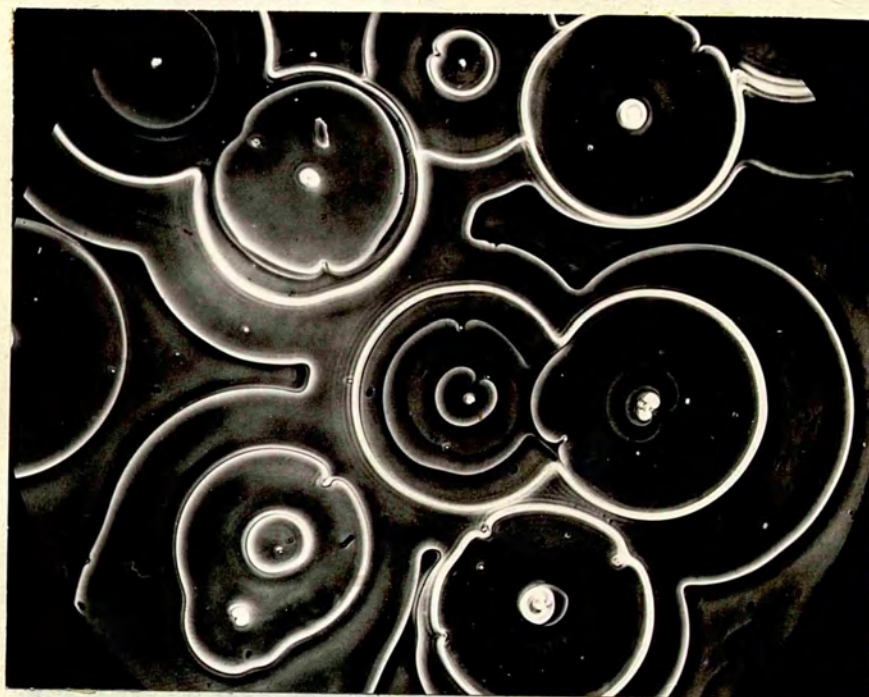


FIG.178a  
x375



FIG.178b  
x300(reduced)



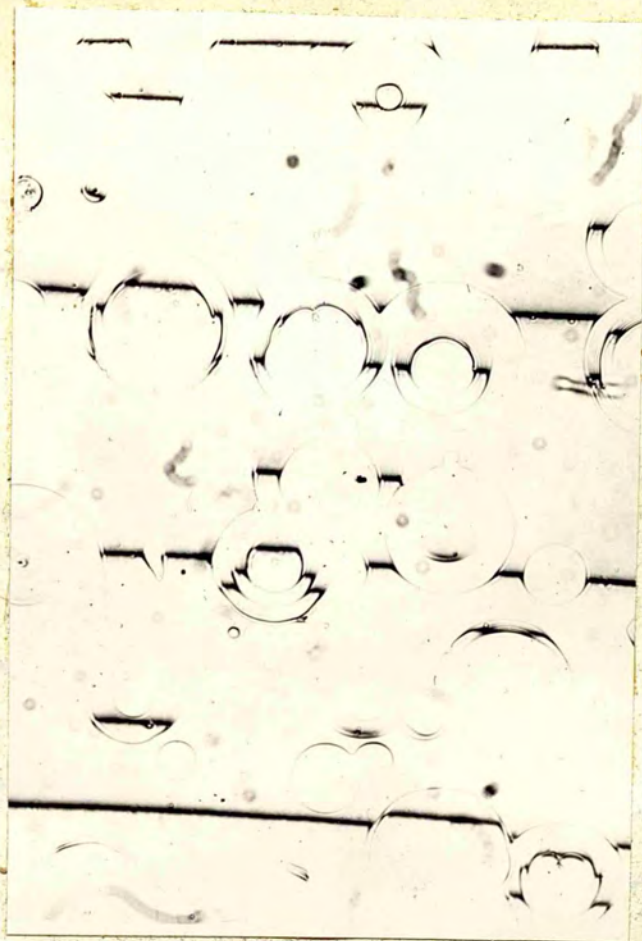


FIG.179  
x300

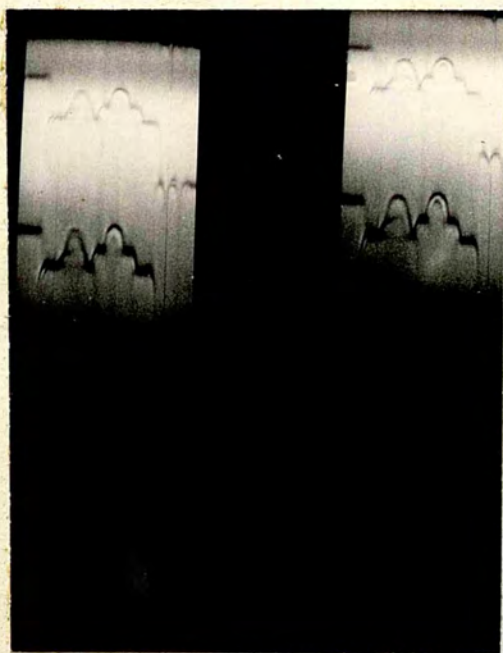


FIG.180

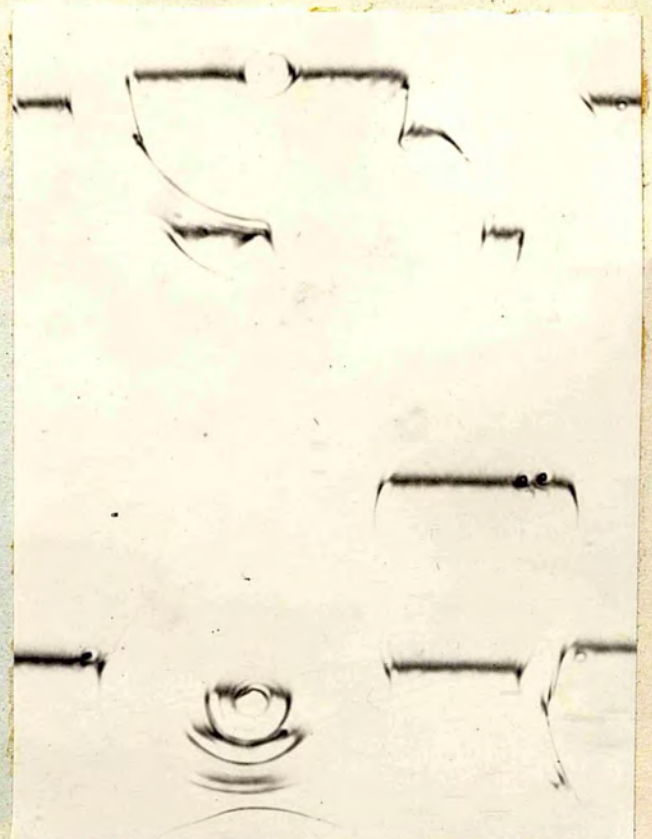


FIG.181  
x450



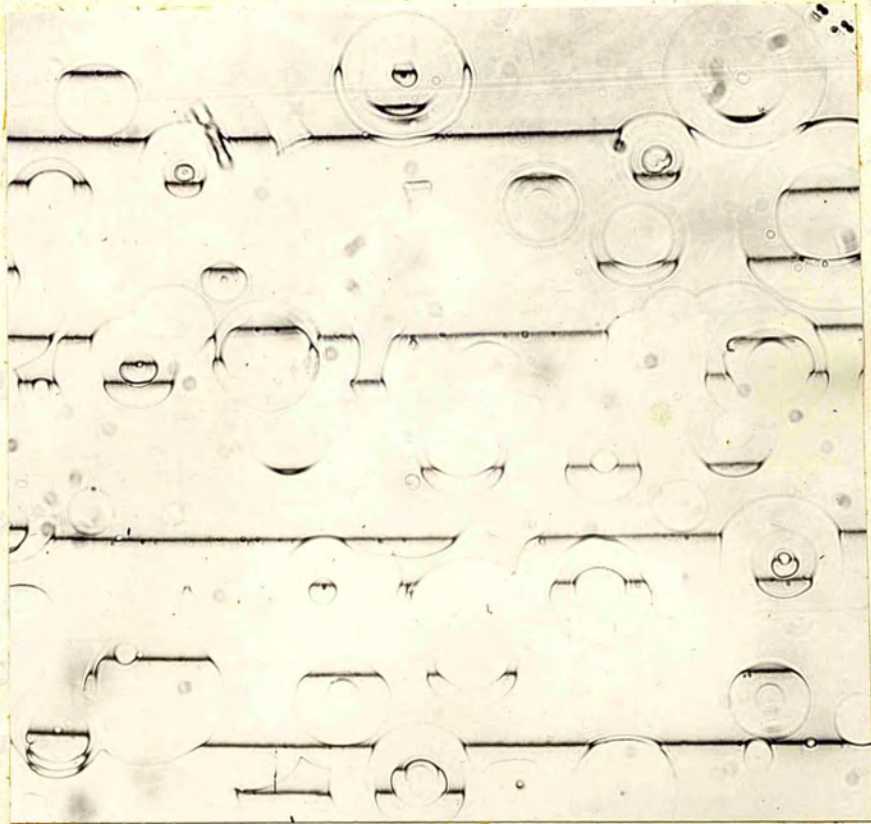


FIG.182  
x300

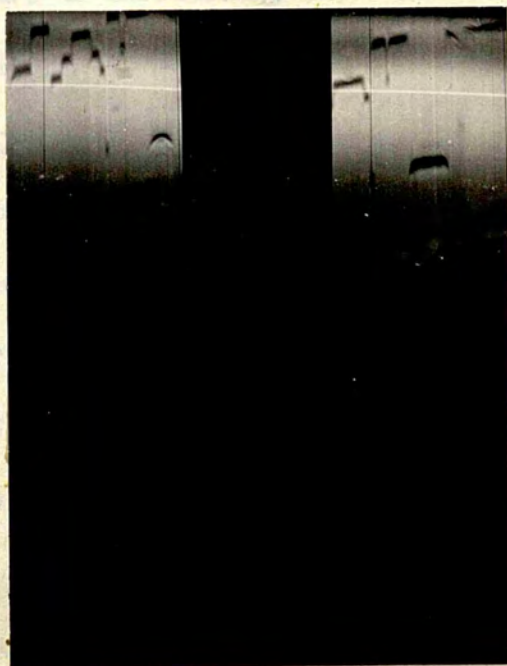


FIG.183



Figure 183 shows the white light fringes for two more pits. They show the same characteristics as figure 180 except that the bottom of the pits in this case is flat. The step-heights in these crystals range from 180A to 910A. The back reflection c-axis Laue photograph of one of these crystals shows a hexagonal symmetry.

### Category (c)

Each crystal under this category was invariably bound with another crystal and often with pressure broke along  $[11\bar{2}0]$  direction. Figure 184 shows a crystal of this type. The left side of this figure shows interlaced spirals and the right side shows isolated and mixed features. Figure 185 gives the Fizeau fringes on a part of the crystal. The fringes on this crystal could not be improved as it showed a tendency to break when pressed too hard against a matching flat.

Figure 186 shows a positive phase-contrast picture of a single-layered isolated circular feature with a dislocation emerging at its centre. Figure 187 is a doubled-layered isolated circular feature, with each of the layers further resolved. Each layer shows a dislocation point near the circumference. Figure 188 is a twin feature; one of them has two circular layers with a dislocation point at the centre. The other is also two layered but the smaller layer is the outcome of two opposite dislocations, although only one dislocation



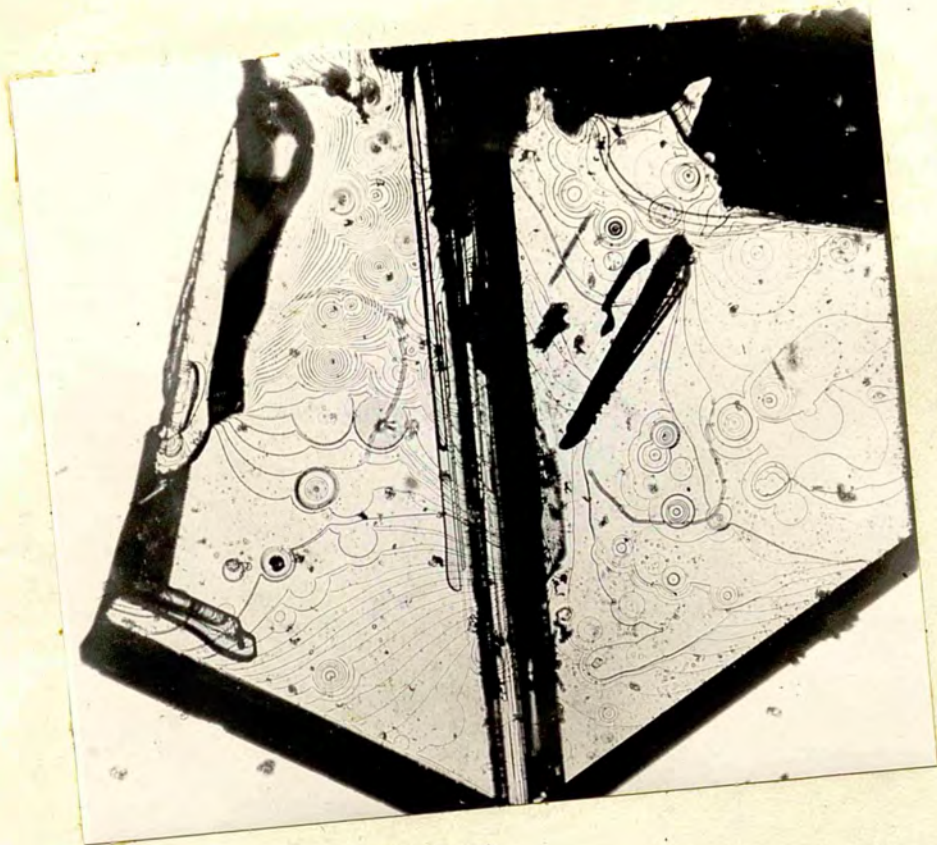


FIG.184  
x45

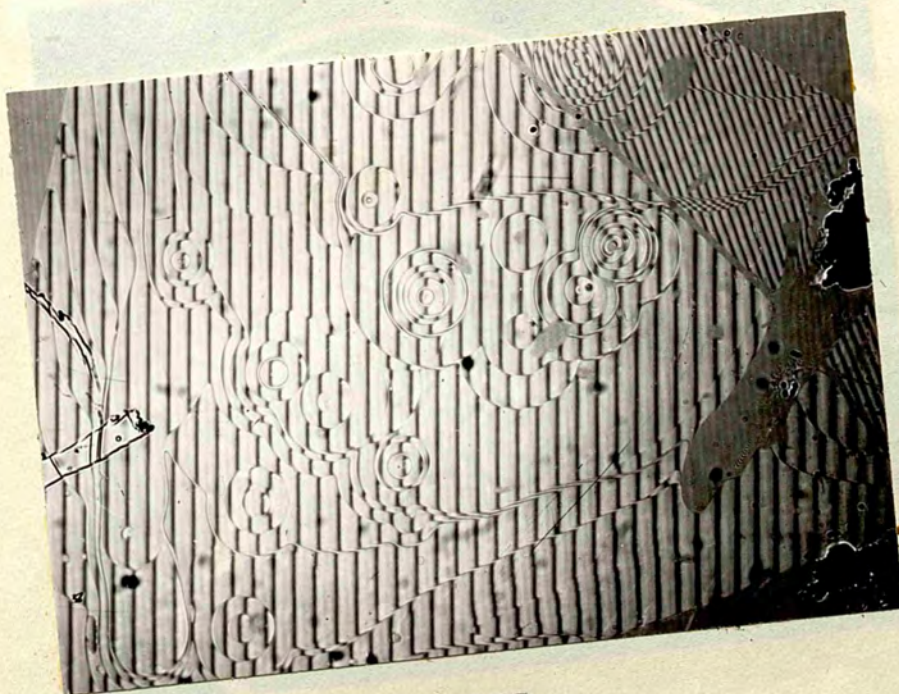


FIG.185  
x110



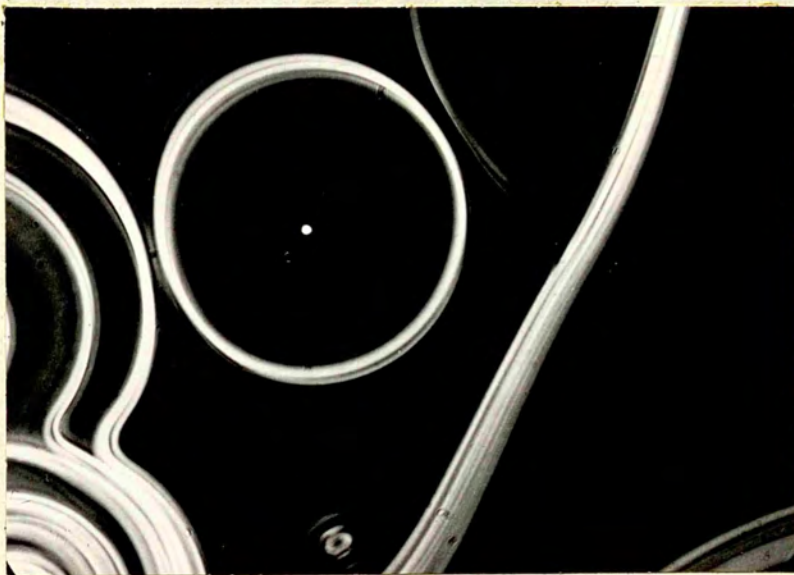


FIG.186  
x600

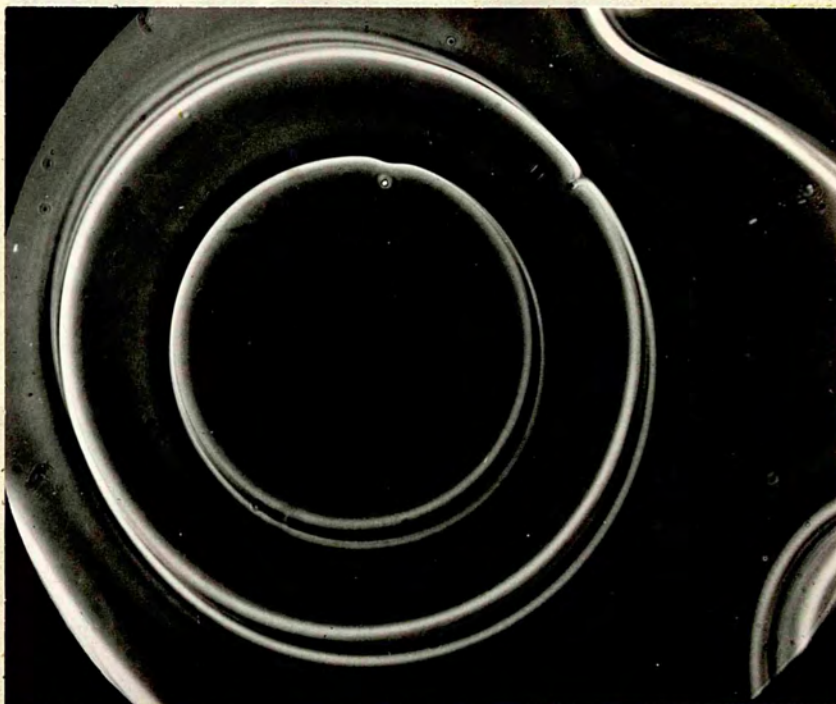


FIG.187  
x600



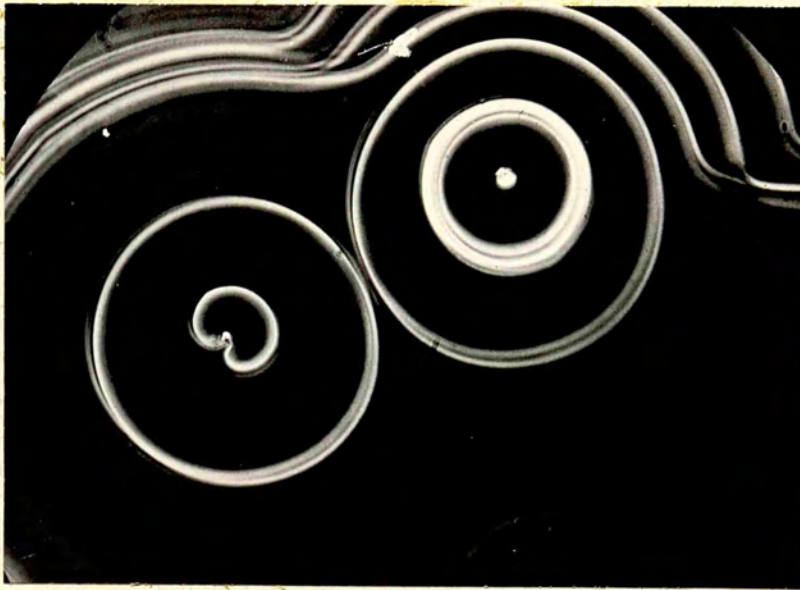


FIG.188  
x600

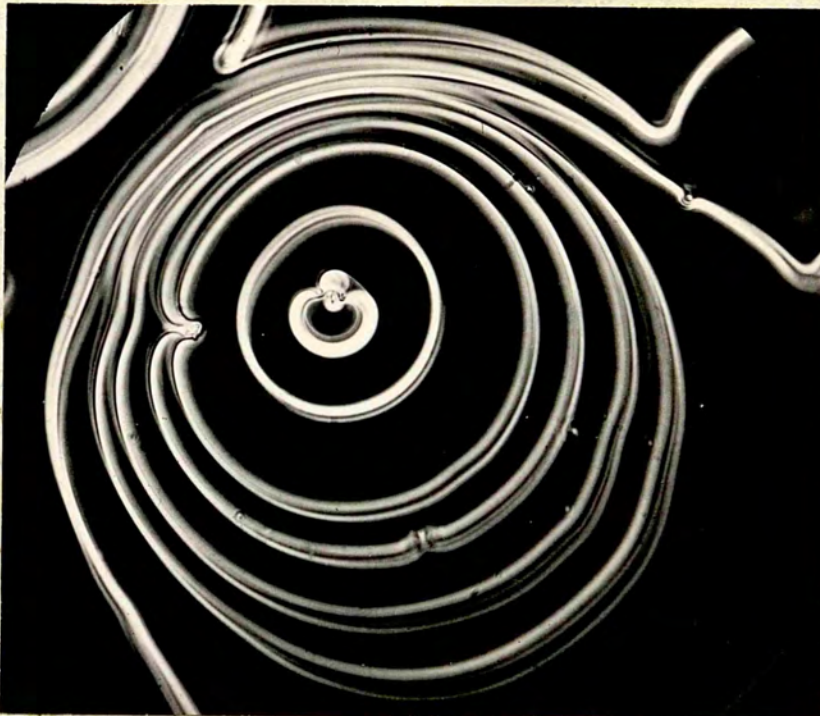


FIG.189  
x600

point is visible at the centre. Some of such features when observed under very high magnifications (phase-contrast) did show two points of emergence of dislocations. Figure 189 is a six-stepped circular feature; in this picture it is interesting to note that the inner most step shows the dislocation emerging at its centre but some of the other steps show the dislocation points at the circumference. Phase-contrast technique has helped in the further resolution of the major steps.

Figure 190 shows the fringe pattern on a feature with mercury light of which figure 190 gives the white light fringes. These fringes are convex towards the red indicating that they represent a depression. Since it was not possible to take white light fringes for every feature, by using oil-immersion objective with the Olympus microscope and noting the direction of motion of the fine-motion screw, it was ascertained that the features were depressions. Also this specimen was lost and hence more white light fringes could not be obtained.

Figure 191 shows Fizeau fringes on two spirals. Table (1) gives the step-heights of the left hand spiral, the step-heights being counted from inside. Figures 192 to 198 give Fizeau fringes obtained on different types of features already described. Table (2) gives the step-heights of the features. It is worth noting that figures 196 and 198 show that the innermost step is an elevation.



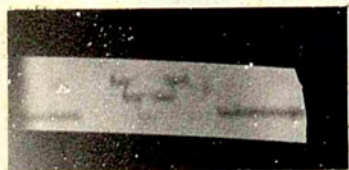
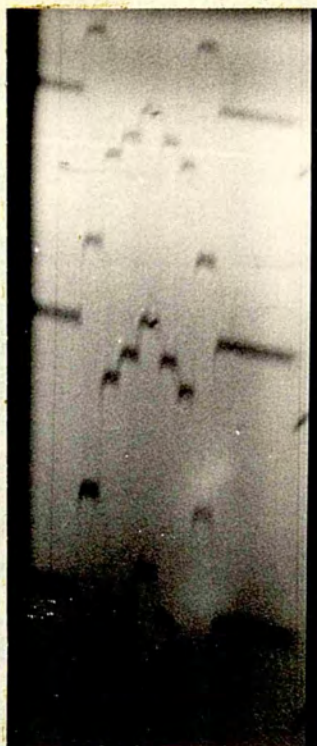


FIG. 190a



R

V

FIG. 190b



FIG. 191  
x225



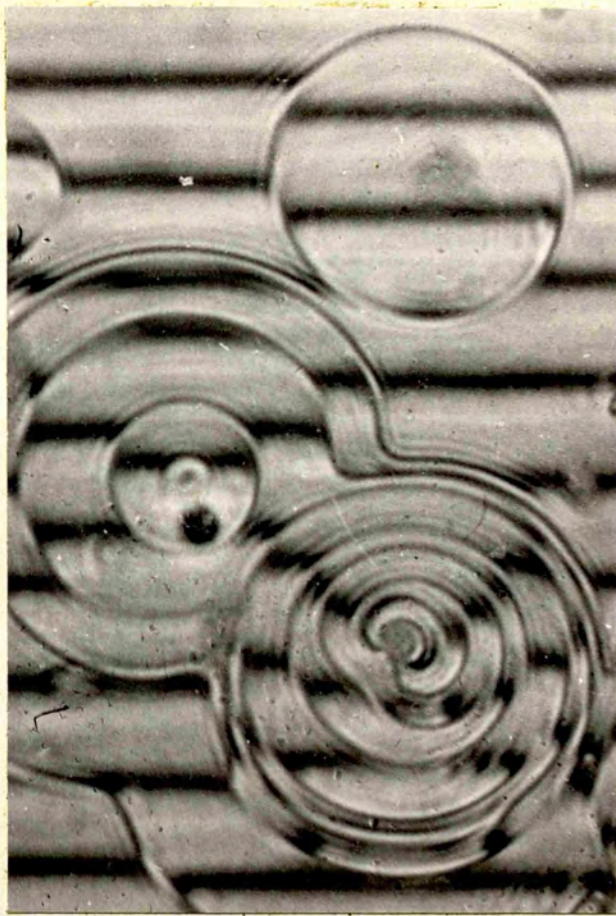


FIG.192  
x600

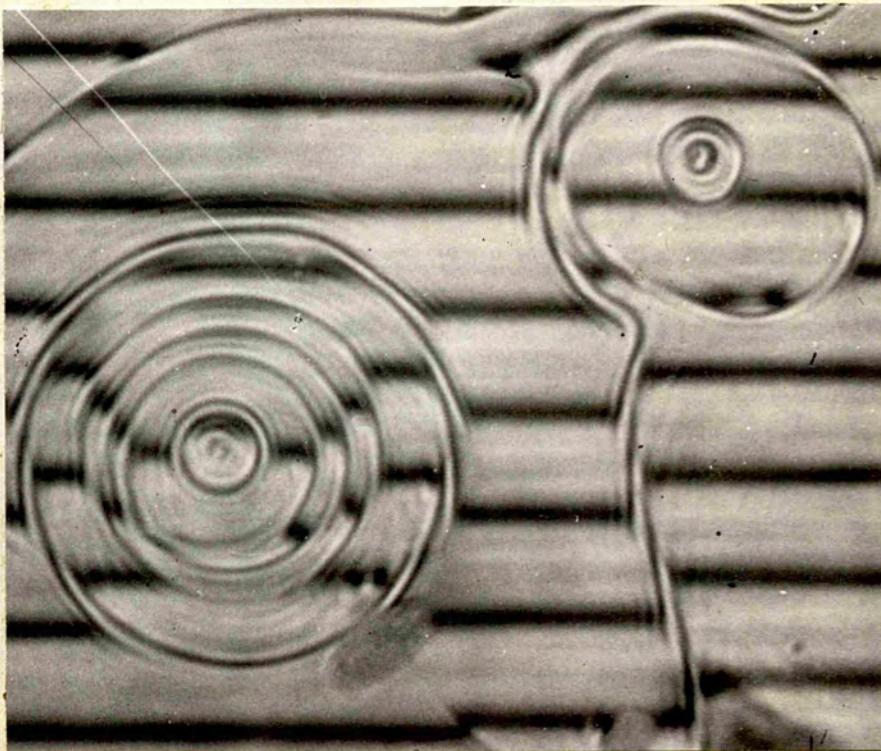


FIG.193  
x600



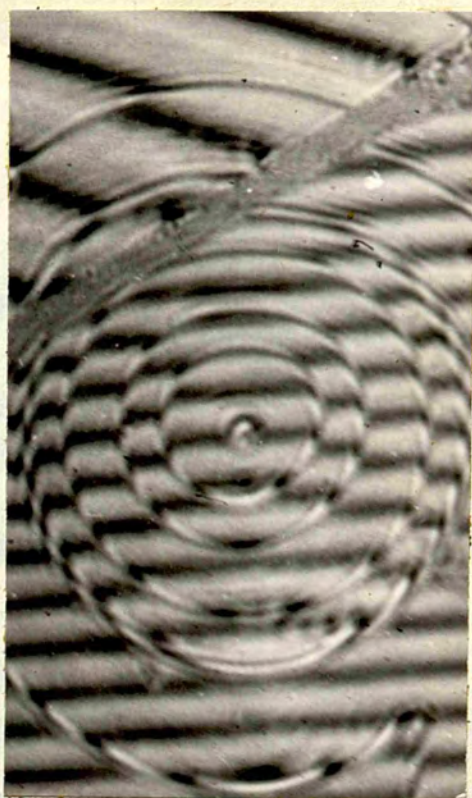


FIG.194  
x600



FIG.195  
x600



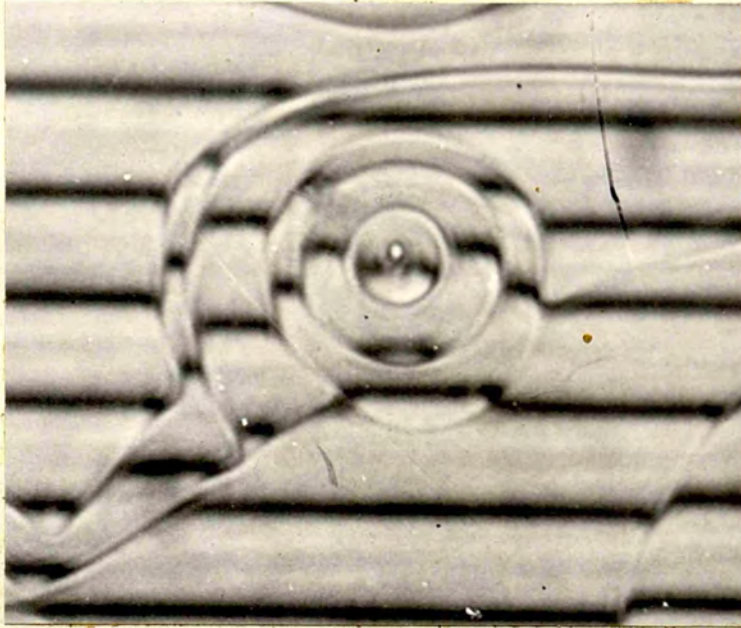


FIG. 196  
x600

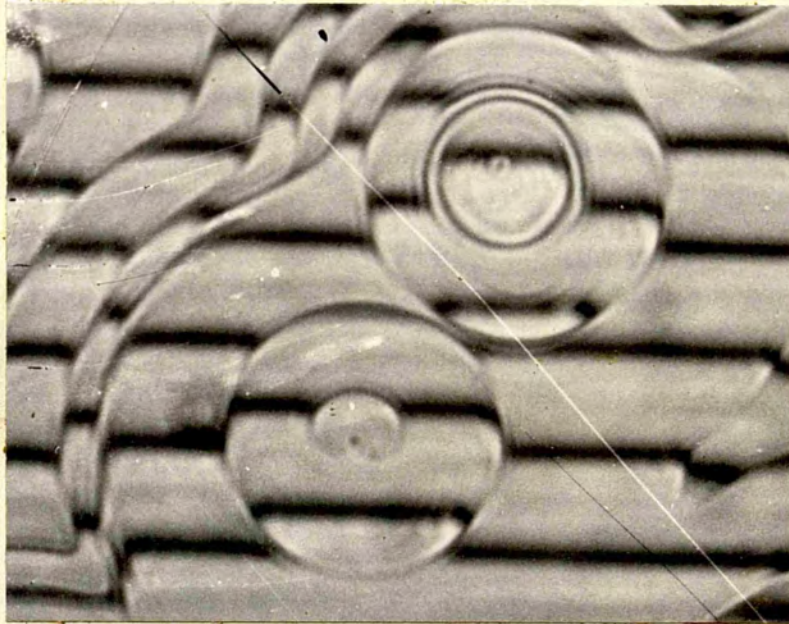


FIG. 197  
x600

Fig-  
193  
(lower)  
194

195 (left)  
195 (right)

196

197 (top)  
197 (lower)

198



FIG. 198  
x600



TABLE 1

(Fig.191, Left Spiral)

Step No	Height in A
1	1057
2	1047
3	1060
4	1030
5	1091
6	1083
7	998
8	1273
9	1284

TABLE 2

Fig.	Step-height from inside in A
193 (lower)	2138,2138,2138,3916
194	1092,1092,1092,3276
195 (left)	712,1069
195(right)	712,356,1069
196	356,1069,356
197 (top)	1424,1069,356
197(lower)	1069
198	356,1069,1069

Category (d)

In this category a description is given of the pits observed in between the steps of a single hollow spiral occupying the entire surface of the crystal. Figure 200 shows a circular spiral whose spacing is non-uniform across its face. From the centre to the left the spacing increases and to the right it decreases. It is in this right region of the spiral that a number of subsidiary circular features have been observed. Figure 201 is a phase-contrast picture of the origin of the spiral taken with an oil-immersion objective. Figures 202 and 203 show the phase-contrast pictures of the subsidiary features. Figure 204 is an oil-immersion negative phase-contrast picture of a twin 10-layered feature and figure 205 is a similar photograph of a single feature.

Figure 206 shows the Fizeau fringes on the entire spiral and figure 207 is also a similar Fizeau pattern with a fringe passing through the 'tongue' of the spiral near the point of emergence of the screw dislocation. Figure 208 is a magnified picture of the fringe pattern on the 'tongue'. Figure 209 is a magnified Fizeau fringe pattern on the steps of the spiral, the step height of which is 161Å. Figure 210 gives the Fizeau fringes on the subsidiary features. Figures 211a and 211b represent respectively the mercury light and white light fringes through one of these features. The



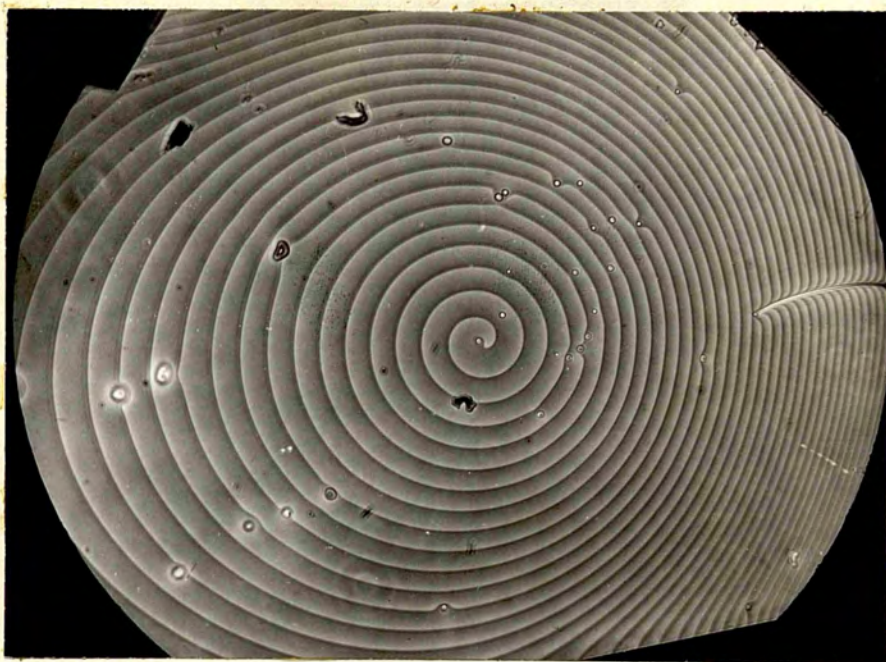


FIG.200  
x75



FIG.201  
x750(reduced)

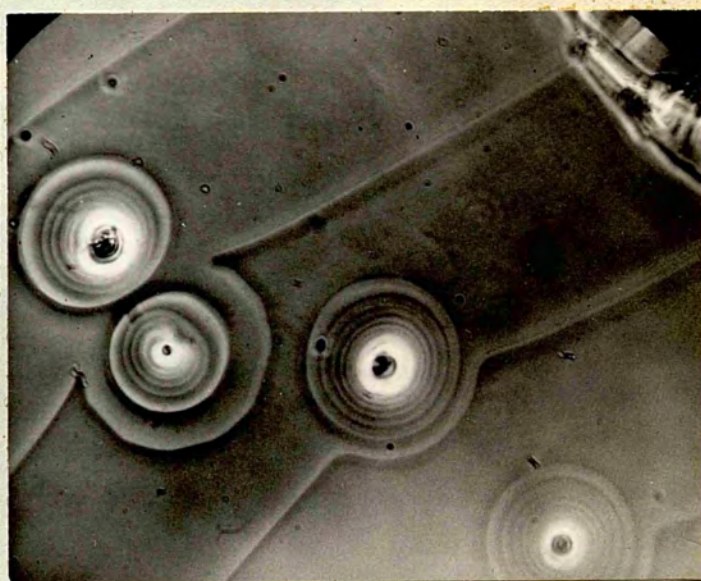


FIG.202  
x300





FIG.203  
x300

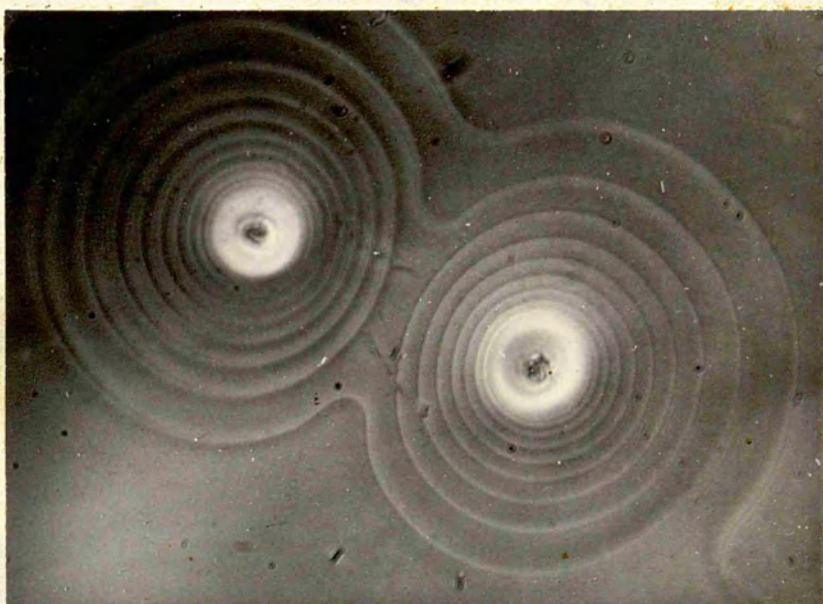


FIG.204  
x1200

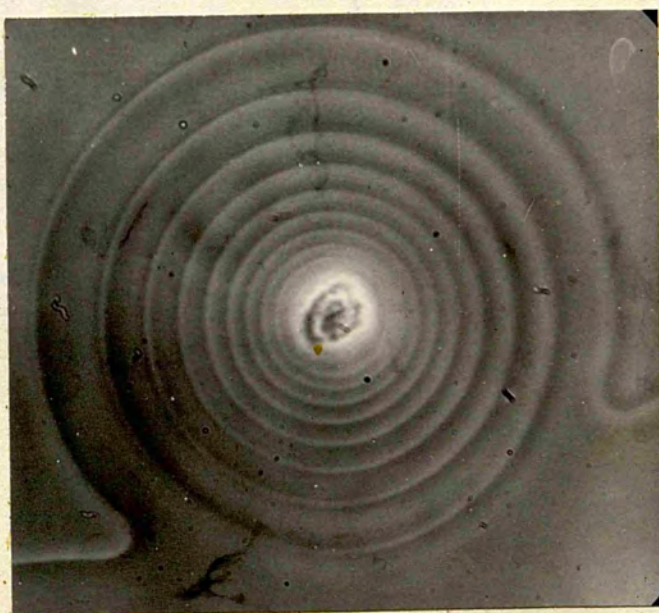


FIG.205  
x1200



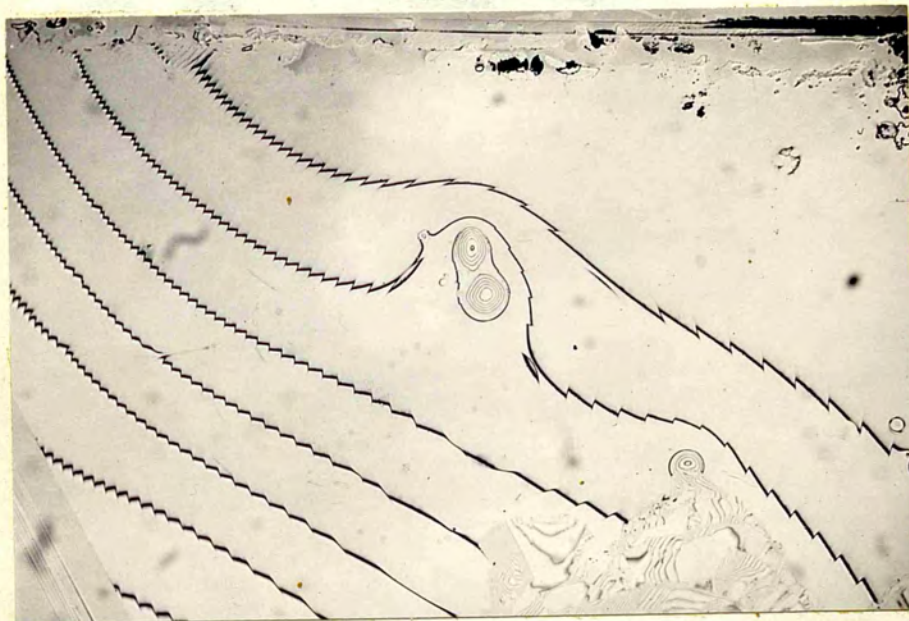


FIG.206  
x95

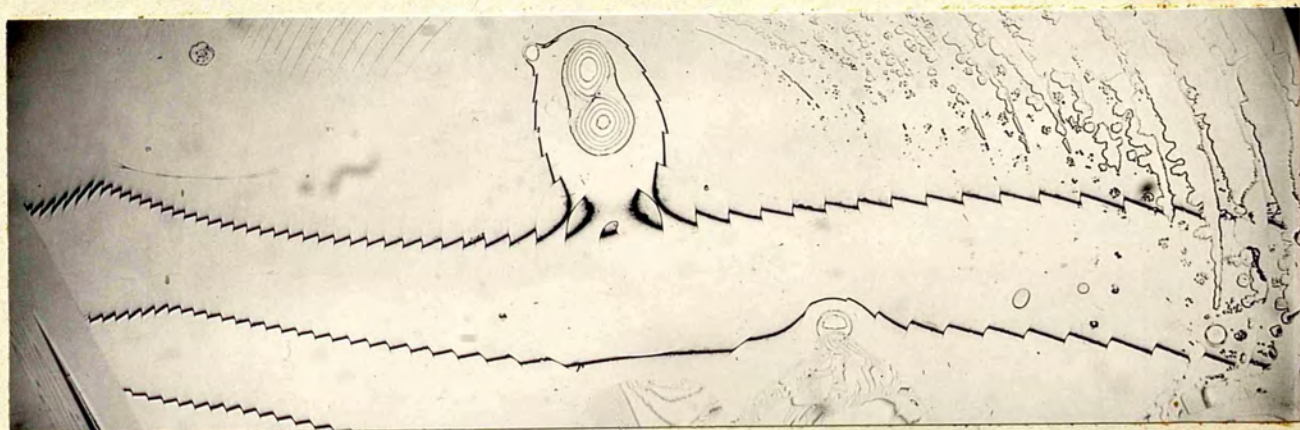


FIG.207  
x110





FIG.208  
x500

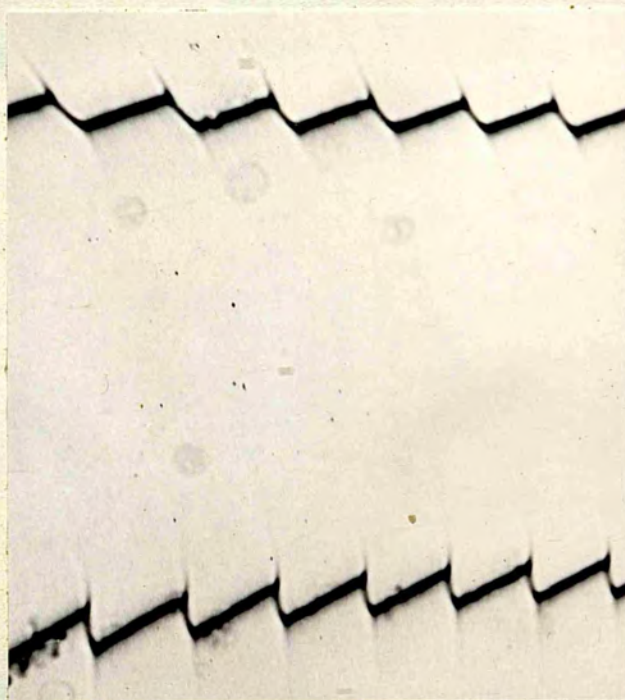


FIG.209  
x500



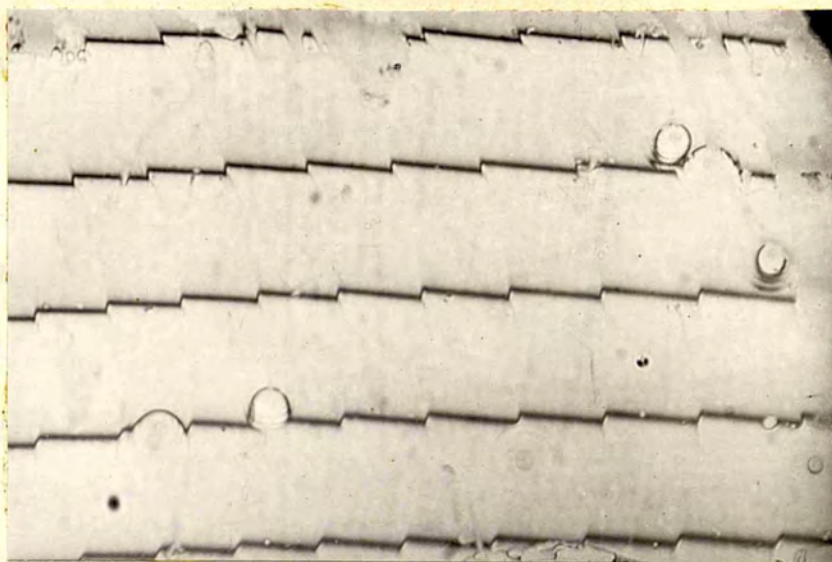


FIG.210  
x150

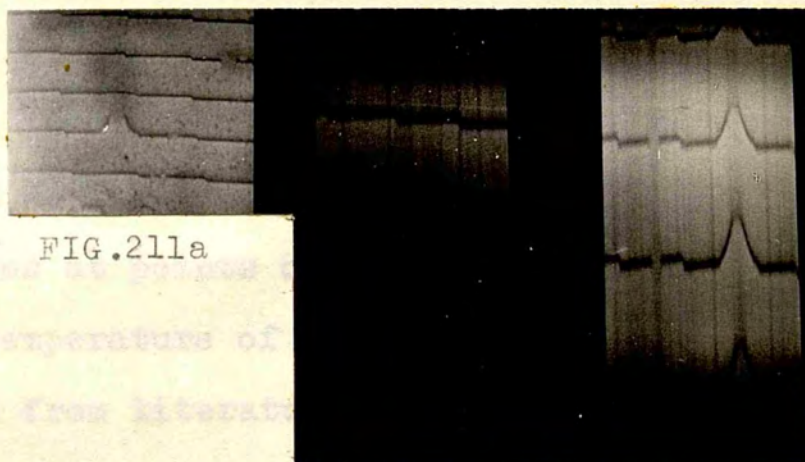


FIG.211a

FIG.211b

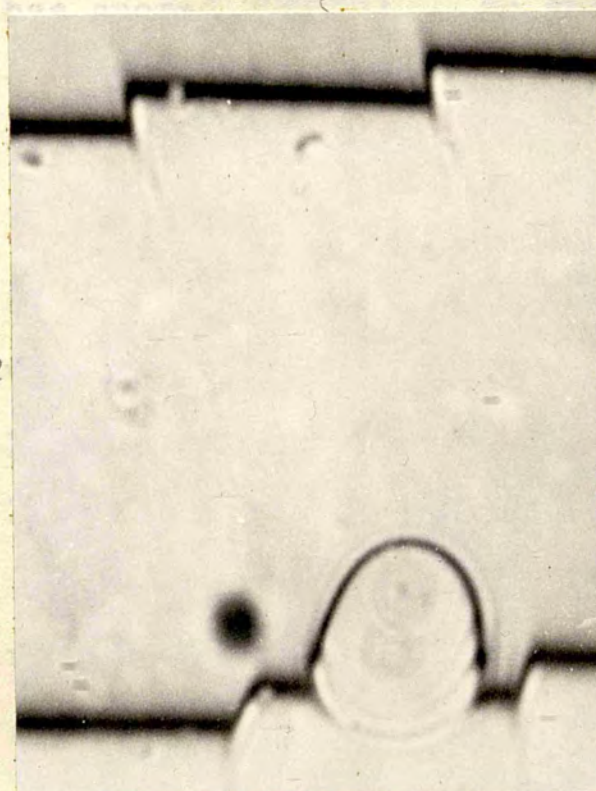


FIG.212  
x690

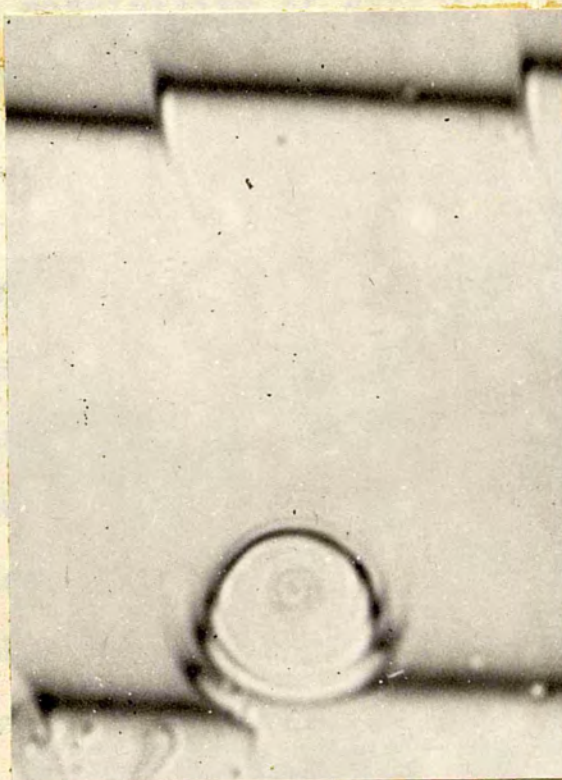


FIG.213  
x690

white light fringes are convex towards the red and hence represent a depression with a slight conical point bottom. Figure 212 is a magnified fringe pattern on a twin feature of depth 730A. Figure 213 is a similar fringe pattern on a single feature of depth 730A.

#### Discussion of the observations

The essential fact about all the features described above is that they are depressions and not elevations. These depressions may have formed during the growth of the crystals or might have occurred after the growth has taken place in the form of evaporation of molecules at points of emergence of dislocations.

The temperature of formation of these crystals is  $2500^{\circ}\text{C}$  and from literature the decomposition temperature of silicon carbide is about  $2200^{\circ}\text{C}$  (although one author has quoted  $2700^{\circ}\text{C}$ ). So the possibility of evaporation taking place at the temperature of  $2500^{\circ}\text{C}$  is definitely there.

Although the actual mode of growth of these commercial samples of silicon carbide is not known, there is evidence (1950,1952) to suggest that the growth takes place either by a vapour-phase reaction or sublimation. If during the process of growth the super-saturation on the surface of the crystal is gradually reduced, a stage will be reached when no further layer will spread on the surface of the crystal; that is growth will cease.



If the vapour pressure is further reduced so that it becomes under-saturated, then the direction of motion of the molecules will be reversed. In such a state the hillocks formed during growth at dislocation points, will become valleys due to evaporation. The depth of these valleys at the points of dislocation will increase if the evaporation is rapid. The actual mechanism of this reversal process from growth to evaporation will, however, be influenced by other factors such as impurities, general layer retraction and uneven evaporation due to different under-saturation across the crystal surface. The reversal from growth to evaporation will take place essentially in an unstable state and hence quantitative deductions from the studies of this process will be difficult, unless information about transition conditions is available.

An attempt will be made here to explain broadly the occurrence of the different types of features described, on the basis of Cabrera and Levine's dislocation theory of evaporation and in the light of the cinemicrographic observations of evaporation process by Lemmlein and his co-workers (1957) and the study of evaporation pits by Dukova (1961).

The important conclusions of Cabrera and Levine's theory have already been summarised in the chapter on 'Crystal Growth'. At the risk of repetition, some of these points will again be considered. The following



are the salient points of the theory:

(a) Spiral rotation during evaporation could be represented by the same set of equations as were found to hold good for growth in the theory proposed for crystal growth by Cabrera, Burton and Frank(1949). To distinguish evaporation from growth, the evaporation theory took account of the supplementary energy localized around the dislocation.

(b) Limiting to only dislocations finishing at the surface with a screw component and giving rise to steps on the surface, the theory showed that, when a crystal is evaporating, there is a limiting value of the undersaturation beyond which the core of the dislocation is unable to remain closed; otherwise it must open up. Then the crystal evaporates from the free surface as well as side-wise from the core of the dislocation outwards, forming a macroscopic pit. At the critical value itself, the radius of the core remains sub-microscopic.

(c) In the simplest cases of evaporation into vapour, a very low undersaturation will be sufficient to open-up a dislocation of large Burgers vector; on the contrary very large undersaturation might be necessary to open-up dislocations with an elementary Burgers vector. The actual value of undersaturation will be very sensitive to the value of the surface energy per unit surface of the edge of the step.

(d) The semi-vertical angle  $\beta$  of the conical surface of the crystal remains very nearly  $\pi/2$  for large Burgers vector but diminishes to values of the order of  $\pi/3$  for smaller Burgers vector.

Lemmlein, Dukova and Chernov (1957) observed evaporation from the whole surface of crystals of p-toluidine and naphthalene. They noted that when a crystal growing from the gas phase is observed as the evaporation temperature is reduced (which reduces the vapour pressure), the layers cease to spread over the surface. The layers are motionless at equilibrium; if the vapour becomes unsaturated the direction of motion reverses. They recorded their observations in a motion picture film.

Dukova (1961) has recorded the layer separation process of an evaporation spiral on crystals of para-toluidine. He came to the conclusion that the mechanism responsible for the formation of a spiral evaporation pit is the process of the layer separation of the evaporation spiral. He observed this from the change in interference colours under crossed nicols.

Amelinckx and Votava (1953) also observed evaporation spirals although failed to detect evaporation pits on NaCl crystals.

Studies on etch figures suggest that dissolution is also a spiral-layer process so that evaporation can

also be thought of as 'thermal etching'.

We can, therefore, conclude that the observed features under category (a), (b) and (c) are due to evaporation at the points of emergence of the dislocations. As long as the dislocation is closed, a growth spiral, on evaporation will retain its entire spiral character and the different step-heights will be the same as the first seven (from inside) steps of figure 191 are. The last two step-heights are higher presumably due to surface evaporation resulting from gradual opening-up of the dislocation. In general the steps of these spiral depressions will not be equal if the dislocation were to open-up, because evaporation will take place from the free surface and sidewise from the core of the dislocation. This is in fact found to be the case in almost all the depressions observed. The annular surface area of most of the steps, nearer the surface of the crystal is wider than the deeper steps; this is because, being nearer the surface, and initially having a larger area, more molecules will evaporate from them than from inside. In other words there is more evaporation from the free surface than sidewise.

If the evaporation from the surface of the crystal is more than from the core of the dislocation, it is possible to expect in such cases the core at a higher level than its immediately higher step as has been noted



in figures 176, 196 and 198.

If on the other hand evaporation takes place only from the dislocation overgrowth and the dislocations do not open-up during evaporation then raised pits can be expected as in category (b). If this is followed by different amounts of evaporation from the entire surface of the crystal, then the steps will be unequal. The overlapping of the features may be due to simultaneous preferential growth and evaporation. The flat bottoms of the pits may be due to larger Burgers vectors and the conical bottoms due to small Burgers vectors of the dislocation.

In category (c) half the crystal (fig. 184) shows spirals with almost same step-heights meaning thereby that the spiral dislocations have not opened-up; where as the right hand side of the crystal shows features with unequal steps indicating that the dislocations have opened-up during evaporation. In between the two sides along the  $[11\bar{2}0]$  direction there was another crystal loosely attached which was removed. Perhaps due to this the two parts might have had different undersaturations and also the surface energy may be different.

In category (d) (figure 200) the entire spiral might have evaporated without dislocations opening-up and hence the step-heights are the same. The interesting feature of this evaporation spiral is that it changes direction

from clock-wise to anti-clock wise, slightly away from its point of emergence forming a 'tongue'(figure 201). Lemmlein and his co-workers actually observed such a 'tongue' in their earlier experiments, while studying the transformation of a growth spiral into an evaporation one. They explained this by applying Cabrera and Levine's theory to the behaviour of the spiral when it is in a nonsteady state. The relevant part of their explanation is as follows:

The angular velocity ( $\omega$ ) of a spiral which derives from a nucleus of critical radius  $\rho_c$  is given by

$$\omega = \frac{v_{\infty}}{r} \left(1 - \frac{\rho_c}{r}\right) \sqrt{1 + (r \theta')^2} \quad (1)$$

where  $v_{\infty}$  is the velocity of advance of a straight step far from the origin and  $\rho$  is the radius of curvature of the spiral at the point  $(r, \theta)$ . Suppose the vapour pressure suddenly falls below the equilibrium value at time  $t=0$ , so that the critical nucleus is  $-\rho_c$  and the layer velocity  $v_{\infty}$ , then it can be shown that

$$\frac{\partial \theta}{\partial t} \Big|_{t=0} = -\frac{2v_{\infty}}{r} \text{ when } r \ll \rho_c \quad (2a)$$

$$\frac{\partial \theta}{\partial t} \Big|_{t=0} = -\omega \left(1 + \frac{2\rho_c}{r}\right) \text{ when } r \gg \rho_c \quad (2b)$$

The angular velocity immediately after the conditions change is then infinity (eq.2a) at the point where the screw dislocation emerges; but only slightly greater

than  $\omega$  far from the centre (eq.2b). The spiral thus begins to uncoil rapidly at the centre; the central area takes the form shown in figure 201. It might be thought that the tip of the 'tongue' (fig.201) would move on and alter the sign of the curvature all along the spiral (reverse the spiral). If this were to occur,  $\omega$  from the origin to the tip should be greater in absolute magnitude than in the area outside the tip. However, eq.(2b) shows that this is not so. The tip will, therefore, not move on along the spiral.

So far our observations are in agreement with this analysis. Their further analysis shows that the distance between the turns will increase with time and the angle at the top of the growth cone will tend toward  $\pi$ . The tip then propagates rapidly along the spiral, and an evaporation pit instead of the outgrowth is got. The rest of the spiral is in general agreement with this analysis except that the distance between the turns increases on one side of the centre and decreases on the other side.

Coming to the subsidiary features, figures 202 and 203 indicate that these features were formed before the formation of the spiral as it is clearly seen that the spiral steps alter their course when they meet these features. It means evaporation from these points took place earlier than from the spiral. The reason why such



features should be observed where the spiral turns are nearer, can be found by extending Frank's theory (1951) for non-uniform spacing of spiral turns in growth spirals. According to this theory the greater the supersaturation the nearer will be the spacing. If likewise it is assumed in an evaporation spiral that the nearer the spacing the greater the undersaturation, then it is reasonable to expect evaporation pits in a more undersaturated area as in this case. Figures 204 and 205 do not give any indication of the points of emergence of the dislocations on the other hand the cores give evidence of some impurity. So these pits may well be centred round these impurities. Figure 211b shows also that these pits have rounded point bottoms which may be associated with these impurities. In that case it may be possible that evaporation centred round impurity points may take place in the form of circular layers as the pictures show.

CHAPTER XIII

STUDY OF SOME ADDITIONAL FEATURES ON SILICON CARBIDE CRYSTALS

Growth Layers on (1011) face of silicon carbide crystal

In the sample of silicon carbide crystals supplied to us, a crystal has been found which is 1.35 cm in length and 0.40 cm in thickness. It shows two (0001) faces, four trigonal pyramid faces and two prism faces very well developed; Goniometric studies indicate that it has a rhombohedral lattice belonging to  $R\bar{3}m$  space group; the crystal is indeed very uncommon because it is rare for this space group to have prism faces, as in this case. There is no mention in the literature of the existence of such a silicon carbide crystal so far.

It is on one of the trigonal pyramidal faces that the feature shown in figure 214 has been found. This feature covers the entire face and consists of a stack of more than seventeen growth layers. Figure 215 is a phase-contrast picture of part of these layers. Figure 216 is a double-beam interference fringe pattern on the feature. Figure 217 shows the multiple-beam fringe pattern on the same taken with low dispersion; figure 218 shows the same with high dispersion. Microscopically it was found that the feature was an elevation. From the Fizeau fringes the step--heights from the first (inside) to the seventeenth layer have been determined;



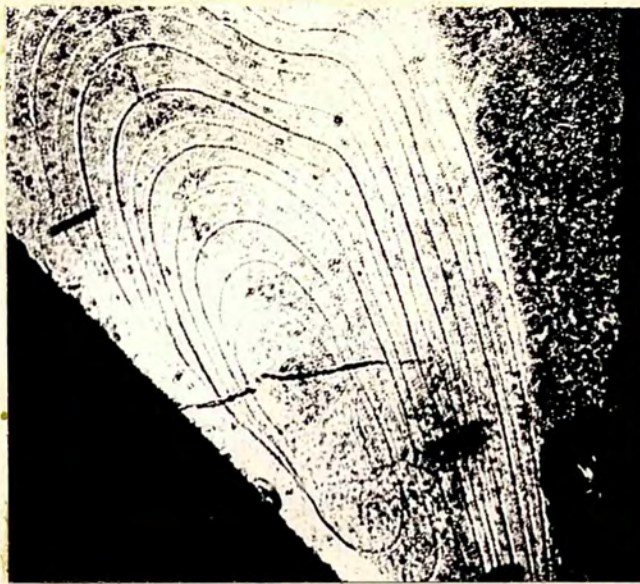


FIG.214  
x90



FIG.215  
x300



FIG.216  
x90





FIG.217

x90



FIG.218

x150



Table (1) shows the observed step-heights.

Discussion of the observations

Figure 214 shows that the layer growth has started from the bottom (left-hand) edge of the face and spread towards the other edges of the face. The right edge seen in the figure is also the edge of the basal plane (000 | ) of the crystal.

Bunn (1949) has pointed out that the edges and corners of a crystal face, are the places where there are most unsatisfied forces and these are the places where nuclei for the inception of new layers would be expected to form. Kossel, Stransky, Brandes and Volmer have calculated the energy yield when adding an ion to various places on a crystal surface and their calculations indicate that, if the event of greatest energy yield is to be statistically preferred, then the inception of new layers is most likely to occur at the edges or corners than in the centre of a face. The observed growth layer pattern is in agreement with this analysis.

As a matter of interest it is worthwhile comparing this observation with the studies made by Bunn and Emmett (1949) on crystal growth from solution. The following are some of their observations:

(1) Layers very often start, not from edges or corners of crystals, but from the centres of faces, spreading outwards towards the edges.

(2) The thickness of the layers on many crystals increases as the layers approach the edges of the crystal face.

(3) The boundaries of the layers are often irregular, especially when growth is rapid; but as growth slows down there is a tendency to regulate shape conforming to the symmetry of the crystal face.

(4) Thick layers have been seen only on crystals of certain ionic and polar substances. They have not been seen on crystals of non-polar substances.

Our observations are contrary to (1) and similar to (3). Table (1) shows that (2) is also not true in this case. Silicon carbide is a homopolar substance and does show thick layers as indicated in table (1). This is in agreement with (4). It may, however, be stated that silicon carbide grows either by a vapour-phase reaction or sublimation and Bunn's observations were based on growth from solution. At the same time it may be emphasized that our observations are more in agreement with theory.

#### Floral patterns on silicon carbide crystals

In a sample of silicon carbide crystals supplied by Phillips (Hollond), certain crystals showed some interesting floral patterns. These crystals were either light green or dark green and had grown with the (0001) face plane, on which the patterns were observed. The crystal faces were mostly about 7-9 mm across and hexagonal



TABLE (1)

No of the step	Step-height in A
----------------	------------------

---

1	219
2	497
3	352
4	352
5	128
6	341
7	273
8	270
9	763
10	382
11	624
12	208
13	663
14	645
15	338
16	546
17	306

---



FIG.219

x90



FIG.220

x90



in shape. The crystals in general were wedge shaped and tapered to form a sharp edge on one side of the basal plane.

The patterns shown in figures 219 and 220 were observed only well away from the edges and corners of the crystals. Figures 221 and 222 show patterns which are spread out along the edges of the crystal, with a slightly higher concentration at the corners. These features also appear very thinly spread out on the rest of the crystal face. Figure 223 shows a feature, like an elephant's trunk, which is limited only to the edges of the crystal surface. The rest of the surface is almost without any pattern at all.

Since these patterns were visible only on pale green or dark green crystals, which are likely to contain iron as an impurity, their existence may perhaps be attributed to this impurity.

Spiral and spiral-like features on basal-plane surface  
edges of SiC

In the Swiss sample of silicon carbide crystals there were some green crystals with well formed basal plane edges and corners without the rest of the plane formed at all. Each crystal consisted of a stack of different layers of such edges and corners displaced with respect to one another and looking like a stair-case from the opposite side of the basal plane. It is on the



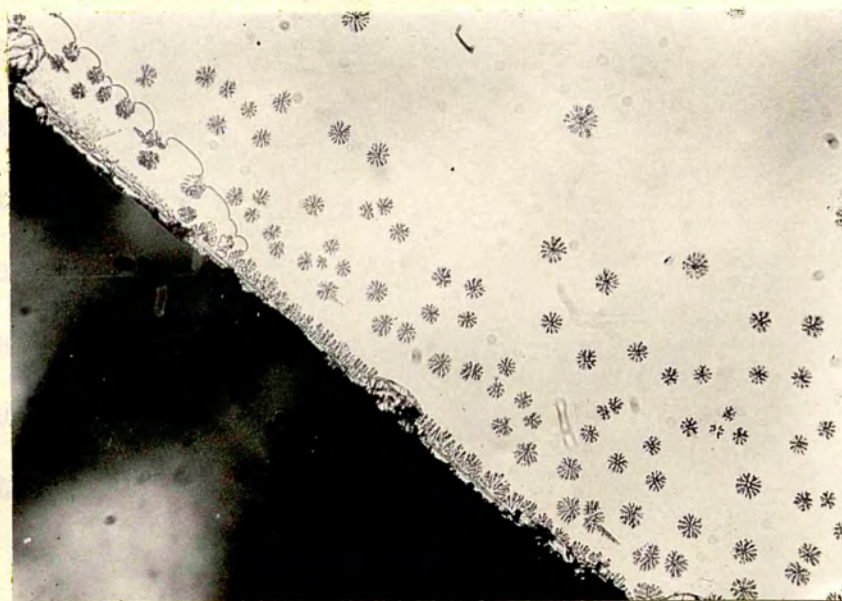


FIG.221

x90

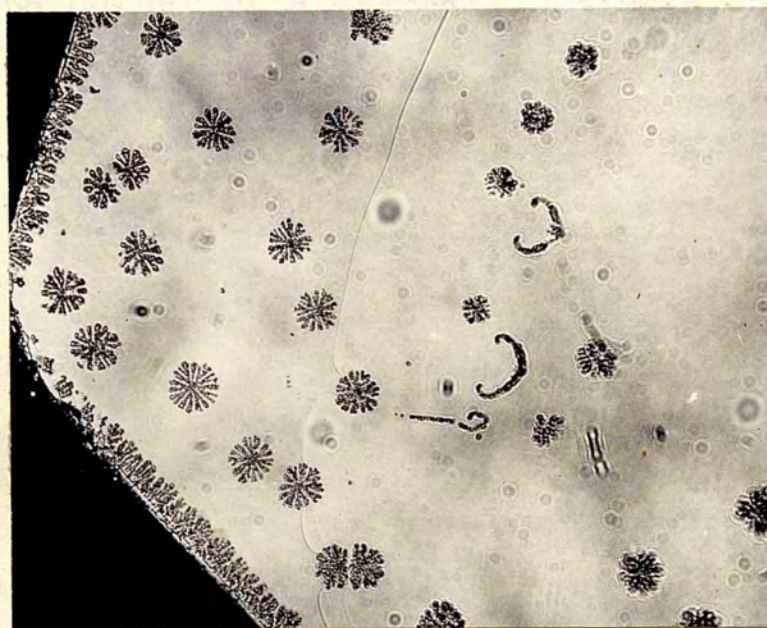


FIG.222

x90

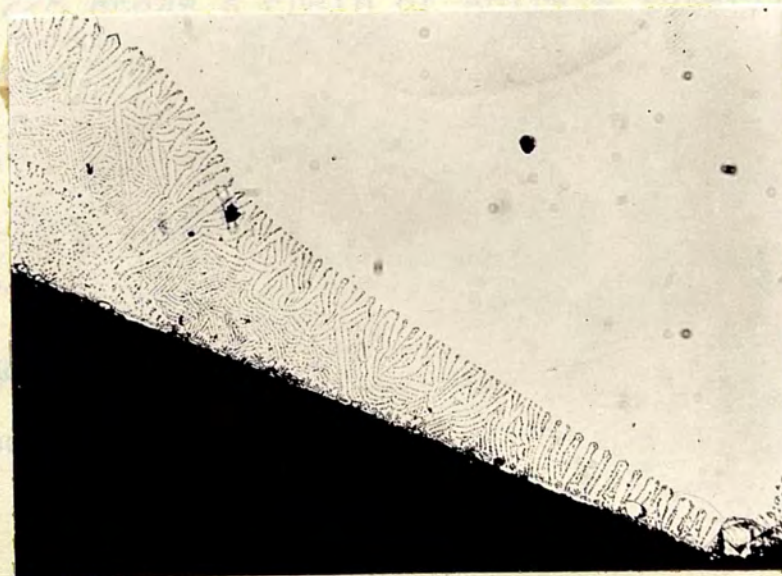


FIG.223

x90

surface-edges of these crystals that the features have been noticed.

Among these crystals one set show a slight similarity in their features; the difference between these features could be due to different stages of growth of the crystals. Figure 224 shows a feature of this set and for convenience sake has been classified as stage (1) of the growth. It consists of curved lines with spots all around. Figure 225 is similar to figure 224 but appears at the corner of a crystal. Figure 226 shows features akin to 224 but with a tendency to form spirals. In the picture one spiral is clearly seen but a closer observation will show that there is a tendency for the formation of two more spirals near the edge of the crystal surface. This has been classified as stage (2) of growth. Figure 227 shows a 'Frank-Reed' spiral at the edge of the crystal surface. This may be treated as stage (3) of crystal growth.

Figure 228 shows a chain of spirals interlinked, starting with a 'Frank-Read' spiral which is linked to a simple right-handed (anti-clockwise) spiral. The simple spiral is linked to another incomplete spiral which is left-handed; this incomplete spiral is further linked to another incomplete spiral which is right-handed. This is classified as stage (4) of growth.



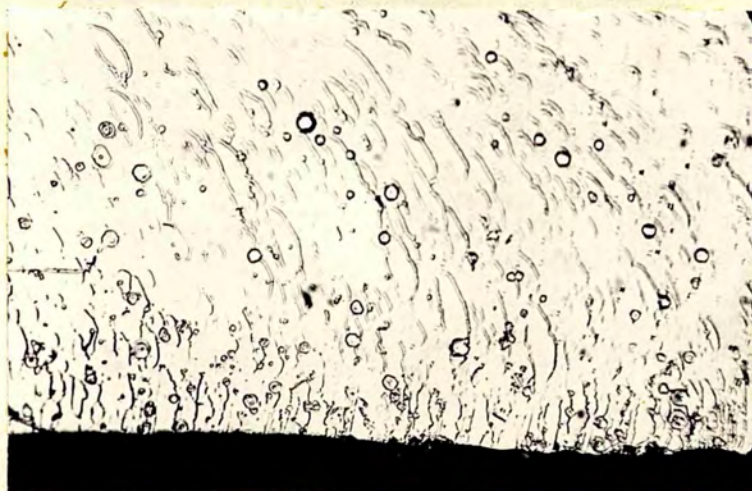


FIG. 224  
x90

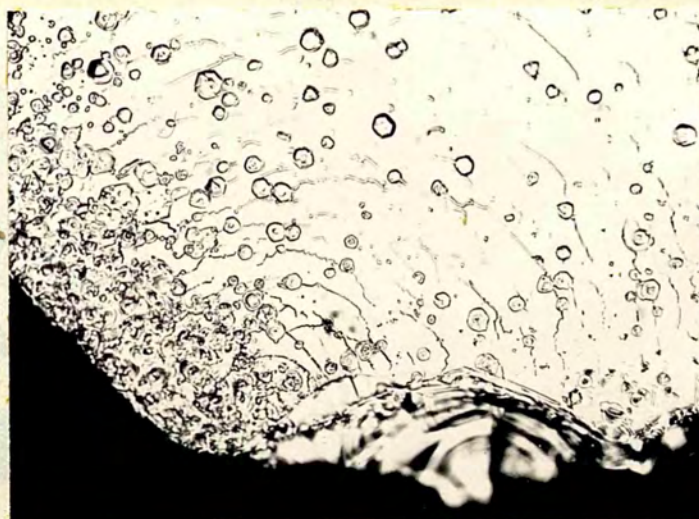


FIG. 225  
x90

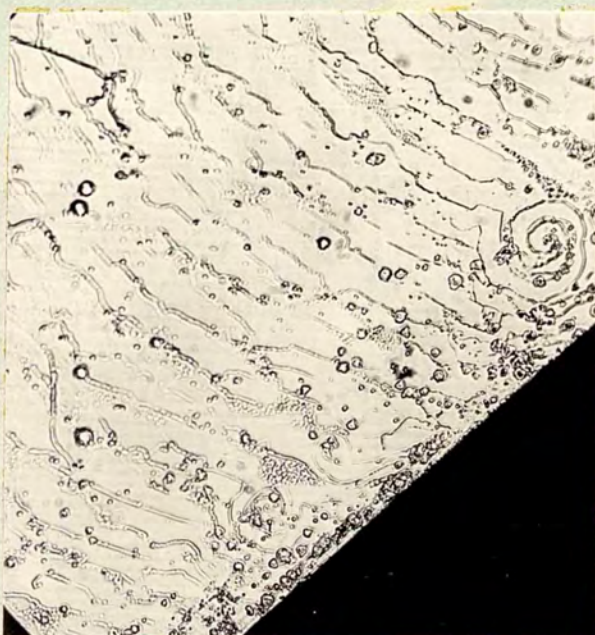


FIG. 226  
x90



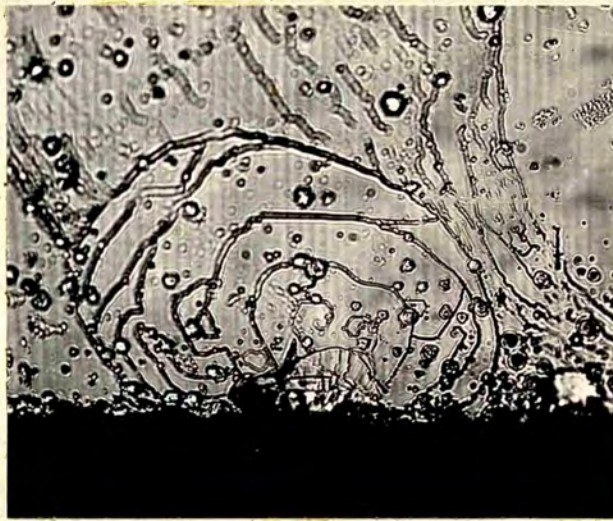


FIG.227  
x90

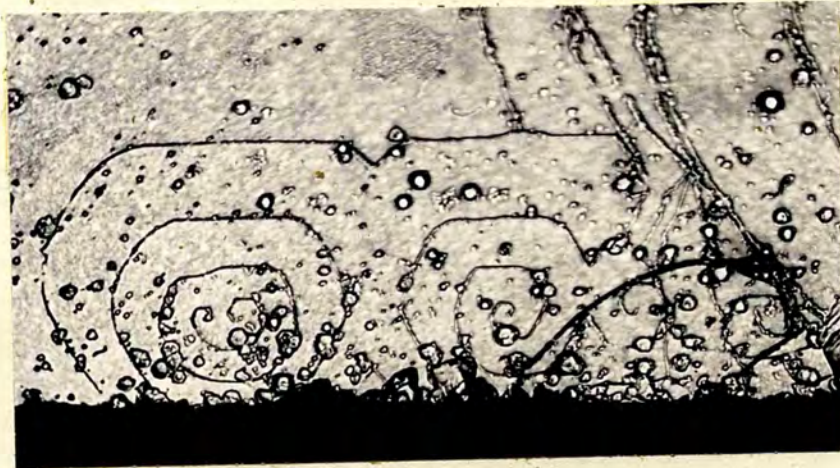


FIG.228  
x90



FIG.229 x90



FIG.230 x90



The classification of the stages has been made on the presumption that if stage (1) is allowed to continue for a longer time, the higher stages might result from it.

It is, indeed, difficult to imagine such concentration of spirals at the edges of the crystal face, if the entire crystal were to grow by spiral mechanism!

Figure 229 shows the surface edge of another class of crystals. The features look like curved strings with cusps.

Figure 230 shows the picture of the side edge of a basal plane.

CHAPTER XIV

INTERFEROMETRIC STUDIES OF THE SAWN SURFACES OF DIAMOND

Introduction

The use of shaped diamonds for trueing and dressing of grinding wheels has increased considerably particularly in regard to the grinding wheels used in the manufacture of precision-ground parts for jet aircraft and guided missiles. More and more of these parts are being produced each year and it is considered that the demand for chisel-edged wheel truers and dressers will increase accordingly.

Although the characteristics of these shaped diamonds are sufficiently superior to those of other materials, their cost of production is, at present, a possible deterrent to their use on a large scale. So attempts are being made to reduce the cost of manufacture of shaped diamond tools to high precision limits.

It is the general practice, when making tools which require shaped stones, to choose diamonds which have approximately the same form as the final tool. Although this might help in making the tool easily and quickly, it may not be possible to ensure that the diamond will be oriented correctly in the tool. There are two important points to be remembered in this connection; first that the cleavage planes in the diamond tool-tip must be perpendicular to the direction of stress applied by



the work and secondly that the diamond must be presented to the work so that any wear will take place in the direction of maximum hardness.

There are two methods of cutting large stones into smaller portions for various purposes, namely

- (1) cleaving (2) sawing.

Cleaving: Diamonds can be divided into smaller pieces suitable for tools by cleaving; that is they can be split along planes which lie parallel to the four octohedron faces. Once the crystalline form of the stone has been recognized, cleaving provides a quick and efficient method of division.

Sawing: Diamonds can be sawn relatively easily into smaller pieces provided the saw cuts are made in the correct directions. The directions in which a diamond can be sawn do not coincide with those in which it can be cleaved; they are parallel to the cube and dodecahedron planes,

#### The Finish of Sawn Diamond

Since sawing plays a very important role in the fabrication of diamond and the production of shaped diamond tools, the study of the sawing process is really important for industry. The saws used are thin circular blades clamped between solid discs to increase stiffness. They are rotated at very high speeds. A cream of oil and diamond dust is fed on the blade and the diamond to

be cut is allowed to rest on the blade, effectively loaded by a gravity feed. In practice a long bank of rotating machines is set up and the oil-diamond cream is replenished at intervals, which may well be half-hourly (1960).

Some work to study the finish of sawn diamond faces has already been done in Tolansky's laboratories. Tolansky (1960) has shown, using interferometry, that the finish after sawing is remarkably good in parts and also sawing action is accompanied by a polishing action. If the sawing process can be improved to give a uniform finish on the sawn surface, then less labour will be involved in final polishing. Based on his interferometric studies, Tolansky had suggested that the sawing technique could be improved if instead of manual intermittent feed, a continuous feed of diamond dust is given to the sawing blades.

#### Present work

In this work seven sawn surfaces of diamond were studied interferometrically and it was found that the observations were similar to those already made by Tolansky. Figures 231a, 231b and 231c show the Fizeau fringes on the entire sawn face of a diamond taken in that order. Figures 232a, 232b and 232c show similar fringes on the other sawn surface of the same diamond. It is interesting to note that there is no similarity in the nature of the fringes on the two faces as one





FIG.231a  
x 900

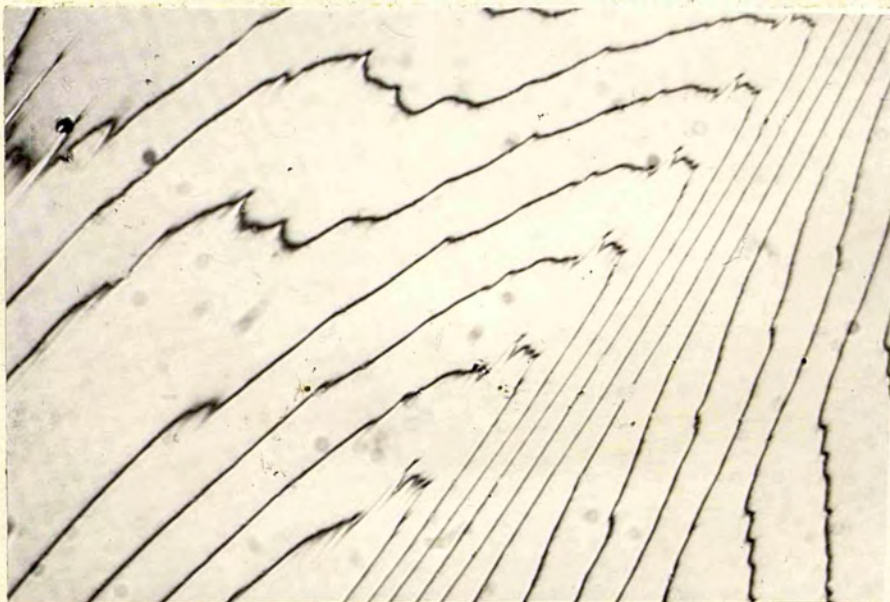


FIG.231b  
x90



FIG.231c  
x90



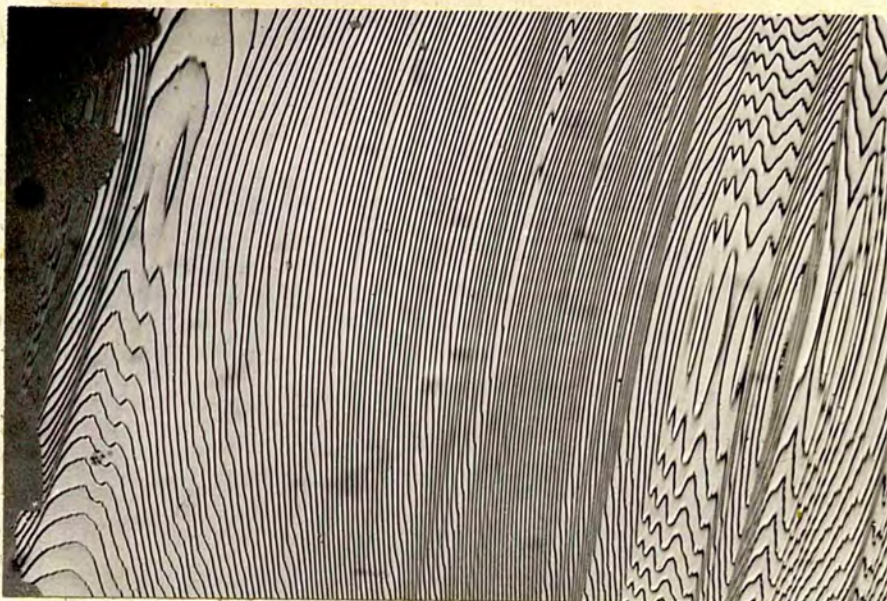


FIG. 232a  
x 90



FIG. 232b  
x90

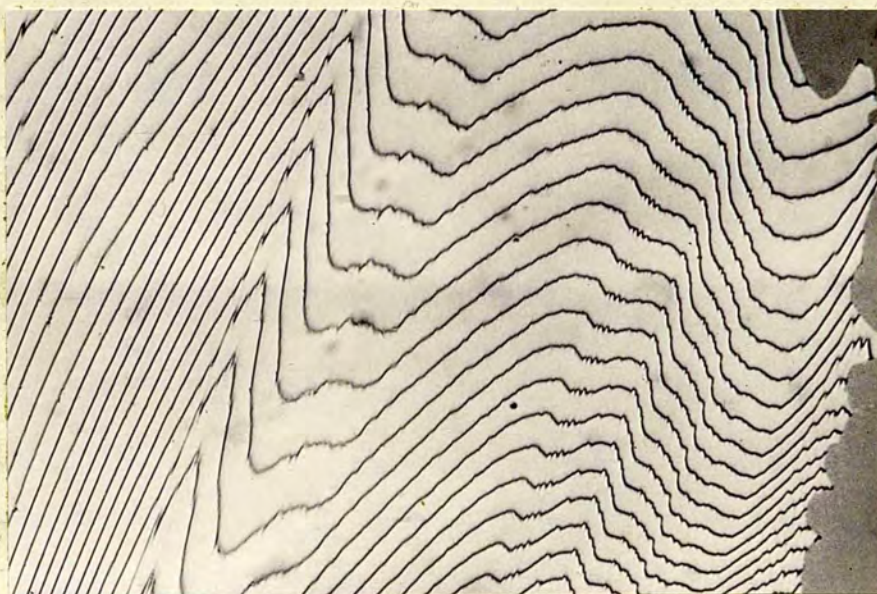


FIG. 232c  
x 90



might expect. Face 231 gives indications of a better finish than face 232. As was pointed out by Tolansky the sawn surfaces show an alternating succession of ragged and smoother regions. This has been found to be the case in the other sawn surfaces.

Figures 233a and 233b show the Fizeau fringes on a different sawn surface. Here the frequency of raggedness is more than in the earlier example. Figure 233b shows the occasional spherical nature of the sawn surface. Treating the fringes as Newtons rings, the radius of curvature is found to be about 30 cm.

Figures 234a and 234b represent the Fizeau fringes on two opposite sawn faces of a diamond. These two faces show a slight similarity in their fringe pattern.

Figures 235 and 236 show the Fizeau fringes on two different sawn surfaces. Figure 235 indicates how sometimes it is possible to get a smooth sawn surface. Figure 236 indicates that though the surface is a little uneven, it is not as ragged as most of the other sawn surfaces.

Figures 237a and 237b show the fringes at different parts of the same sawn surface. Figure 237a gives the fringes near the edge of a sawn surface; the frequent ragged and uneven nature of the surface exhibited by the fringes indicates the wobbling of the sawing wheel in the initial stages of sawing. Figure 237b gives the fringes



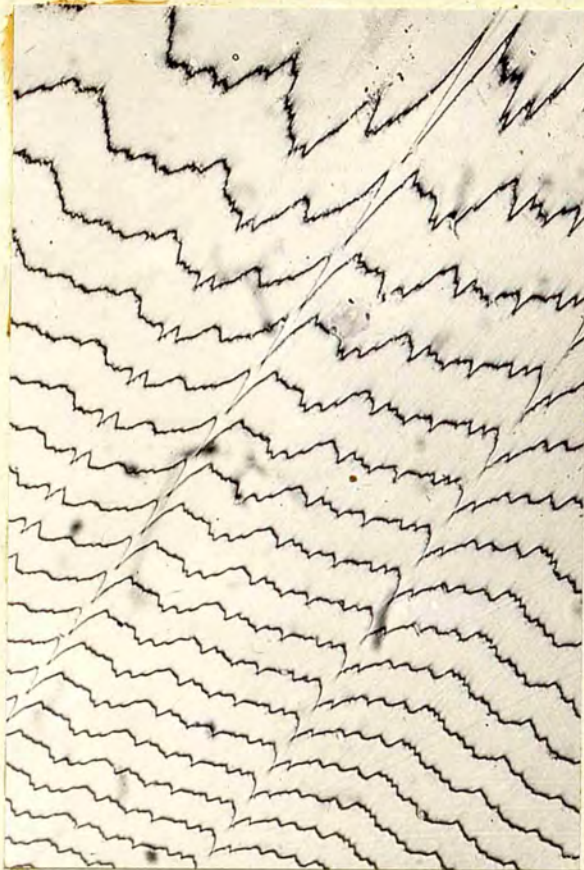


FIG.233a  
x90

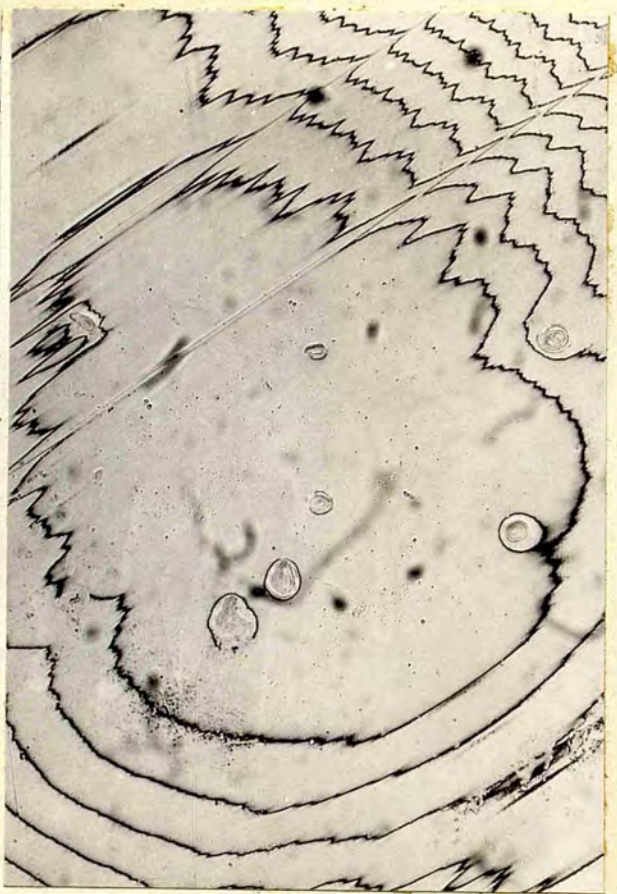


FIG.233b  
x90



FIG.234a x90



FIG.234b x90



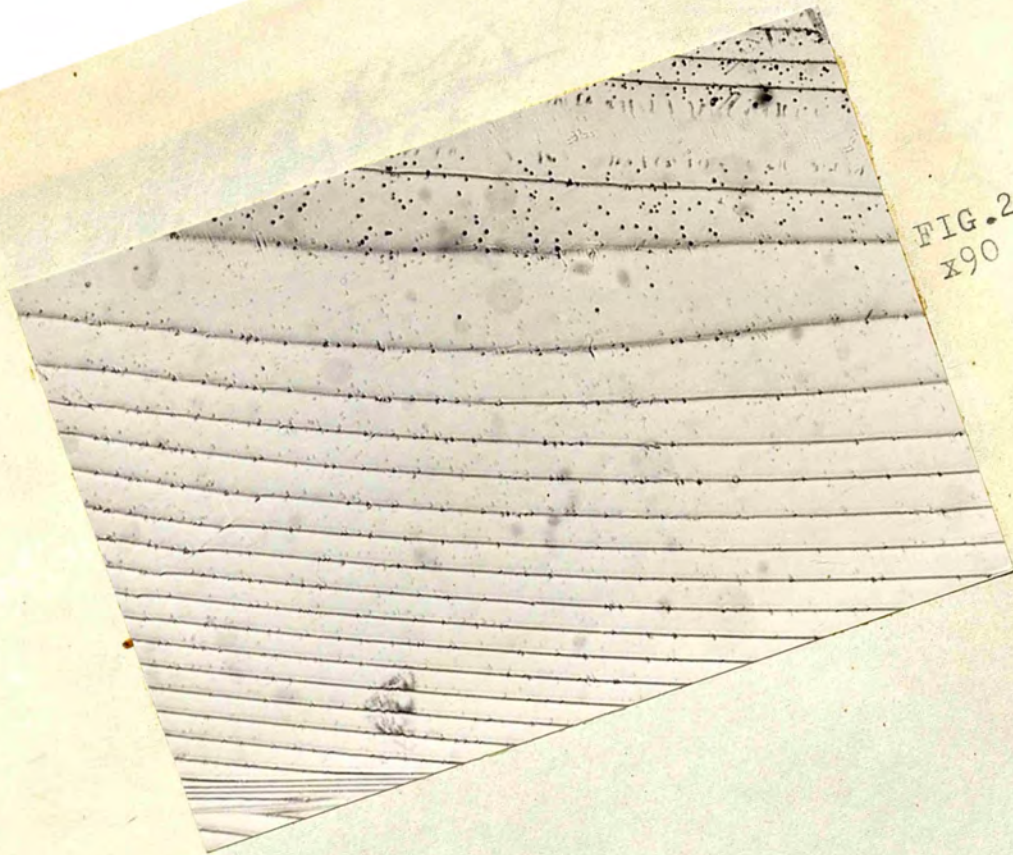


FIG. 235  
x90

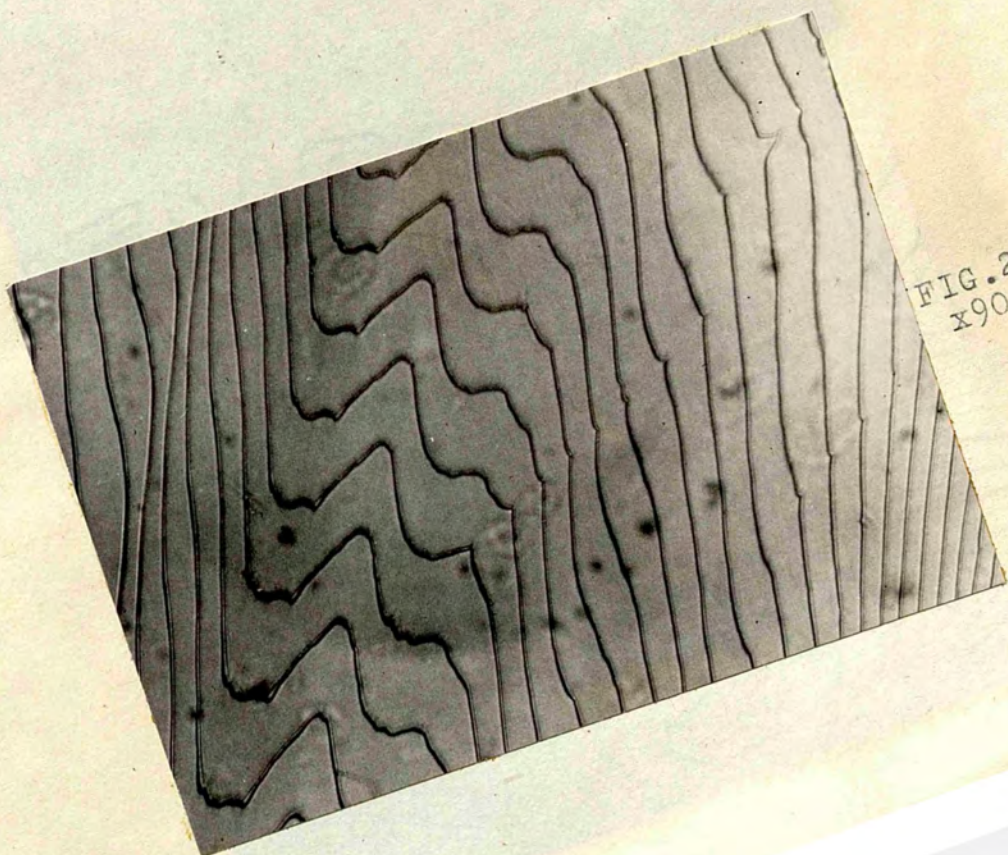


FIG. 236  
x90



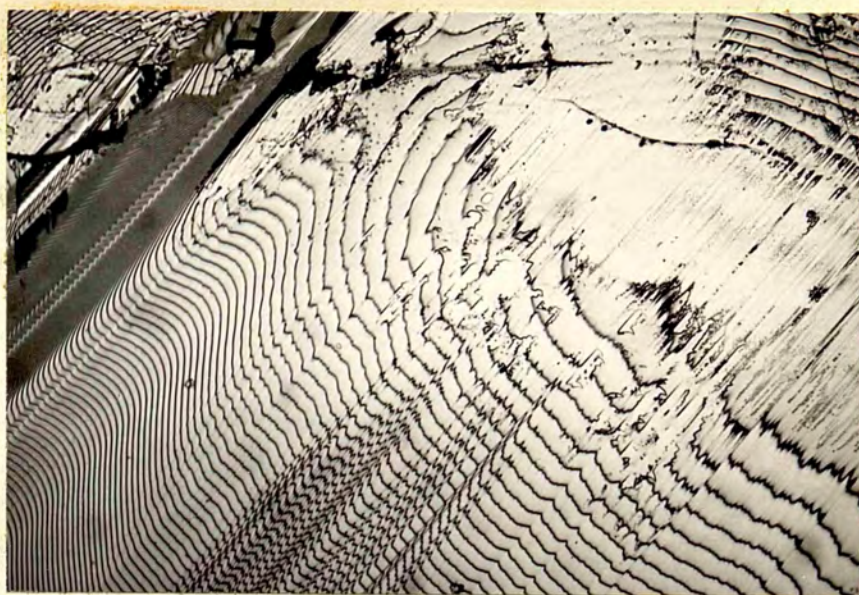


FIG. 237a  
x90

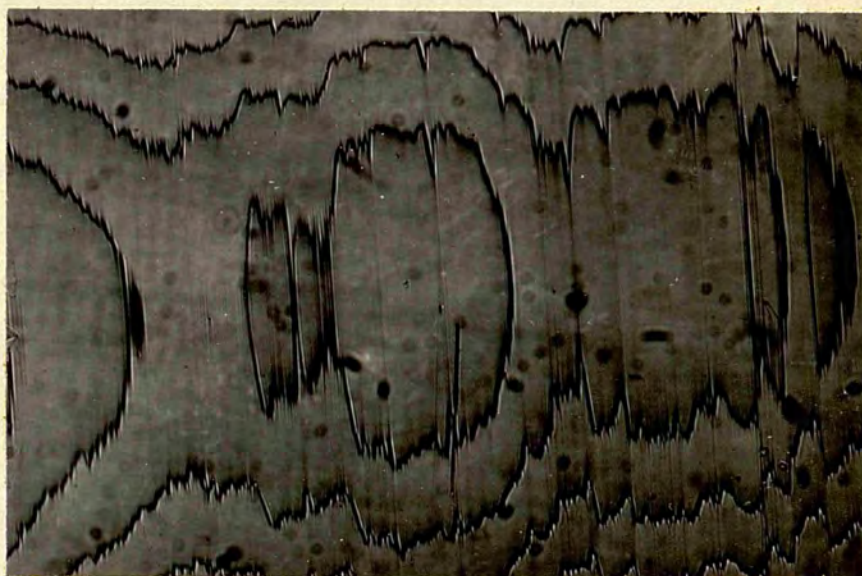


FIG. 237b  
x90



FIG. 238  
x90



on the same surface away from its edge; these fringes also show frequent raggedness. It, therefore, appears that if the saw is not steady right from its initial stage of sawing, it will give a bad finish to the entire sawn surface.

Figure 238 shows fringes at the edge of another sawn surface. The radius of curvature of the ditches is again of the order of 30 cm. The cylindrical depressions shown by the fringes have an approximate radius of 4 cm.

To suggest further improvements to the technique of sawing it will be necessary to study the sawing conditions which could lead to sawn surfaces given by figures 235 and 236.



REFERENCES

- Amelinckx, S and Votava, E. (1953) Nature, 172, 538
- Andrade, E.N. da C., and Roscoe, R. (1937) Proc. phys. Soc.  
49, 152
- Arbittin, E and Murphy, G. (1953) U.S.A.E.C. Publ. ISC-356
- Ashby, N.A. (1951) N.Z. Engng. 6, 1, 33
- Bailey, J. (1939) Glass Ind. Jan-April
- Bennett, A.H., Osterberg, H., Jupnik, H., and Richards, O.W. (1951)  
Phase Microscopy, Chapman & Hall, London
- Becker, R and Doring, W. (1935) Ann. Phys., 24, 719
- Becker, R. (1949) Disc. Faraday Soc., No. 5
- Bergsman, E.B. (1945) The Microhardness Tester, Stockholm.
- Bergsman, E.B. (1951) Am. Soc. Met. Bull, 37, 176
- Braun, A. (1953) Schweiz Arch. angew. Wiss., 19, 67
- Bravais, A. (1866) A Etudes Cristallographiques, Gauttrier  
Villars, Paris
- Brinell, J.A. (1900) 2nd cong. Int. Methodes d'essai, Paris
- Brodie, C.B and Smoluchowski, R. (1945) Trans. Amer. Soc.  
Metals-Disc., 35, 374
- Brumfield, R. (1922) Proc. Amer. Soc. Test. Mat., 22, 312
- Bunn, C.W. and Emmett, H. (1949) Disc. Faraday soc. No. 5. p. 119
- Bunn, C.W. (1946) Chemical Crystallography, Clarendon Press
- Burgers, J.M. (1939) Proc. Acad. Sc. Amst., 42, 293, 378
- " (1940) Proc. phys. soc., 52, 23
- Burton, W.K. (1951) Penquin Science News, 21, 26
- Burton, W.K and Cabrera, N. (1949) Disc. Faraday soc.  
No. 5. (crystal growth)
- " " and Frank. (1949) Nature, Lond. 163, 398
- " " (1951) Phil. Trans. A, 243, 299

- Cabrera, N. (1953). J. Chem.phys., 21, 1111
- Cabrera, N and Levine, M.M. (1956) phil. Mag., 5, 450
- Cardullo, F.E. (1924) Mech. Engng., N.Y. 46, 658
- Cottrell, A.H. (1958) Dislocations and Plastic Flow in  
Crystals - Clarendon Press, Oxford
- Curie, P. (1885) Bull. Soc. franc. Miner. 8, 145
- Daniels, F.W. and Dunn, C.G. (1949) Trans. Am. Soc. Met.,  
41, 419
- Darwin, C.G. (1914) phil. Mag., 27, 315, 675
- " (1922) " " , 43, 800
- Davies, R.M. (1949) Proc. Roy. soc., A, 197, 416
- Donnay, J.D.H. (1937) Am. Min., 22, 446.  
and Harker, D.
- " (1937) C.R. Acad. Sc. Paris, 204, 274
- " (1938) Am. Min., 23, 5
- " (1939) ibid, 24, 184
- Dukova, E.D. (1961) Soviet physics - crystallography  
Vol. 6. No.3. p.357
- Elan, C.F. (1936) The Distortion of Metal Crystals, Oxford.
- Frank, F.C. (1951) phil. Mag., 42, 1014
- Foss, F and Brumfield, R. (1922) Proc. Amer. Soc. Test.  
Met., 22, 312
- Frenkel, J. (1926) Zeit Phys., 37, 572
- " (1945) J. Physics, Moscow, 9, 392
- " (1946) Kinetic theory of Liquids, Oxford.
- Gasilova, E.B., Beletskii, M.S., and Sokhor, M.I. (No.1.1952)  
Dokl, Akad. Nank. sss R, 82, 57-60(in  
Russian)



- Gasilova, E.B. and Sokhor, M.I. (No.2.1952). Dokl, Nank.  
sssR. 82, 249-252
- Gibbs, J.W. (1878) Collected Works (1928) - Longman Green
- Griffith, A.A. (1921) Phil. Trans. Roy. Soc. A, 221, 163
- Grodzinski, P. (1951) J. Sc. Inst., 28 (suppl), 117
- " (1951) Ind. Dia. Inf. List 101 A
- " (1952) " " 102 A
- Hankins, G.A. (1925) Proc. Instn. Mech. Engr., 1, 611
- Henry, N.F.M. and Lipson, H. and Wooster, W.A. (1953)  
The Interpretation of X-ray Diffraction Photo-  
graphs, Mac.Millan & Co.
- Hertz, H. (1881) Miscellaneous Papers(1896) (English  
Translation,) London.
- Hill, R. Lee, E.H. and Tupper, S.J. (1947) Proc. Roy.  
Soc. A. 188, 273
- Hill, R. (1950) The Mathematical Theory of Plasticity,  
Oxford.
- Holm, E. Holm, R. and Shobert, E.I. (1949) J. App.Phys.  
20, 319
- Howes, V.R. and Tolansky, S. (1955) Proc. Roy. Soc.,A,230,287
- " " (1955) Proc. Roy. Soc., A, 230,294
- Huber, A.T. (1904) Czasopismo techniczne, Lemberg .
- Jagodzinski, H. (1954) Acta Cryst.,2, 300
- Knoop, F., Peters, C.G. (1939) National Bureau of Standards,  
and Emerson, W.B. 23 (1), 39
- Kossel, W. (1927) Nachr, Ges. Wiss, Gottingen, 135
- " (1928) in Falkenhagen Quantentheorie and Chemie,  
p 46, Leipzig.
- Krupkowski, A. (1931) Rev. Metal., 28, 641
- Lemmlein, G.G. (1957) Soviet Physics - crystallography,  
and Dukova,E.D. Vol 2, No.3, p.426  
and Chernov. A.A.

- Ludwik, P, (1908) 'Die Kegelprobe' springer, Berlin.
- Lysaght, V.E. (1949) Indentation Hardness Testing
- Machenjie, J.E. (1949) Thesis, Bristol.
- Mahin, E.G. and Foss, G.J. (1939) Trans. A.S.M. 27, 337
- Meincke, H. (1942) Z. Metallk, 34, 289
- " (1950) " 41, 344
- " (1951) Ind. Dia. Rev. 11, 37
- Meyer, E. (1908) Zeit, d. Vereines, Deutsch. Ing., 52, 645
- Meyer, M.A. (1951) Some Aspects of the Hardness of Metals,  
Thesis, Drecht.
- Mises, R. Von (1913) Nachr,d.Gesell, Gottingen. Math.phy.  
Klass, 582
- Mohr, O. (1900) Zeits.d.Vereines, Deutsch. Ingenieure, 44,1
- Mohs. F. (1822) Grundriss der Mineralogie, Dresden
- Mott, B.W. (1956) Micro-Indentation Hardness Testing,  
Butterworths.
- O'Neill, H. (1923) J. Inst. Met., 30, 299
- O'Neill, H. (1934) The Hardness of Metals and its  
Measurement, Chapman
- O'Neill, H. and Cuthbertson, J.W. (1931) J. Inst. Met.,  
46, 288
- Onitsch, E.M. (1947) Mikroskopie, 2, 131
- Orowan, E. (1934) Z. phys. 89, 634
- " (1940) Proc. phys. soc., 52, 8
- Ott, H. (1925) Zeits für Krist. (A), 61, p.515
- " (1925) " " 62, p.201
- " (1926) " " 63, p.1.
- Pandya, N.S. and Tolansky, S. (1954) Proc. Roy. Soc.  
A. 225, 40



- Perryman, E.C.W. (1950) Metal Ind., Lond., 76, 23
- Phillips, F.C. (1949) An Introduction to Crystallography,  
Longmans.
- Polanyi, M. (1934) Z. Phys., 89, 660
- Preston, F.W. (1921) Trans. Opt. Soc. Lond., 23, 141
- Raman, C.V. (1926) J. Opt. Soc. Amer., 12, 387
- Ramsdell, L.S. (1944) Am. Min., 29, p.431
- " (1945) " 30, p.519
- " (1947) " 32, p.64
- Ramsdell, L.S. and Kohn, J.A. (1951) Acta Cryst. 4, 111-13
- " " (1952) " 5, 215-24
- Richer, G.C. (1945) Metallurgia Manchr, 31, 296
- Rockwell, S.R. (1922) Trans. Am. Soc. for Steel Treating 2, 1013
- Schmid, E. (1924) Proc. Int. Cong. App. Mech. Del. 342
- Schmid, E and Boas, W. (1950) Plasticity of Crystals -  
Hughes, Lond.
- Schulz, F and Hanemann, H. (1941) Z. Metallk, 33, 124.
- Smith, R. and Sandland, G. (1922) Proc. Inst. Mech. Eng.  
1, 623
- Stern, W. (1952) Ind. Dia. Rev., 12, 136
- Tabor, D. (1948) Proc. Roy. Soc. A. 192, 247.
- " " Engineering, 165, 289
- " (1951) The Hardness of Metals, Oxford.
- " (1954) Sheet Metal Ind., 31, 749
- Tarasov, L.P and Thibault, N.W. (1947) Trans. Am. Soc.  
Metals, 38, 331
- Taylor, G.I. (1934) Proc. Roy. Soc., A. 145, 362.
- Taylor, A. and Laidler, D.S. (1950) Br. Jour. App. phy.  
1, 174-81

- Thibault, N.W. (1944) Am. Min., 29, p.249
- Timoshenko, S. (1934) Theory of Elasticity, Mc.Graw-Hill,  
New York
- Tolansky, S. (1961) Nature, 190, 992
- " (1960) Surface Microtopography, Longmans
- " (1948) Multiple Beam Interferometry of surfaces  
and Films, Oxford.
- " and Williams A.P. (1955) Proc. Phys. Soc., 68, 548
- Tolansky, S. and Nichols, D. (1952) Phil. Mag., 43, 410
- " " (1949) Nature, 164, 103
- " " (1949) ibid, 161, 840
- Tresca, H. (1864) C.R. Acad. Sc., Paris. 59(2), 754.
- Tuckerman, L.B. (1925) Mech. Eng., 47, 53
- Verma, A.R. (1953) Crystal Growth and Dislocations,  
Butterworths.
- Volmer, M. and Estermann, I. (1921) Z. Phys., 7, 13
- Volmer, M. and Schultz, W. (1931) Z. phys. Chem. A, 156, 1
- Von Mises, R. (1913) Nochr d. Gesellschaftd Wiss. Zu  
Gottingen, Math-phy Klasse, 582
- Waizenegger, F. (1921) Forch. Ing. Wes., 238
- Williams, S.R. (1942) Hardness and Hardness Measurements,  
Am. Soc. Met.
- " (1949) Metal Progress, 56, 811
- Wilson, A.J.C. (1949) X-ray optics, Methuen & Co.
- Wychoff, R.W.G. (1948) Crystal structures, sec I, Inter Sc.  
Pub., New York.
- Yakutovich, M.V. (1948) Zavod Lab., 14, 338  
and Vandyshv, B.A.  
and Surikoya, E.E.
- Zwikker, C. (1954) Physical Properties of Solid Materials,  
Pergamon Press, Lond.



ACKNOWLEDGEMENTS

I wish to express my sincere thanks to Professor S. Tolansky, F.R.S. for his continued guidance and encouragement throughout my stay at Royal Holloway College. I also wish to thank my Colleagues for helpful discussion and to the Laboratory staff for their help and co-operation.

My thanks are due to Professor Bernal for offering facilities to carry out X-ray work at Birkbeck College. I am grateful to Dr. J.W. Jeffery for his suggestions in the X-ray analysis of crystals and to Dr. A.P. Seager for his help in the identification of some crystal faces.

I take this opportunity of thanking Philips Elect.,Ltd., Eindhoven, Holland and Westinghouse, Connecticut, U.S.A for the supply of silicon carbide crystals.

Finally, I would like to thank the Government of Madhya Pradesh (India) for the grant of study leave, the British Council for a travel grant, the University of Jabalpur (India) for financial aid and the Royal Holloway College Council for the award of a post-graduate studentship.